Imperial College London
Department of Aeronautics

Adaptive Shock Control Bumps

Edward Jinks

September 2016

Submitted for partial fulfilment of the requirements for the degree of Doctor of Philosophy in Aeronautics at Imperial College London

Abstract

The evolution of Adaptive Shock Control Bumps (SCB) presented in this work is a result of an investigation into transonic flow control devices. The primary application is on transonic passenger jet aircraft during cruise and within supersonic intakes. It is in these locations that normal shocks of strength Mach 1.2-1.5 typically occur which SCB aim to manipulate and exploit.

The original concept was developed by [Ashill et al., 1992] featured a flexible plate with actuators beneath the surface. The complex fluid-structure interaction (FSI) between the shock and plate has been a focus of this work with panel flutter studies heavily supplementing traditional SCB design methods. Adaptive SCB represent a required approach in order to negate poor off-design performance of static SCB.

A coupled 2D aero-structural solver was developed using OpenFOAM [2017] and ABAQUS [2007] which provides a tool to evaluate the effects of varying plate properties. Cavity pressure, plate length, thickness and material stiffness were found to be influential in the overall performance with four test cases developed. With lengths, $l_b = 150 - 200\,\text{mm}$ and thicknesses $t = 0.4 - 0.6\,\text{mm}$ using Al-7075-T6, experimental models were produced and tested in a Mach 1.4 blowdown supersonic wind tunnel. These were sized using the coupled solver to deform passively and trigger the bifurcation of the shock. This new type of device showed potential for a passive adaptive SCB however all suffered from varying amounts of reacceleration over the rear surface.

An aero-structural optimisation procedure is performed to position displacement constraints beneath the flexible plate to control surface curvature. This was the driving force behind the detrimental reacceleration. The optimiser used a new performance metric which focussed upon smearing the adverse pressure gradient across the SCB which reduced the likelihood of plastic deformation.

Optimal SCB have been shown to deploy and retract beneath an unsteady shock and successfully bifurcated the shock on demand.

Acknowledgements

Firstly I would like to thank my partner Lucy and son Samuel who have made the writing up stage about so much more than just the thesis and added a whole new level of happiness to my life.

I am also very grateful for the support of both my supervisors Dr. Matthew Santer and Dr. Paul Bruce who have tested my understanding and offered constructive insights throughout this research project. Their respective expertise have helped significantly in the development of this multi-disciplinary project. The countless iterations of conference papers and thesis drafts have all been appreciated throughout the project as has their support in the last year whilst it has been a busy time for myself. Their encouragement to present at numerous conferences was a great opportunity to showcase my work on an international level and with very positive experiences.

All of the academic and administrative staff in the Department of Aeronautics have made Imperial College a pleasant place over the past four years of this project and the preceding four during my undergraduate studies. The Aeronautics workshop in particular have both provided excellently machined parts as well as valuable information regarding drill speeds and sizes for machining around flexible plates. This gave me (some) knowledge in order to machine the plates myself and actually put into practice which I thoroughly enjoyed.

I must also recognise the EPSRC for the funding of this research through a DTA studentship within the department. The City and Guilds College Association - Old Centralians' Trust and the IC trust provided the funding for conferences which provided great feedback for the work I was conducting as well as interesting views on the future direction of research.

Sincere thanks must also go to my parents and Lucy's parents for the unfaltering background support they have offered throughout this project and my time entire time at Imperial from my first day as an undergraduate to the submission of this dissertation.

Declaration

I hereby declare that the results presented in this dissertation are the result of my own work and all other views and results have been referenced appropriately.

Signed: .....

Date: .....

The copyright of this thesis rests with the author and is made available under a Creative Commons Attribution Non-Commercial No Derivatives licence. Researchers are free to copy, distribute or transmit the thesis on the condition that they attribute it, that they do not use it for commercial purposes and that they do not alter, transform or build upon it. For any reuse or redistribution, researchers must make clear to others the licence terms of this work.

Contents

1. Introduction **1**

2. Literature Review **4**

2.1. The Transonic Regime 4

2.1.1. Transonic Shock Structures 6

2.1.2. Incipient Separation 10

2.2. Control Devices 11

2.2.1. Boundary Layer Control Devices 11

2.2.2. Shock Control Devices 13

2.3. Current Static SCB 19

2.3.1. SCB Parameterisation 19

2.3.2. SCB Operational Envelope 22

2.3.3. Optimisation 28

2.3.4. Off-Design Performance of SCB 30

2.4. Adaptive Shock Control Bumps 33

2.4.1. Structural Modelling of Adaptive SCB 36

2.4.2. Aerodynamic Modelling of Adaptive SCB 38

2.4.3. Aero-structural Modelling of Adaptive SCB 41

2.5. Summary of Existing Research 48

3. Adaptive SCB Design **51**

3.1. Theoretical and Computational Approach 51

3.1.1. Initial Sizing and design of Adaptive SCB 54

3.1.2. Structural Modelling 59

3.1.3. Designing Plates for Static Shockwaves 61

3.1.4. Panel Flutter Considerations 65

3.1.5. Designing Plates for Dynamic Shockwaves 67

3.1.6. Designing Plates Summary 73

3.1.7. Developing Adaptive SCB for Integration into Aerofoil Design . 73

3.1.8. Aerodynamic Modelling . . . 73
3.1.9. Coupling the Aerodynamic and Structural Solvers . . . 78
3.2. Experimental Approach . . . 80
3.2.1. Wind Tunnel . . . 80
3.2.2. Schlieren Imaging . . . 82
3.2.3. PIV Setup . . . 87
3.3. Summary of Methods . . . 101

4. Flexible Plates for Adaptive SCB **103**
4.1. The Performance of Flexible Plate Based Adaptive SCB upon Aerofoils 103
4.1.1. Integration into an Aerofoil . . . 103
4.1.2. Aerodynamic Response . . . 106
4.1.3. Aero-structural Response . . . 106
4.2. Time Averaged Experimental Response . . . 109
4.2.1. Aerodynamic Response . . . 110
4.2.2. Plate Response . . . 113
4.2.3. Fluid-Structure Interaction . . . 115
4.3. Transient Experimental Response . . . 121
4.3.1. Shock Motion . . . 121
4.3.2. Plate Motion . . . 125
4.3.3. Unsteady Fluid-Structure Interaction . . . 130
4.4. Summary of Flexible Plates for Adaptive SCB . . . 135

5. Optimising Designs for Adaptive Shock Control Bumps **139**
5.1. Approach . . . 139
5.1.1. Bump Parameterisation . . . 140
5.1.2. Integration of the Aero-Structural Solver into the Optimisation Process . . . 144
5.1.3. Performance Metric . . . 145
5.2. Results . . . 151
5.2.1. Optimal Adaptive SCB designs . . . 151
5.2.2. Off-Design Performance . . . 155
5.3. Summary of Optimal Adaptive SCB Design . . . 162

6. Actuated Adaptive SCB **166**
6.1. Optimal SCB Test . . . 166

6.2. Experimental Response of an Actuated SCB 173
6.2.1. Aerodynamic Response 173
6.2.2. Plate Response 180
6.2.3. Fluid-Structure Interaction 185
6.2.4. Dynamic Plate Response 189
6.3. Summary of Actuated Adaptive SCB 194

7. Conclusions **196**
7.1. Adaptive SCB Design 196
7.2. Flexible Plates for Adaptive SCB 197
7.3. Optimising Designs for Adaptive Shock Control Bumps 199
7.4. Actuated Adaptive SCB 201
7.5. Recommendations for Further Work 202
7.5.1. FSI surrounding plates and shocks 203
7.5.2. Application of Adaptive SCB 203

A. Appendix: Design and Manufacture of Wind Tunnel **213**
A.1. Converging-Diverging Nozzle 213
A.1.1. Throat Region 214
A.1.2. Subsonic Contraction 215

B. Appendix: PIV Calculations **217**

List of Tables

2.1. Drag breakdown of ADIF aerofoil fitted with SCB, $h_b = 0.175\%$ and $h_b = 0.35\%, M = 0.757$, for two different C_l values, [Le Balleur et al., 2002]. 26

3.1. FEA mesh attributes. 61
3.2. Calculated pressure values for loading presented in figure 3.8 63
3.3. The effects of varying plate thickness upon a flexible plate sized to typical SCB dimensions. $P_2 = 0.5\,P_0$, $P_{cavity} = 0.75bar$. 63
3.4. Dimensions of plate test cases. Constant span of 150 mm 66
3.5. Mesh Characteristics 76
3.6. Key PIV experimental setup parameters. 90
3.7. Comparison of dynamic spatial and velocity ranges between a selection of PIV studies highlighted by Westerweel et al. [2013] across a range of Re_θ. 99

4.1. A summary of the three discrete cavity pressure loading cases. 104
4.2. Average shock angles away from the wall derived from the Schlieren images in figure 4.6 with effective deflection angle based upon equation 4.2 and a free stream Mach number of 1.38. The average surface deflection up to the plate crest is also included. 116
4.3. The streamwise locations of the shock, the plate crest and the distance between the two expressed as a percentage of bump length. 133

5.1. Optimal SCB decision variables for the initial condition and optimal solution, 2 point actuation. 152

B.1. Key PIV experiment setup parameters. 220

List of Figures

1.1. Qualitative effect of free-stream Mach number on a thin airfoil at constant angle of attack [Massey and Ward-Smith, 2006] 2
1.2. Shock structure illustrated by sonic line. a) Typical transonic aerofoil. b) Transonic aerofoil fitted with adaptive SCB. Adapted from Ashill et al. [1992]. 3

2.1. Typical pressure distribution around transonic aerofoils. a) Turbulent aerofoil. b) Natural laminar flow aerofoil. 5
2.2. Examples of applications within the transonic regime. a) External compression ramp inlet. b) Internal compression inlet. c) Turbine fan cascade. Adapted from Babinsky and Harvey [2011] 7
2.3. Weak shock, adapted from Ogawa et al. [2008] 9
2.4. Strong Normal Shock. Adapted from Seddon [1967] 10
2.5. Typical pressure rises for Mach 1.3, weak interaction and Mach 1.5, strong interaction for both inviscid solution and experimental viscous solutions. Adapted from Ogawa [2006]. 11
2.6. Effect of vortex generator on shock structure. 12
2.7. The Bifurcated shock structure. 14
2.8. Perforated Cavity 15
2.9. Perforated cavity with targeted suction. 16
2.10. Original SCB concept by Ashill et al. [1992] 17
2.11. Ideal shock structure over a SCB. 18
2.12. SCB geometry families as described by Sommerer et al. [2000b]. a) Loaded Beam. b) Wedge. c) Concave polynomial. d) $11th$ Order Polynomial 20
2.13. Typical SCB optimisation parameters. θ, front ramp angle. c_b, location of crest, h_b, height of crest. l_b, length of SCB. 21

2.14. Pressure profile for clean ADIF aerofoil and two SCB geometries with varying height, Stanewsky [2000]. $M_\infty = 0.765, \alpha = -0.5°, Re = 8 \times 10^6, C_l \sim 0.6$. 24
2.15. Shock region of figure 2.14 with key pressure gradient annotations. ADIF Aerofoil. Favourable pressure gradient (FPG), adverse pressure gradient (APG). 25
2.16. C_l vs. C_d polars for clean ADIF aerofoil and two SCB geometries with varying height, Stanewsky [2000]. $M_\infty = 0.765, Re = 8 \times 10^6$. 25
2.17. Schematic diagram illustrating target pressure coefficient distribution around a turbulent airfoil. 27
2.18. General SCB optimisation process flow chart. 29
2.19. Typical shock structures for typical off-design conditions. a) SCB too far upstream. b) SCB too far downstream. 31
2.20. Drag breakdown for variable SCB placement upon DA-LVA-1A NLF aerofoil, $M_\infty = -0.76, Re = 6 \times 10^6, l_b = 0.2c, h_b = 0.003c, c_b = 0.5l_b$. a) Total drag. b) Wave drag. c) Viscous drag. The x/c values represent the crest location as a proportion of the total chord. Adapted from Dargel and Thiede [2002]. 32
2.21. Distributed actuation system envisioned by Wadehn et al. [2002], adapted. 35
2.22. Comparison of distributed actuation system by Wadehn et al. [2002] against the reduced actuator model of Rhodes [2012]. The centreline geometry of the default rounded bump by Ogawa et al. [2008] is included to represent the target for adaptive SCB geometries. 35
2.23. a) 2D Model replication of Default rounded bump centreline. b) 3D Model centreline replication of Default rounded bump centreline. Adapted from Rhodes [2012]. 37
2.24. Lift-Drag polar for DA LVA-1A NLF aerofoil, SCB location, $x_{SCB} = 0.6c, l_b = 0.2c$, Variable h_b. Data adapted from Dargel and Thiede [2002]. 40
2.25. L/D variation with ramp angle and variable spacing for 2D and 3D SCB, adapted from Eastwood and Jarrett [2012]. Bump width, $b = 0.1c$. . . 41
2.26. Influential variables in panel flutter studies. 44
2.27. Inviscid oblique shock structure present in Visbal [2014]. 45
2.28. Effect of cavity pressure for inviscid interaction in figure 2.29b with M_1 = 2:0, p_3/p_1=1.4. Time-averaged (a) panel deflection and (b) surface pressure. Adapted from Visbal [2014]. 45

2.29. Expected shock structures for plate geometries subject to variable cavity pressures and Mach 2 oblique shock interaction described by Visbal [2014]. a) $\min(p_{flow}) > P_{cavity}$. b) $\min(p_{flow}) < P_{cavity} < \max(p_{flow})$. c) $P_{cavity} > \max(p_{flow})$. 47
2.30. Streamwise vibration modes as described by Vedeneev et al. [2010]. Cavity volumes comparisons to initial flat plate condition. a) First mode. b) Second mode. 48

3.1. Effect of pressure loading due to controlled shock position upon plate geometry. The cavity pressures are varied with respect to the upper surface pressure. a) Zero aerodynamic loading. b) Shock loading downstream of the plate. c) Shock loading upstream of the plate. d) Shock loading above the plate. 52
3.2. Effect of 2D aerodynamic pressure loading due to controlled shock position upon plate geometry. a) Shock placed towards upstream edge of plate. b) Shock over central region of the plate. c) Shock downstream of the plate. 54
3.3. The cyclic effect of shock structure, pressure gradient and plate geometry. 54
3.4. Histograms showing the typical SCB heights and lengths investigated in recent literature.[1] a) SCB Heights for SCB studies upon aerofoils. b) SCB lengths for SCB studies upon aerofoils. c) SCB heights for wind tunnel studies. d) SCB lengths for wind tunnel studies. 57
3.5. Boundary conditions of flexible plate. 58
3.6. Illustration of expected actuator loading and initial sizings. 60
3.7. FEA mesh convergence study of a span-wise 2 mm out-of-plane actuation at the central location. 62
3.8. Expected pressure values for initial design stage based upon isentropic, oblique and normal shock theories with relations shown in equations 3.1, 3.2 and 3.3. 63
3.9. Flutter dynamic pressure as described by Dowell [1970] with the variation of Mach number. Included are the plate dimensions from table 3.4. . . . 65
3.10. Plate centreline geometries for varying inviscid shock position with constant cavity pressure of 0.55 Bar. Al-7075-T6, $l_b = 200$ mm, width, $b = 150$ mm, $t = 0.4$ mm. 70

3.11. Plate centreline geometries for varying inviscid shock position and plate thickness with variable cavity pressure. Al-7075-T6, $l_b = 200\,\text{mm}$, width, $b = 150\,\text{mm}$. 71
3.12. von Mises Stresses at plate centre line for varying inviscid shock position and plate thickness with variable cavity pressure. Al-7075-T6, $l_b = 200\,\text{mm}$, $b = 150\,\text{mm}$. 72
3.13. Aero-structural solver module. 74
3.14. Mesh boundary and mesh refinement around the aerofoil nose area (coarse grid shown for clarity). 76
3.15. Mesh Convergence study for RAE2822 aerofoil structured grid. 77
3.16. Experimental and computed CFD pressure profile comparison for the datum RAE2822 aerofoil with no control measures, $\alpha = 3.19°$, M_∞=0.728, $\text{Re} = 2.7 \times 10^6$. Experimental data extracted from Cook et al. [1979] . . 79
3.17. Original concept drawing by Ashill et al. [1992] and the region of interest that is to become the focus of the experimental analysis in the blowdown supersonic wind tunnel. 81
3.18. Z-Type Schlieren arrangement taken from Settles [2001] 82
3.19. Mach 1.4 profile wind tunnel with adaptive SCB fitted. 85
3.20. Example of Schlieren Imaging. Mach 1.4 normal shockwave image taken at 1000 Hz with an exposure time of 10 μs. A vertical knife-edge was used to highlight the streamwise density gradient across the normal shockwave. 86
3.21. Example raw image of supersonic flow over a flexible plate. 88
3.22. Optical setup within Imperial College London blowdown supersonic wind tunnel. a) Schematic. b) Photograph 89
3.23. Lens configuration of laser sheet forming optics. 92
3.24. Photograph during PIV run highlighting the optical distortion in the laser sheet caused by the density changes surrounding the shock region. . . . 94
3.25. Close up views of seeding areas with a) high and low intensity particles. b) shows Glare effects which are caused by 'non-spherical' particles. 95
3.26. Correlation coefficients for each interrogation window from a single image pair taken from a plate length 200 mm, t=0.6 mm subject to Mach 1.4 flow. Field average = 0.79. 96
3.27. Oscilloscope readout with zero timing offset and laser pulse. 97
3.28. Schematic illustrating the timings associated with PIV capture 98
3.29. Zoomed in view in plate region of a) raw image. b) Instantaneous vector field using just 1 image pair. 101

4.1. Typical pressure forces acting upon flexible plate. 104
4.2. Aero-structural response of flexible plate subject to shock loading. The y-axis has been amplified significantly (5×) to show the small difference between each of the aeroelastic iterations. 105
4.3. Mach contours and fields for lower (a,c) and upper (b,d) bounds of crest displacement, iterations 2 and 3 respectively. 107
4.4. Mach contours and fields for the three cavity pressures tested. a) Low cavity pressure, $P_c = \min(P_u)$. b) Mid cavity pressure, $P_c = \text{mean}(P_u)$. c) High cavity pressure case, $P_c = \max(P_u)$ 108
4.5. Aerofoil surface geometries after pressure loading for the three cavity pressures tested and the clean RAE2822 aerofoil. 109
4.6. Schlieren images showing the shock structure for plates of varying length and thickness. a) $l_b = 150\,\text{mm}$, $t = 0.4\,\text{mm}$. b) $l_b = 200\,\text{mm}$, $t = 0.4\,\text{mm}$. c) $l_b = 150\,\text{mm}$, $t = 0.6\,\text{mm}$. d) $l_b = 200\,\text{mm}$, $t = 0.6\,\text{mm}$. 111
4.7. Schematic diagram illustrating the interdependencies governing the flexible plates FSI. 112
4.8. Plate deformation extracted from figures 4.6a & 4.6c $l_b = 150\,\text{mm}$, $t = 0.4\,\text{mm}$ $l_b = 150\,\text{mm}$, $t = 0.6\,\text{mm}$. 114
4.9. Plate deflection angle with respect to the horizontal calculated from the Schlieren images in figure 4.6. 116
4.10. Streamwise velocity for flexible plate $l_b = 150\,\text{mm}$ $t = 0.4\,\text{mm}$. 117
4.11. Vertical velocity for flexible plate $l_b = 150\,\text{mm}$ $t = 0.4\,\text{mm}$ 118
4.12. Streamwise and vertical velocities calculated from PIV data for the flexible plate test cases. 119
4.13. Flow Angles and corresponding plate deflection angles for each of the flexible plate test cases. The plate deflection angles all angles are measured with respect to the horizontal a) $l_b = 150\,\text{mm}$ t $= 0.4\,\text{mm}$. b) $l_b = 150\,\text{mm}$ t $= 0.6\,\text{mm}$. c) $l_b = 200\,\text{mm}$ t $= 0.4\,\text{mm}$. d) $l_b = 200\,\text{mm}$ t $= 0.6\,\text{mm}$. 120
4.14. Normalised pressure outside of plate influence and central cavity pressure tapping from figure 4.16 123
4.15. Test case breakdown for $l_b = 150\,\text{mm}$ $t = 0.4\,\text{mm}$ flexible plate case during aerodynamic loading. 124
4.16. Plate region of experimental test rig fixed in the wind tunnel. 125

4.17. Plate deflection during PIV acquisition process upon flexible plates. a) $l_b = 150\,\text{mm}$ t = $0.4\,\text{mm}$ b) $l_b = 150\,\text{mm}$ t = $0.6\,\text{mm}$ c) $l_b = 200\,\text{mm}$ t = $0.4\,\text{mm}$ d) $l_b = 200\,\text{mm}$ t = $0.6\,\text{mm}$. 127
4.18. Plate deflection during Schlieren process upon flexible plates. a) $l_b = 150\,\text{mm}$ t = $0.4\,\text{mm}$ b) $l_b = 150\,\text{mm}$ t = $0.6\,\text{mm}$ c) $l_b = 200\,\text{mm}$ t = $0.4\,\text{mm}$ d) $l_b = 200\,\text{mm}$ t = $0.6\,\text{mm}$. 128
4.19. Example Schlieren image that illustrates negative displacement prior to shock loading. a) Shock wave is 50 mm upstream of the image at the exit of the nozzle. b) Shockwave has just entered the frame. 130
4.20. Instantaneous PIV stream wise velocity fields and extracted plate geometries for $l_b = 150\,\text{mm}$ $t = 0.4\,\text{mm}$ plate. 131
4.21. Vertical displacement through time of a single, fixed point on the surface located 100 mm from the beginning of the plate for each test case. a) $l_b = 150\,\text{mm}$ $t = 0.4\,\text{mm}$, b) $l_b = 150\,\text{mm}$ $t = 0.6\,\text{mm}$, c) $l_b = 200\,\text{mm}$ $t = 0.4\,\text{mm}$, d) $l_b = 200\,\text{mm}$ $t = 0.6\,\text{mm}$. 132
4.22. Plate crest tracking through time for the $l_b = 150\,\text{mm}$ t = $0.6\,\text{mm}$ flexible plate in a) & b). Graph a) shows the location of the maximum plate displacement with respect to the location of the most rearward shockwave. Graph b) shows magnitude of the displacement due to the aerodynamic loading. 134
4.23. Schematic showing effect of crest position with respect to the rear leg location and subsequent acceleration regions 135
4.24. The effects of shock tracking with the crest travelling too far downstream. 136

5.1. Illustration of expected actuator loading and initial sizings. Adapted from Ashill et al. [1992]. 140
5.2. Flow chart for the optimisation process. 141
5.3. a) The datum RAE2822 aerofoil geometry. b) Design variables for structural morphing to be used during the optimisation procedure. 142
5.4. Illustration to highlight the desired pressure smearing alongside the clean aerofoil pressure distribution and an increased pressure gradient. 146
5.5. Typical SCB geometry when subject to actuator loading. 147
5.6. Schematic diagram illustrating a typical pressure coefficient distribution around aerofoil fitted with an actuated SCB. 148

5.7. a) An illustration to show a typical C_p distribution over an aerofoil fitted with an aero-structurally designed SCB. b) An annotated version to highlight the the locations that make up f in equation 5.4. 149
5.8. Key performance data through the iterations of the optimisation procedure. a) Performance metric. b) Lift coefficient. c) Bump position. d) Bump height. e) Maximum von Mises Stress within adaptive SCB. Where presented, iteration 0 marks the clean aerofoil. 153
5.9. The effect of introducing a SCB. a) Pressure coefficient profiles for the clean aerofoil, $\alpha = 3.19°$, M_∞=0.728, Re $= 6.5 \times 10^6$. b) Mach contours for the clean aerofoil. 154
5.10. Mach fields showing the effects of SCB position focussing upon the supersonic regions for a) upstream SCB ($B_1 = 0.36$), b) optimal SCB ($B_1 = 0.43$), c) downstream SCB ($B_1 = 0.47$). 156
5.11. Structural modelling of adaptive SCB. Surface and centreline vertical displacement and centreline von Mises Stress for upper and lower surfaces. 157
5.12. Performance vs. bump height grouped by streamwise positions. The data was extracted from multiple optimisation and parametric runs. 158
5.13. Performance vs. bump position grouped at various heights. Reduced dataset compared to figure 5.12 for clarity 159
5.14. Pressure coefficient profiles for optimally positioned SCB with varying bump heights with a fixed location of $X_1 = 0.43c$ 162
5.15. Mach values plots for increasing actuator displacement. $\delta = 1, 1.5, 2, 3, 4$ mm. at bump location $X_1 = 0.43c$. 163
5.16. Wall shear stress coefficient for varying bump height in the optimal location $X_1 = 0.43c$. 164
5.17. L/D variation for increasing bump height. Clean aerofoil L/D ratio included for comparison. 165

6.1. A comparison between the predicted and experimental optimal SCB geometries with and without aerodynamic loading. $l_b = 150$ mm $t = 0.6$ mm, $\delta_1 = 1.42$ mm at $0.25l_b$ ($x = 37.5$ mm), $\delta_2 = 1.49$ mm at $0.5l_b$, ($x = 75$ mm) 167
6.2. Plate crest height through time. Optimal plate $l_b = 150$ mm $t = 0.6$ mm, $\delta_1 = 1.42$ mm at $0.25l_b$, $\delta_2 = 1.49$ mm at $0.5l_b$. 170

6.3. Plate displacement through time for the $l_b = 150\,\text{mm}$ $t = 0.6\,\text{mm}$, $\delta_1 = 1.42\,\text{mm}$ at $0.25l_b$, $\delta_2 = 1.49\,\text{mm}$ at $0.5l_b$ actuated plate. Shock position moved upstream by 180 mm for presentation. 170
6.4. Test case breakdown for optimal test cases. $l_b = 150\,\text{mm}$ $t = 0.6\,\text{mm}$ $\delta_1 = 1.42\,\text{mm}$, $\delta_2 = 1.49\,\text{mm}$ actuated plate. 171
6.5. Plate crest tracking through time for the $l_b = 150\,\text{mm}$ $t = 0.6\,\text{mm}$ optimal plate. a) Shows the location of the maximum plate displacement with respect to the location of the most rearward shock. b) Shows the magnitude of the displacement of the plate crest. 172
6.6. Test case breakdown for both flexible and actuated test cases for the times presented in figure 6.22. Left hand side panel shows 6 images throughout $l_b = 150\,\text{mm}$ t $= 0.6\,\text{mm}$ flexible plate. Right hand side panel shows 6 images throughout $l_b = 150\,\text{mm}$ t $= 0.6\,\text{mm}$ $\delta_1 = 2\,\text{mm}$, $\delta_2 = 3\,\text{mm}$ actuated plate. 174
6.7. Shock location during the over-deployed actuated SCB $l_b = 150\,\text{mm}$ $t = 0.6\,\text{mm}$ $\delta_1 = 2\,\text{mm}$, $\delta_2 = 3\,\text{mm}$. 175
6.8. Shock structure in the working section. a) Normal shock, retracted actuated SCB, $l_b = 150\,\text{mm}$, $t = 0.6\,\text{mm}$. b) Rigid wall normal shock. The two Schlieren images in figure 6.8 were obtained at different frame rates, exposure times and knife-edges so these comparisons can only be inferred. 176
6.9. Shock structure over adaptive SCB $l_b = 150\,\text{mm}$, $t = 0.6\,\text{mm}$. a) Normal shock (un-deployed SCB) b) Bifurcated shock (deployed plate) $\delta_1 = 2\,\text{mm}$, $\delta_2 = 3\,\text{mm}$. 176
6.10. Shock structure over a deployed adaptive SCB at various times during the example test case. a) Immediately prior to the actuation signal at 9.75 seconds b) Immediately after the actuation signal at 9.90 seconds c) During established bifurcation at 11.5 seconds. d) After the retract signal was sent to the actuators at 13 seconds. 177
6.11. Effect of shock position on shock structure over actuated plate $l_b = 150\,\text{mm}$, $t = 0.6\,\text{mm}$. a) Retracted $x_{shock} \sim 0.2l_b$. b) Retracted $x_{shock} \sim 0.5l_b$. c) Retracted $x_{shock} \sim 0.75l_b$. d) Deployed $x_{shock} \sim 0.2l_b$. e) Deployed $x_{shock} \sim 0.5l_b$. f) Deployed $x_{shock} \sim 0.65l_b$. 179
6.12. The interdependencies of shock structure, pressure gradient and plate geometry with the addition of actuation constraints. 179
6.13. Un-deployed Actuated SCB under the harsh shock loading environment. 180
6.14. High subsonic Mach number loading $M_2 \approx 0.74$ 181

6.15. Plate crest height variation over time. a) Actuated plate $l_b = 150\,\text{mm}$ $t = 0.6\,\text{mm}$, $\delta_1 = 2\,\text{mm}$ at $0.25l_b$, $\delta_2 = 3\,\text{mm}$ at $0.5l_b$. b) Flexible plate $l_b = 150\,\text{mm}$ t = 0.6 mm. 183
6.16. Plate crest height for Actuated plate $l_b = 150\,\text{mm}$, $t = 0.6\,\text{mm}$, $\delta_1 = 2\,\text{mm}$ at $0.25l_b$, $\delta_2 = 3\,\text{mm}$ at $0.5l_b$ with no aerodynamic flow field. . . . 184
6.17. A comparison between the actuated SCB geometries with no aerodynamic loading and with shock loading. 185
6.18. Comparison between flexible and actuated plate geometries with a constant rear leg shock position. a) Extracted plate geometries. b) Flexible plate shock structure. c) Over-deployed actuated plate shock structure. 186
6.19. Plate displacement through time for the $l_b = 150\,\text{mm}$ $t = 0.6\,\text{mm}$, $\delta_1 = 2\,\text{mm}$ at $0.25l_b$, $\delta_2 = 3\,\text{mm}$ at $0.5l_b$ actuated plate 189
6.20. Plate displacement through time for the $l_b = 150\,\text{mm}$ t = 0.6 mm Flexible plate 190
6.21. Transient plate displacement at multiple locations throughout time. Shock location is also included for reference. a) Actuated Plate, plate displacement at 60 mm streamwise location. b) Actuated Plate, plate displacement at 100 mm streamwise location. c) Flexible Plate, plate displacement at 100 mm. 192
6.22. Plate crest tracking through time for the $l_b = 150\,\text{mm}$ t = 0.6 mm flexible plate in a) & b) and the $l_b = 150\,\text{mm}$ t = 0.6 mm actuated plate in c) & d). Graphs a) & c) show the location of the maximum plate displacement with respect to the location of the most rearward shockwave. Graphs b) & d) show magnitude of the displacement due to the aerodynamic loading. 193

A.1. Method of characteristics generated nozzle. a) Large number of Mach waves. b) Low number of Mach waves 215
A.2. Mach 2 wind tunnel 215
A.3. a) Controlled contraction gradient (-0.4) geometry. b)Controlled contraction gradient (-1.2) geometry. 216

1. Introduction

Since the development of the first aircraft, there has been the aspiration to improve performance. The technological changes in the first 50 years of flight saw the cruise speed increase from 10.9 km/h of the Wright Flyer to 740 km/h of the De Haviland Comet. Whilst the flight speed for passenger jets has not increased at the same rate in the last 50 years, aircraft have become a lot more efficient. This has been driven by operating costs as well as environmental factors.

The commercialisation of flight and globalisation has seen passenger numbers increase significantly with the number of aircraft journeys set to double by 2050 [Busquin et al., 2001]. Aircraft journeys contribute a significant proportion of carbon dioxide gas emissions and this proportion is set to rise. Many initiatives are currently in place to improve efficiency, and reduce the environmental impact of transport aircraft. The Vision 2020 directive, issued by the European commission, targets transport aircraft of the year 2020 to achieve a 50% cut in carbon dioxide emissions per passenger per kilometre and an 80% reduction in nitrous oxide emissions compared to 2001 [Busquin et al., 2001]. Since the publication, the initial work has been extended for the Vision 2050 project which realises the significant changes required of aircraft design to revolutionise the industry and step away from the common silhouette of present day aircraft [Bisignani, 2010].

Refining current airframes is reaching a plateau in terms of improving aircraft aerodynamic efficiencies so engineers are looking to new methods to try to achieve larger changes in performance. The addition of winglets to many existing aircraft designs is one such example of flow control in order to reduce the pressure leakage from lower to upper surfaces of the wing. Other examples include vortex generators situated on the upper surface of the wing which on a global scale aim to reduce drag by reducing the likelihood of buffet onset at a given Mach number. The development of new flow control measures will have to focus upon specific aspects of the flight path in order to extract greater performance.

Whilst airlines may favour faster aircraft, the fuel burn associated with these designs increases with speed and opposes the environmental goals of Vision 2050. A limiting factor on the efficiency and flight speed of many commercial aircraft is the presence of

wave drag. A typical transonic passenger aircraft cruises at Mach 0.8 where the flow over the upper surface of a wing with $\sim 30^o$ sweep is accelerated to supersonic velocities which in turn leads to the formation of a normal shock. The total pressure loss across this shock wave can result in a significant contribution to wave drag. This type of drag increases significantly as the aircraft accelerates beyond the design Mach number. This can be seen in the transonic region of figure 1.1 which shows a large drop in C_l at M$\sim$ 0.8. This sudden drop off in performance is due to the wave drag increase and loss of lift can be mitigated through the use of control.

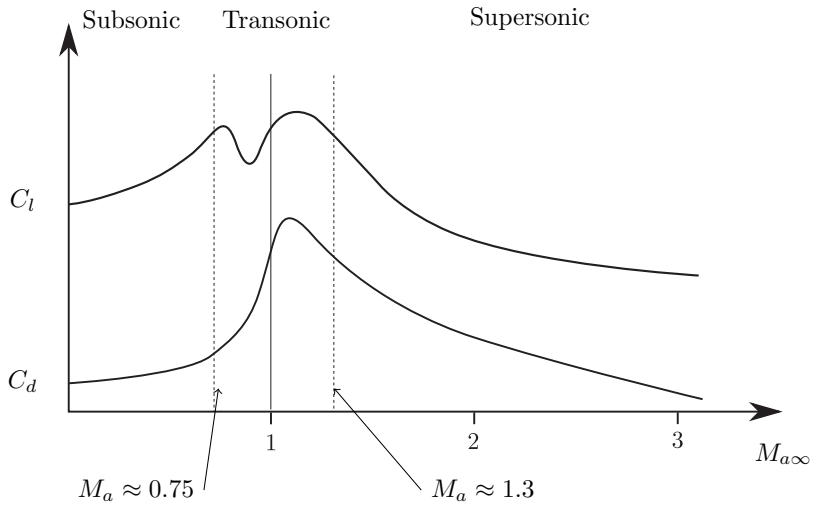


Figure 1.1.: Qualitative effect of free-stream Mach number on a thin airfoil at constant angle of attack [Massey and Ward-Smith, 2006]

Various control devices have been tested in order to reduce the strength of the shock and the associated total pressure losses including surface roughness, perforated cavities and suction. The success of these designs has been limited to specific cases with few providing a consistent overall drag reduction. They often reduce wave drag but suffer from a significant increase in viscous drag and vice versa. The primary technique used to achieve a reduction in wave drag is to bifurcate the shockwave [Babinsky and Harvey, 2011]. Such a shock structure is shown in figure 1.2b close to the wall where the shock foot now comprises of an oblique shock prior to the main normal shock.

The large scale bifurcated shock structure is a common component of shock control and has featured in many of the control techniques that have been tested to this day. Shock control can lead to large reductions in wave drag but also significant losses if poorly designed.

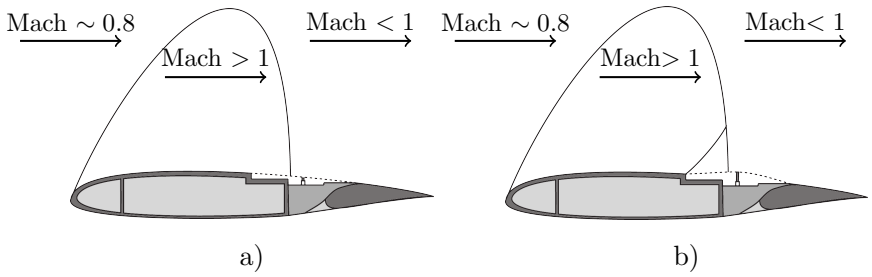


Figure 1.2.: Shock structure illustrated by sonic line. a) Typical transonic aerofoil. b) Transonic aerofoil fitted with adaptive SCB. Adapted from Ashill et al. [1992].

In the following chapter various shock control techniques will be discussed in order identify the common approach and for those capable of avoiding significant loss in performance at off-design flow conditions. Chapter 3 develops the approach of adaptive Shock Control Bump (SCB) design and acknowledges the influence of panel dynamics in the design process. Chapter 4 shows the interaction between an adaptive device and the flow, Chapter 5 showcases a combined aero-structural optimisation tool that combines the two facets involved in designing optimal adaptive SCB. Chapter 6 presents results from wind tunnel experiments undertaken to highlight the shock structures present and the interactions between actuated SCB and the flow.

2. Literature Review

The primary application for shock control is that of a transonic aircraft wing due to the large number of aircraft that operate in this regime. However the flow regime is also applicable to missiles, rockets and engine inlets. If the benefits of shock control could be shown to reduce drag for such applications it would go some way to help meet the emission targets set by the Vision 2020 and 2050 schemes [Busquin et al., 2001, Bisignani, 2010]. The following sections introduce the physics behind the transonic regime and the types of shock structures that occur for a number of cases. These range from the external flows over wings to the internal flows of a supersonic engine inlet or gas turbine blades and importantly, may be able to benefit from an element of shock control.

2.1. The Transonic Regime

The transonic regime describes the range of flight speeds where both subsonic and supersonic flow regions exist. For modern passenger aircraft, the cruise Mach number $M_{cruise} \sim 0.85$ [Roberson et al., 2007] with the flow accelerating to supersonic conditions very soon after the leading edge of the aerofoil. The benefit of accelerating the flow beyond Mach 1 on the upper surface is a further decrease in static pressure which increases the differential between upper and lower surfaces and hence the available lift. However there is a limit as higher cruise Mach numbers result in stronger shock waves which are associated with increased wave drag.

The negative effects of flying in this regime are the occurrence of shocks. Due to the pressure field surrounding the airfoil, the supersonic flow region is abruptly terminated by a nearly-normal shock at typically Mach 1.2 on production aircraft wings [Stanewsky et al., 1997], figure 2.1a. Across the shock a large pressure rise occurs as well as an increase in entropy which evolves into a total pressure loss identified as wave drag.

The effects of the supersonic region have to be considered in the design of a modern transonic aerofoil and the design process is a balance between maximising lift and minimising drag. When successful, this makes transonic flight a potentially efficient

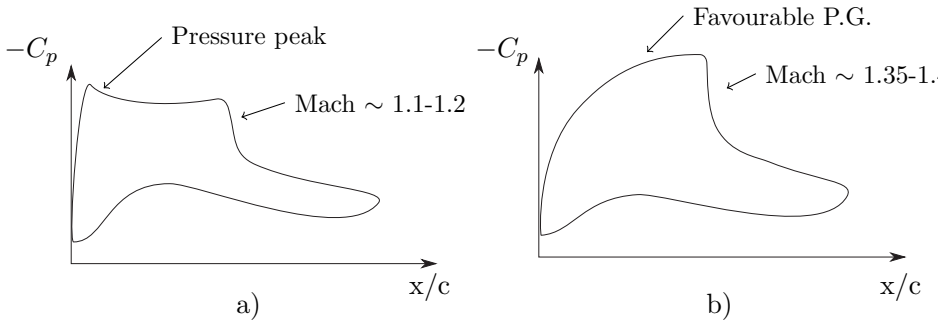


Figure 2.1.: Typical pressure distribution around transonic aerofoils. a) Turbulent aerofoil. b) Natural laminar flow aerofoil.

flight regime where the extra lift outweighs the negative effects due to the presence of a shockwave.

To extend the favourable low pressure region, the size of the supersonic region is often increased. This is the technique behind natural laminar flow (NLF) aerofoils which have been studied for many decades. NLF aerofoils aim to maintain laminar flow over the upper surface of the wing for as long as possible. Early examples included suction to redistribute the energy within the boundary layer however the design approach evolved and NLF aerofoils are now able to achieve laminar flow through geometric influence alone [Barnell and Hussaini, 1992]. Due to the larger favourable pressure gradient and larger region of acceleration, NLF aerofoils often have a stronger shock wave, $M_{shock} \sim 1.35 - 1.4$, which usually sits further back on the airfoil at around 0.55-0.6c [Stanewsky et al., 2002]. A smooth pressure profile is achieved through the minimisation of pressure waves by careful design with a typical pressure distribution illustrated in figure 2.1b. The higher Mach numbers present cause a stronger shockwave and the increased pressure gradient across the shock may cause separation. In order to benefit from the larger low pressure region, the resulting strong shocks may need to be controlled.

Figure 2.1a shows a pressure distribution over an aerofoil designed for transonic flight with a turbulent boundary layer starting very close to the nose. The pressure distributions of these aerofoils typically have a peak at 0.05c followed by a slight drop with a slight favourable pressure gradient across the upper surface until the shock wave. The location of this shockwave is typically around 0.5c and the upstream Mach number is much lower at $M_{shock} \sim 1.2$.

Another example of where the transonic regime is apparent is within aircraft engines, both within the stages of traditional gas turbine engines and also in supersonic intakes.

Both schematic diagrams of the expected shock structures are shown in figure 2.2.

The aim of triggering shockwaves in supersonic inlets as in figure 2.2a and 2.2b is to decelerate the flow subsonic velocities for combustion. The strength of the final normal shock is a balance between the complexity of the intake and the efficiency of the engine. Efficient inlets maximise total pressure recovery which is hindered by having a strong normal shock as is common in external compression inlets such as that in figure 2.2a. Internal inlets, figure 2.2b, usually have a much weaker shock but require more complex geometries to trigger the longer shock train that is illustrated in figure 2.2b. The static pressure rise through each of the shock waves causes an adverse pressure gradient. Each time the flow experiences an adverse pressure gradient, the boundary layer thickness increases and the redistribution of energy within the boundary layer increases the chance of separation [McCormick, 1993]. The separation has the potential to cause the engine to unstart which is damaging to the engine as well as detrimental to the stability of the aircraft. As a result of this risk, many internal compression intakes have an element of flow control with an example being boundary layer suction as in the Grumman F-14 Tomcat.

As for the stages of gas turbine engines, the subsonic inflow is decelerated to the combustion stage however as the flow is passed through the turbine, supersonic regions of flow can appear. The shockwaves present in turbine cascades stem from the acceleration of subsonic flow around the highly curved nose of the turbine blade as in figure 2.2c. In this respect, the supersonic region is similar to the aerofoil flows described previously however the rotational frame of reference and regions of high flow curvature can amplify the pressure gradient effects of the shock [Babinsky and Harvey, 2011] in similar ways to wings and internal intakes.

Three separate transonic interactions have been shown with an overview on the general performance of each application. Whether the goal of the application is to accelerate the flow on an aircraft wing or decelerate the flow for entry to a combustor, the transonic regime occurs and the loss in efficiency must be managed. One way to do that is through flow control. In the following sections a range of possible shock structures will be identified and previous control measures will be discussed and briefly evaluated.

2.1.1. Transonic Shock Structures

The field of shock control requires an understanding of the interaction between the boundary layer and the shockwave. The nature of this interaction is dependent upon local flow curvature, Mach number of the incoming flow, the surrounding pressure field

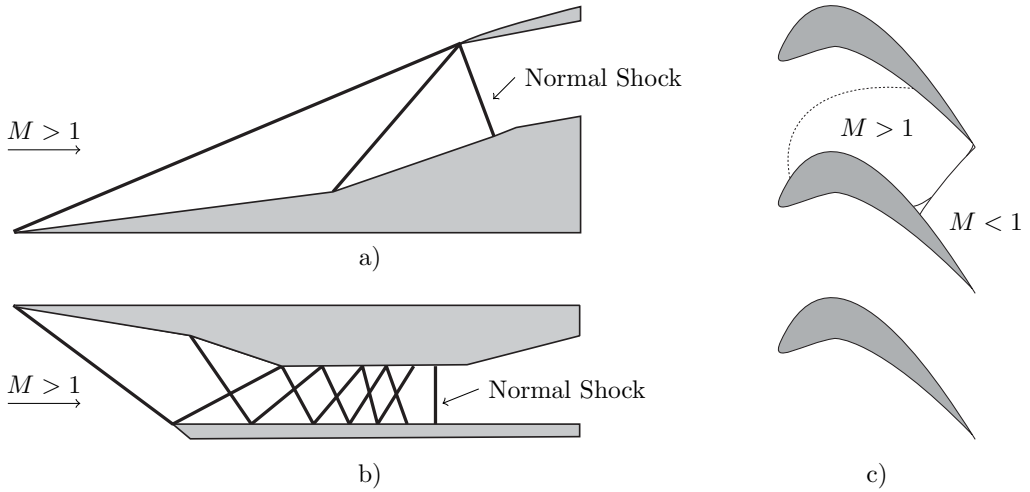


Figure 2.2.: Examples of applications within the transonic regime. a) External compression ramp inlet. b) Internal compression inlet. c) Turbine fan cascade. Adapted from Babinsky and Harvey [2011]

and boundary layer thickness and shape factor. In this work, the two distinct types will be termed weak and strong interactions.

Weak Interaction

Weak shocks generally have an incoming Mach number normal to the shock wave of less than 1.3. They are termed weak because the pressure rise across the shock does not trigger separation but causes a thickening of the boundary layer downstream of the interaction which can be seen in figure 2.3. The result of this pressure-rise-induced thickening is a pseudo-surface which then causes the flow to deflect away from the wall. This triggers pressure waves in the upstream supersonic region which gradually smears the pressure rise. Smearing reduces the pressure gradient and strength of the shockwave near the wall by increasing the streamwise distance of the interaction region [Delery, 1985].

Expanding upon this concept, the presence of the impending shockwave is propagated through the subsonic portion of the boundary layer. These disturbances in the boundary layer cause compression waves to form as the high momentum free stream interacts with the lower momentum boundary layer. Across each pressure wave there are small increases in pressure which contribute to the viscous smearing effect by slowing down the flow and increasing the streamwise interaction length. This is shown in figure 2.3.

These compression waves generated between regions 1 and 2 cause a reduction in the strength of the normal shock between regions 2 and 3. As the pressure waves in the boundary layer communicate information upstream, the energy within the boundary layer is redistributed and the result is much slower flow nearer the wall and a significantly thicker and less full boundary layer profile with higher shape factors [Babinsky and Harvey, 2011].

Further from the wall, the free stream Mach number remains unaffected and the shock strength between region 1 and 4, remains the same. This breakdown of the shock system highlights the zone of influence that near-wall disturbances have on the global shock structure.

The health of the boundary layer can be described through the use of a shape factor which is a ratio between the displacement thickness and the momentum thickness. It describes the distribution of energy within the boundary layer. The compressible displacement thickness is

$$\delta^* = \int_0^\infty \left(1 - \frac{\rho(y)u(y)}{\rho_0 u_0}\right) dy \tag{2.1}$$

where ρ is the local density, u is the local velocity and the subscript 0 represents freestream conditions. This represents the distance perpendicular to the wall that the inviscid solution would have to flow past in order to achieve the same mass flow rate. The compressible momentum thickness

$$\theta = \int_0^\infty \frac{\rho(y)u(y)}{\rho_0 u_0}\left(1 - \frac{u(y)}{u_0}\right) dy \tag{2.2}$$

operates on a similar comparison to the inviscid models however the thickness represents the equivalent momentum.

$$H = \frac{\delta^*}{\theta} \tag{2.3}$$

H is the shape factor and ratio between the two and a higher value generally means the momentum thickness is small in comparison to the displacement thickness and so a larger proportion of the mass is carried further away from the wall. Typically for laminar flows H ~ 2.59 whereas for turbulent flows where greater momentum is carried nearer the wall, the shape factors are much lower with H$\approx 1.3 - 1.4$ [Babinsky and Harvey, 2011].

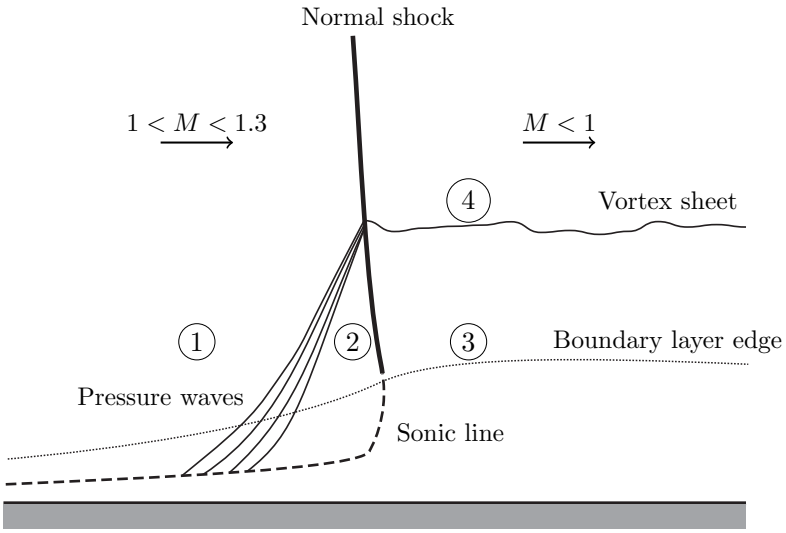


Figure 2.3.: Weak shock, adapted from Ogawa et al. [2008]

Strong Interaction

Strong interactions are characterised by the presence of a shock induced separation bubble and occur where the Mach number is greater than 1.5 due to the stronger adverse pressure gradient. The mechanisms behind the formation are very similar to the weak shock case however the magnitudes of the adverse pressure gradient and boundary layer thickness are much larger. The low momentum fluid inside the separation bubble acts as a larger pseudo-surface that deflects the boundary layer away from the wall even more so than boundary layer thickening [Piponniau et al., 2009]. The presence of the separation bubble is communicated upstream through the subsonic portion of the boundary layer and is thought to be a significant source of shock unsteadiness although it is still the subject of research. The adverse pressure-gradient-induced thickening of the boundary layer causes pressure waves to build up prior to the main normal shock as in the weak interaction. With the increased deflection these pressure waves coalesce to form an oblique shock wave which is much stronger than individual pressure waves. The oblique shock intersects with the main normal shock at the triple point and the shock structure is known as a bifurcated or λ-shock, figure 2.4.

Above the triple point, there is a normal shock with strength dictated by the incoming Mach number. Below the triple point, the shock structure is split between the front leg, a strong oblique shock and a rear leg that is a nearly normal shock of lower strength

than the original normal shock. The Mach number prior to this, between the front and rear legs, is determined by the strength of the oblique shock at the front leg which is a function of deflection angle. The deflection angle of each of the pressure wave varies as the local Mach number where the boundary layer disturbances interact is not constant; nor is there a single location where the compression waves emanate from and so they often coalesce outside the boundary layer away from the wall. The varying angles cause the pressure waves to coalesce into an oblique shock which is much stronger than the individual pressure waves. The formation of an oblique shock is another key difference between the strong and weak interactions.

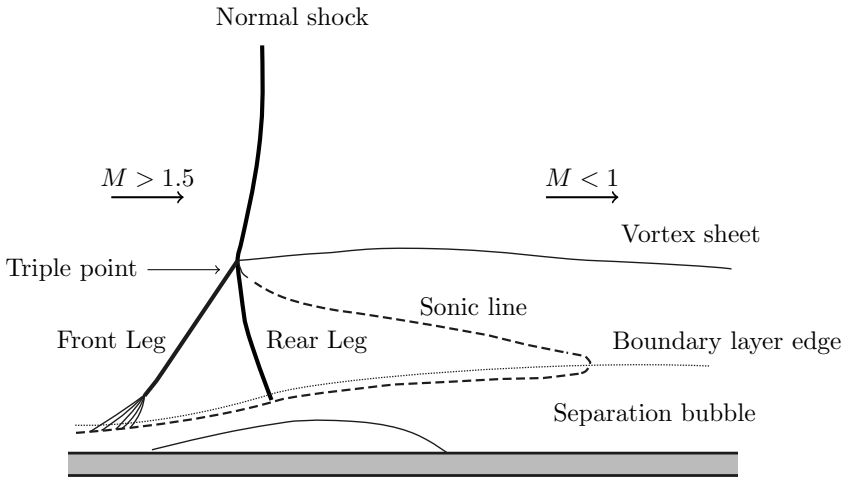


Figure 2.4.: Strong Normal Shock. Adapted from Seddon [1967]

2.1.2. Incipient Separation

The cases which lie between $1.3 < M < 1.5$ provide a very interesting scenario where both weak and strong interactions have been witnessed. In the experiments that form part of this work, the flow has been seen to remain attached at Mach 1.4 in Chapter 3 with separation defined as no large scale separation bubble at the wall. There have been results that have shown the flow to separate at the wall at Mach 1.3 [Delery, 1985, Liu and Squire, 1988].

Figure 2.5 shows the typical increase in pressure ratios across a shockwave and the effects of viscosity which cause the pressure rise to smear across the surface. Even from the wealth of previous experiments, the shock structure that will develop with $1.3 < M < 1.5$ remains case specific.

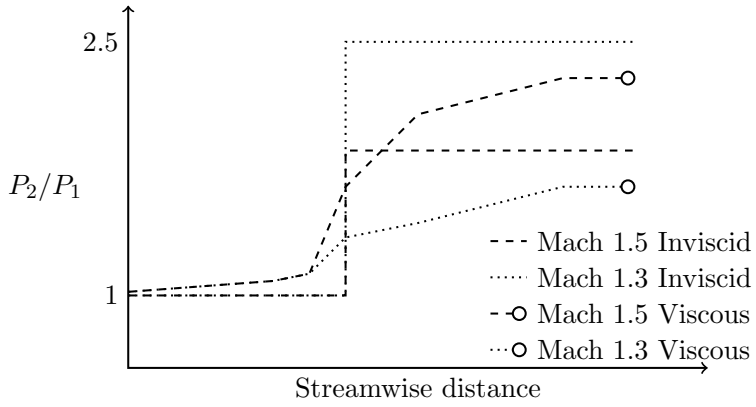


Figure 2.5.: Typical pressure rises for Mach 1.3, weak interaction and Mach 1.5, strong interaction for both inviscid solution and experimental viscous solutions. Adapted from Ogawa [2006].

2.2. Control Devices

The shock structures shown previously highlight the traditional structures associated with shock boundary layer interactions on a flat surface. In order to control the shock, the desired traits must first be identified. Historically the control mechanisms can be split into two groups, those that aim to manage the pressure gradient or reduce the overall thickness of fullness of the boundary layer.

2.2.1. Boundary Layer Control Devices

Boundary layer devices aim to entrain the high momentum fluid from the free stream to increase the energy within the boundary layer. The target is to energise the boundary layer to such an extent that it can overcome the adverse pressure gradient and avoid shock induced separation. This involves the redistribution of energy within the boundary layer and often results in a 'fuller' profile with higher velocities closer to the wall. This is equivalent to reducing the shape factor. The higher velocities closer to the wall give the flow more momentum to overcome the adverse pressure gradient across the shockwave. A number of such devices are introduced and evaluated in the following sections.

Vortex Generators, (VGs)

Early examples of vortex generators were included on transonic wings to increase the energy in the boundary layer to overcome the adverse pressure gradient without separation. Conventionally they have a height of the same order as the boundary layer and as such cause an increase in form drag due to their bluff nature. VGs are often positioned upstream of the main normal shock as depicted in figure 2.6. The redistribution of energy within the boundary layer slightly reduces boundary layer height which has been found to reduce the effect of shock smearing, [Babinsky and Harvey, 2011] This results in a more abrupt pressure rise at the shock and as a result means that less total pressure is recovered downstream of the shock. The energy entrained as a result of these vortices results in highly three-dimensional flow structures and the non-uniformity across the span has been an influential design factor in the development of other flow control devices.

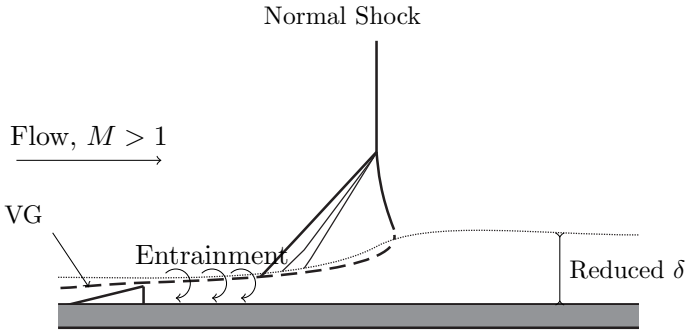


Figure 2.6.: Effect of vortex generator on shock structure.

Low-profile Vortex Generators and D-Strips

To reduce the form drag associated with vortex generators researchers have investigated smaller devices often referred to as low-profile VGs. Schubauer and Spangenberg [1960] first investigated the idea of a sub-boundary layer vortex generator (SBVG) which attempted to keep the positive entrainment benefits of VGs without the form drag. Lin [2002] reviewed a large number of test cases and determined that the most effective supersonic SBVG had a height, $h \sim 0.35\delta$. Ashill et al. [2001] found that in some

configurations SBVG introduced compression waves that actually weakened the shock wave by a small disturbance at the wall which is a desirable characteristic of any shock control method.

Reducing the device height further leads to surface roughness levels of protrusions, D-strips are a section of surface roughness or small bumps prior to the shock that aims to redistribute momentum within the boundary layer without significant entrainment from the freestream. The aim is to increase the height of the subsonic layer by increasing shape factor which would aid upstream propagation and hence knowledge of the impending shock, [Dietz, 2005]. The small changes to the boundary layer do not cause the complete redistribution of boundary layer energy rather the changes are very subtle and significant momentum thickness increases are avoided. Campo et al. [2012] investigated the use of small bumps $\sim 0.1\delta$ height, to change the strength of the interaction. Their findings showed that it was also possible to alter the location of a Mach 2.1, 20° oblique shock reflection and compression ramp interaction from the within the boundary layer upstream of the shock which has applications in supersonic isolators within SCRAMJET engines.

2.2.2. Shock Control Devices

This second category of flow control device operates on the principle of minimising total pressure loss and wave drag in internal flows or facilitating larger favourable pressure gradients for transonic wings. They aim to smear the shock over an extended streamwise area to lessen the adverse pressure gradient in the shock region. Some of the devices used are discussed in the following sections where common features can be seen. The recurrent goal is to generate compression waves upstream of the main normal shock. These can either be a continuous wave as in figure 2.3 or the more established method of bifurcating the shock structure shown in figure 2.7. Both position the control device within the boundary layer. Figures 2.4 and 2.7 show the similarities in shock structure between the formation of a strong interaction on a flat wall and the enforced bifurcation that is a result of shock control. Notably the coalescence of pressure waves into an oblique shock prior to the main normal shock. The control measures however, aim to enforce these shock structures at given locations with a prescribed effect.

Perforated Cavity Control

The idea behind perforated cavity control is to exploit the pressure rise across the shock to raise the upstream pressure. Figure 2.8 shows an example of a typical perforated

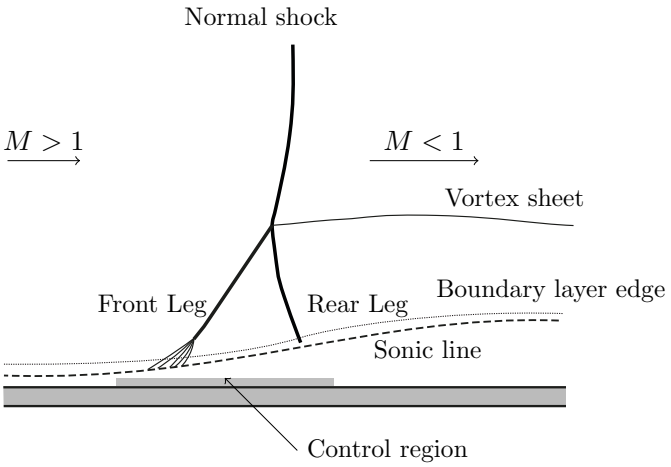


Figure 2.7.: The Bifurcated shock structure.

cavity setup. This thickens the boundary layer and introduces stronger compression waves in a similar mechanism to the formation of the weak shock. The perforations allow for the conventional shock structure to be maintained while the higher post-shock pressure is bled through the perforations and develops a natural pressure driven cycle to raise the pressure in the low pressure supersonic region. The first device evaluated stems from the EUROSHOCK project [Stanewsky et al., 1997] which focussed upon wave drag reduction through the use of a perforated cavity. The purpose of the study was to build upon the flow control techniques available for transonic applications and introduce new concepts to the field.

The flush-mounted device is capable of introducing the desired bifurcated shock structure, however the resultant thickening of the boundary layer led to large viscous losses with a 40% increase in δ^* and a similar increase in θ when compared to the baseline zero-control case. In a large proportion of the cases in EUROSHOCK I these losses outweighed the wave drag saving, [Stanewsky et al., 1997]. It was common for the control measures to suffer from an increase in viscous drag.

The results of this study showed that passive shock control through perforated cavities alone could not provide the drag benefits expected due to the growth of the boundary layer. A solution to this was to introduce an element of active control to the cavity in the form of cavity suction which formed the premise for EUROSHOCK II, [Stanewsky, Délery, Fulker, and de Matteis, 2002]. This saw the combination of cavities and suction to try and decrease the boundary layer height and step away from passive control towards active shock control.

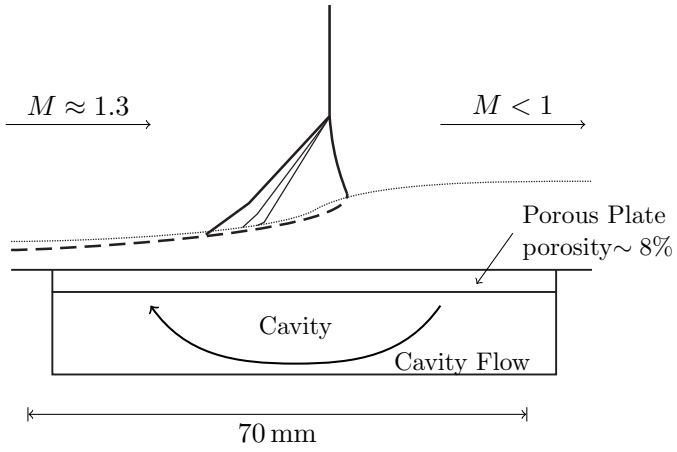


Figure 2.8.: Perforated Cavity

Perforated Cavity with Suction

By introducing the element of suction to perforated cavities, the boundary layer heights were reduced as expected [Stanewsky et al., 2002]. The addition successfully reduced the viscous losses surrounding the system however the thinned boundary layer was less effective at smearing the shock, [Stanewsky, 2000] an effect also witnessed by vortex generators. The deterioration of shock strength based control brought on the investigation of numerous configurations involving active control and perforated cavities. One of the more successful approaches was targeted suction which is illustrated in figure 2.9. This setup allowed for natural growth of the boundary layer beneath the main normal shock whilst reducing the height of the boundary layer downstream. This approach effectively introduced a second control technique to reduce the penalties of the first adding complexity to the system.

The distribution of energy within the boundary layer was also effected by the introduction of suction. In the passively controlled case, without suction, the cavity pressure moved the momentum distribution away from the porous plate in the region upstream of the shock. With targeted suction, the boundary layer profile was found to be significantly fuller as the momentum is brought closer to the surface as reported by Bur et al. [2002] in the Euroshock II project.

As with all active flow control measures the question is raised regarding overall energy saving. Whilst boundary layer suction devices have successfully been introduced in supersonic intakes, the aircraft were designed with ultimate performance in mind.

The application to transonic wings, which are subject to stringent efficiency criteria imposed by operating costs and Vision 2020 and 2050 schemes, mean that any slight performance benefit is overridden by the additional weight and complexity of the system and ultimately the fuel cost. This is a huge driver for the airlines and their fleets of transonic aircraft.

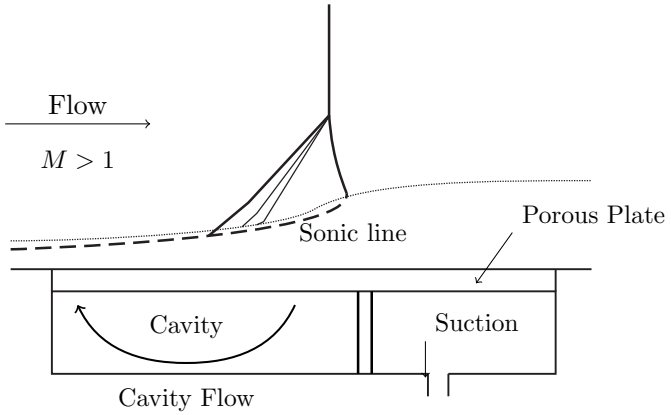


Figure 2.9.: Perforated cavity with targeted suction.

Shock Control Bumps – General Concept

The origins of shock control bumps stem back to the mission adaptive wing concepts of the 1980s, where sections of the wing would deform during flight stages to improve performance. Ashill et al. [1992] are credited for the design of SCB in their current form which introduces a bump beneath the shockwave on a transonic aerofoil to instigate the bifurcated shock structure in figure 2.7. This initial concept comprised of a section of flexible skin as shown in figure 2.10 which allowed for the bump to be deployed and retracted depending upon the flow conditions.

The bifurcated shock structure forms because of the surface deflection induced by the front SCB surface. This causes compression waves to form as the flow has to deflect around the raised surface. The compression waves build up and coalesce to form an oblique shock in a similar fashion to the strong shock interaction in section 2.1.1. This time however the oblique shock is driven predominantly by the SCB geometry rather than the thickening of the boundary layer and as such the oblique shock is forced rather than left to form naturally. Boundary layer thickening downstream of the shock still occurs due to the presence of the adverse pressure gradient as well as the region of convex

curvature on the rear SCB surface but careful design can eliminate the significant viscous loss associated with other control measures [Colliss and Babinsky, 2012].

The main performance goal of SCB is the bifurcation of the normal shockwave. The oblique shock generated by the front SCB surface intersects with the main normal shock at the triple point. The height of this location dictates the vertical extent into the free stream which the SCB can affect. This is dictated by the global position of the shockwave and the angle at which the front SCB surface makes with the incoming flow. The angle of the oblique front leg caused by surface deflection also prescribes the strength of the front and rear shockwaves and the resultant total pressure losses. This formed the basis of an analytical model by Ogawa [2006] which estimated the potential wave drag saving.

The greater deflection caused by the SCB increases the strength of the oblique shock and decreases the strength of the rear leg. However as the SCB design becomes higher and the deflection increases, the curvature over the crest also increases necessarily to a point where the the combination of the surface geometry and the post-shock adverse pressure gradient may cause the flow to separate [Bruce and Colliss, 2014]. This is the challenge of designing a successful SCB.

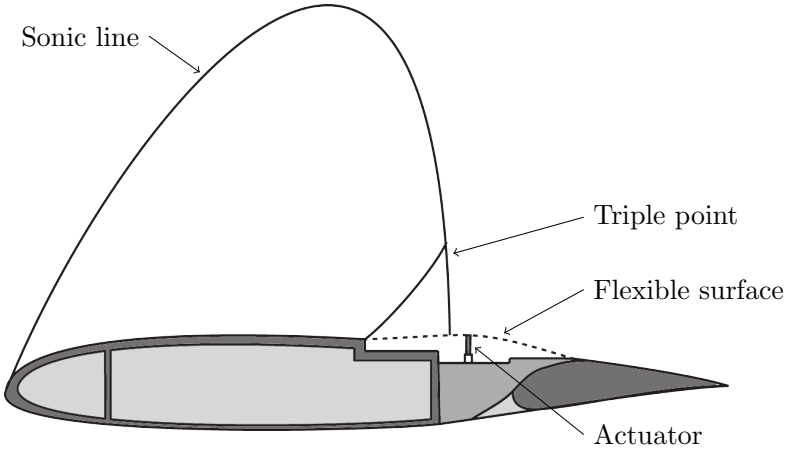


Figure 2.10.: Original SCB concept by Ashill et al. [1992]

The general concept was found to produce favourable results in particular these in the large study of EUROSHOCK II [Stanewsky et al., 2002]. This study moved SCB research in the direction of shape optimisation with numerical and experimental tests. The investigations have progressed from broad scale parametric studies such as the works by Sommerer et al. [2000b], Dargel and Thiede [2002], Ogawa et al. [2008] to

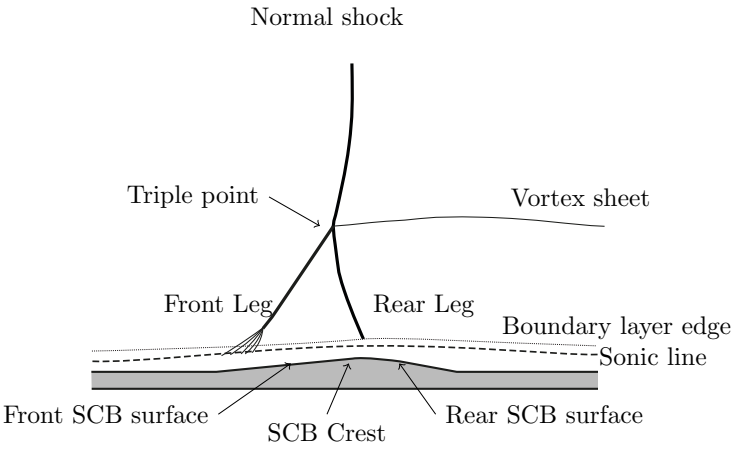


Figure 2.11.: Ideal shock structure over a SCB.

those evaluating much finer optimal geometries by Qin et al. [2008], Lee et al. [2011b], Eastwood and Jarrett [2012], Nübler et al. [2012] who used rigorous computational models to extract the precise near-wall influence of the SCB. The various approaches will be discussed in detail in section 2.3.

Control Device Summary

To summarise the characteristics of the many control measures available to transonic flows, they can be categorised between boundary layer control and shock control and further broken down to passive and active control measures. It was often the case that boundary layer techniques such as vortex generators and suction were used to control separation and reduce the contribution of viscous drag. The shock strength however often increased compared to the clean case due to the reduced smearing of the shock and this penalty outweighed the benefits of viscous drag reduction. The opposite was typical of shock control devices such as perforated cavities and SCB. The desired λ-shock structure was achieved but the viscous drag component was susceptible to large increases. The increase in viscous drag is usually higher with perforated cavities as the shock structure is reliant upon boundary layer thickening beneath the shock. With SCB, the bifurcation of the shock is driven by the geometry change at the wall and the source of the viscous drag stems from the management of the flow around the crest. Careful design in this region has highlighted the potential for shock control without significant viscous drag increases [Nübler et al., 2012]. The following section outlines how SCB have evolved from the initial concept and the techniques used to produce

effective designs which combine the beneficial traits of all of these control devices.

2.3. Current Static SCB

The progression of SCB research has followed the traditional approach of a flow control measure, from the initial concept of Ashill et al. [1992] through initial parametric studies by Stanewsky et al. [1997] to more in-depth aerodynamics studies by Bur et al. [2002], Dargel and Thiede [2002], Rosemann and Birkemeyer [2002] and Vallee [2002]. These established a large platform from which to build on.

These early results showed a consistent reduction in drag brought on by the addition of SCB for both turbulent and NLF wings. The reduction in drag was reported to be of the region 12-15% by Millholen II, W. and Owens, L. [2005] and as much as 21% by the studies of Euroshock II. These investigations primarily focussed on the performance of two-dimensional SCB upon two-dimensional aerofoils. The promising results in the form of drag reduction paved the way for more intensive experiments and numerical simulations of SCB. The following sections describe how the design of SCB has been approached in these studies and which parameters have been identified to contribute to an effective, efficient design. The operational envelope of SCB is discussed as well as the optimisation processes for maximising performance within this envelope and the effects of drifting off-design.

2.3.1. SCB Parameterisation

An initial parametric study of bump shapes was conducted by Sommerer et al. [2000b] and highlighted the families of SCB geometries available to the designer. Figure 2.12 illustrates these families which offer different approaches to achieve in the bifurcated shock structure including the sudden deflection wedge, beam in bending and polynomial expressions for SCB geometry.

Each of the geometries can be described with a number of parameters. The loaded beam geometry is a curve that represents a beam subject to an out-of-plane load.This force can also be represented by an equivalent out-of-plane displacement. Numerous boundary conditions can be easily implemented to maintain C^0 and C^1 continuity with the surface before and after the SCB. These woud involve the pin-jointed and clamped constraints respectively. The wedge type SCB is an example of C^0 continuty where there is a discrete change in the slope across the surface. The wedge type SCB also has the discrete change in slope over the crest which could lead to undesirable flow features

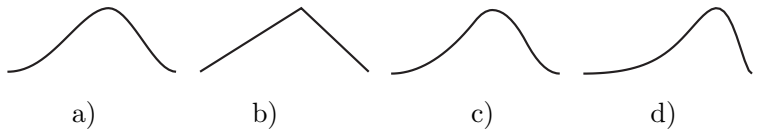


Figure 2.12.: SCB geometry families as described by Sommerer et al. [2000b]. a) Loaded Beam. b) Wedge. c) Concave polynomial. d) $11th$ Order Polynomial

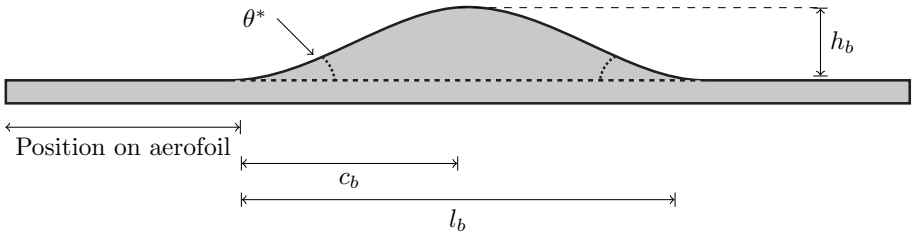
such as separation as seen in the work by Eastwood and Jarrett [2012].

The polynomial shapes are further removed from physical mechanisms of the loaded beam and wedge geometries however the order of the polynomials can be changed to create more complex shapes. Sommerer et al. [2000b] tested two polynomial based shapes. One was named the concave polynomial which was made up of four separate polynomial curves to represent the initial change in deflection from the flat surface, the surface up to the crest, the surface after the crest and the geometry which connects it back to the flat surface. The reasoning behind this was to better manage the flow around the crest region. The polynomial curve in figure 2.12 was an 11th order polynomial which was chosen to allow for large amounts of control of the geometry via an optimisation procedure.

Figure 2.13 shows the parameters that are commonly used to parameterise SCB geometries in the broad Euroshock II project. The project showed that SCB were relatively simple to parameterise using just a few key variables. For example, the loaded beam geometry in figure 2.12a, could be described by as few as two variables, the crest height and the length-wise position of this height. The magnitude of these variables prescribe the strength of the front leg and overall shock structure which has a direct effect upon the potential drag reduction.

From the existing SCB studies, it has been determined that SCB design can be a two-part process split between the forward and rear surfaces of the SCB, which are linked through the position and shape of the crest. The shock structure is largely determined by the front ramp angle and SCB height (forward SCB section) which bifurcate the shock and thus form the main contribution to the wave drag saving. The viscous drag component relies upon the subtle curvature downstream of the crest (rearward SCB section) as the flow rejoins the main aerofoil surface. It can often be the case that there are small viscous drag increases that stem from poorly selected height or position as found by Le Balleur et al. [2002] and Dargel and Thiede [2002].

One approach to mitigate these losses is to focus on the shape of the SCB. In the



*Usually used for wedge type SCB only.

Figure 2.13.: Typical SCB optimisation parameters. θ, front ramp angle. c_b, location of crest, h_b, height of crest. l_b, length of SCB.

parametric studies of Euroshock II the contributors tested the effect of symmetric, $c_b = 0.5l_b$ and asymmetric SCB crest $c_b \sim 0.55 - 0.7l_b$. The results presented primarily focussed upon the pressure distribution on which the small-scale changes in SCB shape had little overall effect. It has since been proposed that the viscous drag contribution is highly sensitive to such small-scale geometry changes as well as the global shock structure as seen by the novel geometries of Colliss et al. [2014]. Recent optimisation studies have taken greater control over the geometry with the addition of multiple control points along the SCB to enable more complicated shapes described by NURBS curves [Rhodes and Santer, 2012]. This control point/spline based procedure lends itself well to optimisation procedures as well as being to replicate the more complicated geometries of 3D SCB which represent another family of SCB geometries.

Another step to reduce the detrimental viscous effects was to significantly reduce the curvature of the rear SCB surface. This was first hypothesised by Millholen II, W. and Owens, L. [2005] as the long term goal of SCB, to redevelop the entire aerofoil downstream of the SCB crest. Colliss et al. [2014] and Nübler et al. [2012] conducted joint numerical and experimental studies into the effects of an extended SCB and found that such a device produced a thinner boundary layer downstream when compared to a typical SCB. The extended geometry was able to achieve this while maintaining appreciable levels of shock control. What these studies highlight is the importance of the region downstream of the crest and how the surface and flow curvature can affect the health of the boundary layer beyond the SCB crest.

The flow physics within the boundary layer over SCB has been studied experimentally by Ogawa et al. [2008], Bruce [2008], Colliss et al. [2014]. These studies were a driving force being the transition from 2D to 3D SCB.

The dimensionality of SCB came under question as researchers began to look at off-

design performance. There was a general consensus that 2D SCB are able to provide a beneficial reduction in drag but only for a single design point with a given shock location and strength. As the design space was explored, the poor off-design performance of static 2D SCB became apparent. This triggered a new design and a growth of the design space with 3D SCB offering lower off-design penalties that 2D SCB suffered from. As such there became multiple approaches to overcome off-design performance which are:

- Use 3D SCB to limit the span-wise deterioration in performance;
- Design an adaptive SCB that is able to deploy and retract.

Three dimensional SCB received greater interest as a result of the increased complexity of an adaptive SCB design. The extra dimension of 3D SCB introduces spanwise curvature perpendicular to the flow field forming vortices as the flow passes over the shoulders of the 3D SCB as identified by Colliss et al. [2013]. The discussion of 2D and 3D SCB and their merits requires more detail and will be covered in section 2.3.4 where SCB off-design performance is considered in more detail. Prior to that, the general advantages of SCB will be reviewed with consideration towards what contributes to a successful SCB design and the importance of selecting a suitable performance metric.

2.3.2. SCB Operational Envelope

The performance envelope of SCB is dictated by the eventual application of the technology; whether NLF or turbulent wings, the shock strength will be set by the aerofoil geometry and the design-point, cruise flight conditions. Once these have been determined, the on-design strength of the shock will be set.

Aerofoil SCB are usually designed for a cruise Mach number, M_{cruise} and lift coefficient C_l with the performance evaluated by any change in C_d. Stanewsky [2000] tested two SCB heights at locations beneath the shockwave on the natural laminar flow ADIF aerofoil. The effect of the SCB can be seen in figure 2.14 by the drop in peak -C_p value. This is a typical result of SCB for both turbulent and NLF aerofoils as the pressure rise in the shock region is smeared through bifurcation of the shock wave. The presence of the pressure rise as presented in figure 2.11 is communicated to the supersonic flow through the underlying subsonic region in a thickened boundary layer. The front leg begins to form upstream of the main normal shock location through the mechanism described in section 2.2.2. The shock system commences at an earlier chordwise position and the acceleration of the flow is halted prematurely and subsequent peak negative pressure of the clean aerofoil is not reached with a reduction in shock strength.

The reduction in shock strength close to the aerofoil surface is a beneficial characteristic of SCB as the adverse pressure gradient is reduced. In the case of the ADIF aerofoil presented here, the favourable pressure gradient over the upper surface is maintained for as long as possible. The continual acceleration of the flow results in a strong shockwave where $M_{shock} \sim 1.35 - 1.4$ [Stanewsky, 2000]. This value represents a shockwave where the resulting adverse pressure gradient is still low enough to retain attached flow downstream of the shock and SCB.

By integrating a SCB into the aerofoil design, the pressure rise is broken down into two stages across the front and rear legs. A study by Stanewsky [2000] showed these two stages are apparent for the $h_b = 0.175\%$c SCB in figure 2.14 with a plateau in the pressure profile commencing at $x = 0.7c$ that separates the two compression stages, the SCB is positioned between $0.6c < x < 0.8c$. This reduction in the adverse pressure gradient in the shock region represents a smearing of the shock and is a result of a successful SCB. With a SCB height $h_b = 0.35\%$c in the same position a secondary low pressure region can be seen at around $x \approx 0.75c$ which corresponds to the crest of the SCB. This suggests that the normal shock is broken down into a two shock system but with undesirable re-acceleration over the crest. The region around the crest $0.69c < x < 0.74c$ in figure 2.15 shows that for the higher SCB, $h_b = 0.35\%c$ there is a reduction in peak pressure with a second low pressure peak which indicates accelerating flow and another secondary normal shock.

The effect of the two SCB heights shown in figure 2.15 illustrate the sensitivity of the design space of adaptive SCB. The lower height showcases one of the key benefits of SCB which is that SCB are able to manage stronger shocks whilst maintaining attached flow. This could pave the way for higher cruise Mach numbers by delaying the onset of an increase in wave drag.

The pressure profiles presented in figure 2.14 represent just one flight condition at a single lift coefficient of $C_l \sim 0.6$. Performance across a range of lift coefficients is shown in figure 2.16. The figure shows the lift-drag performance of clean and modified aerofoils from works by Stanewsky [2000] and the Euroshock II project. The lift-drag polars presented here highlight the range of C_l where short and tall SCB perform well. In a result that has been highlighted in many studies [Dargel and Thiede, 2002, Le Balleur et al., 2002, Rosemann and Birkemeyer, 2002] the lower SCB perform well at lower C_l which are more typical of transonic cruise. The lower SCB produces less drag than the clean aerofoil for $C_l > 0.4$ [Stanewsky, 2000].

In contrast, the higher SCB suffers from increased drag at lower lift coefficients $0.4 < C_l < 0.55$ before improving to a level marginally better than the lower SCB. At higher

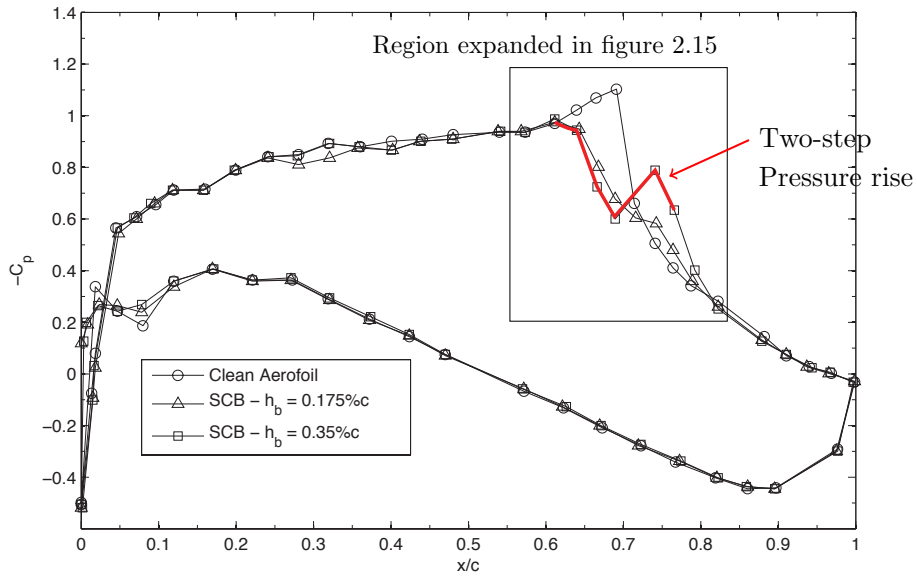


Figure 2.14.: Pressure profile for clean ADIF aerofoil and two SCB geometries with varying height, Stanewsky [2000]. $M_\infty = 0.765, \alpha = -0.5°, Re = 8 \times 10^6, C_l \sim 0.6$.

lift coefficients, $C_l > 0.6$, the higher SCB reduced total drag by $\sim$ 15% compared to the clean aerofoil, whereas the lower SCB reduces total drag by $\sim$12% at $C_l \sim 0.72$. Possible reasons for the poor performance of the higher SCB at these lower C_l values is the detrimental effect of the extra curvature on the health of the boundary layer as it passes over the bump.

A poorly positioned tall SCB may cause the boundary layer to thicken or the cause flow to separate after the crest which would significantly increase the viscous drag component [Dargel and Thiede, 2002]. A lower SCB at the same location would not have such a negative effect and the boundary layer may have enough momentum to remain attached over the crest. This characteristic is desirable for maintaining performance when off-design. A further breakdown of the drag is required in order to evaluate what conditions cause these reacceleration regions. Le Balleur et al. [2002] compared the same bump sizes at numerous flow conditions and identified the breakdown between wave and viscous drag components. The results in table 2.1 show the individual components of drag found at two different C_l values $C_l = 0.5$ and 0.7. These cases were chosen to be presented here as they show the performance of two distinct heights at their design point and also off-design lift coefficients. The results showed a significant reduction

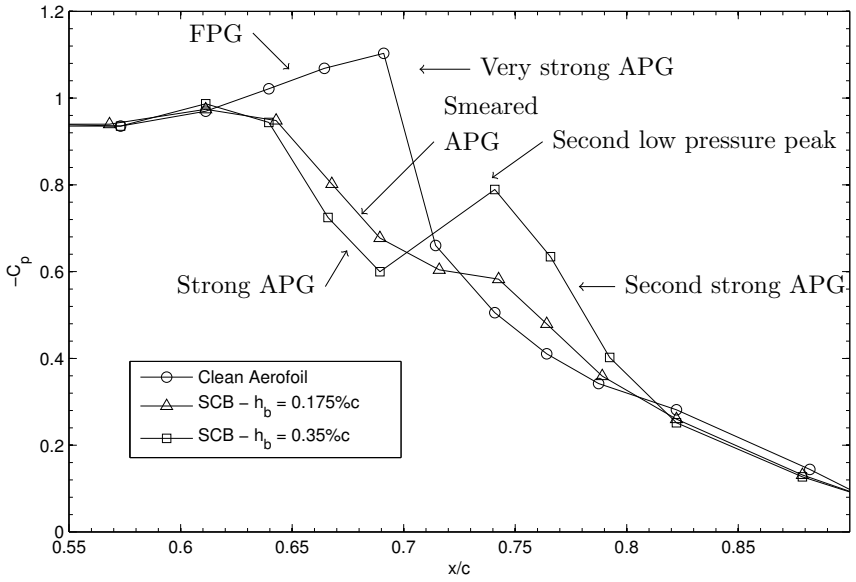


Figure 2.15.: Shock region of figure 2.14 with key pressure gradient annotations. ADIF Aerofoil. Favourable pressure gradient (FPG), adverse pressure gradient (APG).

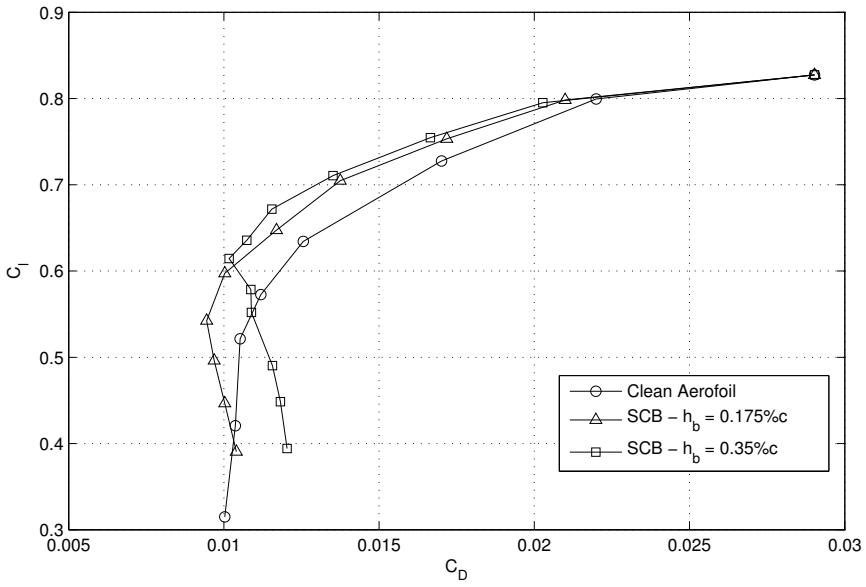


Figure 2.16.: C_l vs. C_d polars for clean ADIF aerofoil and two SCB geometries with varying height, Stanewsky [2000]. $M_\infty = 0.765, Re = 8 \times 10^6$.

		$C_{l\text{design}}$	C_l	$C_{D\text{wave}}$	$C_{D\text{visc}}$	$C_{D\text{Tot}}$	ΔC_d
Case 2	Clean	0.5	0.5259	000082	0.00795	0.00877	-
	$h_b = 0.175\%$	0.5	0.5016	0.00050	0.00797	0.00847	-3.4%
	$h_b = 0.35\%$	0.5	0.4943	0.00314	0.00775	0.01089	+24.2%
Case 4	Clean	0.7	0.7307	0.00492	0.00838	0.01330	-
	$h_b = 0.175\%$	0.7	0.7091	0.00290	0.00831	0.01121	-15.7%

Table 2.1.: Drag breakdown of ADIF aerofoil fitted with SCB, $h_b = 0.175\%$ and $h_b = 0.35\%, M = 0.757$, for two different C_l values, [Le Balleur et al., 2002].

in drag, $\Delta C_d \sim 15.7\%$. The wave drag component was reduced from 36.9% to 25.8% with a negligible decrease in viscous drag. Similar values were found throughout the Euroshock II project for tests with $C_l > 0.6$ Stanewsky et al. [2002].

The performance of SCB at lower C_l highlights the benefits of a lower SCB. The higher SCB ($h_b = 0.35\%c$) suffers from a more pronounced increase in drag which was predominantly wave drag. This is likely to be due to a development of a λ-shock structure with a corresponding change in pressure distribution to that shown in figure 2.14. An extended region of low pressure downstream of the SCB crest could lead to reacceleration of the subsonic flow back to supersonic velocities and lead to a secondary shock structure with further losses in efficiency and effectiveness due to additional wave drag and increased boundary layer thickening or separation.

Quantifying SCB Performance

Being able to quantify the performance of a control device is an important part of the design process and SCB have been subject to many different metrics throughout optimisation studies.

The losses associated with poor SCB design are often combined and presented as global aerofoil quantities such as in the lift-drag polars of figure 2.16. In order to quantify the performance of SCB and produce optimal designs the inefficiencies must be addressed individually. One of the main criteria for the performance of SCB is driven by the requirement to preserve lift whilst optimising the pressure distribution in the vicinity of the upper surface shock.

The tests conducted in Euroshock II by Le Balleur et al. [2002] highlight the importance of maintaining lift coefficients throughout test cases. The pressure profiles presented in figure 2.14 show how the pressure is redistributed over the upper surface due to the presence of a SCB. The effect is clarified and idealised in the schematic

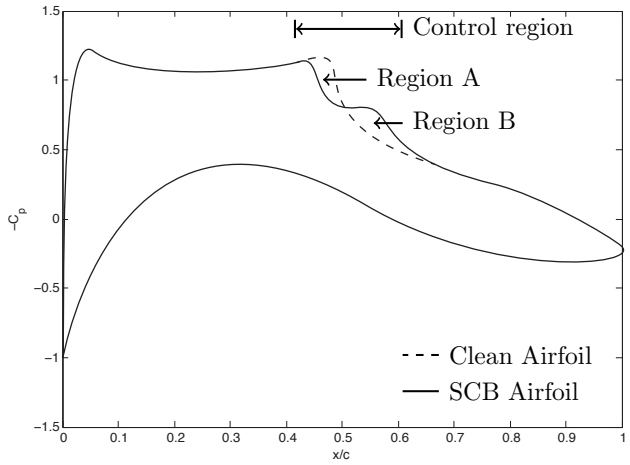


Figure 2.17.: Schematic diagram illustrating target pressure coefficient distribution around a turbulent airfoil.

shown in figure 2.17 where the loss in lift due to region A is counteracted by the gain in region B and thus maintaining a constant C_l [Sommerer et al., 2000a, Lutz et al., 2003, Pätzold, 2006, Qin et al., 2008]. Table 2.1 shows how the lift coefficient can be maintained at an approximately constant level but with significant increases in drag.

Incorporating drag into the design process allows for the inclusion of beneficial wave drag reduction properties of SCB at an earlier stage however designing for drag reduction alone may result in aerofoil design with reduced lift. In order to maintain suitable levels of lift, the L/D ratio is often used [Pätzold, 2006]. Using the lift-to-drag ratio as a performance metric combines all losses into a single value which is beneficial for an optimal design procedure but disguises the cause of change in performance.

SCB geometries produced with this approach performed well, lift was maintained and drag was reduced. There is however no further indication as to where these improvements are made, in particular how each component of drag is affected. Lee et al. [2011b] evaluated the components of drag after an optimisation procedure which used a total drag performance metric which incorporated both viscous and wave drag components however they were not evaluated within the optimisation procedure itself. As experimental interests switch from large scale aerofoil studies [Wadehn et al., 2002] to small scale flow studies [Ogawa, 2006, Bruce, 2008, Colliss and Babinsky, 2012] the focus has moved from the general shock structures to small scale flow features. In comparison to experiments, it is more straightforward to distinguish between different drag sources

in CFD which can provide further insight into the small scale flow features to supplement the experimental tests. This valuable information should be integrated into the optimisation.

As presented previously, there are a number of different transonic shock cases that could benefit from control. In many of these such as internal flows, performance is not necessarily best captured by a drag based metric but would gain from a total pressure recovery based metric. The ability to maintain total pressure is critical for efficiencies within an engine for example and the bifurcated shock structure developed by SCB reduces the total pressure losses incurred by a normal shockwave. The total pressure recovery goals are the same for rotor blades in turbine engines however the chordwise loading and pressure distribution is also important for blade design which is arguably more similar to an aerofoil despite the extreme curvatures. The combination of simple bump parameterisation and the sensitivity of the transonic flow field means that this design problem is well suited to optimisation.

2.3.3. Optimisation

The optimisation of SCB requires a metric to compare the performance of various control measures which typically include lift, drag and L/D values but now the application of the metrics will be discussed through the various optimisation techniques available to the SCB designer.

The main components of an optimisation study are illustrated in figure 2.18. The first step is to parameterise the bump geometry, as described in section 2.3.1. With respect to optimisation, a good choice of parameterisation requires a balance between the number of variables and their influence upon the flow. These input variables are then passed to an optimisation algorithm which evaluates the performance metric based upon these values. The most common technique to extract these values is to use CFD to compute an accurate approximation of the flow field. The use of analytical models during optimisation is uncommon due to the sensitive and complex nature of the flow field. Due to the high velocities and viscous interactions present within a typical case, computations are expensive and require an efficient optimisation process.

The efficiency of the system is strongly affected by the choice of design variables. Referring to the parameterisation section 2.3.1, the most influential variables are bump position on the aerofoil, bump height and the location of this maximum height along the bump length. Incorporating these variables into the SCB design saw the developments of the shapes presented in figure 2.12. These specific bump geometries need to be

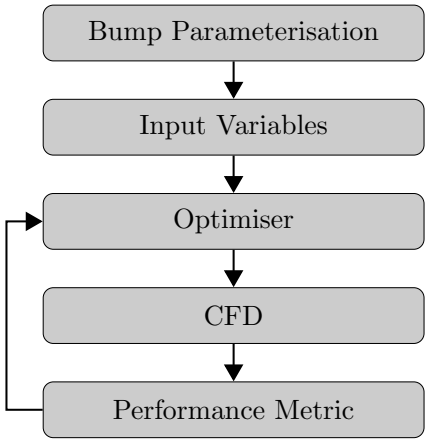


Figure 2.18.: General SCB optimisation process flow chart.

incorporated into the aerofoil as well as the optimisation process. This is an issue that arises with the use of CFD to calculate the flow field as the aerofoil geometry is best represented as a curve to ensure high quality automated meshes. Various methods were compared by Lutz et al. [2003] including Bezier curve representation, Eppler and Joukowski mapping in order to highlight the best method however there was very little difference between the results returned via each representation.

The optimisation algorithm determines how the design space is explored and how efficiently it conducts the search. The large body of parametric studies conducted during the Euroshock II project provided a large amount of data regarding efficient design variables which contributed towards the bounds of the design space. The general guidelines of SCB positioning and height were formed in the project, which significantly aided the construction of future optimisation problems. Many subsequent studies have investigated optimal geometries, with approaches taking the form of evolutionary algorithms [Lutz et al., 2003] including genetic algorithms (GA) and particle swarm optimisation (PSO) [Lee et al., 2012] to approaches which aimed to quickly find a good, local solution rather than a definitive optimal solution [Pätzold, 2006]. The latter technique does not require the objective function derivatives to be calculated which speeds up the process however it can only cope with smooth objective function topologies for which previous knowledge of the design space is readily available. Other approaches have focussed on gradient-based optimisations which systematically find the sensitivity of each design variable [Rhodes and Santer, 2012]. The sensitivity derivatives have been calculated through adjoint solvers by Qin et al. [2008] as well as robustness functions derived from

database methods based upon existing flight data [König et al., 2009, Nübler et al., 2012]. This database method was based upon work conducted by König et al. [2009] that estimated changes in lift coefficient and Mach number during cruise

Regardless of the optimisation technique applied a performance metric is always used to provide a measure of how successful the design is and guide the optimisation process towards an optimal design. Recent developments have extended the traditional optimisation for a single flight condition to include a variety of conditions and an element of robustness to the design. Lee et al. [2012] included a multi-objective optimisation function to the evolutionary optimisation algorithm in order to incorporate robustness.

The bulk of the optimisation studies for SCB produce similar results with the number of iterations for a converged solution ranging from ~ 20 using a gradient-based optimiser [Yagiz et al., 2012] to ~ 1800 using a multi-parallel objective and evolutionary algorithms [Lee et al., 2011b]. The large range of iterations to convergence is primarily a function of the optimisation method applied and the length of time required for a single fluid field computation. In order to minimise the overall time, it is important to construct a well defined optimisation problem with suitable parameterisation within an efficient design space. Often a sensible approach is to chose design parameters based upon the wealth of existing parametric [Tian et al., 2011, Eastwood and Jarrett, 2012] and optimisation studies [Kutzbach et al., 2004, Yagiz et al., 2012, Lee et al., 2011b,a, Wong et al., 2008]. The goal in all cases is to produce a globally optimal design in as few iterations as possible.

2.3.4. Off-Design Performance of SCB

The off-design performance is often discussed at the end of each optimisation study, however there is no definitive study. It is suggested throughout EUROSHOCK II that the sensitivity of the shock structure to SCB positioning has increased the need for robust designs for SCB in order to cope with varying shock position. Figure 2.19 shows the typical shock structures that occur when the shock position is not in an optimal position relative to the SCB. This has been documented previously by Dargel and Thiede [2002] and Bruce and Colliss [2014]. The former changed the location of a fixed-beam based geometry upon the NLF DA LVA-1A aerofoil and monitored the effects on drag. However the flow structures were not discussed.

The work showcased five different SCB locations which consisted of two upstream, two downstream and an optimal location. The change in pressure distribution was due to the formation of shock structures shown in figure 2.19 which caused significant

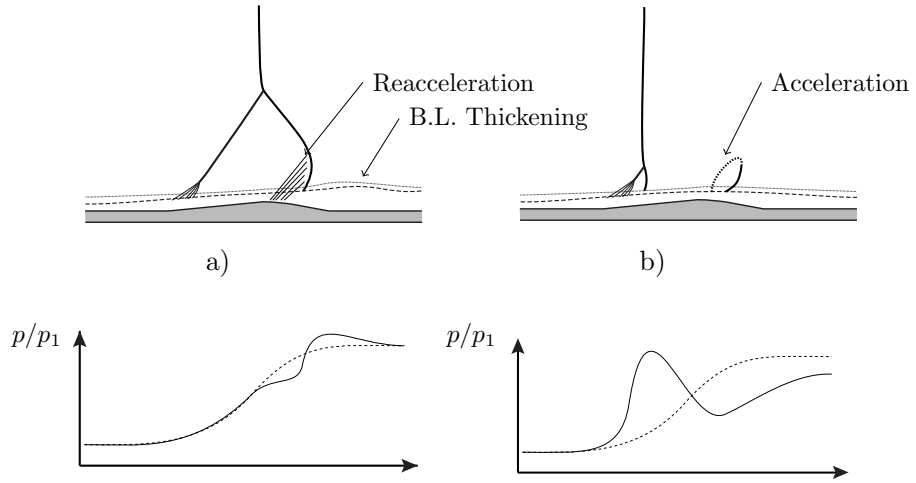


Figure 2.19.: Typical shock structures for typical off-design conditions. a) SCB too far upstream. b) SCB too far downstream.

increases in viscous drag. Figure 2.20 shows the importance of shock placement with respect to the crest of the SCB and how the positioning affects each drag component.

Placing the SCB crest too far upstream, $x_{crest} = 0.6c$, significantly increases the viscous drag of the modified aerofoil as shown in figure 2.20c, the change is approximately 33% when compared to the best total drag reduction position. The effect upon wave drag is minimal with a slight increase at this location. As the crest is moved further downstream to locations $x = 0.65$c and 0.7c, the main normal shock sits close to the crest and the wave component decreases to a minimum. This apparently optimal position reported throughout the EUROSHOCK is supported by further experimental studies by Ogawa [2006] which used a shock holding plate to artificially set the shock position in wind tunnel experiments. The relationship between crest position and shock location also provides information about how the flow field will respond to a change in shock position. The findings from these initial parametric studies provide a valuable insight into the behaviour of shock waves in the vicinity of the SCB and provide initial conditions from which to optimise.

Lee et al. [2011b] studied the effects of single and multi-objective functions for a wide range of lift coefficients on a RAE5243 aerofoil ensuring the resultant optimal design maintained performance across a wider envelope. This was the first inclusion of off-design performance within an optimisation procedure.

The performance envelope of an aerofoil with 2D SCB was found to be very sensitive

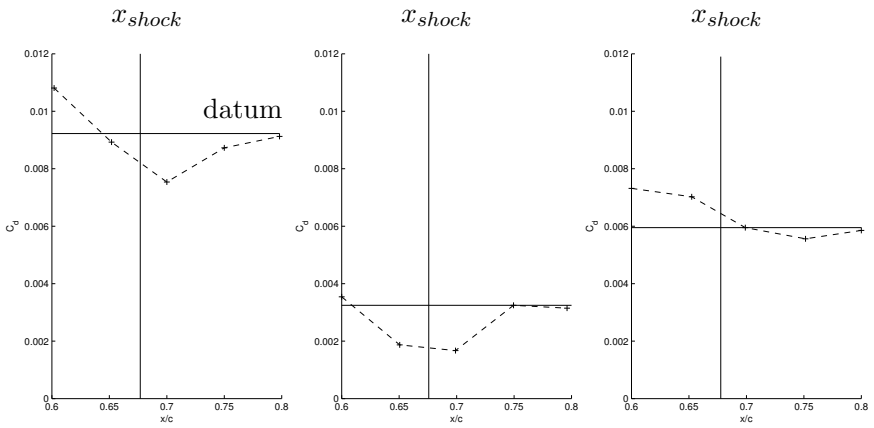


Figure 2.20.: Drag breakdown for variable SCB placement upon DA-LVA-1A NLF aerofoil, $M_\infty = -0.76, Re = 6 \times 10^6, l_b = 0.2c, h_b = 0.003c, c_b = 0.5l_b$. a) Total drag. b) Wave drag. c) Viscous drag. The x/c values represent the crest location as a proportion of the total chord. Adapted from Dargel and Thiede [2002].

to shock position imposed by the flight speed and angle of attack. As a result the field of SCB turned towards three-dimensional studies which required the development of better optimisation strategies in an effort to limit off-design deterioration by limiting the span-wise extent of the SCB [Lee et al., 2011b]. Initially these incorporated investigations into the effects of sweep by Kutzbach et al. [2004] and Pätzold [2006].

3D SCB have been shown to be more sympathetic to the flow at off-design conditions as the geometries do not impart the bifurcated shock structure across the entire span [Ogawa et al., 2008]. Eastwood and Jarrett [2012] conducted a wide parametric study which compared two and three-dimensional SCB using the wedge type geometry in figure 2.12b. In this study it was found that 2D bumps outperformed 3D SCB in terms of ultimate L/D performance metric. The study also highlighted that 3D SCB required a higher ramp angle to achieve optimal performance and that this angle increased with increasing span-wise spacing of the SCB. This idea is that for equivalent L/D performance, narrower SCB need a greater deflection angle to compensate for the limited spanwise extent.

Significant work on the flow physics of 3D SCB was undertaken by Ogawa et al. [2008] who used a variety of experimental techniques such as laser doppler velocimetry (LDV)

to capture the small scale velocity fields present around the SCB. These provided a much greater insight into the flow physics than just the pressure distribution on an aerofoil. It led the way for more emphasis to be placed upon the intricate flow in the vicinity of the SCB. With this notion, Qin et al. [2008] introduced the idea that 3D SCB could impart an element of boundary layer control downstream of the bump. This was a subject investigated further by Bruce and Babinsky [2012], Colliss et al. [2014] and König et al. [2009].

The concept of robust design stems from a requirement to maintain performance of an aircraft wing over a wide operation envelope. Nübler et al. [2012] developed test flight conditions from a database of momentary parameters recorded during long haul flights. This formed a huge design space which was reduced to two key points either side of the design point to drastically simplify the computation. Nübler et al. optimised three bump shapes involving a wedge, a smoothed profile and an extended wedge with a rear surface that continued to the trailing edge similar to a geometry tested previously by Colliss and Babinsky [2012]. The addition of this large tail proved to have a positive effect at the design point however at the second design point a secondary shock system formed over the crest which contributed to a drop in performance similar to the structure illustrated in figure 2.19b.

Although further work is currently being carried out on 3D SCB, the study by Colliss et al. [2014] shows that off-design penalties can still be present upon 3D SCB. Although the second shock penalty is limited to the span-wise extent of the 3D SCB, there are still negative effects present which has let to some researchers exploring alternative methods to negate off-design performance. One such method is the adaptive SCB.

2.4. Adaptive Shock Control Bumps

The adaptivity of the initial SCB concept proposed by Ashill et al. [1992] has been somewhat overlooked by the vast majority of subsequent research into SCB. Almost all studies have focussed upon static SCB with devices fixed to the wing surface throughout flight. As discussed previously there can be severe performance issues for a wing with a SCB if the shock is in an off-design position. An element of adaptability has the potential to eliminate the occurrence of these off-design penalties however it brings with it new design challenges that need addressing.

The design of adaptive SCB requires a combined aerodynamic and structural approach.

The original concept by Ashill et al. [1992] featured a flexible skin capable of deforming

with an actuator and thus an element of adaptivity. This initial concept is illustrated in figure 2.10 and shows a single actuation point that could extend to create a surface deflection and retract to return to the clean aerofoil geometry. There are many benefits to this design as a continuous surface is maintained between the existing skin and that of the control section, thus eliminating any elements of roughness or unnecessary joins and preserving the health of the boundary layer as it enters the control region.

Wadehn et al. [2002] investigated the structural concepts of adaptive SCB and achieved the desired actuation through discrete actuation systems as illustrated in figure 2.21. The study also proposed the use of shape memory actuators. The goal of the study was to produce similar geometries to those optimised during the Euroshock II project with minimal actuation energy. Moderate actuation forces of less than 50 N were applied to achieve the desired geometric deformation, thus allowing small actuators to be used. It should be noted that the structural approach of Wadehn et al. makes it difficult to compare with other studies in terms of aerodynamic performance. However the geometries produced as a result of the energy based performance metric are of a similar shape to those derived from aerodynamic optimisations but are significantly larger.

One major difference is the length of this SCB and in particular the length to height ratio. The vast majority of studies which have focussed on aerodynamic performance typically have bump heights in the range $0.175\%c < h_b < 0.5\%c$ with lengths typically between $0.15c < l_b < 0.2c$. This leads to a height to length ratio range $\sim 0.01 < h_b/l_b < 0.03$. In contrast, the height-length ratio of the distributed actuation system proposed by Wadehn et al. was 0.007.

A comparison between bump heights is provided in figure 2.22 which includes the centreline geometry of the default rounded bump [Ogawa et al., 2008] and the 2D physical model representation of an adaptive SCB Rhodes [2012]. The plot highlights the significant difference in heights that have been optimised for structural metrics [Wadehn et al., 2002] and aerodynamic performance [Ogawa et al., 2008]. This difference demonstrates that adaptive SCB will have to integrate both structural and aerodynamic constraints into the optimisation process. The next two sections look at the structural and aerodynamic components individually and introduce some of the challenges that may arise with adaptive SCB before reviewing the combined aero-structural effects of such a device.

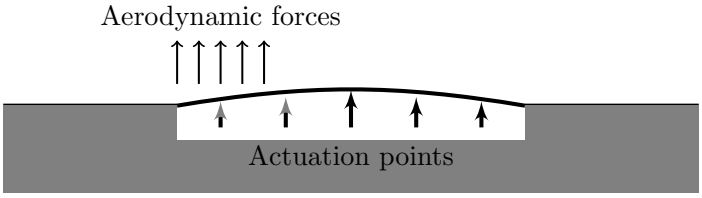


Figure 2.21.: Distributed actuation system envisioned by Wadehn et al. [2002], adapted.

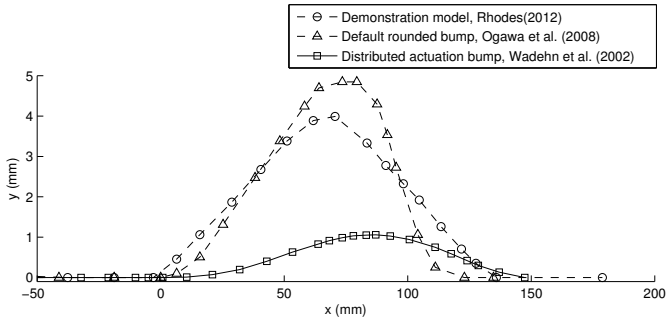


Figure 2.22.: Comparison of distributed actuation system by Wadehn et al. [2002] against the reduced actuator model of Rhodes [2012]. The centreline geometry of the default rounded bump by Ogawa et al. [2008] is included to represent the target for adaptive SCB geometries.

2.4.1. Structural Modelling of Adaptive SCB

The structural aspect of adaptive SCB has been overlooked somewhat as the device usually takes the form of a static geometry that remains rigid during aerodynamic loading. If a potential design is to deploy and retract there needs to be an element of flexibility and also a method to reliably deform the surface.

Bein et al. [2000] were some of the first to study the potential of an adaptive form of shock control. The approach placed a local bump upon the spoiler of a transonic aerofoil. This required large out-of-plane deformations and the design of a new spring mechanism based upon a cylindrical tube. The actuation had a large stroke, up to 55 mm and was capable of moderate forces up to 20 N with a supply pressure of 2 bar. The length of the SCB was very large at $l_b = 2200$ mm which is significantly larger than examples of SCB in the literature and actually results in a height-to-length ratio of 0.25 which is similar to many existing SCB [Qin et al., 2008, Yagiz et al., 2012, Colliss et al., 2013, Nübler et al., 2012]. The large scale of the SCB test model is an atypical size however Bein et al. were not restricted by a transonic/supersonic wind tunnel which often limits the dimensions of SCB models. As a proof of concept for structurally-derived SCB, the work has shown that a system can be designed to deform to suitable levels. However the overall size of the demonstrator model remains too large to test in the wind tunnels used to test SCB designs.

The adaptive SCB concept was investigated more recently by Rhodes [2012] within a more general focus of optimal design of morphing structures. Rhodes aimed to recreate optimal geometries for both 2D and 3D SCB with a deployable design similar to Ashill's concept. The design featured manual screw actuation to produce the deformed structure with the 3D SCB requiring 9 control points.

Figure 2.23 shows the difficulties of achieving static SCB geometries with adaptive structures. Rhodes replicated the centreline geometry of a static 3D SCB, the 'default rounded bump', developed by Ogawa et al. [2008] and selected this geometry as the target for adaptive SCB.

The work undertaken by Rhodes and Santer [2012] produced two physical models that aimed to replicate the geometry of the default rounded bump. The first was 2D and aimed to recreate the centreline geometry and the second aimed to recreate the entire 3D geometry. The models maintained zero displacement until the point of the flexible skin which was fixed in position with zero displacement and rotation. Benefits of this design were that the deformation was able to match earlier bump geometry families whilst maintaining a smooth surface on the flow side. The entire actuation system

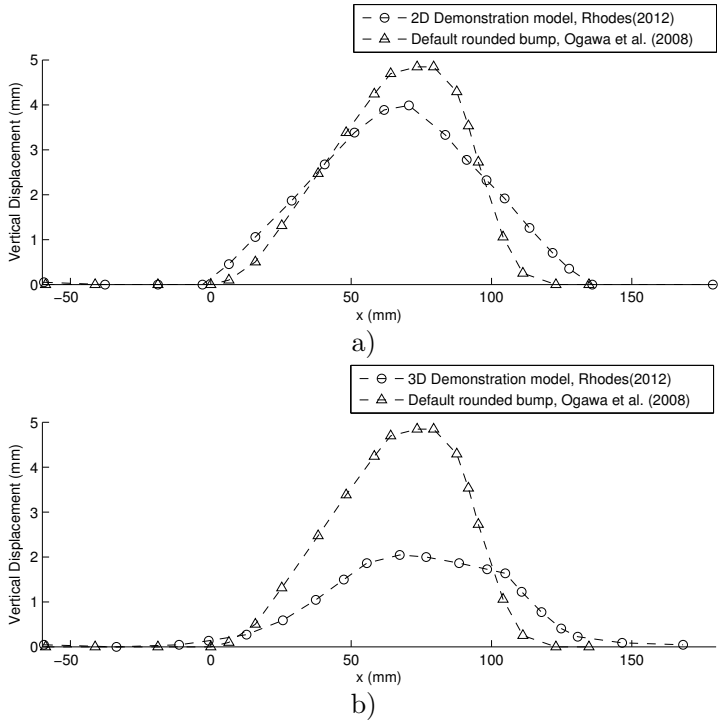


Figure 2.23.: a) 2D Model replication of Default rounded bump centreline. b) 3D Model centreline replication of Default rounded bump centreline. Adapted from Rhodes [2012].

consisted of two actuation points for the 2D model and nine for the 3D model were kept below the surface which would help preserve the quality of the flow over the adaptive SCB.

The deformed geometry of the 2D case is shown in figure 2.23a. The actuation failed to reach the peak displacement values of the target static SCB whilst remaining within the elastic regime. The maximum displacement was 80% of the target of 4.8 mm which showed some promise from an aerodynamic perspective, as will be seen in the following section. From a structural point of view, staying within the elastic limit for deformation is key to designing a successful adaptive SCB that can endure repeated actuation.

The 3D model suffered significantly from stress concentrations at the fixed edges. The elastic regime allowed for a maximum centreline displacement of 2 mm, just 41% of the target displacement, figure 2.23b. Rhodes [2012] concluded that 3D SCB were problematic when aiming to replicate geometries with high changes in Gaussian curvature due the necessity to sustain in-plane strains which surpassed the material constraints. The adaptive 3D model was not capable of reaching the heights achieved by the fixed geometry target suggesting that a change in actuation technique or materials would be required.

These findings relating to the 2D and 3D models highlight how the structural constraints of an adaptive SCB can limit the range of designs. One of the main features of adaptive SCB is their ability to deploy during suitable flow conditions and retract when off-design. Thus in order to create efficient adaptive SCB, the structural constraint must be included into the design process so that the SCB can deform without incurring plastic deformation.

2.4.2. Aerodynamic Modelling of Adaptive SCB

The investigations into adaptive SCB by Bein et al. [2000] and Wadehn et al. [2002] primarily focussed upon the structural aspect of the designs. The main goal was to achieve suitable SCB geometries through the use of novel actuation systems. Rhodes [2012] carried out a numerical analysis that coupled together CFD and FEA that began to quantify the performance of adaptive SCB through an optimisation process. Each of these existing studies did not feed back the aerodynamic response to the structural model which could have a significant effect upon the geometry of these flexible plate based designs.

In order to gauge the effect of aerodynamic loading during deployment, the aerodynamics must first be identified. By including an element of adaptivity, the SCB will be

able to change height during operation. Whilst no transient study of SCB deployment exists, there have been studies that may be able to suggest how a variable height SCB will perform.

Dargel and Thiede [2002] undertook a parametric study that explored the possibility of adaptive SCB. The researchers began to characterise the performance of a typical SCB across a selection of locations and varying heights at a set shock location. This part of the investigation was titled off-design behaviour and the resulting shock structures and pressure distributions may be useful to predicting the performance of an adaptive SCB during deployment/retraction.

Figure 2.24 shows the lift-drag polar for the NLF DA LVA-1A aerofoil with and without a number of different SCB heights. The effects of increasing height can be seen to vary depending upon lift coefficient. For small lift coefficients $0.3 < C_l < 0.4$, the presence of a small SCB improves performance and reduces the drag coefficient. Higher SCB increase the drag at these lower C_l and it is only at higher values $C_l > 0.4$ where we see the higher SCB begin to have a positive effect. This trend for the performance of higher SCB to vary may be due to post-crest separation caused by a mismatch between shock position and SCB crest location. Another possibility is that the flow may separate due to the significant curvature of the aerofoil geometry. Either way, these results suggest the requirement for variable height SCB. For lower SCB the crest curvature is lower and thus the likelihood of separation may be lower.

It was suggested by Lee et al. [2011b] that a robust design should produce a smooth lift-drag profile that monotonically increases. By this metric, the polars generated by Dargel and Thiede [2002] for the lower heights, $h_b = 0.2\%$c and 0.3%c are robust solutions because they do not feature a drop in C_d for an increase in C_l. The $h_b = 0.5\%$c bump on the other hand fluctuates with a drag bucket present at higher lift coefficients $C_l > 0.4$. This variation in performance is not ideal for static SCB and so despite the increased performance at higher C_l the penalty at lower C_l undoes the benefit. This is an instance where an adaptive SCB could be utilised to maximise the drag reduction across a wide range of C_l by varying the height as the C_l is adjusted.

SCB height is not the sole variable which determines SCB performance. As referred to previously in this work, Eastwood and Jarrett [2012] conducted a parametric study that investigated the effect of ramp angle and spacing of 3D SCB on the lift to drag ratio of a wing. The results of the study are plotted in figure 2.25 which shows the effects of moving away from a 2D SCB and increasing the spacing of 3D SCB. Taking a single bump spacing the improvement in performance (L/D) can be seen to increase almost linearly with ramp angle until a critical ramp angle is reached and there is a

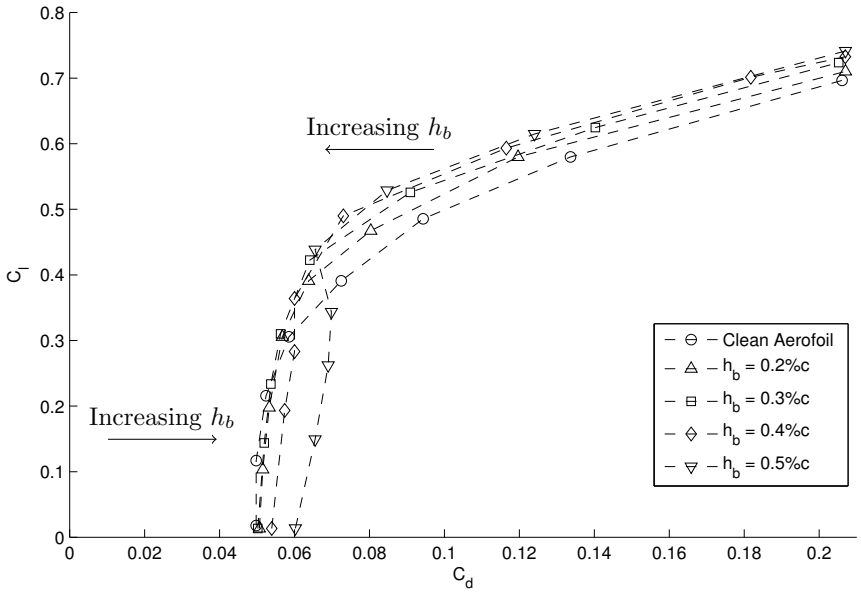


Figure 2.24.: Lift-Drag polar for DA LVA-1A NLF aerofoil, SCB location, $x_{SCB} = 0.6c, l_b = 0.2c$, Variable h_b. Data adapted from Dargel and Thiede [2002].

significant drop in performance.

With the length of the bump fixed at 0.2c, and the location of the crest fixed at $0.5l_b$, the change in ramp angle effectively changes the height. In the previous structural section, the idea was put forward by Rhodes and Santer [2012] that if a 2D adaptive SCB can achieve $80\%h_b$ of a 3D SCB then the aerodynamic performance would be comparable. This trend is also observed in the investigation by Eastwood and Jarrett [2012] and figure 2.25 has been adapted from their work. For a given L/D value in figure 2.25 (see the dotted reference line) it can be seen that a 2D SCB is able to match the L/D of any 3D SCB for a lower ramp angle. As the location of the crest is fixed in this study the ramp angle is directly proportional to SCB height. This shows that when SCB height is a constrained, such as in an adaptive SCB by the material stresses, a 2D SCB is better at minimising material stresses than a 3D SCB.

In terms of adaptive SCB, the steady response to a discrete ramp angle change may provide information with respect to the performance of a deployable SCB. The increase in performance is appreciable until a maximum ramp angle is achieved after which there is a severe drop and it is this behaviour that can offer relevant information to the envelopes of adaptive SCB.

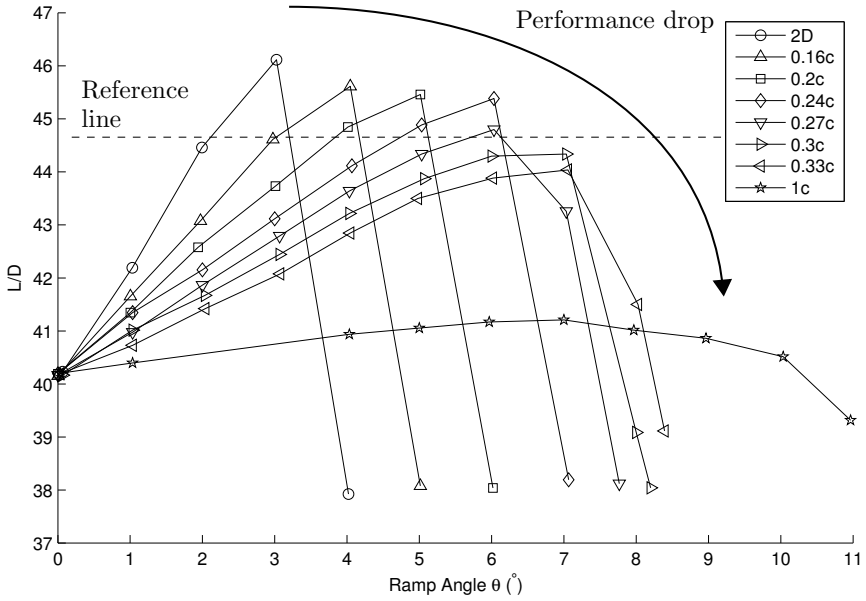


Figure 2.25.: L/D variation with ramp angle and variable spacing for 2D and 3D SCB, adapted from Eastwood and Jarrett [2012]. Bump width, $b = 0.1c$.

Figure 2.25 also shows that with span-wise bump spacings of 1c, a 3D wedge SCB offers a very broad, sympathetic envelope yet fails to reach the maximum performance values of the closer spaced cases. This supports the idea that static 2D SCB are able to outperform 3D SCB but do not necessarily have such a broad performance envelope with respect to ramp angles/heights. Adaptive SCB would be able to maintain an optimum ramp angle for the flow conditions and avoid the sharp drop in performance shown in figure 2.25.

All of this provides valuable information on which to base the design of an adaptive SCB. However the small-scale aerodynamics of this study have been disguised somewhat behind L/D values and it is these aerodynamic changes that will potentially interact with the structure and require a coupled approach.

2.4.3. Aero-structural Modelling of Adaptive SCB

The previous structural and aerodynamic sections have described the expected steady-state performance of a variable geometry SCB. From a structural point of view, suitable actuation and material selection for typical bump geometries is most readily achievable through a two-dimensional SCB. From an aerodynamic perspective, a parametric study

initially conducted to showcase the variation of 3D SCB has highlighted the superior performance of 2D SCB at design conditions. The importance of aerodynamic loads was briefly considered by Wadehn et al. [2002] and Rhodes [2012] who concluded that such forces would have minimal effect upon the geometry.

Ashill et al.'s original SCB concept featured a section of flexible skin. Whilst the characteristics of the material required were not discussed it must maintain enough flexibility to deform and enough stiffness to withstand the aerodynamic loading. Not only do the actuation points offer a change in the boundary conditions out of plane but they effectively reduce the lengths of the flexible skin section. This has a significant effect upon the stiffness/flexibility of the system and perhaps most importantly for adaptive SCB, the panel dynamics. It is the dynamics of the design that are yet to be investigated and a review of panel flutter studies aims to address this with an emphasis on extracting appropriate design cues from the practises developed.

Panel Flutter Considerations

The levels of flexibility required by 2D adaptive SCB to match the heights and geometries of static SCB have been shown to extend beyond what is possible with aerospace-grade aluminium [Rhodes and Santer, 2012] and CFRP (Carbon fibre reinforced plastic) [Bein et al., 2000]. A side effect of this necessary flexibility is the sensitivity of the panel to any aerodynamic forces imparted by the flow field. The flexible plate-based design has many parallels with panel flutter studies completed in the 1960s and 1970s by Dowell and Voss [1963], Dowell [1966, 1970, 1972]. These studies involved experiments and the development of analytical models to investigate the interaction between an unsteady flow field and a thin plate.

Aerodynamic analysis in the above investigations mainly used piston theory, while the structural analysis was based upon various analytical models including Rayleigh-Ritz, Galerkin and multiple finite element and finite difference methods. The authors focussed upon the limit cycles of the interaction and were predominantly theoretical in their approach. The aim of the studies was to identify a procedure for design to avoid catastrophic panel flutter failure where large surface oscillations began to occur. This type of material failure can be viewed as a fatigue-based failure however the time scales are much shorter and often rely upon steady-state loading to provide the failure criteria rather than the extensive cycle based modelling. In summary, these studies aimed to avoid the onset of panel flutter rather than accurately predict panel flutter events.

In the context of these studies, the flutter boundary is commonly defined as the

dynamic pressure at which the onset of panel flutter begins [Dowell and Voss, 1963] which sees oscillations greater than the plate thickness commence. It is known to vary with Mach number. The relationship between the flutter boundary and the panel characteristics is

$$\lambda^* = \frac{2qa^3}{D} \tag{2.4}$$

where

$$D = \frac{Eh^3}{12(1-\nu^2)} \tag{2.5}$$

where q is the dynamic pressure, a is the plate length, E is the Young's Modulus, h is twice the plate thickness, $2t$, and ν is the Poisson's ratio of the material.

In the experiments of Dowell [1970] it was found that below the flutter boundary, random oscillations of the panel occur with frequency components near the panel's lower natural frequencies. Above the boundary, the fluctuations increase and could develop into stable, unstable or limit cycle oscillation modes. The non-dimensional analysis used throughout did not capture any non-elastic behaviour of the plate. The application of Dowell's analysis to the case of adaptive SCB is to be conducted in chapter 3.

Dowell and Voss [1963] extended the linear structural representations to include the non-linear deformations where the deformation exceeded the plate thickness. This was coupled with linear aerodynamic theory to calculate the pressure loading. The model produced was able to highlight the influential factors in plate response illustrated in figure 2.26 covering plate length, thickness and dynamic pressure.

The field has evolved recently with the development of CFD to combine three-dimensional Navier-Stokes solvers that are coupled with finite difference structural models [Gordnier and Fithen, 2003, Visbal, 2014]. Both inviscid and viscous solutions for oblique shock-plate interactions have been investigated. These studies have shown that viscosity delays the onset of panel flutter to higher dynamic pressures possibly due to the smearing of the pressure rise. There are no studies that incorporate the specific case of a normal shock and a flexible plate however the design practices proposed by Dowell [1970] can be applied to any generic case.

Various review papers such as Dowell [1972] and Mei et al. [1999] have collated existing panel flutter knowledge and attempted to bridge the independent fields of aeroelastics,

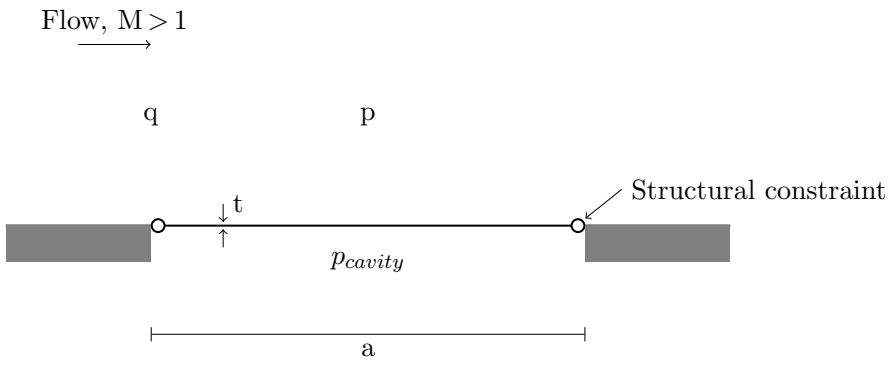


Figure 2.26.: Influential variables in panel flutter studies.

structural dynamics and high-speed compressible flow.

The dominant variable contributing towards the panel response uncovered by Dowell and Voss [1963] was the pressure difference between the upper and lower surfaces. Whilst the dynamics of the system were affected by length and aspect ratio the overall response of the plate was driven by the dynamic pressure and the corresponding static pressure of the incoming flow for a given Mach number. The study went some way to explain the sensitivity to each flutter variable and the results provided guidelines to avoid panel flutter in the design process.

The studies of Gordnier and Fithen [2003] and Visbal [2014] explore a wide range of test cases and include changes in the viscosity models, flow conditions such as the incoming Mach number and strength of the impinging shock as well as the boundary conditions applied to the edges of the plate. An illustration of the inviscid Mach 2 shock structure over the flexible plate considered by Visbal [2014] is provided in figure 2.27. Visbal also conducted a brief investigation into the effects of cavity pressure. Whilst not the main aim of the study it did highlight the effects of oblique shock loading upon flexible plates and the significantly different surface geometries that can be produced whilst solely varying cavity pressure.

Figure 2.28a shows the steady plate response subject to the shock structure in figure 2.27. The corresponding pressure rise across the surface of the plate is shown in figure 2.28b with an initial rise in pressure across compression waves labelled 1. before reaccelerating to a stronger shock. From the study by Visbal [2014] of three critical cavity pressures. The three cases show the effects that cavity pressure can have upon the surface geometry. The inviscid pressure distribution shown has some similarities to that across a bifurcated shock, with a multi-stage pressure increase in the streamwise

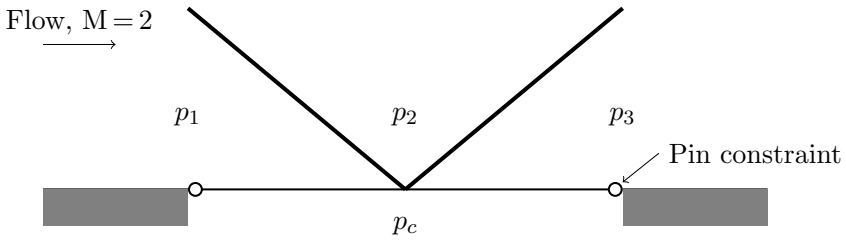
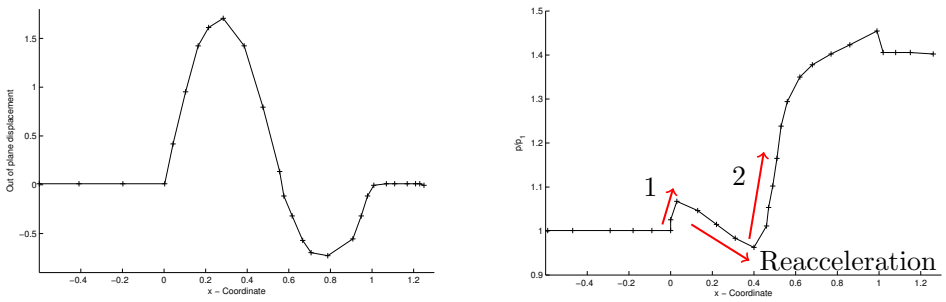


Figure 2.27.: Inviscid oblique shock structure present in Visbal [2014].

direction. This is highlighted in figure 2.28b by the labels 1 and 2 where the choices of cavity pressure relate to the distinct pressure regions on the upper surface of the plate, namely p_1 and p_3 in figure 2.27.



a) b)

Figure 2.28.: Effect of cavity pressure for inviscid interaction in figure 2.29b with M_1 = 2:0, p_3/p_1=1.4. Time-averaged (a) panel deflection and (b) surface pressure. Adapted from Visbal [2014].

When cavity pressures were equal to the upstream pressure, p_c/p_1=1.0, the higher pressure downstream of the impingement location caused negative displacement of the plate. Whilst not presented by Visbal [2014], the expected shock structure is illustrated in figure 2.29a. The negative surface deflection would trigger an expansion fan and a slight acceleration resulting in a strengthening of the shockwave. If the panel was very flexible, the existing flow curvature could be too severe for the flow to remain attached and potentially cause the flow to separate. In this instance the flexible plate would lead to increased viscous losses downstream of the system as well as potentially unrecoverable plastic deformation.

For the case where $p_c/p_1 = 1.2,\ p_1 < p_c < p_3$, the lower pressure over the front of the

plate has a suction effect whilst the higher pressure downstream still causes a negative displacement. The effects of this type of surface geometry upon the performance of adaptive SCB would be positive in terms of shock structure but the overall performance could be hampered by significant boundary layer thickening in the suppressed region. This is illustrated in figure 2.29b The initial positive displacement would instigate compression waves however the crest that follows would cause expansion waves to appear. This would result in an expansion fan that would accelerate the supersonic flow to higher Mach numbers and increase the strength of the shock. The severity of the effect depends entirely upon surface deformation and the resultant angle, the magnitudes of which are dictated by material characteristics and plate dimensions.

When $p_c = p_3$, the highest upper surface pressure, there is no negative displacement and the geometry is primarily controlled by the large suction forces caused by the pressure differential over the front section of the plate. The geometry produced by this loading is shown in figure 2.29c and is more typical of a traditional SCB. Only consisting of positive surface displacement rather than any negative displacement. The designs aim to reduce significant thickening of the boundary layer by reducing any reacceleration regions or regions of high convex curvature that may cause separation. This suggests that the smallest cavity pressure to guarantee a traditional SCB shape would be equal to the largest pressure on the upper surface.

The geometries uncovered by Visbal [2014] are dependent upon an inviscid flow solution. If viscosity were included, the pressure rises would become smeared. This will lessen the effect of the pressure gradients shown in figure 2.28b so there will be a more continuous loading over the plate.

Experimental studies of plates have been conducted across a wide range of Mach numbers by Vedeneev et al. [2010] and have predominantly focussed on the structural response of the plate. This ties in with the limit cycle studies of Dowell [1966] and Visbal [2014] however the flow structure was not investigated to the extent of modern SCB such as those designed by Colliss et al. [2014]. The cases investigated by Vedeneev et al. are focussed upon the fluid-structure interaction for a panel subject to a supersonic free stream flow over the upper surface. The study is one of very few tests that records the response of a plate for a range of Mach numbers, $0.857 < M < 1.298$. The upper end of this range provides the most suitable information regarding the design challenges that face adaptive SCB.

The experimental setup in the study conducted by Vedeneev et al. [2010] considered a plate with flow passing above and below and incorporated the effects of cavity pressure as well as significant boundary layer suction to reduce shock smearing and the effect of

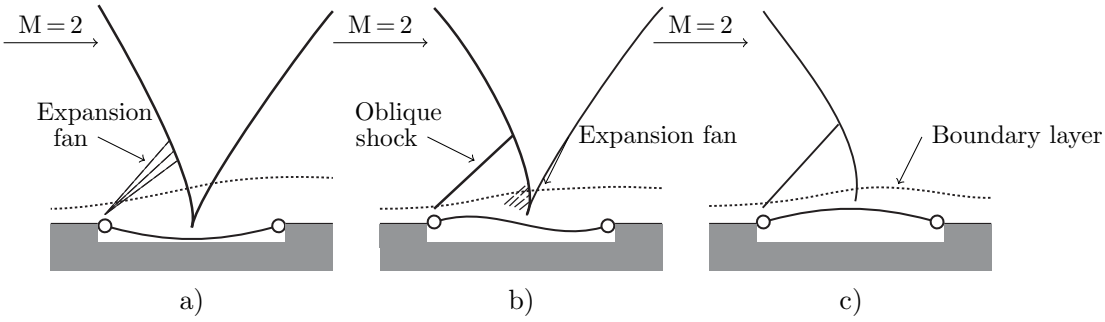


Figure 2.29.: Expected shock structures for plate geometries subject to variable cavity pressures and Mach 2 oblique shock interaction described by Visbal [2014]. a) $\min(p_{flow}) > P_{cavity}$. b) $\min(p_{flow}) < P_{cavity} < \max(p_{flow})$. c) $P_{cavity} > \max(p_{flow})$.

viscosity over the plate. It was noted however that whilst the pressure changes were small across the plate, the pressure difference across the plate varied and affected the mode of vibration.

The first two vibration modes are shown in figure 2.30. Figure 2.30a shows the deformation of the plate when the upper surface pressure is lower than the lower surface. This first mode increases the cavity volume and essentially works as an aerodynamic spring. The second mode was not found to affect the oscillations as the volume beneath the cavity is equal to the unloaded flat plate. The formation of the geometry in figure 2.30a was also identified by Visbal [2012] and caused significant stiffening of the panel due to the pressure difference across the plate. As the plate deforms the stiffness of the plate also increases and it is this stiffening of the plate that limits the large-scale deformation which may lead to destructive panel flutter.

This effect will become important in the design of flexible plates for adaptive SCB and is an element that was not considered with static SCB due to their lack of flexibility.

The pressure differential across the plate will therefore not only drive the static geometry of the plate such as the geometries in figure 2.29, but also the dynamics of the system due to the stiffening of the system. These aspects are new to SCB design as a result of the adaptivity and must be investigated further in order to create a successful adaptive design.

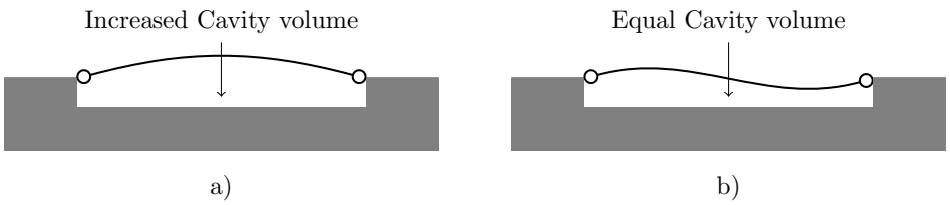


Figure 2.30.: Streamwise vibration modes as described by Vedeneev et al. [2010]. Cavity volumes comparisons to initial flat plate condition. a) First mode. b) Second mode.

2.5. Summary of Existing Research

The review of existing literature has incorporated the knowledge gained from existing static SCB studies as well as from the field of panel flutter. This combination of existing fields have been considered in order to provide an insight into the relatively new field of adaptive SCB. A summary of the findings are provided here with the key points that relate to adaptive SCB presented. The points illustrate the evolution from static SCB through panel flutter to adaptive SCB.

- Numerous transonic flow control techniques have been identified with two distinct groups of control. Those that aim to manipulate the boundary layer and those that aim to change the shock wave structure. The successes of the the two approaches were mixed and often a reduction in viscous losses resulted in an increase in wave drag and vice versa. Of the devices surveyed, the shock control bump has shown the most promise in providing a significant wave drag saving with minimal change to the viscous losses.

- SCB achieve a drag reduction through bifurcating the shock, that is initiating an oblique shockwave prior to the main normal shock in order to reduce the strength of the normal shock in a region local to the wall up to the triple point. This reduces the total pressure losses across the main normal shock which reduces wave drag.

- The sensitive nature of the flow around the shock region means that the surface geometry is a hugely influential factor and small changes at the wall have a significant impact on the health of the entire downstream boundary layer. This facet signifies the applicability of optimisation to this problem which has seen many studies dedicated to achieving optimal solutions for SCB in a range of cases varying from aerofoils to inlets and also turbine blades.

- SCB performance is sensitive to flow conditions and lift-to-drag polars have shown the performance of SCB across a wide range of lift coefficients. This summarises the issues that designers are facing with respect to the off-design performance. For example a change in desired lift coefficient for a wing causes a change in shock position which is no longer optimal with respect to SCB position and potentially large separated regions may occur over the rear half of the aerofoil with a corresponding increase in drag. It is these instances where the ability to deploy and retract a SCB would be extremely beneficial.

- The initial designs by Ashill et al. [1992] showcased a flexible skin which will require careful design in order to withstand the shockwave environment. The steady-state performance measures of an adaptive device with variable height can be inferred from some of the parametric studies [Eastwood and Jarrett, 2012] however the transient bump deployment characteristics are still an unknown.

- Structural adaptive SCB models have been constructed by Bein et al. [2000], Wadehn et al. [2002] and Rhodes [2012] but the aerodynamic results have not been presented in the manner typical of SCB studies. Promise has been shown in their designs as it is possible to achieve similar bump heights to their static counterparts whilst maintaining adaptivity.

- The influence of the aerodynamic load upon the flexible structure may cause the large scale oscillations of the skin that forms the adaptive SCB. The panel flutter avoidance guidelines formed by Dowell [1972] provide a solid starting point to base adaptive SCB designs on. The studies carried out by Visbal [2014] show that a flexible plate can greatly influence the shock structure with a smearing of the pressure gradient whilst remaining beneath the yield stress of the material. Despite the different shock structure the results show that the FSI could be controlled, possibly by the cavity pressure.

- The challenge for adaptive SCB is to achieve the formation of a λ-shock whilst maintaining a design that possesses enough flexibility to achieve typical SCB heights and the stiffness to withstand the harsh aerodynamic loading in the shock environment.

These points require careful design and an approach that takes into account an optimal design of both aero and structural components as well as an experimental study that identifies the mechanisms required for adaptive SCB deployment. The subsequent

chapters aim to cover each of these points and develop a guide to designing adaptive SCB that merges traditional design approaches with a new dynamic fluid-structure interaction aspect.

3. Adaptive SCB Design

The review of the development of SCB in the previous section has uncovered the approach for traditional devices as well as presented considerations towards future designs. The evolution of SCB from the initial 2D studies to 3D SCB has been considered as a means to overcome the poor off-design performance of static 2D SCB. An alternative approach to help overcome the inefficiencies is to focus upon adaptive SCB which brings additional complications that were not an issue with static SCB.

Developing the original concept of Ashill et al. [1992] allows for new avenues to be researched. In particular, the addition of a flexible skin to existing SCB design methods requires a new approach and an understanding of dynamic panel response. This element is not necessary in existing static SCB work but is likely to become a significant factor in the design of adaptive SCB and the inevitable fluid-structure interaction (FSI) that forms.

In this chapter, the various methods used to design adaptive SCB are discussed. First, a theoretical approach similar to the panel flutter studies is discussed for a flat plate configuration to evaluate the foundations of the design space and determine initial size of the device. This is extended to a coupled quasi-steady aero-structural solver using a finite element method and a finite volume CFD method for the structural and aerodynamic components respectively. The aero-structural solver is designed to analyse the effect of a control device on an aerofoil to compare against existing studies. The unsteady behaviour surrounding the control device is to be analysed in a blowdown supersonic wind tunnel. High-speed Schlieren imaging and planar PIV (particle image velocimetry) techniques were used and are introduced towards at the end of this chapter.

3.1. Theoretical and Computational Approach

Figure 3.1 shows an inviscid 1D shock passing over a flexible plate and the associated pressure downstream. Coupling of the aerodynamic load and structural response is captured by a force balance approach to the initial concept in figure 3.1. There are three key areas with three distinct pressures that drive the response:

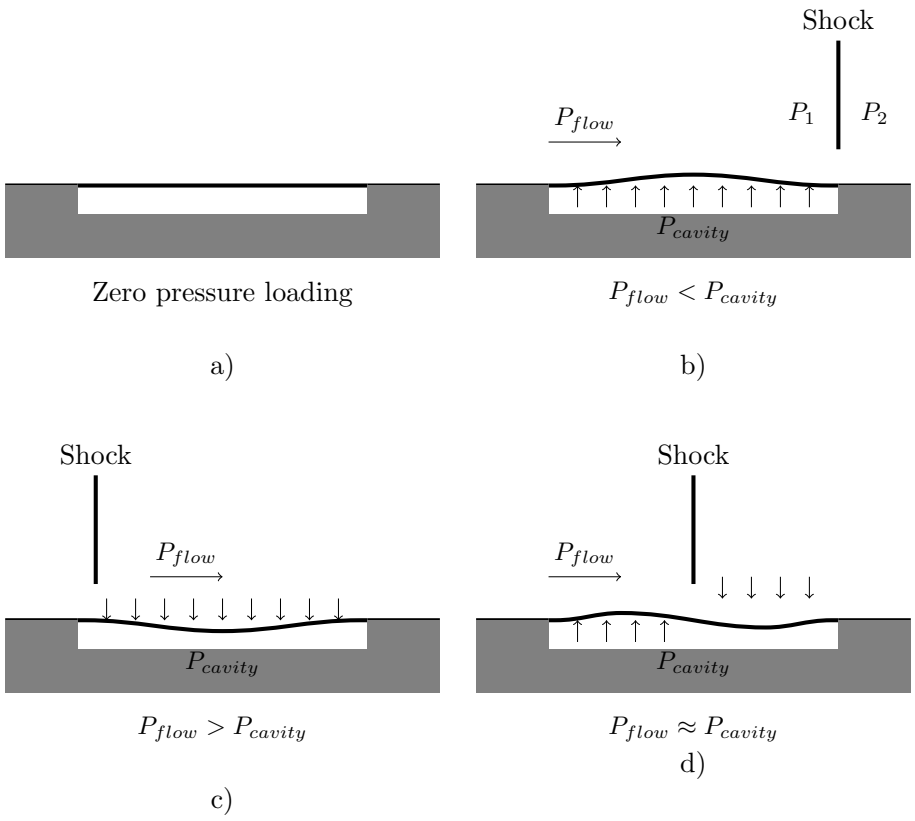


Figure 3.1.: Effect of pressure loading due to controlled shock position upon plate geometry. The cavity pressures are varied with respect to the upper surface pressure. a) Zero aerodynamic loading. b) Shock loading downstream of the plate. c) Shock loading upstream of the plate. d) Shock loading above the plate.

1. Upstream pressure, P_1
2. Downstream pressure, P_2
3. Cavity pressure, P_{cavity}

This analysis is similar to the approach adopted in early panel flutter studies by Dowell [1966] who utilised piston theory; where a 1D shock and associated pressure gradient were assumed to be invariant with time and independent of plate deformation. Of particular interest is the the volume of air beneath the plate and the subsequent pressure of this cavity, which was shown to be influential in determining the final geometry of the plate. The effect of the cavity pressure upon plate geometry is shown in

figures 3.1b-d with significantly different deformations possible. In a real flow, such geometry changes would significantly affect the flow field structure once the aerodynamic model is expanded.

Extending the above model to consider two-dimensional effects leads to a more complex flow field and shock structure. Deformation of the plate plays an important role in determining shock structure. Whether the plate is subject to a convex deformation such as those in figure 3.1b & d or concave as in figure 3.1c, the shock structures will look quite different.

Figure 3.2 shows the effect of the surface geometry on the flow when two-dimensions are considered. The main aerodynamic difference is the formation of expansion or compression waves that occur due to the change in the geometry and the resultant positive or negative deflections. These changes in geometry will directly affect the plate curvature and ultimately the pressure loading across the plate. In each of the cases shown in figure 3.2 the cavity pressure is set to a value between the upstream and downstream pressures.

In the case of figure 3.2a the shockwave is located on the upstream portion of the plate and the pressure above the plate is greater than the cavity pressure. The pressure differential causes a negative deflection which triggers expansion waves that emanate from the start of the plate where the curvature accelerates the supersonic flow prior to the shock resulting in a marginally stronger shock near to the wall.

When the shock is positioned over the centre of the plate as in figure 3.2b the pressure distribution over the flexible surface is close to that of the cavity, the field can be split into two main regions. The first is the low pressure supersonic region between the front and rear legs of the main bifurcated shock. The second is downstream of the rear leg where the flow is subsonic and the pressure over the upper surface is higher. Figure 3.2c shows how the position of the shock downstream of the plate places the low pressure supersonic region over the plate causing a positive deformation which results in a large positive deflection angle for the flow to overcome.

In this global inviscid analysis, the behaviour of the plate and the shockwave are coupled in a classic FSI. Figure 3.3 emphasises the cyclical nature of the process. Starting with a pressure field, a change in upper surface pressure brought on by the flow deforms the plate to a new plate geometry which in turn creates a new shock structure and hence a new upper surface pressure, thus completing the cycle. The challenge facing the designers of adaptive SCB is to evaluate this interdependence and identify effective solutions that would be less sensitive to FSI effects. In the following section a conceptual design process is described to explore whether adaptive SCB are feasible with current

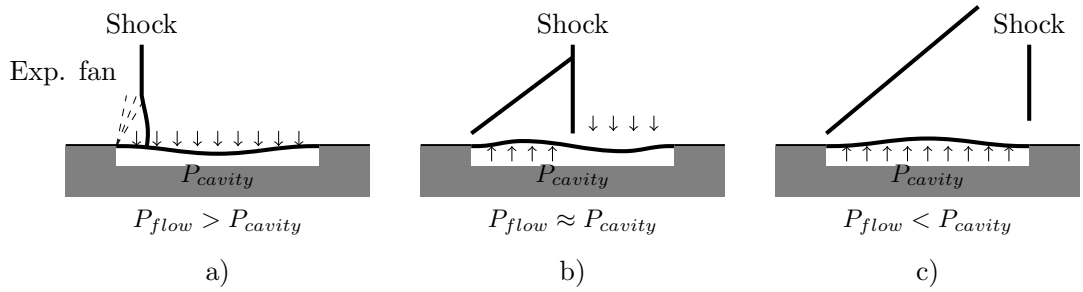


Figure 3.2.: Effect of 2D aerodynamic pressure loading due to controlled shock position upon plate geometry. a) Shock placed towards upstream edge of plate. b) Shock over central region of the plate. c) Shock downstream of the plate.

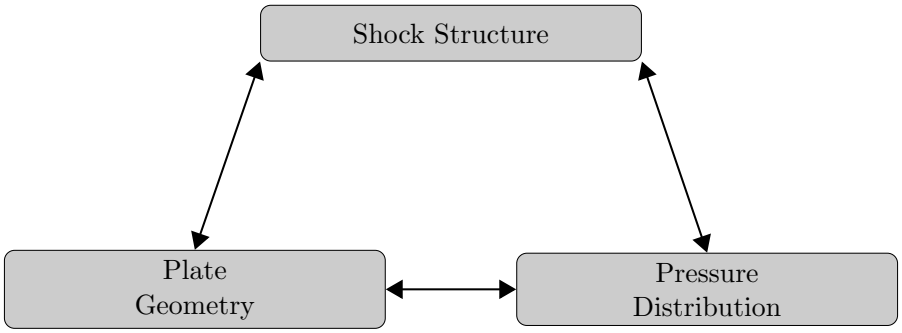


Figure 3.3.: The cyclic effect of shock structure, pressure gradient and plate geometry.

technologies.

3.1.1. Initial Sizing and design of Adaptive SCB

The structural design of the initial Ashill et al. concept proposes a flexible plate that is subject to an actuation force that acts perpendicular to the plate surface in order to achieve a suitable out-of-plane deformation. The bending of plates is a classical field with many analytical and numerical techniques at the designer's disposal. In order to implement a suitable design process for SCB the requirements must first be outlined. The initial requirements for adaptive SCB are to:

1. Improve upon the off-design performance of static SCB.
2. Maintain or improve on-design performance.
3. Be capable of achieving bump heights comparable to existing SCB.

4. Return to the original undeformed geometry after aerodynamic loading and actuation is removed.

5. Facilitate integration into existing airframes.

In order to begin the design process an initial sizing must first take place that takes in to account the aerodynamic and structural forces present and the dimensions of the control device. Existing static SCB optimisations can be utilised to provide initial starting points for plate lengths and deformation heights to narrow the design space.

Broadly speaking there were two approaches highlighted in Chapter 2 which are those studies that evaluate the performance of an aerofoil or wing with SCB and studies that consider SCB geometries mounted on the floor of a wind tunnel. Sizing for aerofoils is almost exclusively done as a percentage of chord length with SCB heights varying from $0.1\%c < h_b < 1.7\%c$ and SCB lengths $0.1c < l_b < 0.5c$. Experimentally, much SCB testing has taken place in blowdown wind tunnels that facilitate high resolution analysis in the area close to the wall and as such experimental aerofoil models have become less common. Examples include the studies by Ogawa et al. [2008], Bruce [2008], Colliss and Babinsky [2012] where the SCB were sized with respect to the boundary layer with heights ranging from $0.6\delta_0 < l_b < \delta_0$. Comparisons between tests on aerofoils and wind tunnel floors are difficult as boundary layer heights are often omitted from the aerofoil studies and so a typical reference chord length is used in order to compare SCB heights in equivalent S.I. units.

Data has been extracted from existing SCB literature to provide an insight in to the dimensions of existing SCB. Results from optimisations, parametric and experimental studies were included to cover the entire design space. Figure 3.4 shows the number of SCB that have been found to provide the best performance from each study.[1] The aerofoil based studies shown in figures 3.4a and 3.4b are more common. From the data collected in figure 3.4 there are common values for SCB height and lengths and are presented to provide a benchmark for adaptive SCB. The lengths of SCB tend to be discrete values that are dictated by the shock position on aerofoil studies or tunnel constraints in experimental investigations. The number of wind tunnel studies is significantly lower due to the constraints imposed by the expense of such facilities. Those studies that have been undertaken often aim to replicate a good performing SCB

[1]The following references feature in the figure 3.4. Dargel and Thiede [2002], Rosemann and Birkemeyer [2002], Le Balleur et al. [2002], Bein et al. [2000], Birkemeyer et al. [2000], Bruce and Babinsky [2012], Colliss and Babinsky [2012], Eastwood and Jarrett [2012], Nübler et al. [2012], Kutzbach et al. [2004], Lee et al. [2011a,b], Millholen II, W. and Owens, L. [2005], Ogawa et al. [2008], Pätzold [2006], Qin et al. [2008], Rosemann et al. [2000], Sommerer et al. [2000b], Wong et al. [2008], Yagiz et al. [2012]

proposed in the work by Ogawa [2006] which limits the number of new designs. An adaptive SCB would offer a method to investigate the effects of SCB height to identify SCB heights that perform well. The index of dispersion, c_v (ratio of the variance to the mean values) is a useful way to calculate the dispersion of a data set. The data in figure 3.4 suggests that SCB lengths vary less than heights with $c_{v,lengths} = 0.43$ compared to $c_{v,heights} = 0.77$. However it is often the case that studies fix the location of the SCB in order to speed up the optimisation process. SCB height is known to have a large influence on the performance and is always included in some form in the optimisations in footnote[1]. The significant influence of this variable in the shock wave boundary layer interaction region means that the optimisations invariably focus upon SCB height. In the case of experimental studies, SCB height is often a chosen relative to boundary layer thickness which varies between wind tunnels. The general trends of the optimisation studies such as Pätzold [2006], Ogawa et al. [2008], Yagiz et al. [2012], Dargel and Thiede [2002], Millholen II, W. and Owens, L. [2005] seem to favour short SCB. However the more recent studies of Qin et al. [2008], Colliss and Babinsky [2012], Nübler et al. [2012] have seen a preference for longer SCB especially when the entire rear section of the aerofoil is included in the analysis.

In all of the existing work behind static SCB there is a split in the approach between SCB on aerofoils and SCB on a surface beneath a shock wave. These are almost exclusively split between numerical and experimental studies. Even in the joint experimental-numerical investigation in Colliss and Babinsky [2012] a numerical study of a SCB fitted to an aerofoil was presented alongside a SCB fitted to the floor of a wind tunnel. The reasoning behing the experimental models attached to a wind tunnel working sections rather than an aerofoil is the size of the field of view achievable. Figure 3.6 shows what an aerofoil fitted with a SCB would look like. In order to match the physical size of an entire aerofoil, the wind tunnel would have to be large and thus the energy consumption much higher. By focussing on the shock region it allows for larger SCB in wind tunnels that are capable of high resolution experimental methods such as PIV and LDA [Colliss and Babinsky, 2012]. As such the same approach is undertaken here with the further distinction of quasi-steady numerical analysis and unsteady experimental analysis.

With regards to the initial sizing, the modal values were targeted by the initial design. A bump length, $l_b = 0.2\,\text{m}$ was selected which equates to 0.2c on a 1m chord aerofoil. A bump height of 5 mm is the objective with $\delta_{max} = 6\,\text{mm}$ chosen as an ultimate goal to incorporate 80% of existing SCB. For practical (experimental) reasons of matching the geometry of the wind tunnel and also maintaining a suitable aspect ratio of the flexible plate Dowell [1972] which will be deformed to provide the SCB geometry the

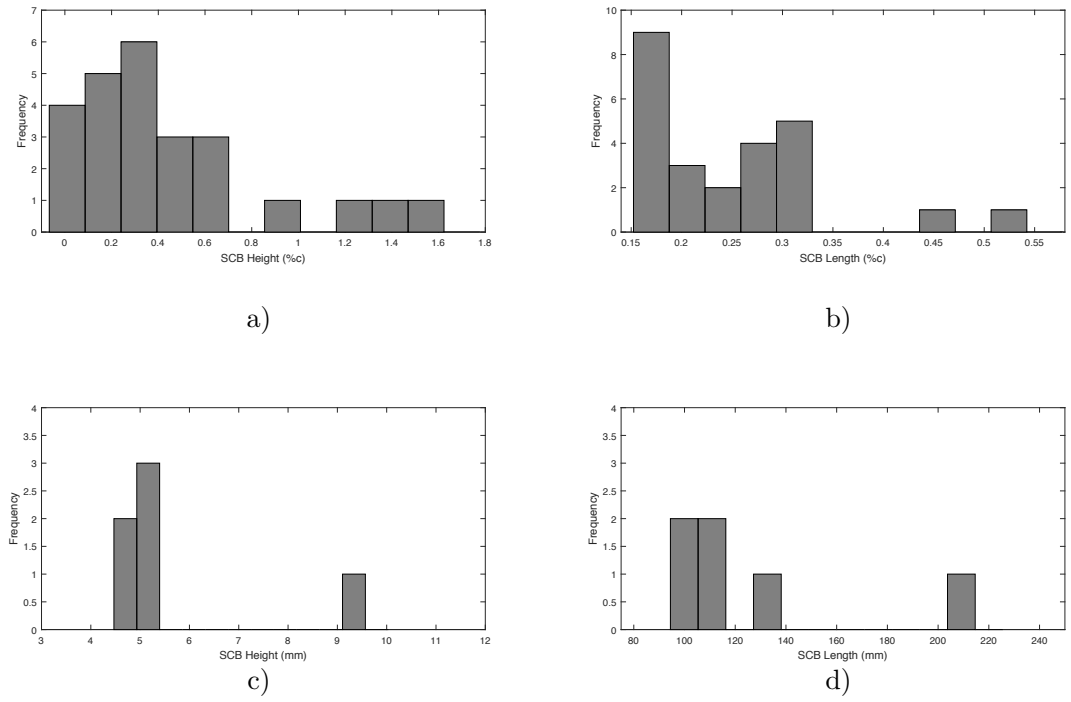


Figure 3.4.: Histograms showing the typical SCB heights and lengths investigated in recent literature.[1] a) SCB Heights for SCB studies upon aerofoils. b) SCB lengths for SCB studies upon aerofoils. c) SCB heights for wind tunnel studies. d) SCB lengths for wind tunnel studies.

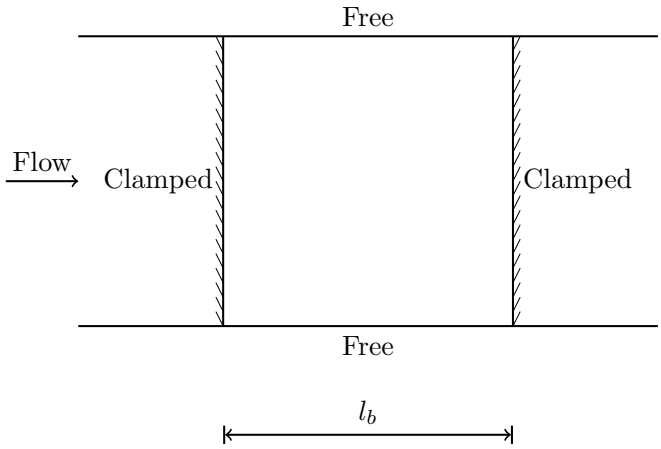


Figure 3.5.: Boundary conditions of flexible plate.

width of the flexible section was chosen to be 0.15 m. For the experimental model, lengths of 150 mm and 200 mm were selected to facilitate comparison with the large body of existing work on static SCB. As well as maintaining an aspect ratio determined by evaluating the panel flutter studies of Dowell [1972] by selecting one that provides a high flutter boundary. This is discussed further in section 3.1.4. An aspect ratio of 1.33 represents a balance between the desired 2D nature of the adaptive SCB whilst maintaining a sufficiently stable enough solution to avoid panel flutter. The following sections will look at the flexibility/stiffness requirements and use these selected SCB sizes to determine the required stiffness.

Flexibility/Stiffness requirements

For a plate to deform out-of-plane an appropriate level of flexibility is required. The challenge of adaptive SCB is to achieve suitable levels of deformation that can affect the flow whilst remaining within the elastic region of plate displacement given suitable boundary conditions. Figure 3.5 shows the boundary conditions selected in order to achieve such deformations and enforce C_1 continuity which defines that there is no slope at the clamped ends. These boundary conditions were chosen as a result of the work of Rhodes [2012] who demonstrated them to be appropriate to mimic the geometries of static SCB.

Imposing the clamped boundary conditions resulted in a notable constraint at either end of the SCB. It is at these boundaries where stress concentrations are likely to occur which may have consequences for the deployable SCB concept with its goal to remain

within the elastic regime. Due to the magnitude of deformations required and the clamped edges, the stresses at these constraints are high and as such a material with a high yield stress was required. Al-7075-T6 was selected for its superior yield stress and existing widespread use in the aerospace industry. This will make the integration into aircraft wing design much easier. The material has been tested by Rhodes and Santer [2012] and showed promise with optimally-designed SCB capable of deploying and retracting without any plastic deformation whilst achieving suitable SCB heights.

3.1.2. Structural Modelling

Structural modelling is necessary in the analysis and optimisation of adaptive SCB due to the flexibility for deployment and retraction requirements. The original concept illustrated in figure 3.6 by Ashill et al. [1992] featured a section of skin thin enough to deform under reasonable actuation loads. Whilst no further details were included in the work, it is an aim of this investigation to determine suitable actuation methods and to establish design protocols for adaptive SCB.

The majority of research into static SCB has concluded that bump height is an influential variable [Sommerer et al., 2000b, Lee et al., 2011b, Qin et al., 2008] and so any design must be able to achieve the values identified in the previous section.

In the validation part of this demonstration case, a high-grade Aluminium sheet was selected for the design. With the boundary constraints of the model set by the design of the adaptive SCB, the choice of material determines if the design is capable of meeting the specification points for adaptive SCB.

A reference case is set up in order to select a suitable material thickness that can achieve the design requirements within the elastic regime. A finite element analysis (FEA) is outlined here to enable many different loading scenarios to be tested quickly with specific focus on flexibility requirements. The results are presented in section 3.1.3.

Finite Element Solver

A finite element approach was selected to accurately model the plate deformation. The approach offers suitable levels of control over the necessary boundary conditions, in particular the modelling of the interaction between the actuators and the plate. *Abaqus* ABAQUS [2007] is used to construct a geometrically nonlinear, quasi-static analysis performed using a Newmark Algorithm with adaptive time stepping.

The actuation points are modelled as line displacements which remain constant along the span. This follows the original concept and will feature in the experimental model to

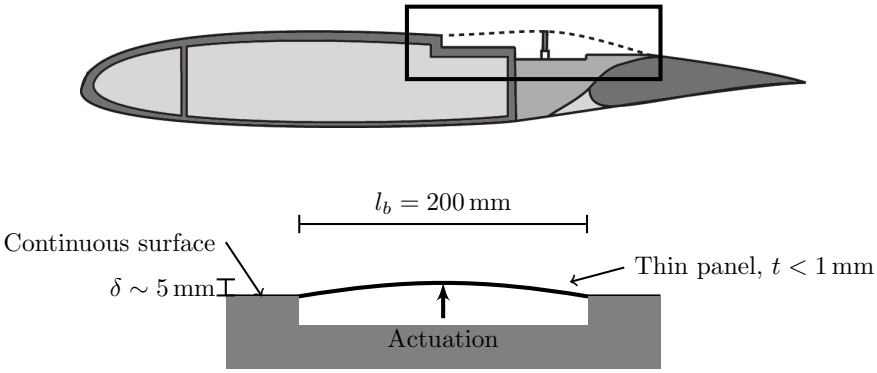


Figure 3.6.: Illustration of expected actuator loading and initial sizings.

maintain the two-dimensionality of the actuation which is to be discussed in section 3.2. The actuation strips are controlled via displacement rather than actuation force. This is to allow ease comparison with the typical aerodynamic approach of existing static SCB designs which stipulate SCB height.

The finite element analysis was solved for a three-dimensional SCB. This was to provide an indication of the stresses within the corners of the plate which would not be calculated in a two-dimensional beam model. The effects of three-dimensionality occur on the free edges of the plate which will deform more than the centreline location at the same freestream position. it was these two effects and the computational cost of running a three-dimensional simulation was small compared to the cost of the CFD analysis.

Meshing

The flexible skin section is modelled as a simple rectangular plate. Using the modal values from figure 3.4 with the aspect ratio of 1.33 based upon recommendations of Dowell [1972] provides a flexible region of 200 mm×150 mm. In order to model the plate using the FEA method, the dimensions of the plate must be considered. As the length and width of the plate are much larger than the thickness, a shell method is used with elements capable of undergoing large strains. The meshing process was conducted in Abaqus standard [ABAQUS, 2007] with the position of each node defined to control the size of the elements. Standard large strain elements (S4R, Shell element, 4 nodes, reduced integration) were used to avoid shear and membrane locking. Quad elements were enforced to guarantee mesh quality. The rectangular nature of the test piece ensured a very high quality mesh was produced with zero non-orthogonality.

The solver was validated against a beam-in-bending solution for a 2 mm out-of-plane

No. Elements	σ_{vM} (MPa)
825	93.61
3000	130.17
4800	142.30
7500	147.60
13400	150.24
30000	152.82
53200	153.50

Table 3.1.: FEA mesh attributes.

displacements that remained constant along the span. The maximum von Mises Stress for a number of total elements is presented in table 3.1 and figure 3.7 shows mesh independence.

3.1.3. Designing Plates for Static Shockwaves

Compliant plates used in adaptive SCB require a balance between flexibility to deform and stiffness to resist the aerodynamic load. An influential factor in the flexibility of plates is the thickness [Dowell, 1966] therefore it is useful to conduct a study to evaluate the effects. This initial test involves a constant pressure differential across the plate The magnitude of the pressure differential was determined by assuming a uniform upper surface pressure, the procedure is based upon the free stream Mach number and then calculated using two-dimensional inviscid shock theory for a shock structure similar to that in figure 3.2b.

The pressure gradients due to the shockwave will affect the geometry of the plate as seen in previous studies by Visbal [2014] who showed the displacement of a plate subject to a Mach 2 oblique shock. The impingement angle was such that the pressure rise across the shock system was similar to the interaction of a normal shock and a SCB. Similar pressure loading is applied via 2D aerodynamic theory to the shock structure in figure 3.8. The plate is subjected to a uniform M=1.4 inflow inline with many existing aerodynamic SCB studies [Ogawa et al., 2008, Colliss and Babinsky, 2012]. Using the isentropic relationship

$$\frac{p_{0,1}}{p_1} = \left(1 + \frac{(\gamma - 1)}{2} {M_1}^2\right)^{\frac{\gamma}{(\gamma-1)}} \tag{3.1}$$

and a stagnation pressure of 1.3 bar, the static pressure is calculated to be ~ 0.5 bar. Assuming an approximate 5° deflection angle based upon the *default rounded bump*

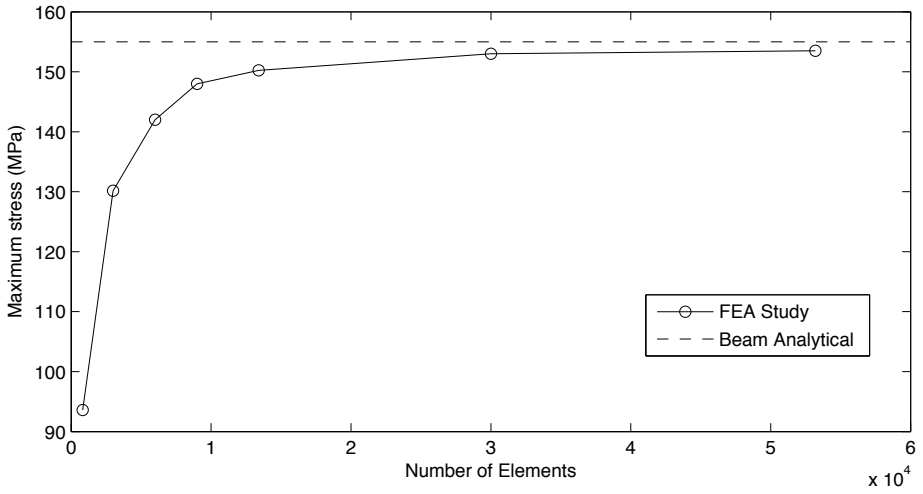


Figure 3.7.: FEA mesh convergence study of a span-wise 2 mm out-of-plane actuation at the central location.

[Ogawa et al., 2008], the pressure in region 2 in figure 3.8 is calculated by

$$\frac{p_2}{p_1} = \frac{2\gamma {M_1}^2 \sin^2\beta - (\gamma - 1)}{(\gamma + 1)} \tag{3.2}$$

and $p_2 \approx 0.5\,\text{bar}$ and $M_2 \sim 1.2$. This results in a weaker normal shock at the rear leg with pressure downstream of this rear leg by

$$\frac{p_3}{p_2} = \frac{2\gamma}{(\gamma + 1)} {M_2}^2 - \frac{(\gamma - 1)}{(\gamma + 1)} \tag{3.3}$$

with the subscripts relating to the regions in figure 3.8 and $p_3 = 0.75\,\text{bar}$. These calculations have their limitations as the viscosity will have a significant effect but for initial sizing they provide good initial estimates of the aerodynamic loads.

Figure 3.8 shows that the front leg and thus the downstream static pressure is determined by the initial deflection angle of the plate. In practice, the slope of the plate section will be driven by the pressure gradient across the shock and hence the pressure differential across the plate which ultimately controls the aerodynamics. The starting point for the thickness study will evaluate these loads assuming a shock position downstream of the plate. In this initial test, the FSI must be evaluated. The values presented in table 3.2 will form the upper surface pressures. The cavity pressure held constant at $p_c = 0.65\,\text{bar}$ $(0.5\,P_0)$.

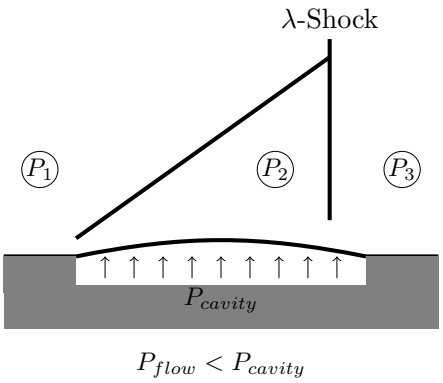


Figure 3.8.: Expected pressure values for initial design stage based upon isentropic, oblique and normal shock theories with relations shown in equations 3.1, 3.2 and 3.3.

P_{01}	M_1	θ_1	P_1	M_2	P_2	M_3	P_3
1.3 bar	1.4	5^o	0.5 bar	1.2	0.65 bar	0.75	1 bar

Table 3.2.: Calculated pressure values for loading presented in figure 3.8

Thickness (mm)	Displacement (mm)	Max σ_{vM} (MPa)
0.4	3.73	380
0.5	3.44	331
0.6	3.21	292
0.7	3.03	260
0.8	2.87	234
0.9	2.72	213
1.0	2.59	194

Table 3.3.: The effects of varying plate thickness upon a flexible plate sized to typical SCB dimensions. $P_2 = 0.5\,P_0$, $P_{cavity} = 0.75bar$.

By selecting this cavity pressure, the pressure differential across the plate was found to be limited to sensible magnitudes which would avoid high displacements and irreversible plastic deformation. This cavity pressure sits between the lower pressure supersonic flow on the front surface of the plate and the higher pressure on the rear surface. The shock structure produced is similar to that in figure 3.2. The largest pressure differential is present when the shock is located beyond the downstream edge of the plate as in figure 3.2c.

Table 3.3 shows the displacements and stresses obtained from analyses with constant aerodynamic loading. For the given pressure differential across the plate, thicker plates deformed less than thinner plates. The purpose of this test was to confirm the choice of AL-7075-T6 and the performance under the applied aerodynamic pressure load. It also confirmed that reasonably large deflection heights are achievable without the need for actuators utilising the plate thickness and resultant stiffness to control the deformation.

The range of heights achieved by the thinnest plates, ($t \leqslant 0.6\,\text{mm}$) are within the most common range of SCB heights in figure 3.4b therefore plate thickness of 0.4 and 0.6 mm are to be evaluated further in order to provide a comparison. The stresses presented in table 3.3 are all below the yield stress of Al-7075-T6 which supports this choice of material. The stress levels show a compromise between achieving suitable bump heights and minimising stress levels within the plate. The process of sizing the plate length and width is essential for the ability to deploy to suitable SCB heights, (design specification point 3) and retract back to the original geometry, (point 4). With lengths $l_b = 150\,\text{mm}$ and 200 mm and t = 0.4 mm and 0.6 mm predicted to be able to match static SCB geometries and withstand the aerodynamic loading.

By designing the plate to deform in response to pressure loading alone there are many potential weight savings as an actuation system is not needed which makes integration into the airframe an easier process. With a flexible plate based design possible, further development is required and in the following section the dynamics of the shock loading are discussed with particular attention to the passive flexible plate structure now suggested.

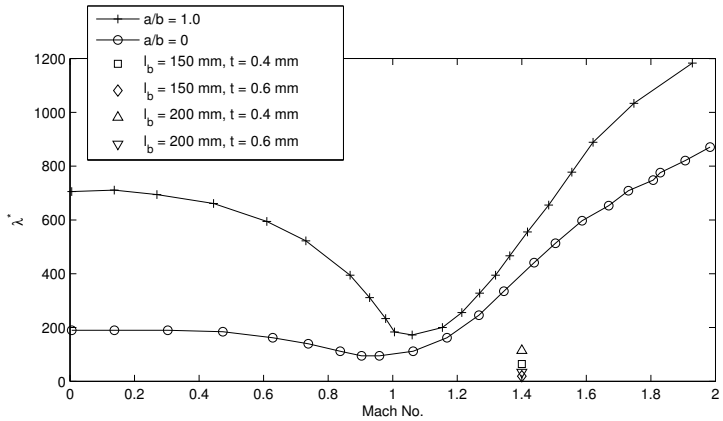


Figure 3.9.: Flutter dynamic pressure as described by Dowell [1970] with the variation of Mach number. Included are the plate dimensions from table 3.4.

3.1.4. Panel Flutter Considerations

Dowell [1970] indicated that the fluctuations in a turbulent boundary layer above a thin plate can begin to introduce small oscillations of the plate. It was observed that the amplitude of these vibrations was of the order of the thickness of the plate and recommended that panel flutter problems could be 'designed around' by using thicker plates or reducing panel length. These approaches involved increasing the weight of the panel itself or the supporting structure required to shorten the plate. If panel flutter did develop during further flight tests, it had to be shown that the flutter was not destructive and remained below the flutter boundary. Figure 3.9 shows the variation of the flutter dynamic pressure boundary with respect to Mach number for two different aspect ratios. The plates considered in the current study in table 3.4 are presented on the graph and indicate that the plates are well below the flutter boundary.

The flutter boundary was defined by Dowell as the dynamic pressure where oscillations were larger than the plate thickness. Below this boundary the oscillations were typically less than the plate thickness and not considered to be destructive. As the dynamic pressure increases beyond the flutter boundary the oscillation is observed to become nearly sinusoidal and with an amplitude that increases as the dynamic pressure increases with the static pressure maintained.

In order to investigate panel response due to aerodynamic loading the flutter boundary

l_b (mm)	t (mm)	a/b	δ_1 (mm)	δ_2 (mm)	D (N/m)	λ^*
150	0.4	1	-	-	0.3422	64.5
150	0.6	1	-	-	1.1549	19.1
200	0.4	1.33	-	-	0.3422	114.6
200	0.6	1.33	-	-	1.1549	34.0
150	0.4	1	2	3	0.3422	16.1 (max)
150	0.6	1	2	3	1.1549	4.8 (max)

Table 3.4.: Dimensions of plate test cases. Constant span of 150 mm

must first be calculated. Dowell [1970] defined the critical dynamic pressure, λ^*

$$\lambda^* = \frac{2qa^2}{D} \tag{3.4}$$

where D is defined as

$$D = \frac{2h^3E}{3(1-\nu^2)} \tag{3.5}$$

where q is the dynamic pressure, a is panel length, D is the flexural stiffness of the plate, h is twice the plate thickness, E is the Young's Modulus and ν is the Poisson ratio.

The relationship was developed for simple isotropic panels and crucially incorporates plate thickness, modulus of elasticity, and length into a single parameter. The magnitude of the flutter boundary for a fixed Mach number and aspect ratio determines the severity of the oscillations.

The flutter onset dynamic pressure is calculated for each setup presented in table 3.4. The dynamic pressure component, q, was evaluated from the total pressure ratios in initial wind tunnel results from the setup described in section 3.2.1 and taken as the difference between total and static pressure. The pressure ratio placed a shock in the region of the flexible plate. Placing the shock in this region required a tunnel pressure ratio of $P_{01}/P_{atm} \sim 1.3$ which is consistently achievable. The critical flutter dynamic pressure values calculated for each plate placed the test cases well beneath the destructive flutter boundary, figure 3.9. It should be noted that this model assumes that the cavity pressure is equal to the static pressure of the flow over the top surface which as Dowell acknowledged may not always be the case.

A high cavity pressure beneath the plate causes it to stiffen [Vedeneev et al., 2010].

The initial studies by Dowell [1970] acknowledged the effect of the cavity pressure in the theoretical models and introduced acoustic cavity models which were found to be very reliable in predicting the effect of natural frequencies for panel flutter. By adding this extra parameter to the panel flutter analysis it was found that the system becomes very sensitive to pressure difference across the plate rather than the pressure gradients in the flow.

The physical models of the test cases in table 3.4 are to be manufactured and tested in the Imperial College Supersonic Wind Tunnel which is described later in this chapter. The combined numerical and experimental approach is a key feature of this work which aims to utilise the benefits of both approaches to design adaptive SCB. Maintaining the pressure difference under aerodynamic loading is a significant challenge experimentally due to leakage as a result of plate deformation. Figure 3.8 shows the relative magnitudes of pressure acting on each region for the setup in the wind tunnel, section 3.2.1.

As aluded to in the earlier design process, there are interdependencies between the fluid and the structure with the plate deformation caused by the pressure differential across the plate. The deflection interacts directly with the flow and create large scale shock structures. These vary according to the pressure distribution over the upper surface of the plate and can lead to further deformation. The initial plate thickness study showed that plates of typical SCB dimensions ($150 < l_b < 200\,\text{mm}$) are capable of withstanding the typical mean pressures present in and around the shock region. It is however the goal of adaptive SCB to be integrated into transonic wing design which are designed to operate in unsteady flows. This means the location of the shock with respect to the plate may vary over the position of the plate as the global pressure field changes. The next section will begin to look at the response of a travelling shock wave on these initially flat flexible plates.

3.1.5. Designing Plates for Dynamic Shockwaves

The static response of the 'worst-case-scenario' has been discussed with the panel subject to supersonic flow across the entirety of the upper surface causing the largest pressure differential across the plate. However, the movement of the shock over the plate and the subsequent unsteady loading has not yet been taken into account. The combination of pressure difference across the plate and pressure gradient across the shock could lead to structural failure. It is the goal of this subsection to exploit the coupling between aerodynamic loading and structural response illustrated in figure 3.3 to design a shock control device based upon a flexible plate.

In order to determine the plate behaviour when subject to the shock motion, the preliminary study was extended to focus upon the pressure gradients across the shock as well as across the plate. Initially this involved an inviscid 2D shockwave at various locations over the flexible plate model which used equation 3.2 to estimate a pressure distribution. This is later extended to a coupled aero-structural solver that studies the effect of a flexible plate upon an aerofoil.

Possible loading and plate geometries have been shown illustrated in figure 3.1 for a constant cavity pressure. The pressure in the cavity was selected to lie between the pre and post-shock values providing a starting point for passive SCB. This leads to a combination of positive and negative deflections of the plate.

The centreline plate geometries shown in figure 3.10 represent those subject to a shock pass over the plate with a constant cavity pressure beneath the plate. The geometries indicate that for $P_{cavity} = 0.55\,\text{bar}$ there is a significant region of negative plate displacement downstream of the shock that is present for all shock positions tested. The curvature resulting from this deflection will affect the shock structure through the development of expansion and pressure waves as the plate deforms.

For the case where the low pressure upstream of the shock is lower than the cavity pressure, there was an upwards deflection of the plate. In contrast, downstream of the shock where the pressure is greater than the cavity pressure provided a net downward force on the plate. The continuous nature of the plate blended these two regions of different pressure loading to enforce continuous plate curvature. For shock positions just upstream of the plate the surface was negatively displaced, the convex curvature seen by the flow at the leading edge of the plate generated expansion waves and accelerated the flow causing a stronger shockwave. This resulted in increases pressure downstream of the shock. The resulting acceleration also acted to reduce the pressure ahead of the shock, which will induce a suction upstream of the shock counter-acting the convex curvature due to the high pressure downstream region.

For a given flow across the upper surface, the magnitude of suction effect caused by the flow upstream of the shock is controlled by the cavity pressure beneath the plate. The plot in figure 3.10 shows that this level of suction is capable of producing the positive displacements typical of static SCB such as those shown in figure 3.10e. The resultant centreline geometry therefore shows promise for a pressure based passive control design.

The effects of dynamic loading and plate characteristics upon flexibility

The response of the plate to the pressure gradients across it is dependent upon the plate characteristics. These have a significant effect upon plate performance throughout the operational envelope. The effects of thickness and cavity pressure are investigated using the same 2D shock model. Figures 3.11 and 3.12 show the resultant geometries and stresses as a shockwave passes over the two plates with thicknesses of 0.4 mm and 0.6 mm. The differences in plate deflection between thicknesses are relatively small with a mean difference of 0.01 mm for the highest load case, $P_{cavity} = 0.8$ bar where $x_{shock} = 0.75 l_b$, figure 3.11i. For reference the upstream and downstream pressures are $\sim P_2 = 0.65\, bar$ and $P_3 = 1$ bar as illustrated in figure 3.8.

The aim of the structural model is to quickly produce plate geometries for a desired loading and as such the plastic deformation is not included in the analysis. Plates are deemed to have plastically deformed when the maximum von Mises stress has exceeded the yield stress of AL-7075-T6, $\sigma_y = 525$ MPa. Figure 3.12 shows that $\sigma_{max} > \sigma_y$ for many instances of shock position and cavity pressure.

The only cavity pressure that would permit elastic deformation of the plate throughout a complete shock pass would be where $P_{cavity} = 0.6$ bar, with $P_{cavity} = 0.7$ bar the deformation only remains elastic for $x_{shock} < 0.55\, l_b$ beyond which the stress at the upstream edge becomes greater than the yield stress. With $P_{cavity} = 0.8\, bar$, the yield stress is reached with a shock position of $0.32 l_b$ with plastic deformation expected to occur as the shock moves further downstream.

The effect of thickness upon flexibility can be seen in figures 3.11g, 3.11h and 3.11i which correspond to high cavity pressures and therefore a high pressure differential. Varying thickness has the greatest effect when the shock is furthest downstream. The flexibility of the thinner (t=0.4 mm) plate allows for greater deformations due to the reduced stiffness whereas the thicker (t=0.6 mm) plate has increased resistance to the bending imposed by the pressure loading. Figure 3.12 show that a major drawback of using thinner plates is that the stress levels are much higher. However figure 3.11 highlights the obvious benefit of thinner plates is that higher potential deformation heights are achievable for a given pressure loading.

As the suitability of flexible plates for use as SCB is analysed, a trade-off between maximum permissible deflection and stress concentrations at the clamped edges emerges and the final design must find a balance between these opposing characteristics.

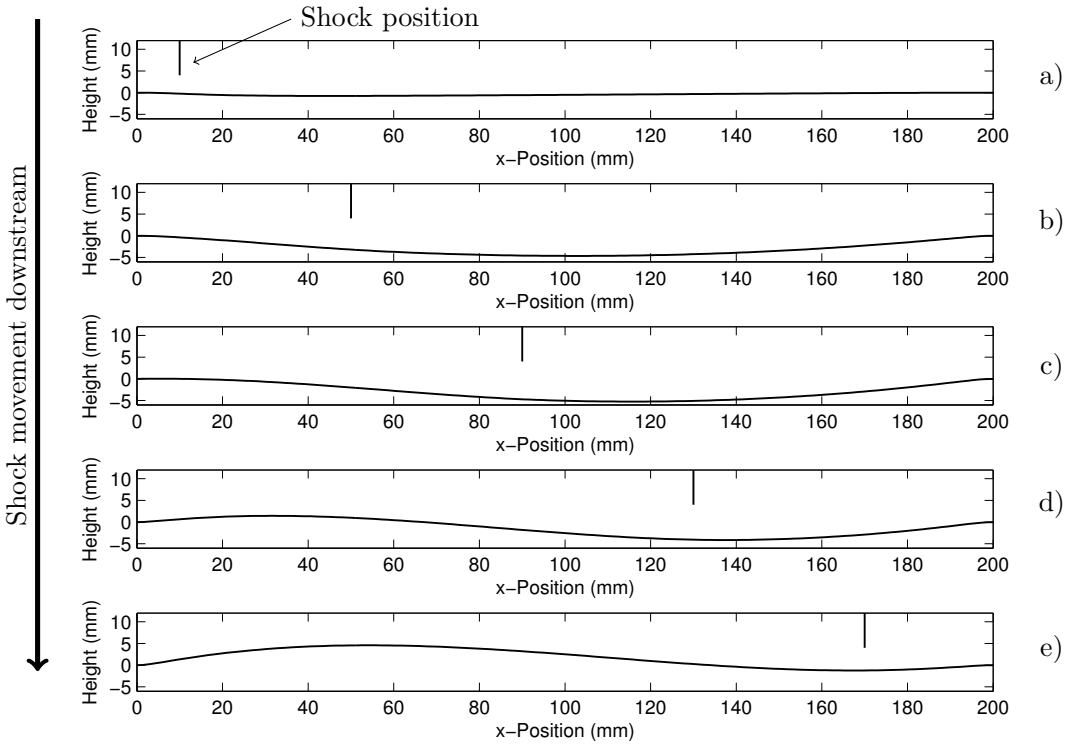


Figure 3.10.: Plate centreline geometries for varying inviscid shock position with constant cavity pressure of 0.55 Bar. Al-7075-T6, $l_b = 200\,\text{mm}$, width, $b = 150\,\text{mm}$, $t = 0.4\,\text{mm}$.

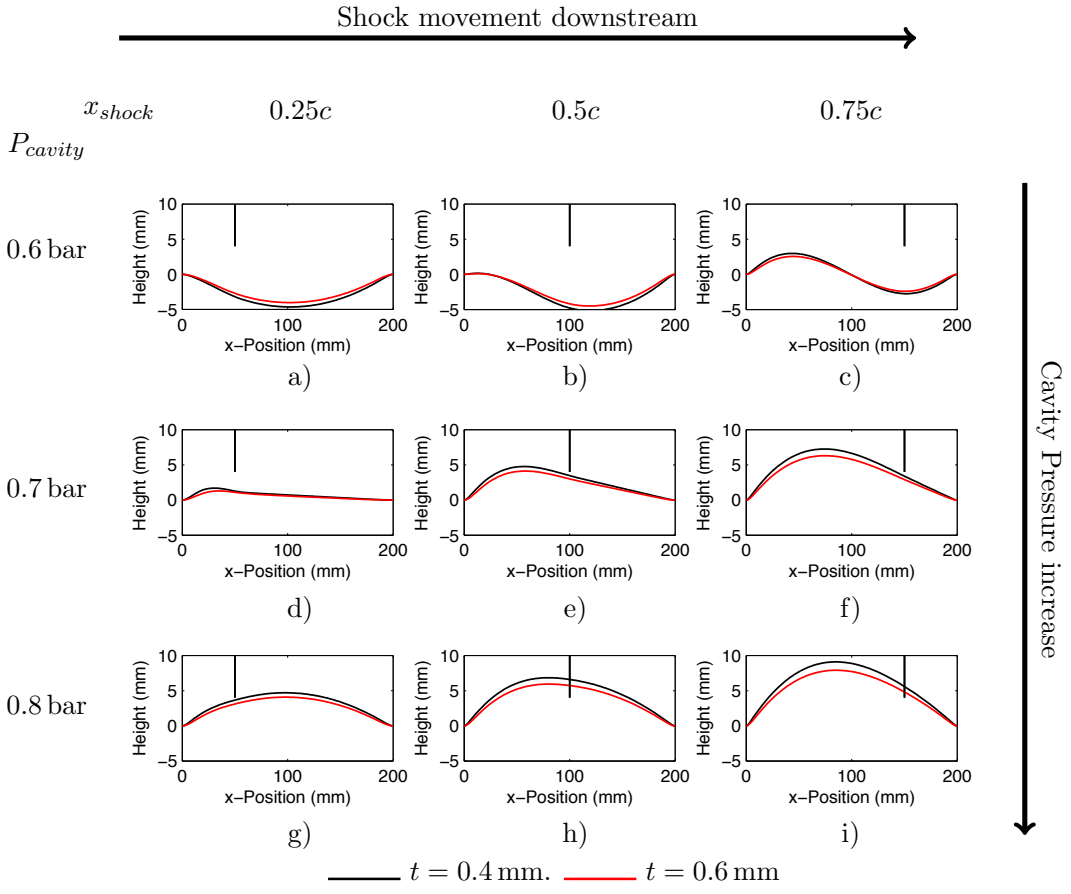


Figure 3.11.: Plate centreline geometries for varying inviscid shock position and plate thickness with variable cavity pressure. Al-7075-T6, $l_b = 200$ mm, width, $b = 150$ mm.

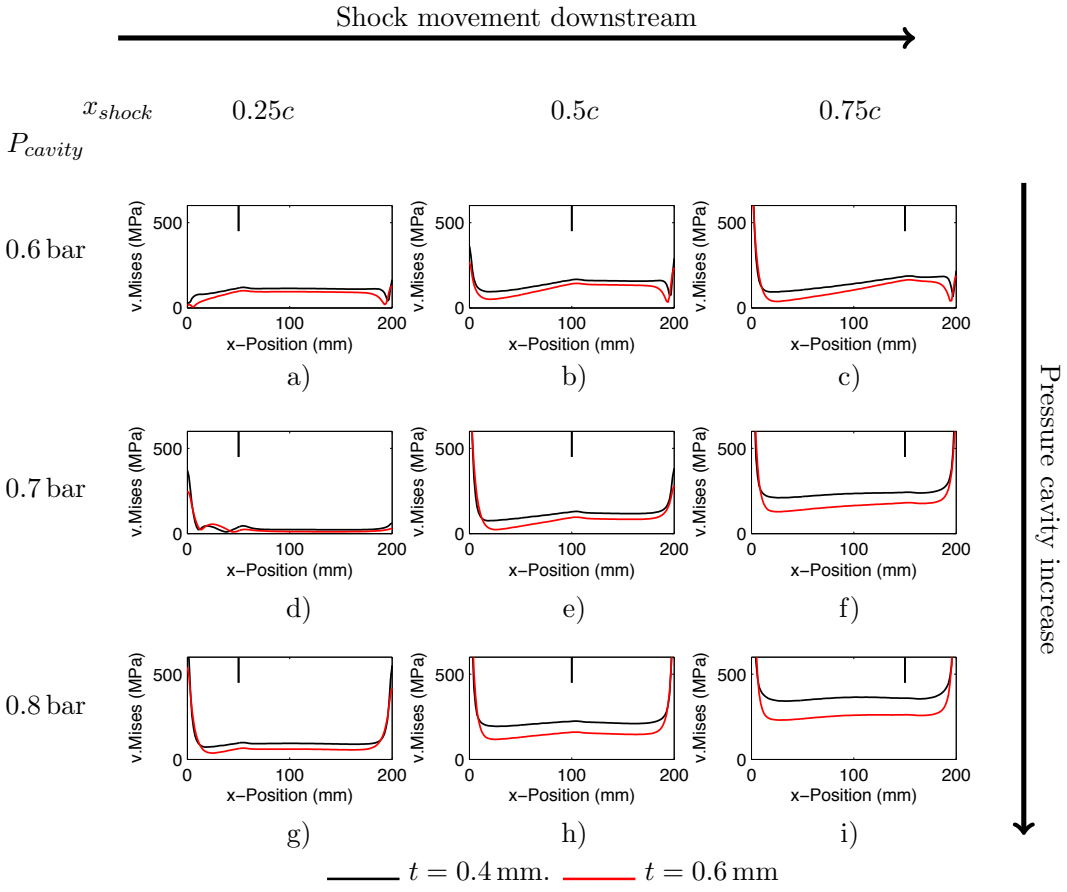


Figure 3.12.: von Mises Stresses at plate centre line for varying inviscid shock position and plate thickness with variable cavity pressure. Al-7075-T6, $l_b = 200\,\text{mm}$, $b = 150\,\text{mm}$.

3.1.6. Designing Plates Summary

The quasi-steady plate analysis suggests that the pressure gradients surrounding the plate are capable of producing similar geometries to traditional static SCB. Not only are they capable of reaching such heights but they can achieve these heights whilst remaining within the elastic regime. This is dependent upon a suitable cavity pressure and thickness being selected. There were some limitations of the 2D inviscid aerodynamic model which does not incorporate the viscous interaction between the shock and the boundary layer.

Early supersonic flow-plate interactions [Dowell, 1966] used 1D piston theory to approximate the pressure loading. Whilst this allowed for initial feasibility studies, the techniques now available to the designer are much more rigorous. In particular advances in the power and fidelity of computational simulations and advances in experimental techniques can be exploited to improve on this decades old approach. The FSI aspect has only recently been included in shock-plate studies by researchers such as Gordnier and Fithen [2003] and Visbal [2014] with coupled Navier-Stokes solvers and Finite Element structural models. These investigations have brought the aerodynamic model of FSI studies up to the same standard and resolution as static SCB CFD analyses.

The challenge now is to construct an aero-structural model that bridges the gap between these initial studies with 2D inviscid aerodynamics over flexible panels to more advanced numerical aerofoil studies.

3.1.7. Developing Adaptive SCB for Integration into Aerofoil Design

The aero-structural solver developed here uses the FE structural model outlined in section 3.1.2 with an aerodynamic pressure load computed via CFD. The process which starts with a clean aerofoil and the corresponding converged pressure loading is illustrated in figure 3.13. This initial solution is then mapped to the upper surface of the plate. The cavity pressure beneath the plate is set to the average pressure on the upper surface of the plate with the new geometry of the plate calculated with this distribution. The new aerodynamically-loaded geometry is then added to the previous geometry and remeshed ready for another CFD analysis. This process is referred to a single evaluation and represents an aeroelastic iteration shown in figure 3.13.

3.1.8. Aerodynamic Modelling

In order to model the performance of SCB, a suitable baseline aerofoil is required. The modifications to the aerofoil will specifically target the shock region so a typical

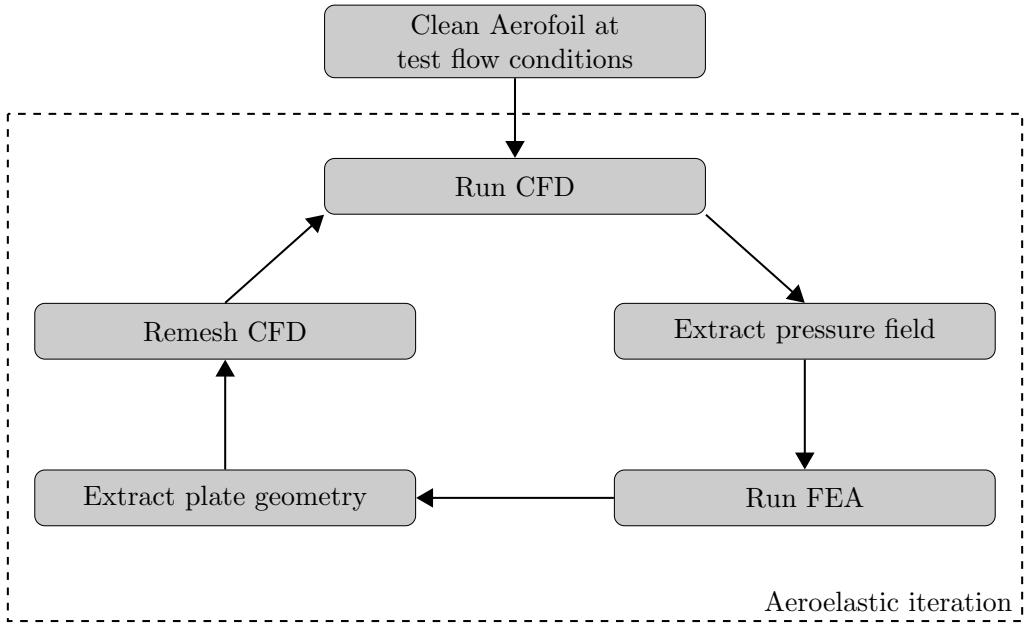


Figure 3.13.: Aero-structural solver module.

supercritical profile is selected. The RAE2822 aerofoil provides a suitable baseline geometry with gentle upper surface curvature and widely validated test cases from AGARD-AR-138. The sharply rounded nose and concave region on the lower rear surface are features that are commonly seen in transonic aerofoils to quickly accelerate the flow and control the pressure recovery downstream of the aerofoil respectively. The turbulent boundary layers that form on the RAE2822 aerofoil at these Reynolds and Mach numbers are typical of those found on modern aircraft wings.

To analyse the performance of each SCB design it is necessary for the aerodynamics around the aerofoil to be modelled and CFD is chosen to do this. The stages of selecting a suitable model and approach are discussed here.

The design flight phase for SCB on transonic passenger jets is during cruise, where modern aircraft with swept supercritical wings cruise at $0.8 < M_{cr} < 0.86$ for a large proportion of the flight [Roberson et al., 2007]. Designing for this portion is not only representative of the design condition for SCB but it also reduces the problem to a single flow condition for which the numerical analysis can be conducted. The constant Mach number approach to modelling is also representative of typical cruise profiles [Roberson et al., 2007] where the pilot varies altitude during cruise to compensate for

the reduction in weight due to fuel burn whilst maintaining a constant Mach number and lift coefficient.

The design cruise conditions for the RAE2822 aerofoil chosen for this study are $M_{design} = 0.73$ at $\alpha = 3.19, Re = 6.5 \times 10^6$, [AGARD-AR-138]. This causes an upper surface shock strength of $M_{shock} = 1.25$ with a location at $x = 0.49c$. By selecting this single on-design case for aerodynamic analysis, the design space is reduced significantly which lends itself to design optimisation.

CFD Meshing

With many previous optimisation studies for static SCB, the design space and the control parameters used to define the geometries are well known. The variation between existing designs is small which means that meshing a design for a given set of control parameters results in similar meshes for the majority of test cases.

The similarity between each mesh allows for the construction of a case-specific meshing tool that can handle the small differences associated with each SCB design. A structured mesh requires a rigorous grid to be calculated for each case however the subtle differences between each iteration mean that the development of a structured mesh generation algorithm is a beneficial option and means that many controls can be put in place to produce high quality meshes.

The geometry of a transonic aerofoil is ideally suited to a structured mesh due to a dominant velocity component in the streamwise direction. The aspect ratios of each cell can be adjusted accordingly to suit the flow velocities and can be aligned with the flow relatively to suit dominant flow features such as shocks easily due to the level of control available with structured grids. The computational expense and time associated with developing a structured mesh generator is worthwhile due to the ability to specify the location of each point, especially within the boundary layer as well as the region surrounding the shock. The potential to prescribe points close to the surface ensures a well defined wall-normal direction for accurate boundary layer modelling. This is particularly important as the interaction between the boundary layer and the shock is known to be highly influential of the overall performance of SCB.

The mesh is constructed with the use of transfinite interpolation schemes as well as elliptic smoothing between the aerofoil surface and the bounds of the domain. The former is predominantly used to initialise the grid based upon the bounding conditions specified by the user. For this case a standard D-mesh is used to allow the flow to become established upstream of the aerofoil and to monitor the wake downstream. The

C-mesh radius	No. elements	y^+	Avg. Skew	Non-Orthogonality
10c	200,000	4.7	0.78	0.2

Table 3.5.: Mesh Characteristics

overall extent of the mesh is shown in figure 3.14a.

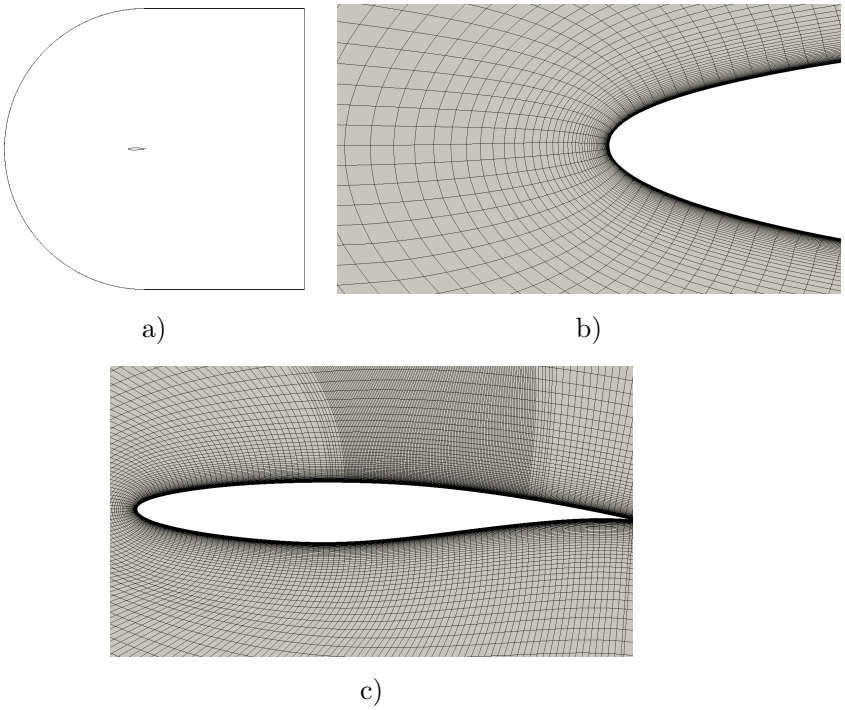


Figure 3.14.: Mesh boundary and mesh refinement around the aerofoil nose area (coarse grid shown for clarity).

Mesh refinements were added to the boundary layer and expected shock regions to better capture the flow shown in figure 3.14c, the first point was placed so that $y^+ \approx 5$ in order to capture the physics in the boundary layer suitably close to the wall. This led to an overall number of cells in the region 2×10^5. This value was chosen following the results of a mesh convergence study shown in figure 3.15 and satisfied the requirement of a suitably short time to final solution for the eventual integration into an aero-structural solver and optimisation study.

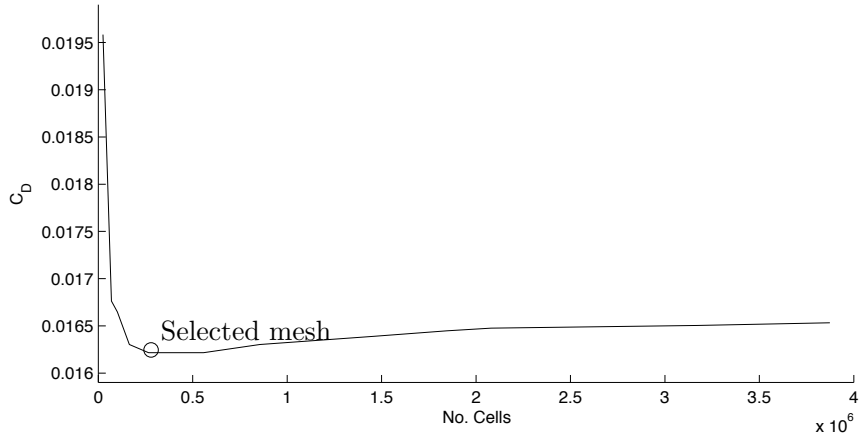


Figure 3.15.: Mesh Convergence study for RAE2822 aerofoil structured grid.

CFD Solver

The CFD solver was completed using the *rhoCentralFoam* solver within OpenFoam. It solves the conservative form of density-based Reynolds Averaged Navier-Stokes equations through the finite volume method with Kurganov flux scheme coupled with the van Leer flux limiter method [OpenFOAM, 2017]. The system is closed using the one-equation Spalart-Allmaras turbulence model due to the robust nature of the scheme for attached flow [Spalart and Allmaras, 1992].

The Kurganov-Tadmor flux scheme [Kurganov and Tadmor, 2000] is a centred scheme based on a mass flux and the monotonic upstream-centered scheme for conservation laws (MUSCL) of Van Leer [1979]. This scheme is second order accurate in space which is useful in regions of high gradients, such as the shock system in transonic flows and boundary layers. Time derivatives are managed by a first order, bounded, implicit Euler scheme and the gradient and divergence terms are dealt with by a second order, unbounded, linear Gauss scheme.

An explicit non-orthogonal correction procedure is undertaken to check the skew of each element with the limit set to 88^o based upon the neighbouring edges to ensure orthogonality in the mesh.

The benefits of the Kurganov and Tadmor scheme lie within the wave propagation properties which is of significant importance in this transonic flow case. The wave propagations need to be dealt with at the boundaries of the CFD domain to ensure the correct passage of the pressure waves. The aerofoil is represented by a solid wall which is set to a no-slip condition which forces the solution to allow for zero flow velocity near

the wall. The cells in this near wall region need to be sized accordingly in order to model the correct physics of the flow described as in the previous meshing section.

Validation

The CFD results have been compared to an experimental study on the RAE2822 aerofoil, case 12, [AGARD-AR-138]. The AGARD report is a comprehensive evaluation of the RAE2822 aerofoil and covers test cases from subsonic to supercritical flow. The range of Mach numbers was $0.6 < M < 0.75$ with Reynolds number varying between $2.7 \times 10^6 < Re < 6.5 \times 10^6$. The experiment was setup in order to replicate a 2D aerofoil and reduce the effects of three-dimensionality with a swept wing model spanning 75% wind tunnel to minimise wall interference effects. The span of the aerofoil was three chord lengths and the pressure measurements presented were taken from the centreline, again to minimise any undesirable three-dimensional effects.

The pressure profile is shown in figure 3.16 and demonstrates good agreement between the model and the results from the experiment. The agreement is particularly good in the shock region which has been know to be a region of poor performance for the Spalart-Allmaras turbulence model [NASA, 2017]. The smaller difference between the CFD and experimental results in the current study is due to the high level of mesh refinement in the shock region that allow for more precise capturing of the shock. The mesh generation method and flow conditions form the aerodynamic aspect of the aero-structural solver. The experimental lift coefficient was recorded at 0.721 AGARD-AR-138 which is slightly above that recorded in the CFD at 0.715 of which the difference is attributed to the variation in pressures towards the front of the lower surface. Due to the transonic velocities present the changes made in the shock region do not significantly affect the flow in the free stream, nor the lower surface or upstream of the control region. Preliminary computations with and without SCB have confirmed that the global flow field beyond 0.5c from the surface is similar between SCB designs. This allows for the numerical flow field to be initialised as a converged solution on the structured mesh for the clean aerofoil which aids computation time for each aero-structural iteration. The ability to initialise the flow field stems from the capacity to map the solution between designs, the main factor in this is due to the construction of a reliable structured mesh.

3.1.9. Coupling the Aerodynamic and Structural Solvers

Coupling the aerodynamic loading with the structural model allows for the aero-structural properties of adaptive SCB to investigated. The aim of the coupling is to accurately

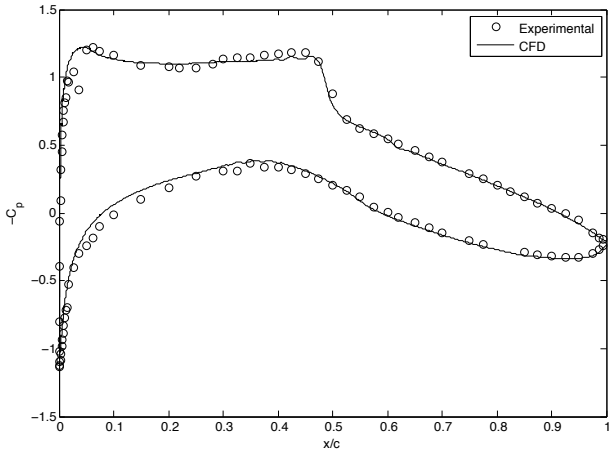


Figure 3.16.: Experimental and computed CFD pressure profile comparison for the datum RAE2822 aerofoil with no control measures, $\alpha = 3.19°$, M_∞=0.728, Re = 2.7×10^6. Experimental data extracted from Cook et al. [1979]

predict the performance of these flexible plate-based adaptive SCB and also to determine whether the continuous loading of the plate would lead to unstable aerodynamic loading that would cause the plate to fail by exceeding the yield stress. By applying the aerodynamic load to the flexible plate the stresses can be calculated in order to determine whether or not the design can remain within the elastic regime and meet the design specification of adaptive SCB.

This quasi-steady approach involves extracting the pressure at the wall in the plate region of the converged field and applying it to the structural mesh in the finite element solution as described in figure 3.13. Due to the difference in stream-wise spatial resolution required for the CFD and FEA methods, the precision of the aerodynamic load is reduced in the FE model however the accuracy of the solution is maintained. A typical CFD cell is of streamwise length 6×10^{-4} m whereas an FEA element is approximately 2.5 times larger at 15×10^{-4}m The static pressure is used to provide the upper surface loading which is then mapped to each element. The 2D pressure profile from the CFD is extended in the span-wise direction to maintain a constant spanwise aerodynamic loading.

The surface pressure is imported into the FEA (Abaqus ABAQUS [2007]) through the use of the subroutine DLOAD. For each element, the subroutine is called upon and returns the necessary pressure loading. This allows for the higher resolution CFD pressure load to be discretised and represented upon each element of the lower resolution FE model.

The lower surface of the plate is subject to the cavity pressure applied which, from the initial study, has been shown to have a significant effect upon plate geometry and its subsequent response to the upper surface shock loading. Many options are available for the choice of cavity pressure for flexible plates and integrating such a flexible device onto an aerofoil adds further options. As aircraft cruise at different altitudes, the atmospheric pressure varies and thus the pressure distribution over the wing will vary. Therefore a constant cavity pressure beneath the plate may not be optimal for all flight conditions. The approach in this numerical study is to focus upon single point cruise condition so a technique to control the pressure difference across the plate is required.

The FEA produced surface displacements and the CFD meshing algorithm was implemented with the new displaced geometry. This provided the CFD mesh for an aerodynamically loaded plate subjected to the boundary conditions presented in the previous section. The process forms an aeroelastic iteration. Finally the aerodynamic solver was run with this mesh until convergence which provides the deformation of the flexible plate for the initial design phase prior to experimental investigation.

3.2. Experimental Approach

The coupled aero-structural solver is a valuable design tool that enables the evaluation of a new passive design for adaptive SCB. The combination of the high-speed flow and the shock-plate interaction is very computationally expensive which is the reason for limiting the coupled solver to a quasi-steady analysis. The transient response of the FSI on the other hand is to be investigated using a blowdown supersonic wind tunnel. The focus is upon the area surrounding the shockwave illustrated in figure 3.17.

3.2.1. Wind Tunnel

The supersonic facility at Imperial College is a blowdown wind tunnel capable of run times of approximately 60 seconds. Atmospheric air is dried, compressed and stored in four $12\,m^3$ tanks at 27 MPa at ambient air temperature. This high pressure air is fed through to a pneumatic control valve that is controlled remotely by a National Instruments, LabView VI. The air then enters a settling chamber of diameter 300 mm, length 450 mm where a total pressure measurement is taken via a pitot probe. Pressure data is recorded using two PSI-netscanner 9116s connected to National Instruments hardware.

The air passes through a honeycomb and a set of screens that straighten the flow and

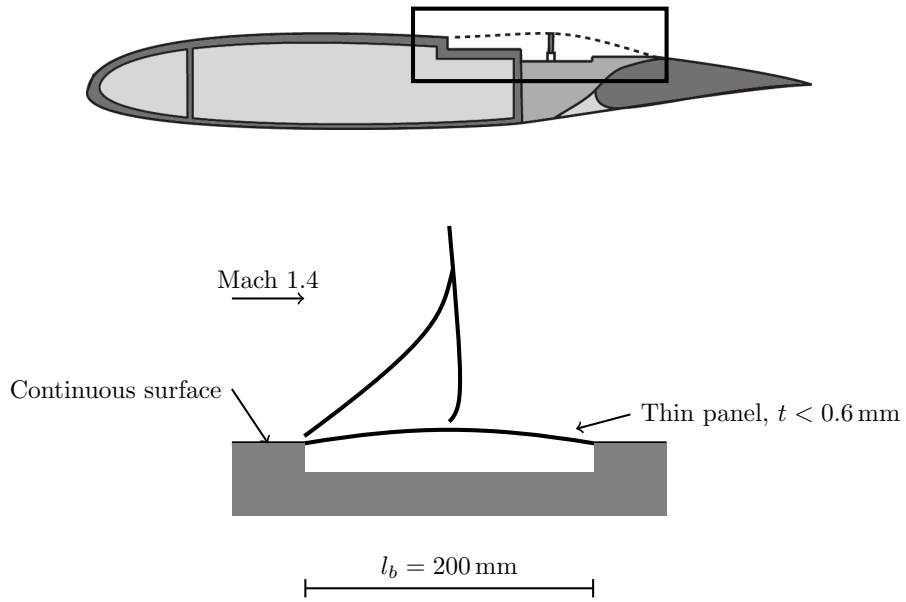


Figure 3.17.: Original concept drawing by Ashill et al. [1992] and the region of interest that is to become the focus of the experimental analysis in the blowdown supersonic wind tunnel.

lower the turbulence intensity before the round to square contraction.

A pair of Mach 1.4 nozzle sections were designed using a method of characteristics approach specifically for this project to replicate the flow regime that occurs on the upper surface of transonic wings. The design process for the nozzles and integration into the wind tunnel is discussed in appendix A. The design Mach number was chosen to showcase the capabilities of adaptive SCB. With a nozzle exit Mach number M=1.4 was chosen to be representative of a strong shock on a wing with corresponding pressure gradients. The severe pressure gradients will form a challenging test case for adaptive SCB.

The nature of adaptive SCB is very sensitive to shock position and the associated pressure field. The experimental techniques used to capture the interaction must be able to capture the unsteady shock position as well as the large-scale bifurcated shock structure that SCB aim to introduce. The following sections 3.2.2 and 3.2.3 detail the principles behind two of the techniques used in this investigation.

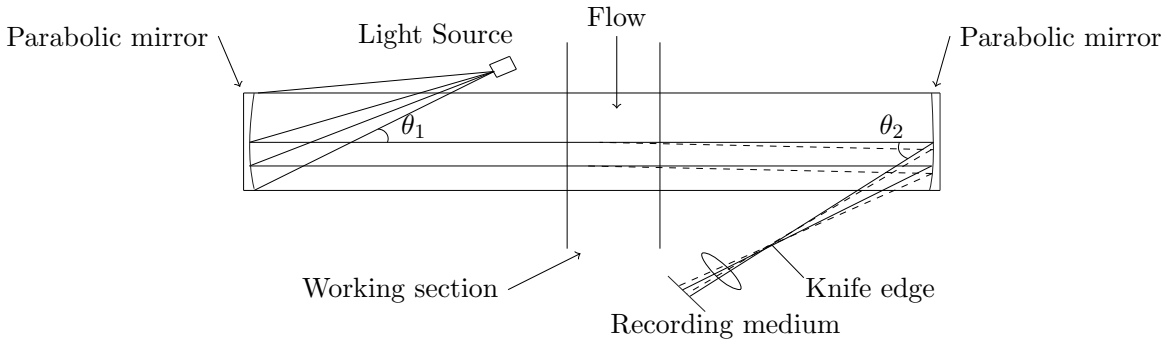


Figure 3.18.: Z-Type Schlieren arrangement taken from Settles [2001]

3.2.2. Schlieren Imaging

Schlieren imaging has been used since 1562 and used as a means of flow visualisation since the 17$^{\text{th}}$ century. Settles [2001] notes Robert Hooke as the first author of the Schlieren technique through his book *Micrographia*, Observation LVIII, which provides a thorough and cogent discussion of light refraction through density variations in a test fluid. The technique is able to capture the density gradients through the principle of refracting light. Figure 3.18 shows the principle behind Schlieren photography. The equipment illustrated shows the typical setup of a Z-type Schlieren arrangement with the region of interest located in the centre of the parallel light. The measurement region can be anywhere along the collimated light section as long as density gradient changes avoid overlapping with the focussing regions.

The left parabolic mirror produces collimated light from the light source which is positioned at the focal point of the mirror. The second mirror collects the undisturbed collimated light and focusses the light back down through the focal point and on to a viewing device. Figure 3.18 shows two dashed lines which are representative of the path of the selected light rays after refracting through a density gradient. The magnitudes of the deflections have been amplified for clarity. These refracted light rays are also reflected and focussed from the parabolic mirror and collected on the viewing device but at a different location. The choice of viewing device could be a blank surface or photographic film however modern day Schlieren utilises high speed cameras to record the results.

The sensitivity of the system is controlled by the position of the parabolic mirrors. Placing them further apart requires a more precise setup however it offers greater sensitivity to the density gradients that can be captured. The focal length of the mirrors used

is 1200 mm which is a compromise between maximising focal length and the available space surrounding the wind tunnel. The optical knife-edge positioned at the second focal point represents the difference between Shadowgraph and Schlieren imaging. Shadowgraph photography uses the Z-type arrangement but does not use a knife-edge. The images produced as a result of Shadowgraph photography are not as defined as with Schlieren imaging. The use of a knife-edge in Schlieren imaging blocks any light that has been refracted in a given direction. The choice of the user is to determine which direction to block off, either horizontally or vertically depending upon the application, the choice is explained in a subsequent paragraphs.

Schlieren imaging is a proven method to collect qualitative information regarding the density gradient of compressible flows with sufficient detail to extract key flow features. In order to analyse the results, it is important to understand the techniques limitations.

The main limitations are collectively called off-axis aberrations, individually these effects are termed coma and astigmatism. They are the effects that result from the Z-type arrangement which imposes skew on the collimated light. Coma occurs when the direction of reflected light from a mirror is dependent upon the location of the point of reflection. In the Z-type arrangement in figure 3.18 this is a consequence of tilting the parabolic mirrors off their optical axis so the focal point becomes smeared into a line away from the point source [Settles, 2001]. This results in a flared region with a bright spot akin to a comet which influences the name. The effect increases with the angle between the incident light ray and the collimated light, ($\theta_{1,2}$ in figure 3.18).

The coma grows proportionally with the offset angle $\theta_{1,2}$ and inversely with the square of the focal length, f^2. In order to reduce the effects of coma it is beneficial to minimise the offset angle and use mirrors with a long focal length. Another benefit of the Z-type arrangement is the ability to eliminate the effects of coma. With careful setup, the angles θ_1 and θ_2 of mirror tilt can be matched to cancel out any effects of coma given that the centrelines of mirrors, light source and camera all lie on a common plane.

The second aberration is astigmatism and results from the failure to focus a point to a point. The cause of this aberration stems from the differences in path length along the optical centreline and the light at the mirror periphery. Due to the fact that there will always be a small difference between θ_1 and θ_2 there will always be some astigmatism with large focal length mirrors. Another contributing factor is the width of light source which smears the illumination across the test area to two short lines near the focus of the second mirror. The second of these lines is called the sagittal focus and spreads the focal point in a horizontal direction. If a horizontal knife-edge is used then the variations are equally cut off which reduces the effects of uneven illumination and visible astigmatism

errors. The same is true for vertical dispersions in front of the sagittal focus point where a vertical knife-edge can be used to limit the variations

Schlieren Experimental Setup

The practical applications of the Schlieren technique will focus upon the specific case of adaptive SCB and the testing within the Imperial College London Supersonic facility.

The collimated of light is placed perpendicular to the direction of flow so that density gradients captured are capable of visualising the shock structure over the SCB. The point light source is a powerful LED with mount options from THORLABS with a small pinhole aperture to replicate the point light source required for Schlieren Imaging. The slender body of the LED enables the light source to be placed very close to the collimated light to minimise the angles within the Z-type arrangement. Other light sources such as flash lamps require a much larger body and require positioning further away from the collimation which increases the likelihood of aberration as discussed previously [Settles, 2001].

The use of a knife-edge at the second focal point allows for specific density gradients to be highlighted. A horizontal knife-edge is capable of accentuating density gradients in the vertical direction and has practical uses in the visualisation of the boundary layer. An application for this is for the visualisation of oblique shocks where there is a vertical density gradient $\frac{\partial \rho}{\partial y}$. The streamwise gradient $\frac{\partial \rho}{\partial x}$ however are best viewed with a vertical knife-edge. Precise positioning of the knife-edge has the effect of letting more or less light into the image and has the effect of reducing or increasing the sensitivity of the system.

The choice of recording medium has a significant effect upon the quality of results taken. A high speed Phantom v641 camera is positioned along the optical centreline with a 105 mm lens so that the light that travels through the windows of the working section fills the physical space of the light sensor chip. The 4 MegaPixel sensor allows for a very high resolution of image and when coupled with the 105 mm lens allows for a large field of view that covers a significant proportion of the sensor whilst maintaining a suitable frame rate. With this arrangement, it was possible to acquire images 2560 $\times$ 1560 pixels to be collected at 350 Hz for 35 seconds with 32GB of storage. This time was sufficient to capture tunnel start up, a 10-20 second period of steady flow and tunnel shut down. The capture of the entire transient wind tunnel run is important in the characterisation of adaptive SCB and unsteady FSI.

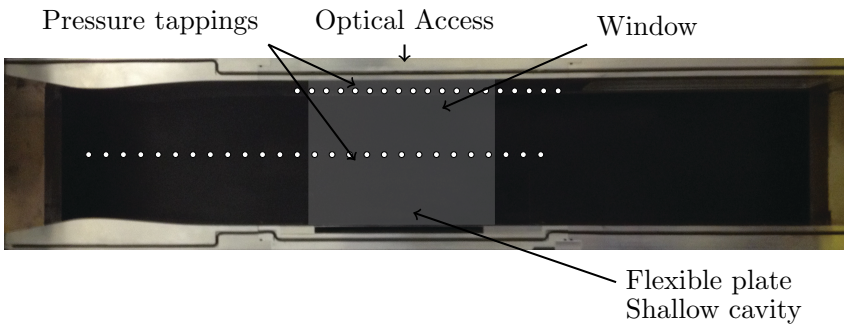


Figure 3.19.: Mach 1.4 profile wind tunnel with adaptive SCB fitted.

Example of Results

A typical Schlieren image is shown in figure 3.20. The image is of a Mach 1.4 normal shock with the field of view spanning 130 mm × 75 mm, half of the working section height however this is variable. The flow is from left to right which can be seen by the presence of pressure waves in the supersonic left hand side of the image. These are small variations that emanate from the initial expansion at the throat that are left un-cancelled by the nozzle section. They will be visible in each of the images presented however the effect upon free stream Mach number is small.

The normal shock can be identified by a thick black line running vertically through the image. The width of the shock representation in the image is determined by the degree of light that is blocked off by the knife-edge. The image presented in figure 3.20 was captured with a carefully positioned vertical knife-edge that is suitable for the visualisation of this Mach 1.4 flow and the density gradients in the stream wise direction. The width of the shock portrayed here is a function of the spanwise averaging that is a result of the collimated light passing through the entire width of the wind tunnel. This is an unavoidable side-effect of Schlieren photography and must be acknowledged in the analysis of any images produced. spanwise density gradients in the working section are minimised by the use of a two-dimensional nozzle however the boundary layer on the windows perpendicular to the collimated light will also cause some distortion of the shock density gradient across the shock.

The viscous smearing highlighted by the white box is the region near to the wall where the boundary layer interacts with the main normal shock. In this region the process outlined in figure 2.3 in section 2.1.1 begins to take place with the thickening of the boundary layer forming a pseudo-surface which triggers the build up of pressure

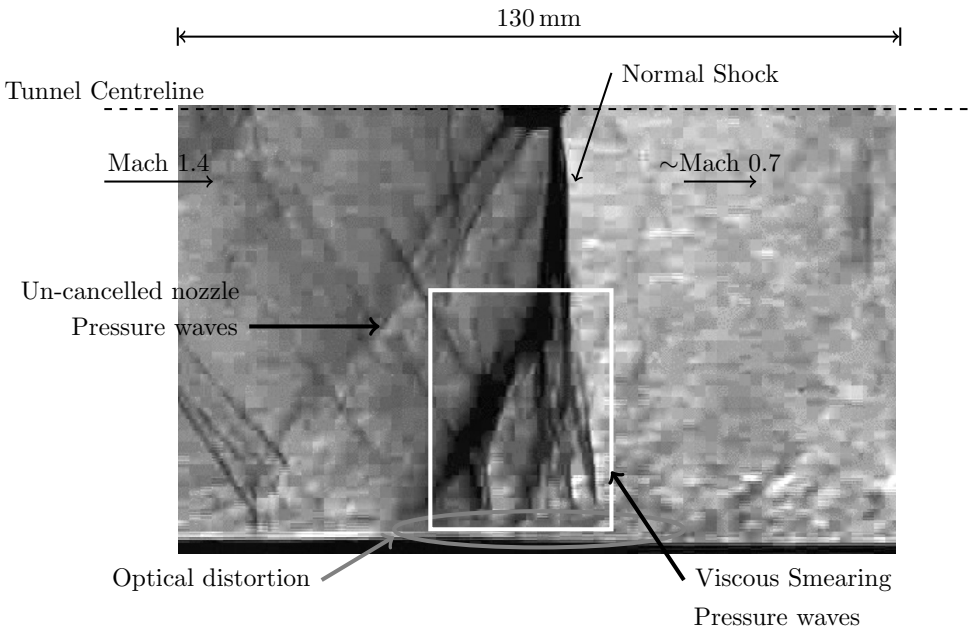


Figure 3.20.: Example of Schlieren Imaging. Mach 1.4 normal shockwave image taken at 1000 Hz with an exposure time of 10 μs. A vertical knife-edge was used to highlight the streamwise density gradient across the normal shockwave.

waves which are seen as dark, blurred lines in figure 3.20. The effect of viscosity and the interaction with the wall is significant when the blurred lines near the wall are compared to the sharp black lines at the top of the image in the free stream at the centre of the tunnel.

Also of note is that the wall is also subject to optical distortion particularly in the supersonic region. The wall in the wind tunnel is a solid, flat surface however in the region with the ellipse a gradual slope can be identified. This effect is not due to surface movement but an optical effect of the density gradients close to the wall. Such an effect has significant implications for adaptive SCB as the plate surface is under an unsteady load and is likely to vibrate.

Application to Adaptive SCB

The analysis of the Mach 1.4 normal shock image has highlighted some of the key features of the Schlieren imaging process. The application of the method to adaptive SCB provides useful information regarding the overall shock structure imposed by the flow control device. The ability to capture a large proportion of the wind tunnel with

a field of view up to 170 mm×130 mm at 350 Hz allows for a field of view that includes the resulting shockwaves formed from the successful bifurcation of the normal shock.

The spanwise averaging of Schlieren imaging is a feature of the process and has to be taken into account in future sections of this work. However, for the following series of experiments this span-averaged result is assumed to be representative of the centreline of the tunnel which is typical of many other experiments in similar wind tunnels [Bur et al., 2002, Ogawa et al., 2008, Bruce and Babinsky, 2012]. The displacement of the plate can also be inferred by each of the Schlieren images although these are also influenced by the spanwise effects within the experiment.

The aerodynamic loading of the plate was considered two-dimensional in the aero-structural model with the plate showing only small signs of span wise deformation where the free edges deform slightly more than the centreline. The differences between the centreline and edge displacements were of the order 0.2% in the structural FEA model. These results from section 3.1.7 provide assurance that averaging across the span will not significantly affect the results. The ability to infer shock position and structural displacement from the Schlieren image is valuable. In practice the technique will be able to capture the upper and lower bounds of the flexible surface for the given shock loading as well as the shock movement over the upper surface. These simultaneous measurements are very useful for investigating the FSI.

With shock structure and plate displacement obtainable from the sequence of images it is possible to build up the shock-plate relationship as the FSI develops. Using the camera settings detailed previously, it was possible to capture the complete evolution of the interaction from zero aerodynamic loading to full shock loading and back.

3.2.3. PIV Setup

Principle

The principle behind PIV is to quantify the velocity of a fluid using tracer particles that are able to closely follow the trajectory of the fluid. In water and other similar fluids, solid particles are often used providing they are able to remain buoyant within the flow. In air, liquid particles are more common as they remain buoyant within the air and can be reliably produced to a range of sizes depending upon the type of injection method used [Adrian and Westerweel, 2011]. Illumination is required in order to increase the visibility of the particles on the recording medium, this is commonly achieved through the use of lasers which offer very intense, consistent light at repeatable high frequencies. As with Schlieren photography the process is made much easier with the use of high

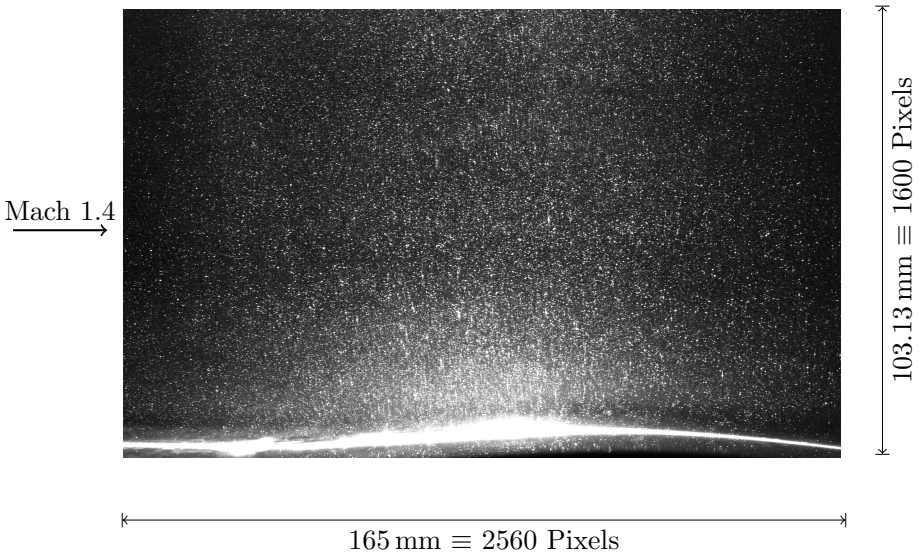
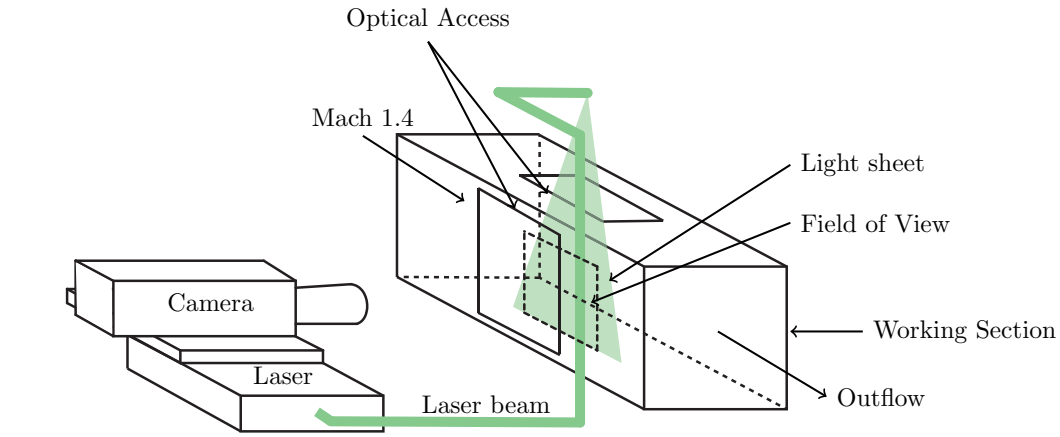


Figure 3.21.: Example raw image of supersonic flow over a flexible plate.

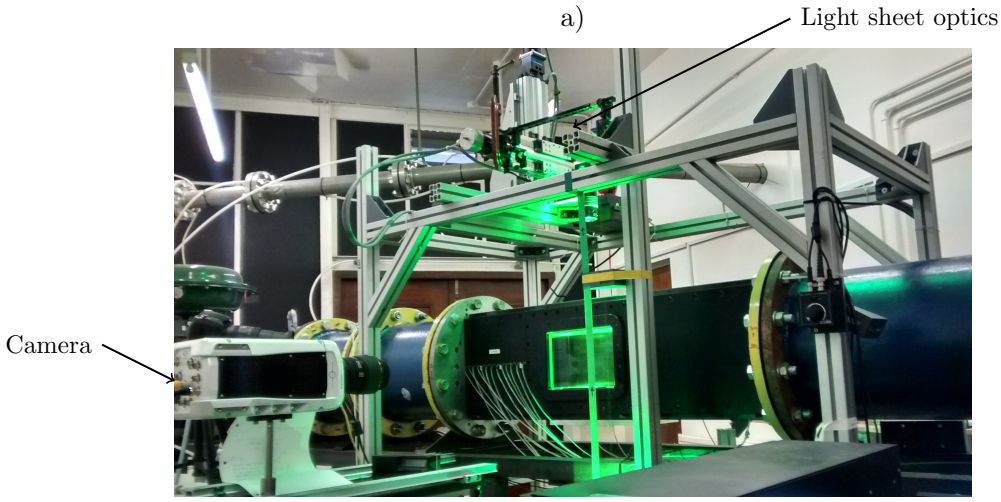
speed digital cameras. They enable the particles to be photographed at precise time intervals. This can either be a sequence of single frames taken at a time separation of Δt apart or a pair of images straddling a given time, dt, which is termed a double frame image, a double frame image is then captured every Δt. The value of *dt* is critical for the quality of results that can be produced via PIV especially when applied to transonic flows where the particle velocities can be very high with large velocity gradients.

The normal PIV process used in this investigation uses a single camera positioned perpendicular to the light sheet as shown in figure 3.22. Due to the time scales involved, the double frame exposure is required in order to achieve suitable spatial and temporal resolution of the transonic interaction. The two frames produced as a result of a double frame image capture represent two particle fields with a temporal separation dt. The displacement of the particles between the two images provides a length scale which combined with the *dt* provides a velocity.

The real power of PIV is that the particles in the images are not merely subject to a differencing algorithm that tracks the particles but algorithms based upon the cross correlations of small sections within the image. The small sections are termed windows and the optimal size of these is case specific and will be covered in more detail in the following sections. The size of each interrogation window dictates the resolution of the velocity field and is dependent upon the resolution of the image and the physical size of



a)



b)

Figure 3.22.: Optical setup within Imperial College London blowdown supersonic wind tunnel. a) Schematic. b) Photograph

M_0	FOV	$f^{\#}$	λ	d_{diff}	d_τ	δ_z	dt	DSR	DVR
0.155	$165 \times 110\,\mathrm{mm}^2$	5.6	532 nm	8.11 μm	8.12 μm	6.27 mm	1.69 μs	98.92	77.42

Table 3.6.: Key PIV experimental setup parameters.

the particles. Upon successful computation each window is assigned the average velocity of the intensity field within. Therefore the size of each window dictates the resolution of velocity vectors.

Once the velocity vector field has been computed there can often be errors in the velocity field due to poor image quality or unsuitable cross correlation parameters. The low signal to noise ratio (SNR) typical for PIV can in many cases lead to spurious values which need to be eliminated or replaced through post-processing [Adrian and Westerweel, 2011]. The post-processing techniques applied in this work will be discussed in more detail when they are used.

PIV Experimental Setup

The general concept of PIV requires many sub-systems to provide the seeding particles, the illumination, image capture and image/post processing. Each sub-system relies upon the others with the setup of the experiment a significant contributing factor to the quality of the results.

The calculations behind the setup of the PIV experiments can be found in appendix B with a schematic of the setup shown in figure 3.22. A summary of the key parameters can be found in table 3.6. The general discussion regarding each aspect will be covered here.

Seeding

The particles seeded in the flow were selected based upon previous experiments in similar flows [Sartor et al., 2012, Hartmann et al., 2011]. Di-ethyl-hexyl-sebacate (DEHS) was used as the seeding medium as the particles have been seen to faithfully follow the flow [Adrian and Westerweel, 2011, Threadgill and Bruce, 2016]. Atomising the DEHS liquid in to the blowdown supersonic tunnel was conducted through PIVTEC PIVpart160 and PIVpart45 seeders which are able to reliably produce particles $\sim 1 - 3\,\mu$m diameter. This particle size allows for widely available optical equipment to be used in the imaging of the flow field whilst maintaining suitable fields of view. Solid particles were not used over concerns about their ability to faithfully follow the flow and effects of agglomeration which affect the correlations in the image processing.

The seeders were driven by a high pressure air supply which forced air into the DEHS reservoir causing atomised liquid particles to be formed. The two seeders combined had a total of 205 Laskin nozzles in order to generate the required number of particles within each image. Initially a seeder with 45 Laskin nozzles was used as there had been successful PIV with the Mach 2 nozzle [Threadgill and Bruce, 2015] however the increased mass flow rate associated with the Mach 1.4 nozzle meant that the seeding density did not produce meaningful velocity fields as the spatial resolution was too poor.

Figure 3.21 shows a typical raw image taken during a tunnel run. The seeding density is relatively good and uniform throughout the image. The high intensity region near the crest of the plate is a result of the reflections from the surface which increase the background intensity and reduce the signal to noise ratio in this area. The apparent lack of seeding at the entrance and exit of the frame is due to the divergence of the laser sheet and the distribution of energy as a result of the light sheet forming optics and the distribution of energy within the laser sheet which is the subject of the following section.

Illumination

The light source selected for the experiments is a Litron Nd:YAG laser, which provided a maximum output of 33 mJ per laser pulse which is passed through a number of optical components to manipulate the path and shape of the beam. Figure 3.22 shows how the light source was integrated in to the existing wind tunnel setup. The support framework has been omitted for clarity however the changes in direction of the laser beam were achieved with high-quality ThorLabs optical mirrors with a gold coating on the surface in order to reflect maximal laser energy. Ideally the number of mirrors would be kept to a minimum in order to minimise the energy lost through reflections, the equipment manufacturers claim 96% energy reflection between 20 nm and 800 nm wavelengths meaning approximately 81% of the initial laser energy was used to form the light sheet in the 5 mirror system. There were however some unavoidable trade-offs with the beam shape emanating from the laser which meant more mirrors had to be used in order to make best use of the imperfect beam shape. The small losses of intensity were counteracted with an increase in laser power which was possible due to the high power output of the laser.

The Nd:YAG laser consisted of a two cavity system producing infra-red laser light produced at 1064 nm frequency doubled to 532 nm. The output energy at 1 kHz was measured at 32.5 mJ and 33 mJ for each pulse. Due to the experimental setup and

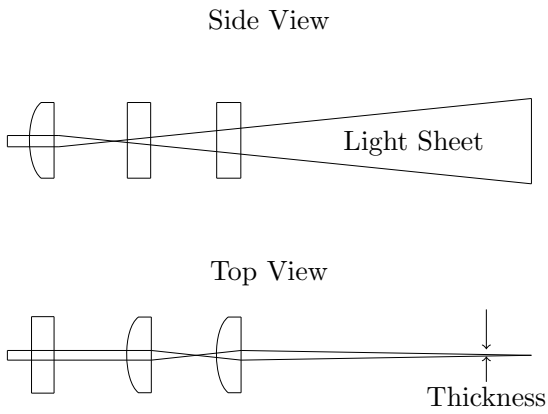


Figure 3.23.: Lens configuration of laser sheet forming optics.

the curvature of the surface of interest during operation, the results presented were obtained from pulses at 13.2 mJ. This value represented a compromise between good illumination of the field of view without unacceptably bright reflections at the regions of high curvature on the surface.

The light sheet was formed through a a Dantec lens holder which contained a series of optical lenses that deformed the shape of the beam. Figure 3.23 shows the construction of the module. The layout of the lenses allows for very thin laser sheets to be created. The first cylindrical lens controls the streamwise spread of the light sheet and was chosen to give the required field of view. The second lens controls the thickness of the light sheet in a spanwise direction and was positioned to create a very thin light sheet to best approximate a 2D streamwise plane of illumination. In practise, this was varied to allow for an increased number of particles to be illuminated. The sensitivity of the solution to light sheet thickness was observed to be high and precise selection of the optimal setting was chosen via an iterative procedure in the blowdown wind tunnel environment. The final lens adds further control to the spanwise thickness of the laser sheet.

The benefits of using this setup are that light sheet thickness is minimised however the energy per unit area in the beam becomes high and so the equipment can become hot during setup. It can also become sensitive to dust causing scattered reflections which are minimised by either covering the beam/lens regions and ensuring clean, dust-free surfaces where possible. it should also be noted that the levels of illumination have a direct affect upon the quality of the results that are possible as the changes in light are recorded upon the camera sensor and therefore the final image which are directly used in the cross-correlation computations.

A spreading angle of 40^o for the laser sheet was chosen as a compromise between the illumination of the desired field of view and the intensity of the reflections at the surface. Spreading the beam with a larger angle (50^o) reduces the intensity of the beam across the sheet which affects the intensity over the field and ultimately the quality of the images collected. There is a simple counter measure that the intensity of the laser can be increased in order to cover the field of view with a higher intensity light however this is no substitute for the repositioning of the focussing module to allow for a wider sheet in the streamwise plane. A compromise was found with the lens positioned at $h = 530\,\text{mm}$ above the plate with a cylindrical lens of 40^o that managed to position the focussing module and cylindrical lens so that enough light intensity was provided across the entire field of view.

The source of the light sheet also has to account for the variation in flow density and hence seeding across the shockwave. Figure 3.24 shows this effect caused by the shock structure that formed over a flexible plate. The associated refraction does not affect the intensity of the light greatly, however, the introduction of the particles does decrease the amount of light that reaches the plate. The balance between maximising light intensity over the entire field of view and minimising the reflection near the wall required an iterative approach to position the lenses to ensure that enough particles close to the wall were illuminated. With respect to the example raw image in figure 3.21 the light-sheet forming optics are located at $h = 530\,\text{mm}$ above the intense plate line and 15 mm from the beginning of the plate. This allowed for a near vertical light source which reduces the effect of refraction through the stronger streetwise density gradient. The small streamwise adjustment provides enough of an angle to provide illumination over the entire field of view using a smaller angled cylindrical lens (40^o) which helps preserve laser intensity across the light sheet.

Adaptive SCB pose new problems to the typical PIV process due to the unsteady displacement of the surface caused by the unsteady shock loading. This causes the intense laser light to reflect from the surface in an unsteady manner making post-processing techniques such as masking and background subtraction difficult. The effects of this were particularly apparent in the crest region at the centre of the field of view where the light source is centred and the highest light intensity. To compound this it also has the highest levels of surface curvature.

The reflections are a side-effect of the curvature of the plate and as such could only be corrected for after testing where the effects of the aerodynamic load are known. The significant difference between flow on and flow off meant that during setup, the surface had to be raised 2 mm in order to simulate an element of aero-loading whilst remaining

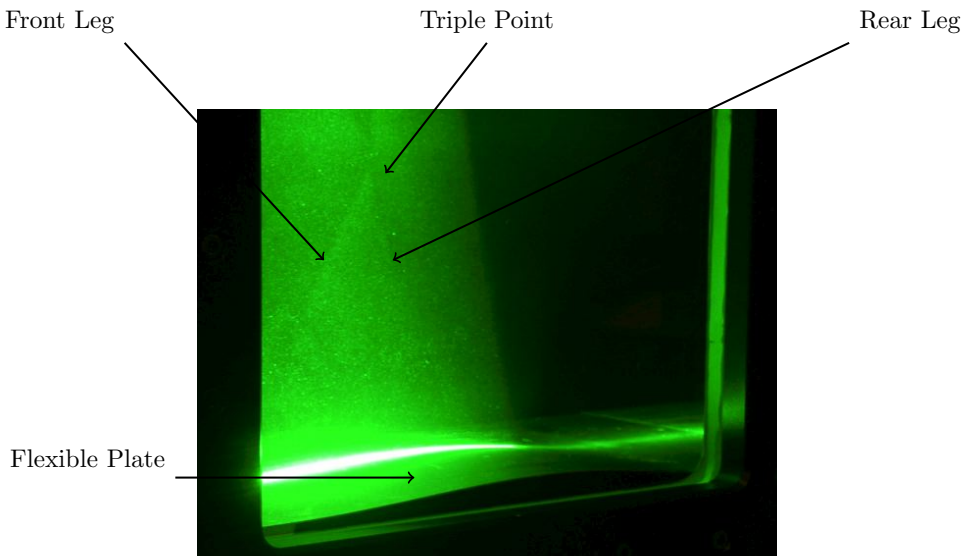


Figure 3.24.: Photograph during PIV run highlighting the optical distortion in the laser sheet caused by the density changes surrounding the shock region.

well within the elastic limit. This allowed optimal laser sheet positioning with live feedback from adjustments. The images of a typical deformed plate were capture and the average intensity of the laser reflection across the entire plate was recorded and the position of the sheet was set.

Image Collection

The most influential control variable with respect to image collection is timing. With such small dt values associated with transonic and supersonic PIV the cameras used are pushed to the limits of their capability. Table 3.6 shows the dt value required for good quality PIV, it follows the rule-of-thumb measurement that a particle should roughly travel a quarter of an interrogation window. This again requires an approximate knowledge of the flow. The time between frames, $dt = 1.69\,\mu$s is calculated in equation B.9 based upon the preceding optical measurements in appendix .

For the PIV image acquisition a Phantom v641 camera is used which has a 25.6 mm $\times$ 16.0 mm sensor and a full-frame resolution of 2560 pixels $\times$ 1600 pixels. Each pixel has 12 bit depth which is beneficial for PIV as it allows for greater detail around each particle. This aids troubleshooting when validating the experimental setup with respect to pixel shape and size with both characteristics effecting image processing. Figure 3.25

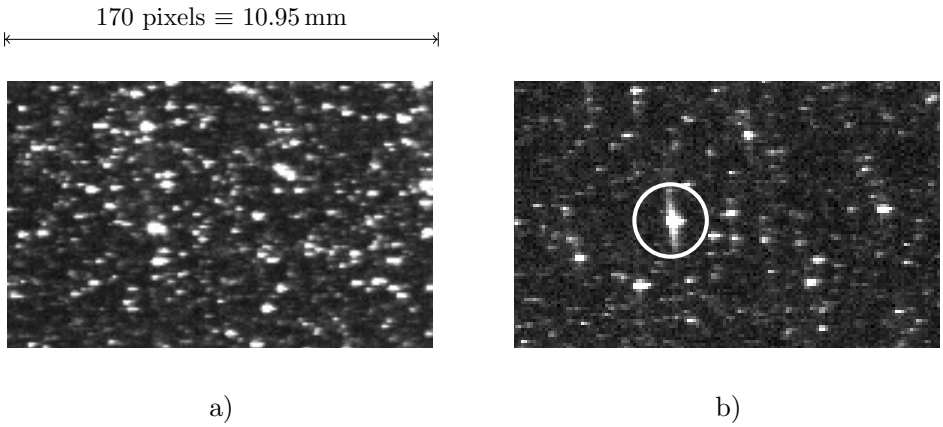


Figure 3.25.: Close up views of seeding areas with a) high and low intensity particles. b) shows Glare effects which are caused by 'non-spherical' particles.

shows the variation of particle shape and size that can occur within the frames whilst maintaining high quality correlations. For the raw image presented in figure 3.21 the average particle size was 2 × 2 pixels, with an average correlation coefficient of 0.8, a standard deviation of 0.247 pixels which all contribute to the quality of the PIV results.

The chosen value of $dt = 1.69\,\mu$s was driven by the high velocities present in the supersonic flow. In the case of a transonic flow where there is a significant and sudden change in velocity, the smaller Δt must be used. The shortest time difference between frames on the Phantom v641 camera is quoted at $dt_{min} \sim 1\,\mu$s however in practice the actual value was found to slightly higher. The two distinct velocities upstream and downstream of the shockwave have been known to cause problems when it comes to the processing of transonic PIV images. For comparison, the optimal dt for the subsonic portion downstream of the shock, $M \approx 0.72$ is approximately twice as long at $dt = 3.29\,\mu$s. This illustrates the difference surrounding the shock region which can subtly be identified in the plot of correlation coefficients shown in figure 3.26 where the PIV correlation values are much lower in the region of the bifurcated shock. The location of these poor cross-correlation values is very similar to the expected shock structure.

A Thorlabs DET10A/M light sensor was used to accurately quantify the delays experienced between the laser trigger and the laser response. The light sensor is capable of picking up changes in light intensity between 200-1100 nm and 1 ns rise times making it possible to capture both laser pulses which are milliseconds apart. The results of the delay test are presented in figure 3.27. A similar process was carried out for the second

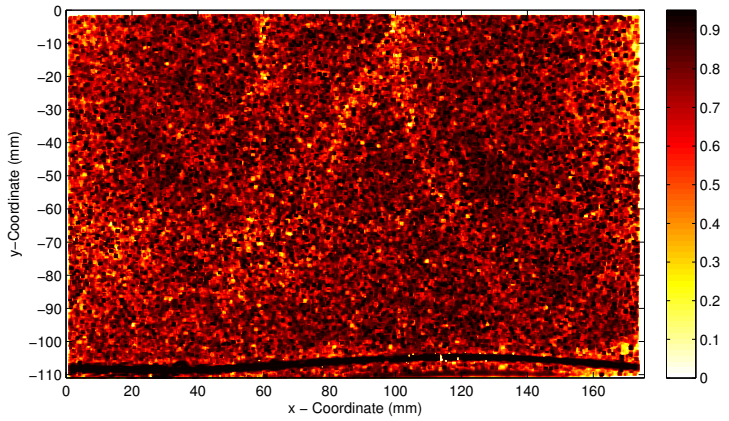


Figure 3.26.: Correlation coefficients for each interrogation window from a single image pair taken from a plate length 200 mm, t=0.6 mm subject to Mach 1.4 flow. Field average = 0.79.

laser pulse in order to find the laser build up time so that an accurate offset could be used. These offsets measured from the working section incorporate all errors and delays across the optical system.

Measuring the time delays proved valuable with regards to the overall timing of the system and accuracy of the results. It can be seen that when the dt value between frames is small, the light of the first laser pulse can be seen in both frames. Figure 3.28 illustrates the timing procedure and the small timing differences that this method aims to eradicate. The double frame, double pulse technique is vital for the flow velocities of most transonic flows in order to capitalise upon the small straddle time, dt of the camera.

The sampling frequency S_f in figure 3.28 was selected based upon the high-speed Schlieren imaging technique outlined in the previous section. Through extracting the shock position the frequency of the large-scale shock motion of flow over a flexible plate is calculated. The sampling frequency of the PIV was set to 700 Hz. The double frame images which were positioned a time $dt = 1.6\,\mu$s apart which meant that 2732 images filled the 32GB buffer representing 3.9 seconds of realtime flow. The image recording was triggered once the shock passed the start of the plate. The trigger is a pressure tapping on the opposite wall which was monitored for a drop in pressure to signify supersonic flow above the plate section. The position of the shock was free to move with the oscillations of the plate as introduced by the plate dynamics investigations. This allowed for the shock structure in the FSI to be captured in the images during the

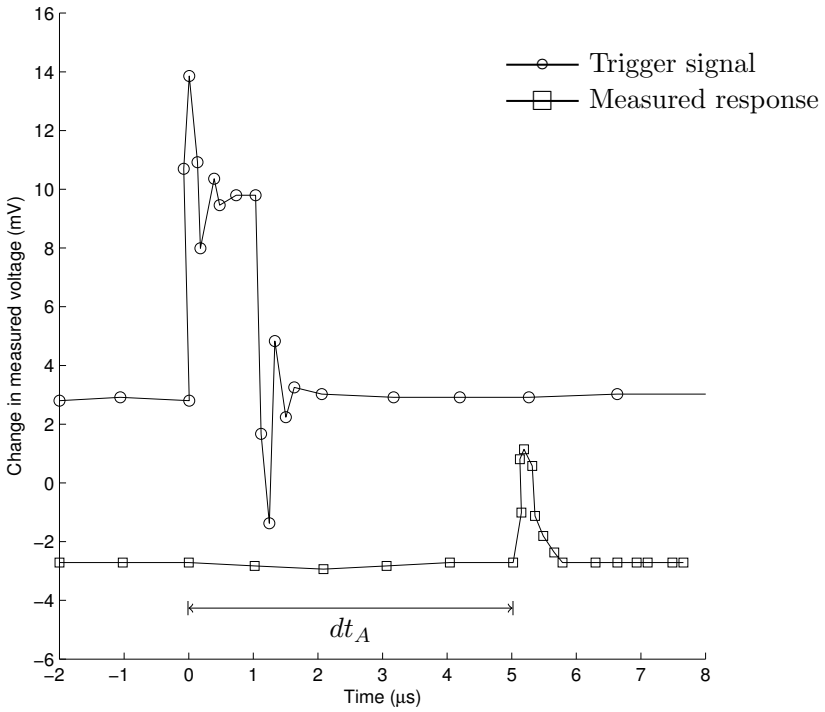


Figure 3.27.: Oscilloscope readout with zero timing offset and laser pulse.

PIV acquisition process. The initial location of the shock was set by the total pressure ratio across the tunnel working section and this was kept constant throughout each run to minimise any control-valve-induced oscillations of the shock.

Image Processing

The image processing stage of PIV aims to present the best quality images to the correlation algorithms. Whilst high-quality raw images are preferential, there are a number of techniques available that can further improve the suitability of the images.

In order to highlight the quality of the raw data captured, the images and subsequent velocity fields are only subject to a spatial calibration. This is a spatial adjustment for any misalignment between the camera image plane and the measurement plane. This is conducted using a known calibration grid of 5 mm circles placed precisely at the centreline of the wind tunnel. An image of this pattern was taken and the experimental setup calibrated for the position of the camera plane with respect to the wind tunnel.

The PIV algorithm used was a standard multi-pass cross-correlation approach with

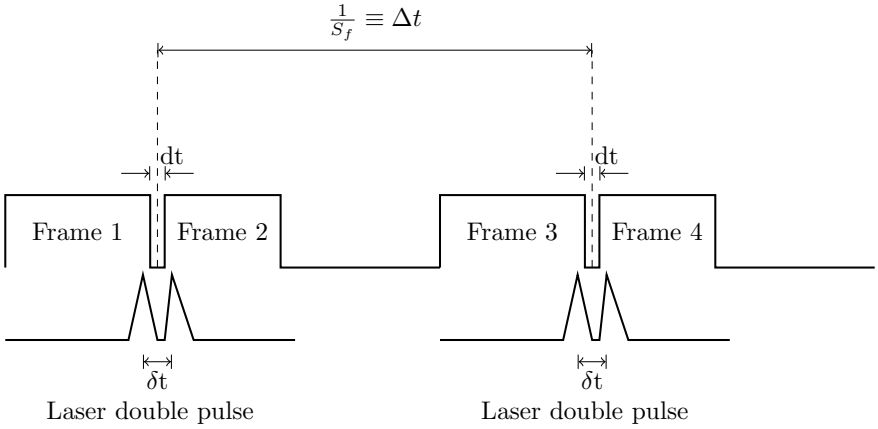


Figure 3.28.: Schematic illustrating the timings associated with PIV capture

decreasing window sizes. The process of multi pass interrogation aims to increase the signal to noise ratio of the correlation peak and reduce uncertainty in the estimated displacement. It achieves this by introducing a window offset to cater for instances where particles move between windows. As the windows are overlapped, the number of these lost particles between frames decreases hence increasing signal to noise ratio. This can be countered by the addition of a spatial overlap and is often computed multiple times for each window size.

The high quality raw images allowed for window sizes of 24 × 24 pixels providing vector spacing of 0.417 mm with 50% overlap with some images capable of resolving accurate vectors down to window sizes of 16 × 16 pixels with vectors every 0.274 mm. For the spatial resolution required for this study this vector resolution was more than adequate to provide an insight into the large scale flow structure. The dynamic spatial range (DSR) is

$$\mathrm{DSR} = \frac{l_x}{\Delta x_{p,max}} \tag{3.6}$$

where l_x is the linear dimension of the field of view, $\Delta x_{p,max}$ is the maximum measurable displacement within an interrogation window, 0.25× window size [Westerweel et al., 2013].
And Dynamic velocity range (DVR) is

$$\mathrm{DVR} = \frac{U_{max}}{\sigma_u} = \frac{M_0 \Delta x_{p,max}}{c_\tau d_\tau} \tag{3.7}$$

Study type	Re_θ	l_x	DSR	DVR	DSR × DVR
Pipe flow (stereo-PIV)	5300	40 mm	126	65	8148
Jet flow (Planar-PIV)	1000	100 mm	114	74	8475
Pipe flow (Stereo-PIV)	10000	40 mm	126	120	15097
Turb. BL (Planar-PIV)	2370	151 mm	273	91	25000
Adaptive SCB (Planar-PIV)	~ 8000	160 mm	99	77	7623

Table 3.7.: Comparison of dynamic spatial and velocity ranges between a selection of PIV studies highlighted by Westerweel et al. [2013] across a range of Re_θ.

where U_{max} is the maximum measurable velocity within the interrogation domain. $U_{max} = \Delta x_{p,max}/\mathrm{dt}$. $c_\tau d_\tau$ is the minimum resolvable difference in the particle image displacement for a given particle image diameter d_τ.

These are useful performance indicators when it comes to the scope of the analysis that can be conducted with the experimental setup. Presented in table 3.6 the DSR = 98.92 and the DVR = 77.42. These parameters aim to quantify the range of vectors that are possible from the optical setup and window size with a given particle size. Typically those studies that focus upon the free stream with very large FOV will have a high DSR whereas those focussing upon boundary layer turbulence have a higher DVR [Adrian and Westerweel, 2011]. Westerweel et al. [2013] summarised a collection of PIV studies with varying Reynolds numbers and field of view of which a few are included in table 3.7 to show how this study compares. This PIV setup is a shows a very good balance between the dynamic spatial and velocity ranges and the size of the field of view compared to the studies shortlisted by Westerweel et al. [2013].

Figure 3.26 shows an example of the correlation that is computed between two frames at a given sampling time. Even with the low signal to noise ratio typical of PIV the correlation coefficients show a mean equal to 0.79. Of particular note are the low correlation values in the centre of the image which are of a similar shape to the expected shock structure. These are due to the large velocity gradients across the shock that not only cause issues for the interrogation windows that cover the shock and have to assign a single velocity for supersonic and subsonic sections but also the optical capture of the particles as the scattered light passes through strong density gradients. Due to the inherent non-uniformities in seeding high speed flow, erroneous vectors in the calculated velocity field. The number of erroneous vectors can be reduced by the introduction of post processing. One effective technique is to place an allowable range on the vector field. This is particularly useful where the flow is predominantly in one direction and there is

little chance of reversed flow such as in the free stream of a supersonic inflow. After some trial and error, the range of permissible streamwise velocities is set to $300 \pm 200\,\mathrm{m/s}$ and vertical velocities $0 \pm 30\,\mathrm{m/s}$. This provided a check condition for the calculated velocity values for each interrogation window and reduced the magnitude of erroneous data points.

The statistical nature of PIV and the capabilities of equipment used means velocity fields can be temporally averaged to reduce the effects caused by outlying data. Whilst the high frequency information is then lost, the low-frequency data can still be of use for detecting large-scale shock movement and overall mean flow structures such as the flow curvature caused by the addition of an adaptive SCB.

Application to Adaptive SCB

The application of PIV to adaptive SCB has been introduced briefly in the preceding sections and the fluid-structure interaction causes many complications when compared to static surface PIV. The first obstacle is the curvature of the plate when subject to the aerodynamic loading. Very close to the surface, a thick band of intense reflected light exists where particles cannot be distinguished from the background and poor correlations are obtained. Figure 3.29 shows a zoomed view of this near surface region highlighting these issues. These regions of high intensity light are processed by the cross-correlation algorithm and may result in velocities that are not physical and are attributed to be an artefact of the reflected light. A pre-processing mask below the plate section would have been ideal however due to the transient plate deformation, applying an individual mask for each image would require a complex multi-pass algorithm to be developed that is beyond the scope of this work. Instead, a post-processing mask was applied to the fields in order to eliminate the effect of particles below the average plate position during the sample period. This goes someway towards eliminating the false results that appear below the plate.

The very intense regions of light scattered by the plate geometry are also beneficial as they can be utilised to provide information regarding the transient deformation of the plate. The thickness of the laser sheet on the image can be extracted from the raw images to provide an indication as to the movement of the plate subject to shock loading. Using the centreline of the intense region and taking this as the centreline of the plate, the plate can be tracked in each image. The validity of this technique assumes that the power distribution within the laser beam is focussed in the centre of the light sheet in the plane parallel to the floor and ceiling. This becomes a powerful tool for the

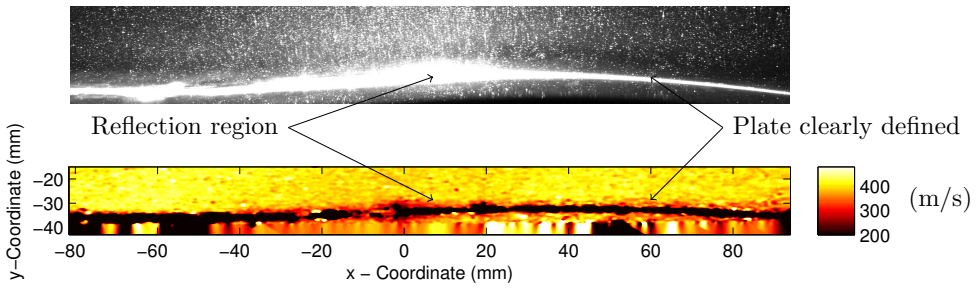


Figure 3.29.: Zoomed in view in plate region of a) raw image. b) Instantaneous vector field using just 1 image pair.

analysis of the fluid structure interaction between the shock and the plate.

3.3. Summary of Methods

The methods outlined in this section have introduced the techniques that will be used to design and test adaptive SCB. The initial sizing of the devices took inspiration from existing static SCB dimensions as well as from the field of panel flutter which helped clarify the role of aero-structural coupling in to the design.

An initial 2D aerodynamic model combined with a finite element analysis of the plate was implemented to complement the knowledge generated by Dowell [1966]. The results from this initial study suggested that the desired deformation heights to match static SCB would be possible with a plate with two built-in ends and two free sides. The stresses within the material would be high but below the yield limit of AL-7075-T6. The model also considered quasi-steady shock movement to include a varying shock position in the analysis to highlight performance under an unsteady load.

The flexibility of the system is found to vary significantly with cavity pressure which is an important variable, not only to the static shape of the plate under loading but also the dynamic response under the aerodynamic load due to the stiffening of the plate. The findings showed that cavity pressure is as influential as plate thickness and length when it comes to varying the stiffness of the plate.

Extending the aerodynamic solver of the 1D model to a coupled 2D aero-structural solver allows for a more realistic calculation of the aerodynamic flow field. It provides a 2D viscous solution to the aerodynamics due to the surface deformation. The quasi-steady approach undertaken allows for a wide variety of adaptive SCB setups to be evaluated whilst varying the most influential parameters.

The transient FSI of the adaptive SCB is to be examined using the experimental techniques outlined in this chapter. Schlieren Imaging and PIV will be used to provide valuable information regarding the shock structure and plate deformation. The experiments are performed in the Imperial College Supersonic Wind Tunnel in which a Mach 1.4 nozzle had to be designed in order to provide a suitable flow field to test SCB.

Simultaneous data on shock structure and plate deformation is obtainable from Schlieren imaging and PIV and this will provide useful data regarding the FSI for the duration of each wind tunnel test. The ability to capture the entire wind tunnel test with Schlieren Imaging allows for a large field of view to be recorded over the duration of each test. The parameters for the PIV study were selected as a compromise between attempting to match the Schlieren field of view and maintaining a suitable timing between images to produce reliable velocity vectors.

All of these methods are used in the following three chapters to evaluate the performance of adaptive SCB in a transonic environment to demonstrate the potential of such a device.

4. Flexible Plates for Adaptive SCB

The performance of adaptive SCB is evaluated in this chapter using the techniques described previously to record the FSI surrounding the design concept. The flexibility of the plate is examined in detail drawing upon both the numerical and experimental techniques previously introduced. The aim is to design a passive device that is able to bifurcate the shock under typical aerodynamic loading. The investigation utilises the coupled aero-structural solver for quasi-steady analysis upon aerofoils and the experimental setup for time dependent analyses.

4.1. The Performance of Flexible Plate Based Adaptive SCB upon Aerofoils

The starting point for quantifying the performance of static SCB was their effect upon the lift and drag of transonic aerofoils in the EUROSHOCK project. Stanewsky et al. [1997] evaluated the performance alongside other passive and active flow control devices. In order to verify the potential of adaptive SCB, a similar approach is taken here.

Utilising the aero-structural solver described in section 3.1.9 the analysis of three key scenarios is presented. These loading scenarios represent three discrete cavity pressures to illustrate the effects of this influential variable upon the plate geometry and the flow field.

4.1.1. Integration into an Aerofoil

The flexible plate region is placed beneath the shockwave of the clean aerofoil and is 0.2 m in length. This was chosen from the wealth of existing static SCB studies with the additional influence of panel flutter design practices suggested by Dowell [1972]. When positioned on an aerofoil, the SCB commences at 0.43c and finishes at 0.63c. Under zero aerodynamic loading the geometry of the plate is equivalent to that of the clean aerofoil. These locations were selected based upon the shock location on the RAE2822 aerofoil at the test flight conditions (0.49c).

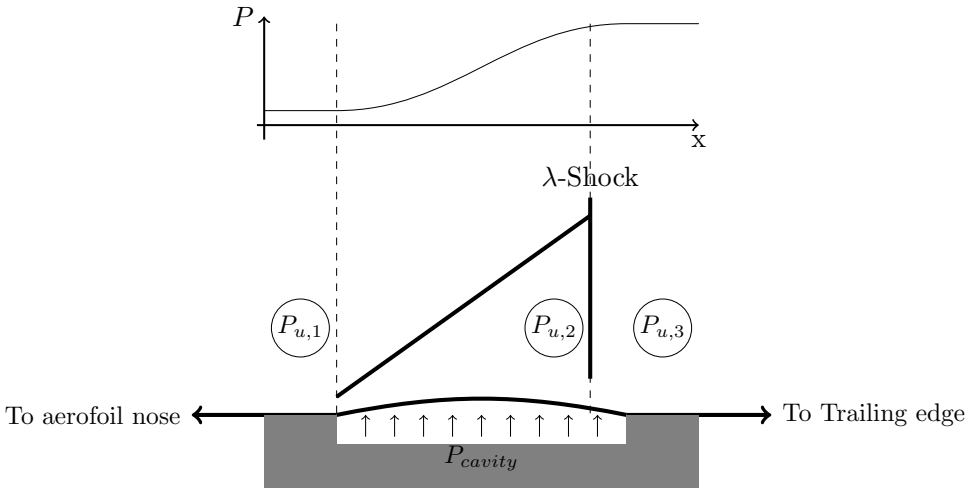


Figure 4.1.: Typical pressure forces acting upon flexible plate.

Passive case	1	2	3
Cavity Pressure	$\min(P_u)$	$\text{mean}(P_u)$	$\max(P_u)$

Table 4.1.: A summary of the three discrete cavity pressure loading cases.

The three loading scenarios presented here show the effect of cavity pressure with the estimated pressure magnitudes shown in figure 4.1 and table 4.1. The upper surface pressures are initialised by the pressure field around the clean aerofoil and represent the pressure loading applied to the first flow field computation in the first aeroelastic iteration. The subsequent displacements are incorporated into the CFD mesh generation algorithm and subsequent aeroelastic iterations. The plate response is discussed for these three discrete cavity pressures in the following sections.

Plate Response

Table 4.1 shows the cavity pressure of the three cases presented here, with the upper surface pressure equal to

$$P = \frac{1}{l_b}\left[\int_0^{x_{shock}} P_{u,2} \quad \mathrm{dx} + \int_{x_{shock}}^{l_b} P_{u,3} \quad \mathrm{dx}\right] \tag{4.1}$$

where P_u, i is the index of the location defined in figure 4.1.

For case 1 in table 4.1 the cavity is set to equal the minimum upper surface pressure

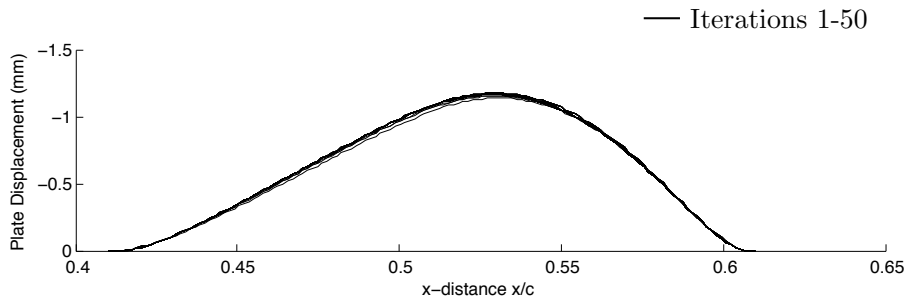


Figure 4.2.: Aero-structural response of flexible plate subject to shock loading. The y-axis has been amplified significantly (5×) to show the small difference between each of the aeroelastic iterations.

where the cavity is connected to the upstream flow. Case 2 has a cavity pressure equal to a mean value of the upstream and downstream shock pressures. This would require some control and management of the pressure field. Case 3 represents a high cavity pressure case with the pressure set to the maximum upper surface pressure which would be achieved by bleeding high pressure downstream of the shock and plate interaction in to the cavity.

Each of these conditions are introduced to the aero-structural solver. The aero-structural solver computes the resultant pressure field which is then mapped to the FEA model and the subsequent displacements are extracted. The aero-structural solver is run for 50 aero-elastic iterations and the plate response is monitored.

The plate geometry for case 1 can be seen in figure 4.2 to vary small amounts between aeroelastic iterations. The other cases exhibited similar variations and the geometries are presented in figure 4.5. For case 1 the maximum displacement from the clean aerofoil oscillated around a value of -1.17 mm (1.17%c). For case 2, the mean value for maximum deflection was 2 mm (2%c) at an average location of 0.528c ($0.49l_b$) with very little variation between aero-elastic iterations. For case 3, the mean plate displacement was 4 mm (4.1%c) with an average crest location of 0.53c ($0.5l_b$). From this quasi-steady analysis, the variation of plate crest height and crest position is small.

4.1.2. Aerodynamic Response

The aerodynamic response is dictated by the general deformation of the plate with the relatively small oscillations between each iteration having little effect upon the large scale flow features. As such, the location of the main normal shock and the shock structure do not vary significantly between aeroelastic iterations. The small variation is shown in figure 4.3 which presents the effect of the plate oscillations on the flow field for the lowest cavity pressure case 1. A slight increase in maximum pre-shock Mach number was seen which was attributed to a depression of the plate surface. This caused the flow to accelerate further over the resulting convex curvature. The higher Mach number had a lower pressure on the upper surface which resulted in a slight rise of the upstream portion of the plate for the next iteration.

Changing the cavity pressure had a significant effect upon the response of the plate and the subsequent deformation. Figure 4.4b shows how a cavity pressure equal to the mean of the upper surface pressures, loading case 2, is able to maintain a more rigid structure and deform into the flow which triggered the bifurcation of the shockwave. The maximum Mach number in the shock region in case 2 is 1.223 which indicates the successful bifurcation and further reinforces the effects of cavity pressure. The bifurcation is highlighted by the contours in figure 4.4b.

Increasing the cavity pressure further results in an increasingly stiffer plate that deforms further into the flow as a result of the increased pressure differential across the plate. The deformation of the plate is entirely positive (into the flow field) causing an oblique shock to form at the start of the flexible plate section as indicated by the contours in figure 4.4c. The detrimental aspect of this bifurcation was that the post-shock flow continued to accelerate over the crest resulting in another supersonic region on the rear surface of the SCB. This acceleration is due to the increased curvature around the crest region which also made it harder for the flow to remain attached as it passed over the rear surface of the plate. This can be seen in the near-wall region of figure 4.4c.

4.1.3. Aero-structural Response

The three key cavity pressure scenarios have highlighted the key difference between static and adaptive SCB. By varying the pressure difference across the plate, three distinct plate geometries were created that resulted in three distinct flow fields. A cavity pressure equal to the average of the upper surface pressure proved to be least detrimental in terms of shock structure and reacceleration regions on the rear surface. A low cavity pressure resulted in local acceleration and a stronger shock whereas a higher

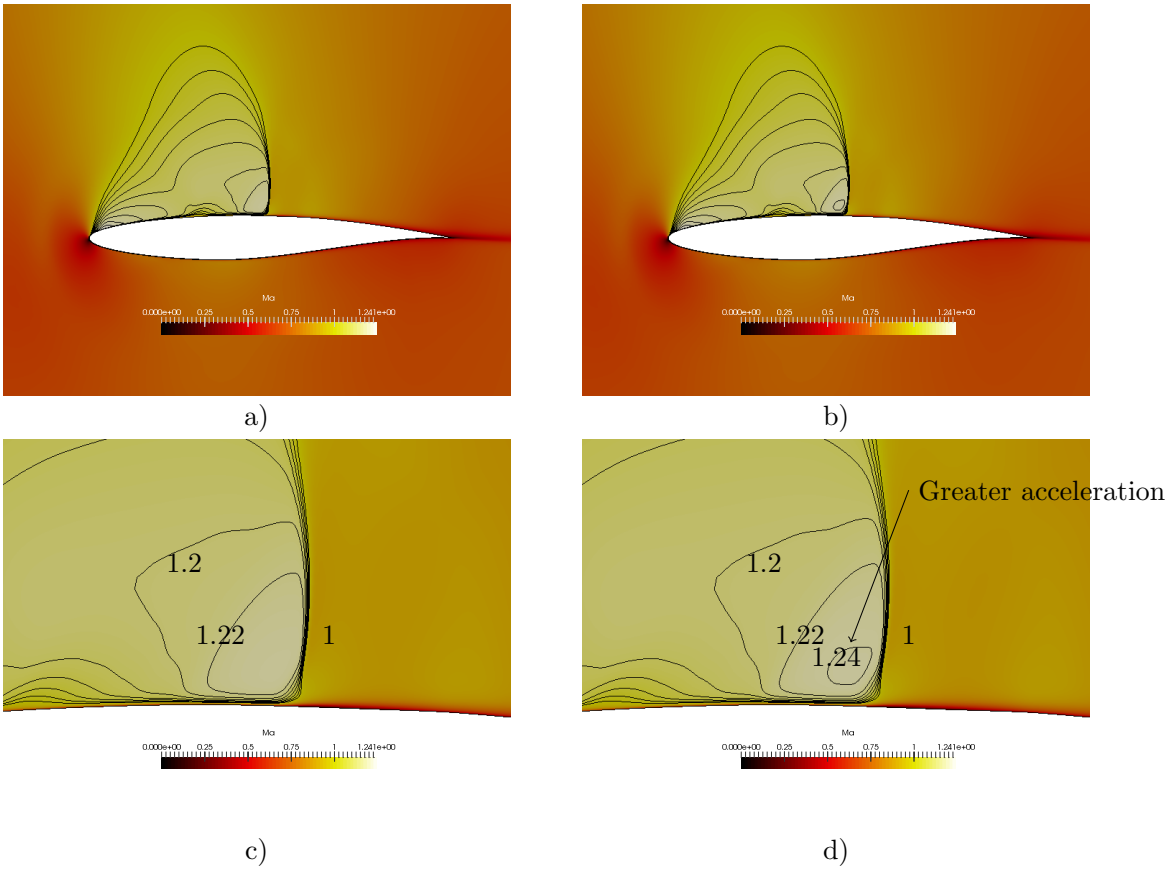


Figure 4.3.: Mach contours and fields for lower (a,c) and upper (b,d) bounds of crest displacement, iterations 2 and 3 respectively.

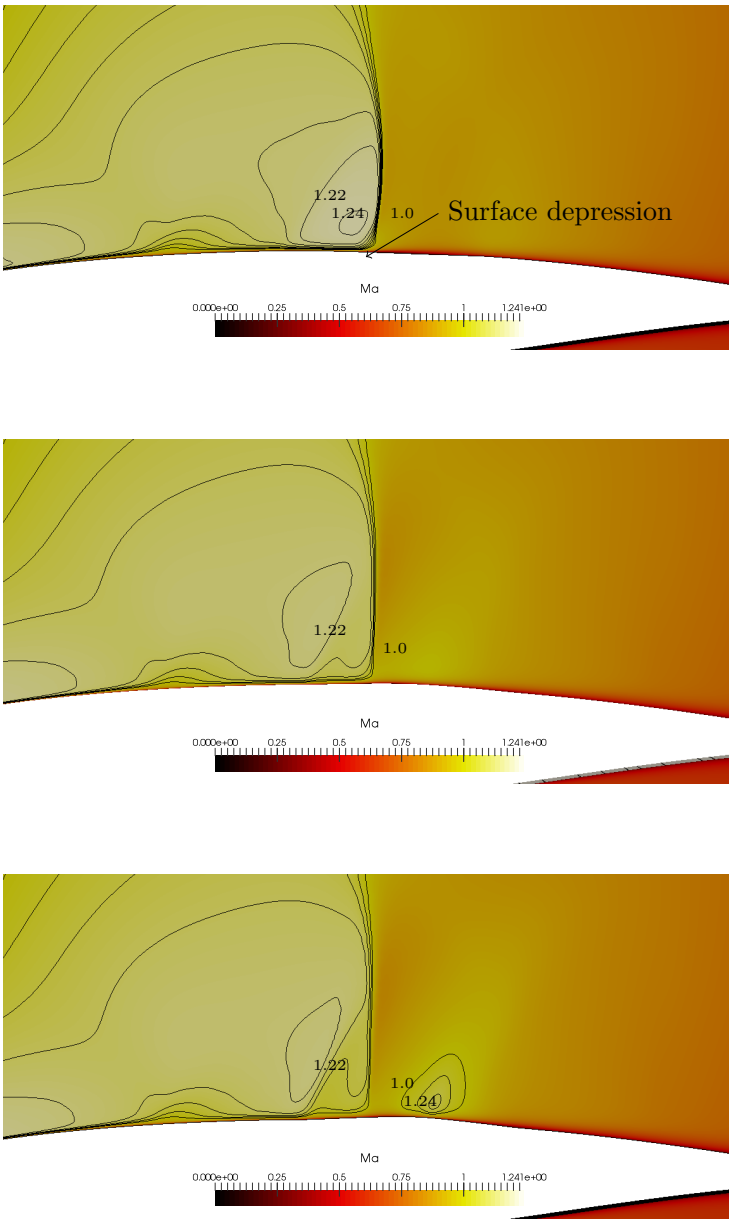


Figure 4.4.: Mach contours and fields for the three cavity pressures tested. a) Low cavity pressure, $P_c = \min(P_u)$. b) Mid cavity pressure, $P_c = \text{mean}(P_u)$. c) High cavity pressure case, $P_c = \max(P_u)$

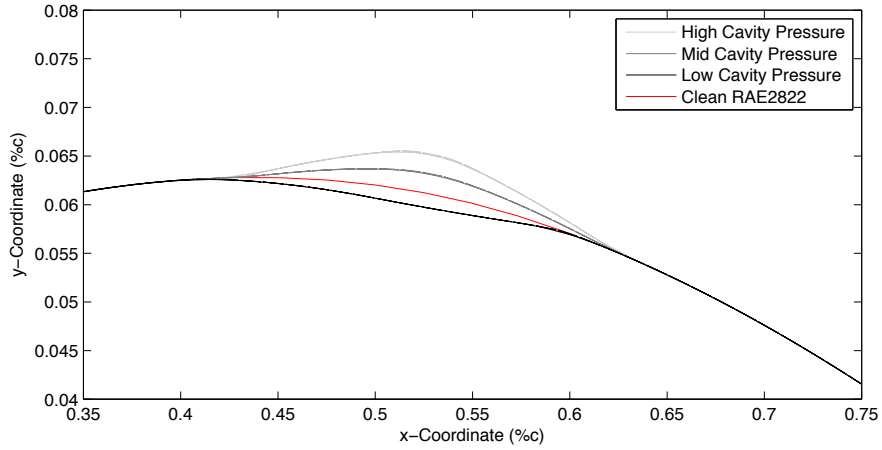


Figure 4.5.: Aerofoil surface geometries after pressure loading for the three cavity pressures tested and the clean RAE2822 aerofoil.

cavity pressure bifurcated the shock but caused local re-acceleration downstream of the shock.

It is these detrimental effects that feature close to the surface that require a more targeted approach to mitigate them. One such approach is to test the flexible plates in a blowdown supersonic wind tunnel which focusses on the control region and allows for a variety of experimental techniques to be used to analyse the FSI between the transonic flow and the flexible plate.

4.2. Time Averaged Experimental Response

The aero-structural solver is a powerful tool to quickly test the effects of varying parameters that contribute to the performance of adaptive SCB. Changing the cavity pressure significantly affected the flow with a mixture of positive and negative effects. It was noticed however that the effects were limited to the vicinity of the flexible plate. An approach that has been undertaken by other researchers including Ogawa et al. [2008] and Colliss and Babinsky [2012] is to focus the region of study to the shock region and place the SCB in a blowdown supersonic wind tunnel which allows for a wide variety of experimental techniques to be used to investigate the flow field.

A wind tunnel model was constructed to test and evaluate the physical response of the plate. The flexible plate based design pushes adaptive SCB towards a passive control

device that has shown potential for aerodynamic control in the previous section. The Mach 1.4 nozzle sections designed as presented in appendix A were also installed. Tests were conducted with a clean, rigid-walled working section in order to determine the pressure ratio to place a normal shock in a suitable position. A tunnel pressure ratio of $P_{0,sc}/P_{atm} = 1.286$ was chosen and used to evaluate the four test cases in table 3.4.

From the three cavity pressure scenarios in the previous section, traditional SCB shapes were generated when the cavity pressure was between the minimum and maximum values of the upper surface pressure. This is the loading case examined in these tunnel tests. All experimental results will feature a cavity pressure that is between the minimum and maximum pressures over the upper surface of the plate. This was achieved by controlling the flow of air around the edges of the plate between the cavity and the freestream.

The ability to deform to suitable heights relies upon the stiffness of the entire plate system which is determined by overall length and the material properties. The thickness of the plate has also been shown previously to have an effect upon the response of the system when subject to a constant pressure (chapter 3). Two of the smaller thickness values that showed potential have been used in the experimental test rig which provides a flexibility/stiffness comparison to be analysed in tandem with the effects of length. The test cases investigated are presented in table 3.4 in chapter 3.

4.2.1. Aerodynamic Response

The typical shock structure representative of the time averaged response of a flexible plate subject to shock loading is presented in figure 4.6. These images indicate the global shock structures that develop during a 30 second run. There are many similarities between each of the shock structures in figure 4.6. The position of the main normal shock at the top of each of the images is the same for each of the images presented.

The second common feature is the development of an oblique shock at the front of each of the plate sections. This is the result of the plate deforming due to a pressure load similar to that illustrated in figure 4.1 and discussed previously in chapter 3. It forms the start of the complex fluid structure interaction that takes place. The FSI illustrated in figure 4.7 builds upon the cycle presented earlier in figure 3.3 through the addition of cavity pressure.

The global shock structure and the associated pressure distribution was evaluated around the time averaged plate geometry. The pressure differential across the plate caused the plate to rise up into the flow and triggered pressure waves as the supersonic

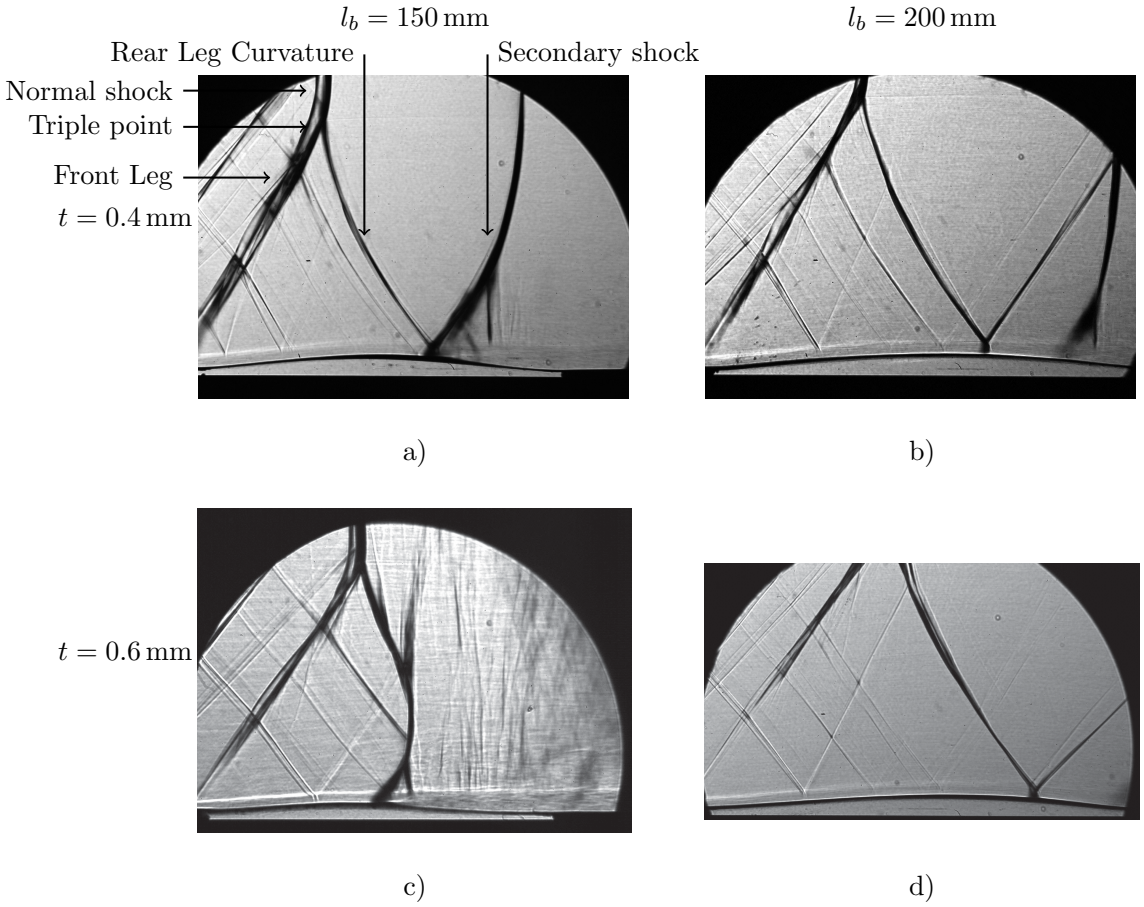


Figure 4.6.: Schlieren images showing the shock structure for plates of varying length and thickness. a) $l_b = 150\,\mathrm{mm}$, $t = 0.4\,\mathrm{mm}$. b) $l_b = 200\,\mathrm{mm}$, $t = 0.4\,\mathrm{mm}$. c) $l_b = 150\,\mathrm{mm}$, $t = 0.6\,\mathrm{mm}$. d) $l_b = 200\,\mathrm{mm}$, $t = 0.6\,\mathrm{mm}$.

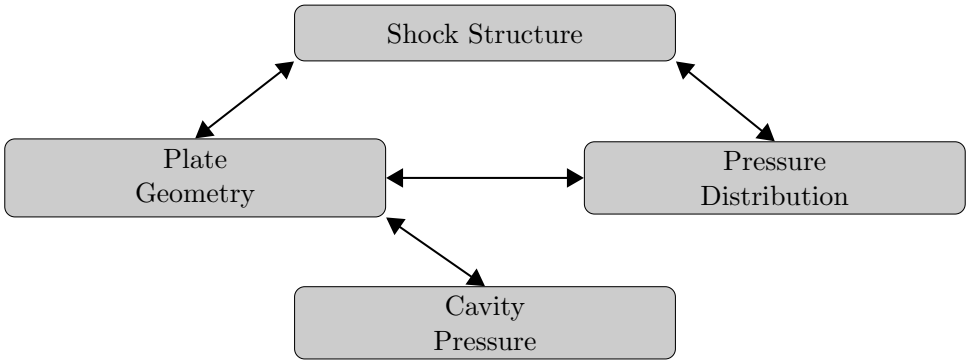


Figure 4.7.: Schematic diagram illustrating the interdependencies governing the flexible plates FSI.

flow responded to the presence of a deflection at the wall. These pressure waves emanate from the region around the beginning of the plate and coalesce to form the oblique shockwaves visible in each of the images in figure 4.6.

The oblique shock structure intersected with the main normal shockwave at the triple point. Below this point, a weakened rear leg structure exists. This reduction in strength is caused by the deceleration of the flow across the oblique shock prior to the rear leg. The rear leg is one of the key differences between each of the test cases and provides a valuable insight as to the characteristics of the flow over the SCB.

The rear legs in figures 4.6a, 4.6b and 4.6d that form below the triple point are significantly curved and deviates from the vertical rear leg in the inviscid 2D flow model previously described. The difference is thought to be a result of the continuously changing plate curvature. As the flow becomes aware of the plate deflection, pressure waves begin to form as the plate surface bends during the aerodynamic loading. At the crest of the plate, the curvature becomes convex as the plate turns towards the downstream constraint. In between these two regions, the sign of the plate curvature changes and as a result there are many incremental turning points that change the direction of the supersonic flow. When a supersonic flow is subject to convex curvature, expansion waves form. The smooth curvature of the plate leads to a continuous fan of these expansion waves which influences the flow field away from the surface causing local changes in pressure which to an extent, the direction of the flow. It is this combination of variations in local pressure and flow curvature between the legs of the λ-shock that lead to variations in the curvature and position of the rear shock leg

The effect of plate curvature upon the rear leg shock structure was also apparent in

the shortest, thickest plate tested (figure 4.6, l_b = 150 mm, t = 0.6 mm) where there was a similar region of rear leg curvature just below the triple point in figure 4.6c. It is this structure that is also seen in the equivalent aerofoil study presented in figure 4.5b. There are small differences in the main rear leg structure immediately below the triple point courtesy of the shock being positioned slightly more downstream of the crest in figure 4.6c. However the shock structure of this rear leg is notably different with the flow field downstream of the rear leg appears to be less curved in comparison to the other test cases. It is suggested that the resultant curvature of the flow is directly affected by the curvature of the plate and which is dictated by the stiffness of the plate. Being shorter and thicker, the plate does not deform to the same levels as the longer, thinner, more flexible plates. The following section explores this further.

4.2.2. Plate Response

Plate curvature is directly related to the deflection of the plate which is caused by the aerodynamic loading. Assuming steady pressure loading across the plate, the level of deflection is dictated by the stiffness of the system. The flexural stiffness, D presented in table 3.4, is a measure of the rigidity of the system per unit width and represents a limiting factor of the displacement for a given loading.

A lower flexural stiffness allows a greater displacement for a given loading. For a higher displacement, the level of curvature needs to increase around the crest region in order to maintain a continuous surface bound by the fixed conditions at both ends. The difference in vertical displacement between the test cases can be observed visually in figures 4.6a and 4.6c; the variation in thickness causes a 34% difference in maximum plate displacement. The displacements presented in figure 4.8 show $\delta_{\max}$ = 4.8 mm for the l_b = 150 mm t = 0.4 mm test case and $\delta_{\max}$ =3.6 mm for the t = 0.6 mm thick plate. The vertical scale is enlarged for clarity.

Although care has been taken to present results from a given normal shock position there is a difference in the loading that the two plates are subject to however this is a direct result of the plate stiffness. The comparison in figure 4.8 is between the main normal shock location and the amount of vertical deflection, with the shock structure being a function of the plate deformation.

The values for plate displacement are extracted from the Schlieren images and allow for the plate deflection to be measured alongside the aerodynamic loading for the entirety of the wind tunnel operation. The pixel by pixel tracking of the plate in the Schlieren image gives a very high resolution around the plate with 1700 pixels across the 150 mm

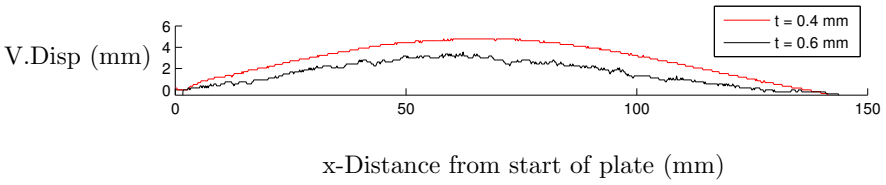


Figure 4.8.: Plate deformation extracted from figures 4.6a & 4.6c $l_b = 150\,\text{mm}$, $t = 0.4\,\text{mm}$ $l_b = 150\,\text{mm}$, $t = 0.6\,\text{mm}$.

length and 6-9 pixels covering the thickness of the plate. The variation of pixel density across the thickness is due to the optical distortion present in the surrounding flow field. It is especially apparent where the near-wall density gradients are particularly large such as upstream of and around the shock structure. This enables very accurate tracking of the out-of-plane displacement of the plate. As the Schlieren imaging process averages across the collimated light, the span-wise variation in plate deformation is not captured in the same way that information about the span-wise variation in the shockwave is lost. Despite this limitation, Schlieren imaging does provide an efficient method to give an excellent insight into the FSI of the plate response and the shock structure simultaneously.

In order to quantify the effects of span-wise deformation, the thickness of the plate is compared between flow-off and flow-on cases. There is little variation between the two cases based upon the reference point at $0.66l_b$ where the thickness is found to be 7 pixels and 9 pixels for flow off and on conditions respectively. There is however a significant discrepancy in plate thickness at the front of the plate, 8 pixels versus 16 pixels. The cause of this is the optical distortion created by the density gradients close to the wall. In practice, the supersonic flow creates an optical effect that appears to raise the upper surface of the plate. In order to account for this optical effect, an average thickness for the plate is calculated for the specific plate in the no-flow case and this value is then added to the lower surface of the plate. Tracking the lower surface where the flow is stagnant inside the cavity and no density gradients exist eliminates any potential source of error when distinguishing between the plate and the shock structure occurring on the upper surface.

The geometries generated by the aerodynamic loading and the cavity pressure are of similar heights to static SCB and show that the size and material of the plate are well suited to passive control. The plates also return to the initial non-deformed geometry with no visual deformations on the plate surface. This result is vital for the feasibility

of adaptive SCB as it shows the design is structurally viable given the interaction with the aerodynamic load.

4.2.3. Fluid-Structure Interaction

The FSI between the plate and the shockwave is key to the overall performance of adaptive SCB. The steady state response to the shock loading is dominated by the generation of the front leg which is generated by the curvature of the plate. In order to compare between the different test cases, a single parameter for an effective surface deflection angle is calculated from the angle of the front leg in each of the Schlieren images. From these shock angles it is possible to calculate an equivalent surface deflection angle through the 2D shock relation

$$\tan(\theta_{r,eff}) = 2\cot\beta\frac{{M_1}^2\sin^2\beta - 1}{{M_1}^2(\gamma + \cos 2\beta) + 2} \tag{4.2}$$

where β is the shock angle and M_1 is the upstream Mach number taken as $M_1 = 1.4$.

Table 4.2 shows the effective (θ_{eff}) and maximum actual (θ_{plate}) surface deflection angles for each of the cases. The relationship between actual θ_{plate} and θ_{eff} is important for calculating the angle of the oblique shock which could be used to estimate the height of the triple point. It is potentially a step towards the development of an analytical model where the continuous variation of the front surface of the adaptive SCB could be represented by a single deflection angle. It also serves as an important comparison factor to be used against static 2D and static 3D SCB.

In the l_b = 150 mm t=0.6 mm test case, a maximum deflection angle of 2.7° was achieved which resulted in a shock angle of 54.0°. This would have led to an 'effective' plate deflection angle of 5.0° which is greater than the maximum physical deflection angle calculated in table 4.2 of 2.7° and shown for the representative Schlieren images in figure 4.6. It is often the case that nozzles designed via the method of characteristics with a viscous correction run slightly lower Mach numbers than designed for [McCabe, 1967]. A working section Mach number of 1.38 would result in $\theta_{eff} = 5.0$ and at Mach 1.4, $\theta_{eff} = 5.6°$ which shows the sensitivity to free stream Mach number. The viscosity of the fluid may also have affected the actual θ_{eff} as the source of the pressure waves is not a single position.

The curvature of the plate is quantifiable from Schlieren imaging with approximate shock/plate angles measured across the span of the shock. The analysis would benefit from a more quantitative method of calculating flow angles. Particle image velocimetry

Case		Shock		Plate
l_b	t	β	θ_eff	θ_{plate}
(mm)	(mm)	o	o	o
150	0.4	60.6	7.7	3.54
150	0.6	54.0	5.0	2.70
200	0.4	59.7	7.5	5.61
200	0.6	54.2	5.3	5.23

Table 4.2.: Average shock angles away from the wall derived from the Schlieren images in figure 4.6 with effective deflection angle based upon equation 4.2 and a free stream Mach number of 1.38. The average surface deflection up to the plate crest is also included.

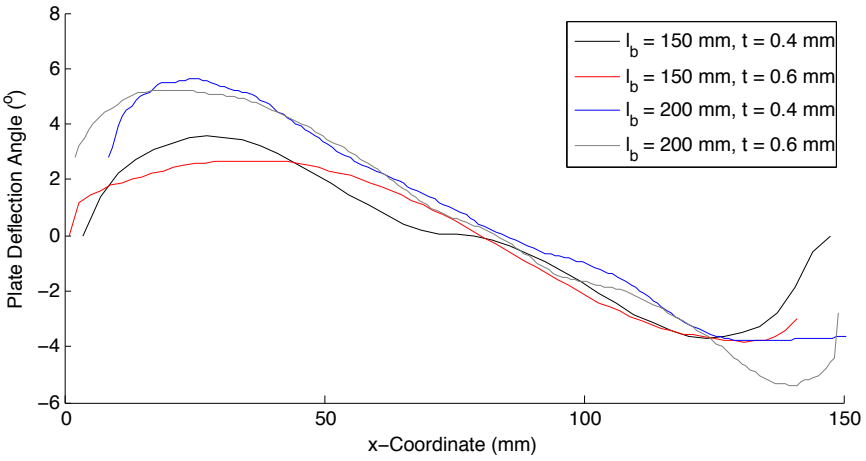


Figure 4.9.: Plate deflection angle with respect to the horizontal calculated from the Schlieren images in figure 4.6.

(PIV) was used in order to provide numerical velocity vector fields and quantify the levels of curvature within the flow. The technique provides a high resolution data field with a resolution of 0.417 mm/vector with window sizes of 24 pixels and 75% overlap.

For the $l_b = 150\,\text{mm}$ $t = 0.4\,\text{mm}$ case, a time averaged flow field is presented in figures 4.10 and 4.11 which represent the streamwise and vertical velocity fields respectively. Comparative results for the other test plate cases are presented in figure 4.12. The shock structures are consistent with the Schlieren images in figure 4.6 in particular the key features such as the curved rear leg and the formation of the front leg. The main normal shock is just out of view as a result of size restrictions of the field of view. The secondary shock structure can also be identified towards the rear of the vector field at x-coordinate 120 mm in figure 4.10.

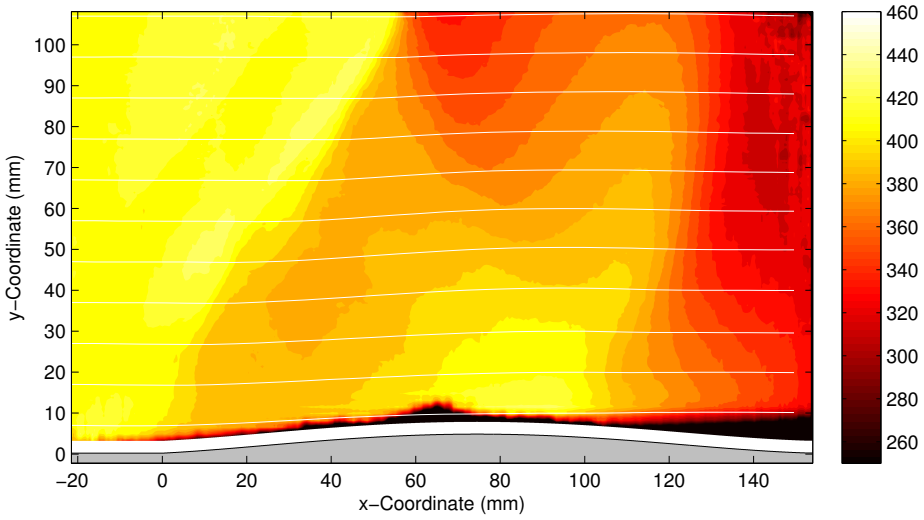


Figure 4.10.: Streamwise velocity for flexible plate $l_b = 150\,\text{mm}$ $t = 0.4\,\text{mm}$.

The plate deformations extracted from the PIV raw images were very similar to those extracted from the Schlieren images. However this technique outlined in section 3.2.3, removed any errors due to the span-wise curvature of the plate. The values represented the centreline displacement by evaluating the movement of the laser sheet. There are of course errors that propagated through with respect to the perspective of the camera and the thickness of the light sheet however these were kept to a minimum by using the mid-pixel of the intense region rather than the upper or lower bounds. The absolute value of the tracked particle was equivalent to 0.0695 mm, which was the physical size

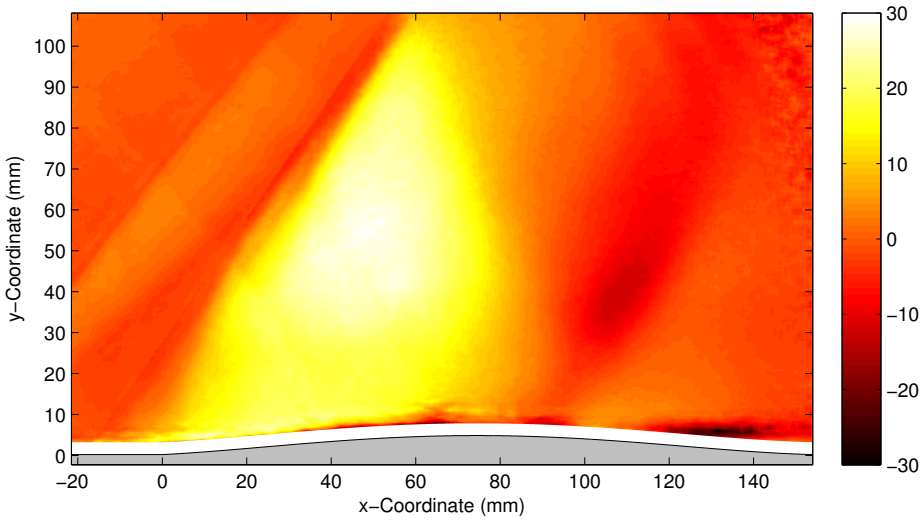


Figure 4.11.: Vertical velocity for flexible plate $l_b = 150\,\text{mm}$ $t = 0.4\,\text{mm}$

of 1 pixel in the measurement plane.

With the geometry of the plate varying very little throughout the 3.9 seconds of PIV image capture, the relationships between the time-averaged flow structure and the time-averaged plate motion can be evaluated. The effects of the plate deformation are most easily compared when viewed as deflection angles. Figure 4.13 shows the flow deflection angles and the plate surface deflection angle that can be calculated from the stream wise and vertical velocity fields generated via PIV. The flow angles have been calculated with respect to the horizontal as have the plate deflection angles. These graphs show the extent to which the plates affect the free stream flow. When there is a flexible plate such as the $l_b = 200\,\text{mm}$, $t = 0.4\,\text{mm}$ plate (figure 4.13c) the larger flexibility permits a larger deformation. This in turn increases the plate deflection angle present on the front surface which the flow has to react to.

As the stiffness of the plate is increased by either increasing the thickness to $t = 0.6\,\text{mm}$ in figure 4.13d or decreasing the length to $l_b = 150\,\text{mm}$ in figure 4.13a, the maximum deflection angles of the plate are decreased. This results in decreased flow deflection which is hypothesised to be the cause of the curvature and weakening of the rear leg and re-acceleration downstream of the plate crest.

The stiffest plate tested, $l_b = 150\,\text{mm}$, $t = 0.6\,\text{mm}$, allowed for some plate deflection into the free-stream but the material constraints limited the maximum plate deflection

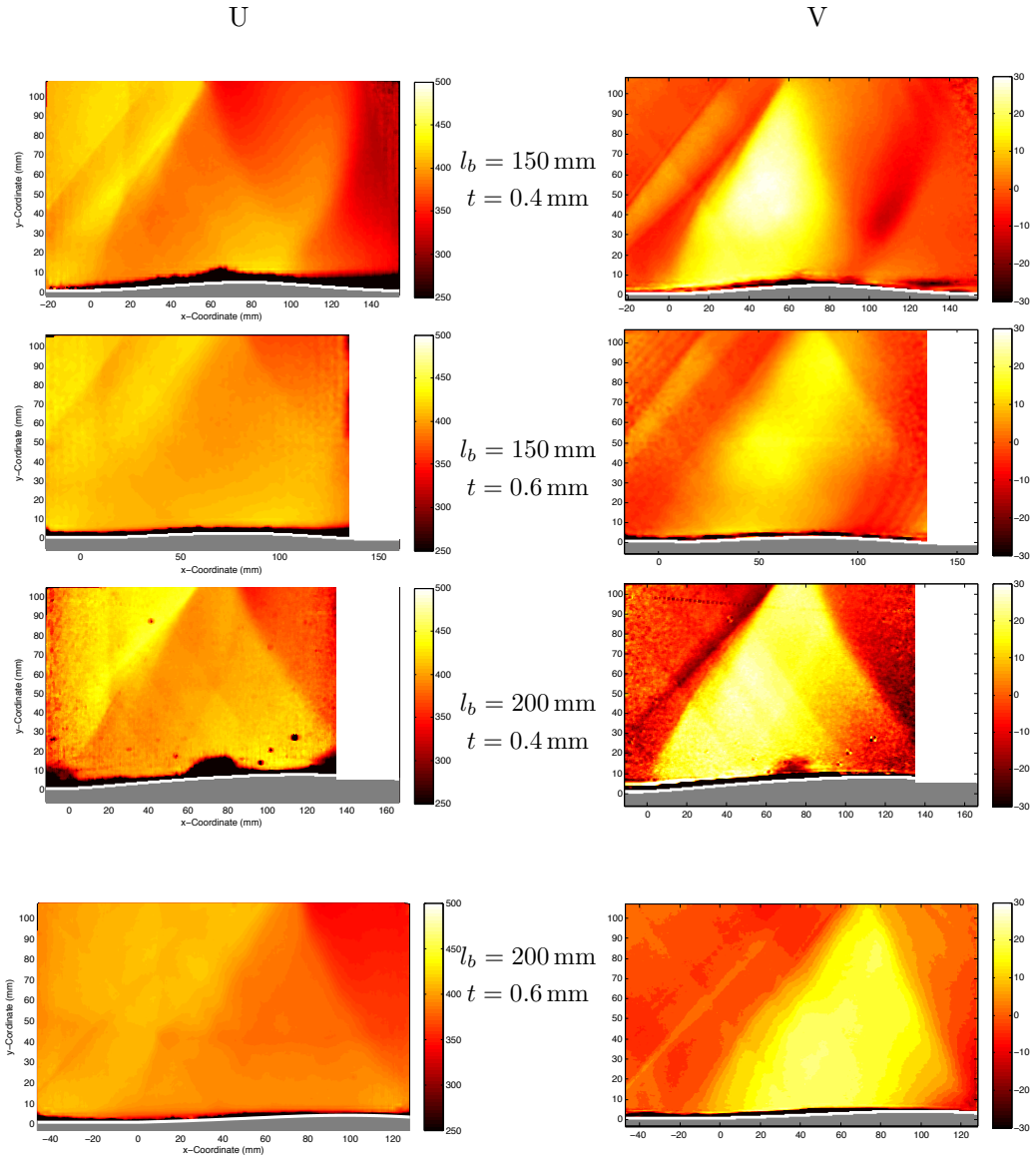


Figure 4.12.: Streamwise and vertical velocities calculated from PIV data for the flexible plate test cases.

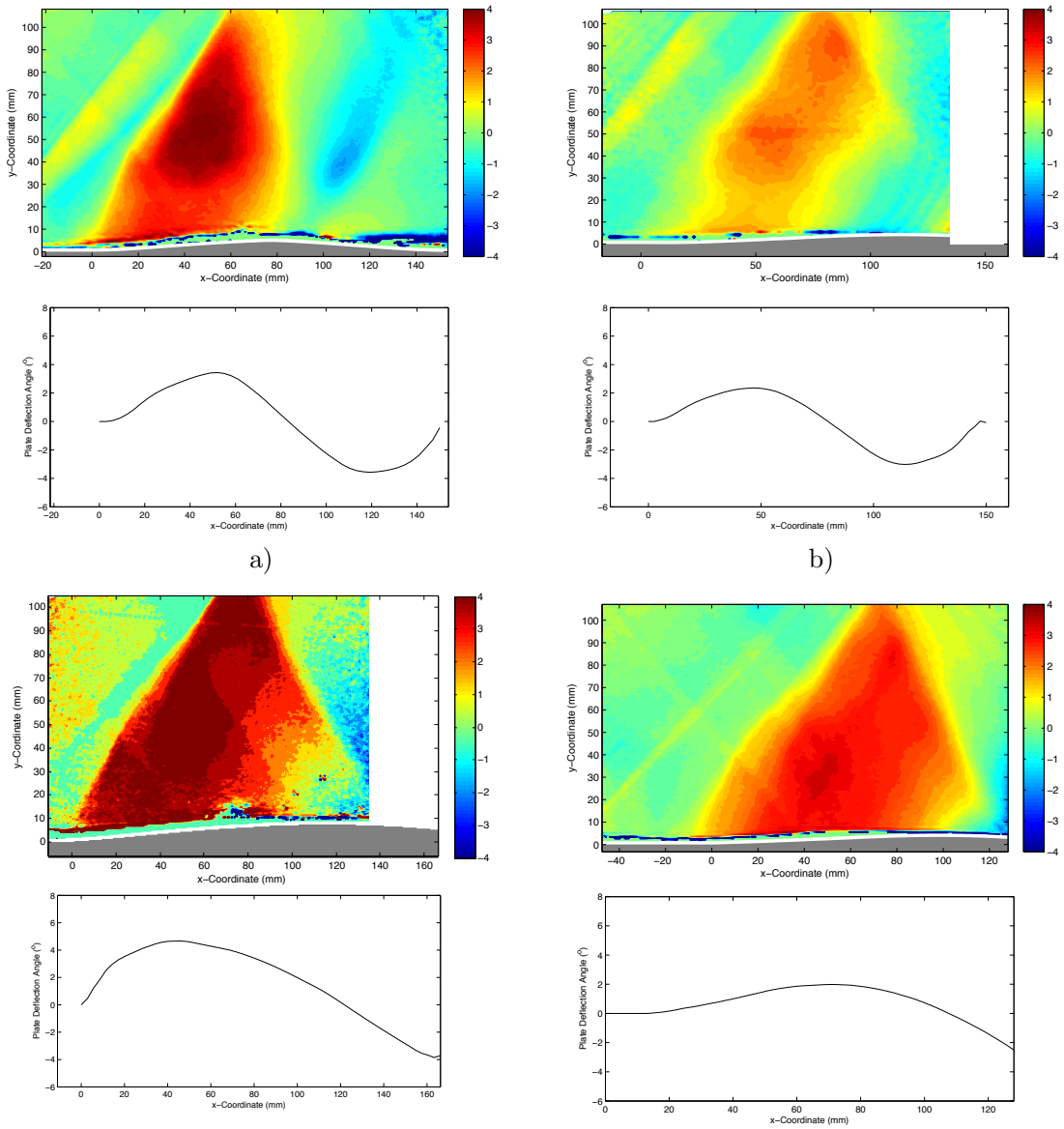


Figure 4.13.: Flow Angles and corresponding plate deflection angles for each of the flexible plate test cases. The plate deflection angles all angles are measured with respect to the horizontal a) $l_b = 150\,\text{mm}$ t $= 0.4\,\text{mm}$. b) $l_b = 150\,\text{mm}$ t $= 0.6\,\text{mm}$. c) $l_b = 200\,\text{mm}$ t $= 0.4\,\text{mm}$. d) $l_b = 200\,\text{mm}$ t $= 0.6\,\text{mm}$.

angle to 2.7^o. This meant that the flow field was subjected to minimal curvature which helped maintain attached flow downstream of the plate crest with no secondary shock systems present. In combination with the Schlieren images, it can be seen that the stiffest plate permits enough plate deformation to trigger the bifurcation of the shockwave but the structural constraints of the design also limit the plate curvature and hence the flow curvature.

Each of the flexible plates have been shown to bifurcate the shock via a passive technique with the flexibility of the plate an important design variable that is able to control the shock structure. The fact that these passive devices can bifurcate the shock in a time-averaged sense show promise for the design of adaptive SCB. The shockwave is however a very transient flow structure and in order to validate the design, the effects of the unsteady shock motion on the system must be analysed. The following section identifies the unsteady behaviour of the FSI between the shockwave and the plate.

4.3. Transient Experimental Response

The global time-averaged shock plate interaction has been evaluated with plate curvature suggested to be the cause of reacceleration and separation of the flow downstream of the plate crest. The deformation of the passive SCB also triggered a steady front leg and the successful bifurcation of the shock. The rear leg structure however was seen to vary significantly as a result of surface curvature between different length/thickness configurations. The unsteady behaviour of the aerodynamics is the source of the unsteady FSI and the following sections will focus upon shock structure, plate geometry and the coupled interaction.

4.3.1. Shock Motion

The case of a normal shockwave in a parallel duct is an inherently unsteady flow structure of which the underlying cause for the associated large-scale motion is still the subject of research [Dussauge and Piponniau, 2008]. Breaking down the bifurcated shock structure into three components highlights the varying levels of unsteadiness. The most steady is the front leg which is triggered by the deflection angle of the plate. In each of the cases presented there is a positive deflection into the flow caused by the pressure differential across the plate.

The rear leg is more unsteady as it is just a continuation of the main normal shock with various levels of curvature imposed by the surface. The third section is the region

above the triple point which shares many characteristics with the rear leg of the λ-shock although it remains unaffected by the deformation at the wall. The combination of a steady front leg and an unsteady rear leg introduces a complex FSI.

In each of the test cases, the rearmost shock structure is tracked during a tunnel run at a wall normal distance of 10 mm. This is illustrated in figure 4.15. The pixels that are monitored are above the plate crest in all of the cases. This eliminates the risk of tracking any dark pixels that may represent the plate as well as avoiding the smearing of pressure waves close to the boundary layer

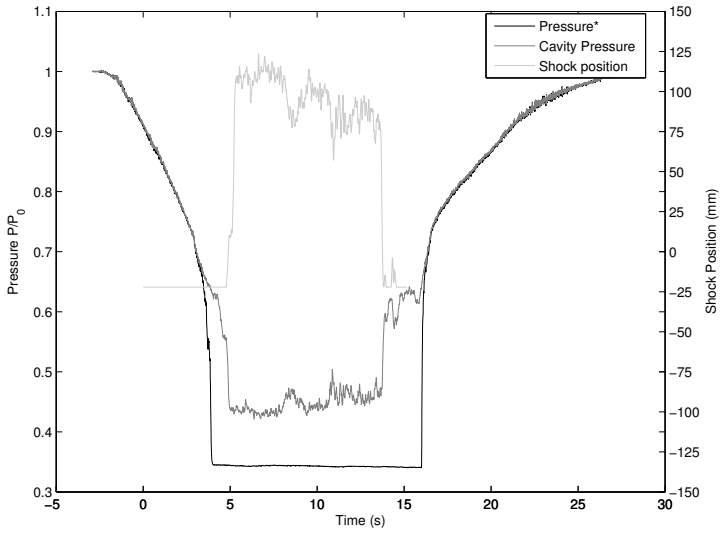
In the case of the $l_b = 150\,\text{mm}$, $t = 0.4\,\text{mm}$ plate the rearmost shock structure is downstream of the crest shown in figure 4.6a. This secondary shock will be tracked as this will indicate where upon the plate surface the shock will sit. This will show where on the surface the plate is subject to a rise in pressure loading. For the case of the $l_b = 150\,\text{mm}$, $t = 0.6\,\text{mm}$ plate with a representative shock structure shown in figure 4.6c, the traditional rear leg is tracked.

Figure 4.15 shows the Schlieren images extracted from a test case of the flexible SCB $l_b = 150\,\text{mm}$, $t = 0.6\,\text{mm}$. The images show the formation of a bifurcated shock structure with a curved rear leg as seen in the steady state response. The curved shock beneath the triple point then intersects with the secondary normal shock structure. This is visible in the PIV velocity fields in figure 4.10.

The location of this rearward shockwave is presented in figure 4.14 alongside two pressure readings, one in the cavity and another in the supersonic region outside of the influence of the bifurcation. These locations are annotated in figure 4.16. The shock position is included in figure 4.14 for reference and shows how the pressures and the shock movements are related.

Figure 4.15 shows the $l_b = 150\,\text{mm}$ $t = 0.6\,\text{mm}$ test case at various stages of shock loading. The first two images in are taken during the tunnel start up which is approximately 5-7 seconds duration. The pressures during the tunnel start-up can be seen in figure 4.14.

During the tunnel start-up, prior to choking, the plates are subject to gradual pressure gradients in the flow. As such the pressure differential across the plate is not as great as during the shock-loading portion of the run and therefore the deformations remain small with $\delta < t$. It should also be noted that the response of the plate prior to the tunnel starting is a useful indicator for the off-design performance of adaptive SCB. The performance of the plate under no-shock or a misplaced shock is almost as important as the on-design performance when the plates are integrated on to wings operating at multiple flight conditions.



*Normalised pressure reading at the end of the nozzle.

Figure 4.14.: Normalised pressure outside of plate influence and central cavity pressure tapping from figure 4.16

The relationship between the cavity pressure and the shock position is of particular importance to the aero-structural coupling that develops as a result of the shock loading which will be discussed in section 4.3.3. The cavity beneath the plate is not sealed off from the flow and air is free to pass around the edges of the plate. This is partly due to the difficulties of sealing a thin flexible skin whilst avoiding contact with the optical glass windows.

Figure 4.14 shows how the cavity breathes and how the pressure beneath the plate is a function of shock position with downstream shock excursions causing drops in cavity pressure and vice versa. This is particularly noticeable at times = 11 s with excursions at 9 s and 14 s also visible. This is because the low pressure supersonic region passes above the plate which creates a pressure differential that pulls the air from beneath the plate. The suction effect is not strong enough to cause the cavity pressure to reach the low pressures of the supersonic region above the front section of the plate but the pressure is lowered and is dependent upon the flow above.

Possible causes for the non-equalising of pressures are the possibility of a small atmospheric leak in to the cavity. The length of test could also be a limiting factor however due to the small cavity volume $70 \times 280 \times 80\,\mathrm{mm}^3$ this is unlikely. A more likely source

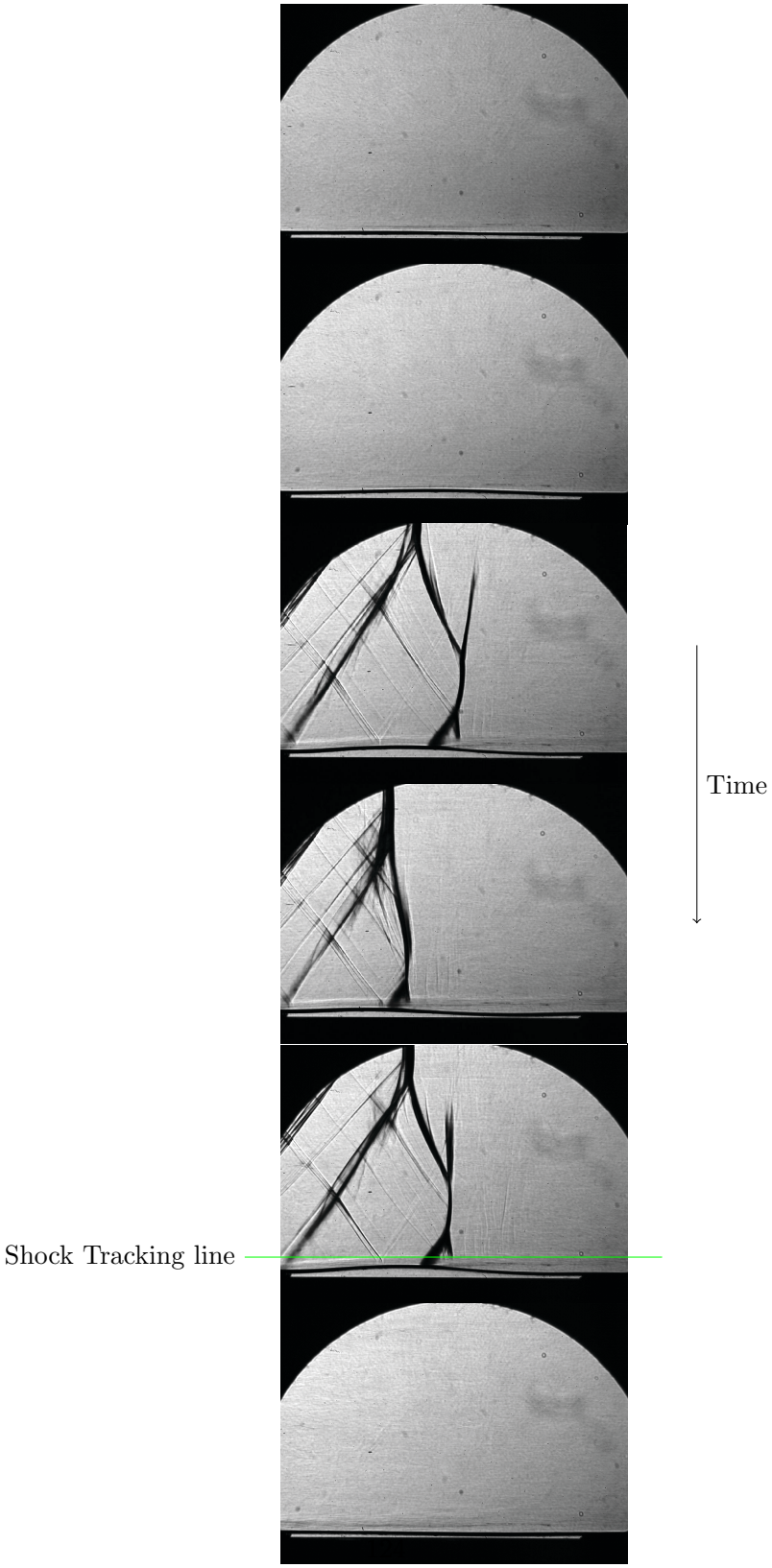


Figure 4.15.: Test case breakdown for $l_b = 150\,\text{mm}$ $t = 0.4\,\text{mm}$ flexible plate case during aerodynamic loading.

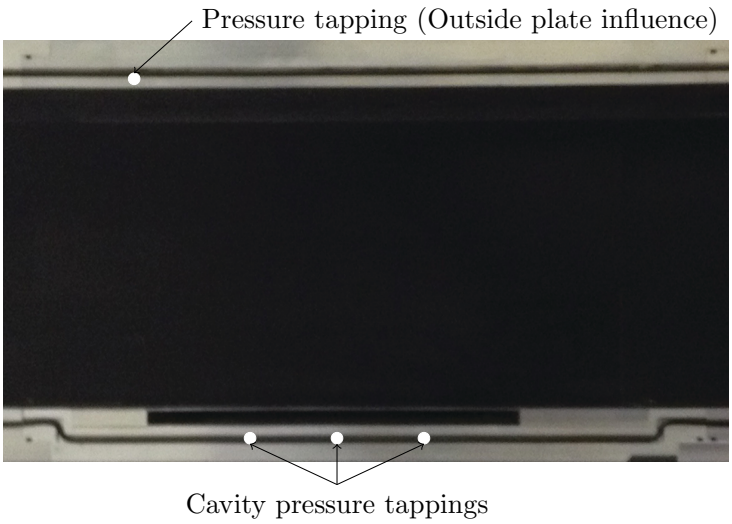


Figure 4.16.: Plate region of experimental test rig fixed in the wind tunnel.

of higher pressure air is downstream of the shock which may also enter the cavity and create a 'breathing' cavity that is partially evacuated by the low pressure supersonic flow and replenished by the higher pressure post-shock.

The presence of any supersonic flow above the surface immediately sees a reduction in cavity pressure for example at $t = 5\,\mathrm{s}$ in figure 4.14. The estimated magnitudes of this pressure driven flow around the edges are small with the optical window and edge of the plate $\Delta x < 0.05\,\mathrm{mm}$. From the instantaneous Schlieren images in figure 4.6 there would be significant thickening of the plate which would represent span-wise bending of the plate. As there is not significant thickening across the span it is suggested that the flow leakage around the sides is not of a large magnitude and does not contribute to the deformation of the plate.

4.3.2. Plate Motion

The plate deformation has already been extracted from each of the time-averaged PIV and Schlieren images by the techniques described previously. Figures 4.17 and 4.18 show the plate geometries throughout time for each of the flexible plate test cases. The geometries exhibited by each case are similar due to the similarities in loading however the varying stiffnesses resulted in different levels of deformation.

This is well illustrated in figure 4.17 which shows the plate geometries extracted from the PIV procedure. These results were acquired at a moderate frequency of 700 Hz

during the period where the plate was subject to shock loading. The maximum displacements did not vary significantly for the thicker plates tested, with $l_b = 150\,\text{mm}$, $t = 0.6\,\text{mm}$ $\delta_{max} = 3.2\,\text{mm}$ and $l_b = 200\,\text{mm}$, $t = 0.6\,\text{mm}$ $\delta_{max} = 3.7\,\text{mm}$. When the thickness was reduced to t = 0.4 mm the flexibility of the plate can be identified in the large deformations of figure 4.17c where $l_b = 150\,\text{mm}$, $t = 0.4\,\text{mm}\delta_{max} = 4.55\,\text{mm}$ and $l_b = 200\,\text{mm}$ $t = 0.4\,\text{mm}$ $\delta_{max} = 7.3\,\text{mm}$. These values alone indicate the levels of flexibility within the structure. These flexible plates permit deformation heights exhibited by existing static SCB and show that the flexible plate based design can bifurcate the shock.

The overall performance of adaptive SCB will also need to be analysed under off-design conditions. The PIV technique used here is able to provide a quantitative insight into the flow field which allows for the estimation of a number of flow qualities. The limit is the memory capacity of the Phantom v641 cameras which were unable to record at the required frame rates for longer than 3.9 s. Switching to the Schlieren technique traded the quantitative benefits of PIV for the ability to record entire tunnel runs which enabled the recording of tunnel start-up and tunnel shutdown. These results provided an insight into the FSI between the shock and the plate over a much greater time span.

Figure 4.18 shows the vertical deformation of the plates through time via the Schlieren images with very little variation throughout a sustained period of shock loading. The oscillations of the plate are less than a plate thickness which Dowell [1972] suggested were triggered by turbulent structures within the boundary layer. The small variations also confirm that the plates have been appropriately sized and offer enough stiffness to not only withstand the general shock-based aerodynamic load but also the dynamic loading.

The pressure difference across the plate and the pressure gradient over the upper surface are directly related to the deformation of the plate. The total pressure is maintained at a constant value throughout the main portion of the run and after the initial 7-8 second start up, the total pressure ratio across the working section was 1.286±0.005. In the experimental model the cavity pressure is driven by this large scale pressure gradient and also a small leakage which has been previously recorded in this investigation. The variations in cavity pressure can be seen in figure 4.14 with the pressure gradient remaining reasonably steady, $\Delta P_{cavity} = 0.55 \pm 0.005\text{bar}$. However the dependence upon the shock position as can be observed at $t \approx 11\,\text{s}$ where a downstream shock discussion triggers a drop in cavity pressure.

The sensitivity of the cavity pressure to the free stream flow is shown in figure 4.19 with Schlieren images taken prior to shock loading. The shock is not visible in the upper

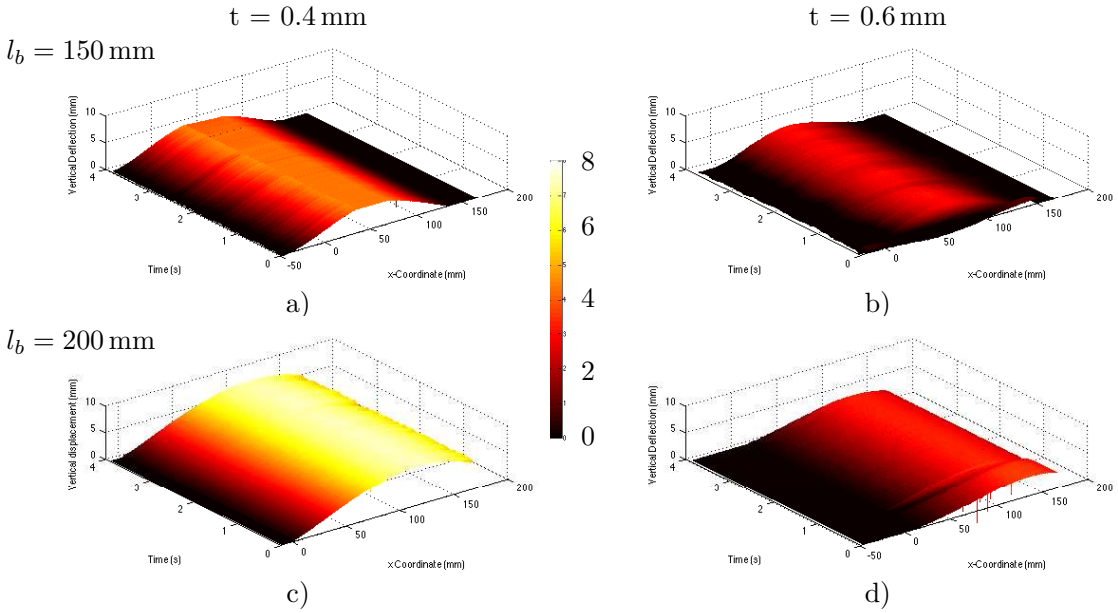


Figure 4.17.: Plate deflection during PIV acquisition process upon flexible plates. a) $l_b = 150\,\text{mm}$ t = 0.4 mm b) $l_b = 150\,\text{mm}$ t = 0.6 mm c) $l_b = 200\,\text{mm}$ t = 0.4 mm d) $l_b = 200\,\text{mm}$ t = 0.6 mm.

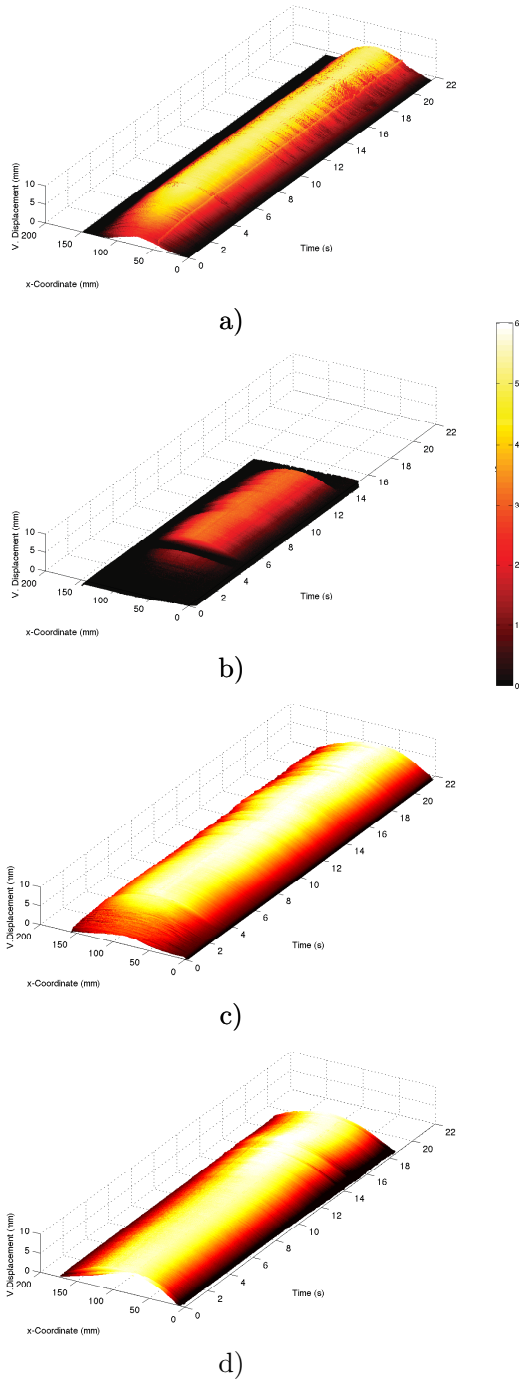


Figure 4.18.: Plate deflection during Schlieren process upon flexible plates. a) l_b = 150 mm t = 0.4 mm b) l_b = 150 mm t = 0.6 mm c) l_b = 200 mm t = 0.4 mm d) l_b = 200 mm t = 0.6 mm.

image, however, pressure tappings in the nozzle suggest that it is 50 mm upstream of the frame at the exit of the nozzle, the shock can be seen entering the frame in the lower image. The Mach number is estimated from the P/P_0 value measured on the wall of the working section. $M_{ws} \sim 0.6$ is estimated from the pressure tapping outside the plates region of influence shown in figure 4.16. Figure 4.19b shows how the aerodynamic load may cause a temporary negative deflection of the plate. This transient effect is caused by the post-shock pressure being momentarily higher than the cavity pressure. The natural unsteadiness within the flow, acceleration of the starting tunnel and the corresponding pressure changes all contribute to the oscillatory motion of the plate. Further oscillations can be seen throughout tunnel start-up at the times $0 < t < 4$ s in figure 4.21a.

The negative deformation immediately prior to the shock is an indication of the pressure fields surrounding the flexible plate during a shock pass. Although the shock pass was very quick at 0.02 s, the PIV technique captured the shock entering the frame and reaching the steady-state structure shown in the previous section. Figure 4.20 shows instantaneous PIV vector fields for a number of key frames prior to shock loading. The flexible plate in figure 4.20 shows how the aerodynamic load actually causes a negative deflection of the plate prior to shock loading, this was seen to some extent for all test cases however it is most prominent in the thinner plates that were tested. As the shock moves over the plate, the crest position varies with the shock position and the shock structure can be seen to take the form presented in the steady-state images in figure 4.6. The movement of the plate during shock loading has been shown in the surface plots of figures 4.17 and 4.18 which highlight the global deformation throughout the tunnel run. However in order to present the data, a single point was selected on the rear surface of the plate at 100 mm in order to highlight the amplitudes of the oscillations.

Figure 4.21 shows the displacement of a single point located at $0.66l_b$ for the flexible plates. This control point in the flexible plate case in figure 4.21b is seen to negatively displace from the subsonic rise at two distinct aerodynamic loading conditions. This happens just prior to the shock passing over the start of the section of flexible plate between 4.2 s$< t <$ 5 s of the flexible test case. This negative displacement is mirrored when the shock passes back over the plate towards the end of the shock loading, at a time $t >$ 13.9 s in figure 4.21 however the response is not symmetrical due to the differing magnitudes of acceleration/deceleration.

On the subject of plate motion, the range of motion of the plates during shock loading are indicated in table 4.3. The flexible plate crest height remains relatively constant at 3.2 mm with a standard deviation of 0.7 mm at an average stream wise location of

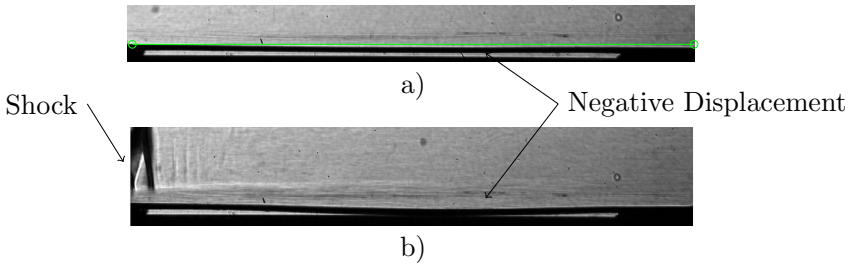


Figure 4.19.: Example Schlieren image that illustrates negative displacement prior to shock loading. a) Shock wave is 50 mm upstream of the image at the exit of the nozzle. b) Shockwave has just entered the frame.

$\sim 0.45 l_b$ with little variation despite an unsteady shock on the surface

The general transient behaviour of the flexible plates is promising with respect to their potential use in adaptive SCB. Even with the unsteady shock motion, the plate geometry remains relatively stable with changes being very small between Schlieren images recorded at 350 Hz. The small unsteady variations in deformation, $\delta < 0.2$ mm witnessed in this set of experiments are well within the structural limits of the plate and show that the large-scale destructive oscillations in flexible plates identified by Dowell [1970] are not present in this particular setup. This is due to the added stiffness that the cavity pressure adds to the system which reduces the likelihood of failure by panel flutter as a failure mode of this FSI.

4.3.3. Unsteady Fluid-Structure Interaction

The fluid-structure interaction that occurs between the plate and the flow has been previously introduced in section 4.2.3 and in this section the unsteady aero-structural behaviour will be analysed with particular focus upon the interaction between the plate crest and the position of the shockwave. It is proposed that this relationship has a significant effect upon the behaviour of the shockwave with regards to the unsteadiness and location of the interaction.

Figure 4.22 shows the location of the plate crest with respect to the rearmost shock location for the flexible plates, the left hand image column shows the location of the plate crest and the shock location. The right hand column of images show the maximum plate deformation which is caused entirely by the pressure loading. Each row of graphs represents a single test case.

There are broad similarities between each of the test cases despite the varying stiff-

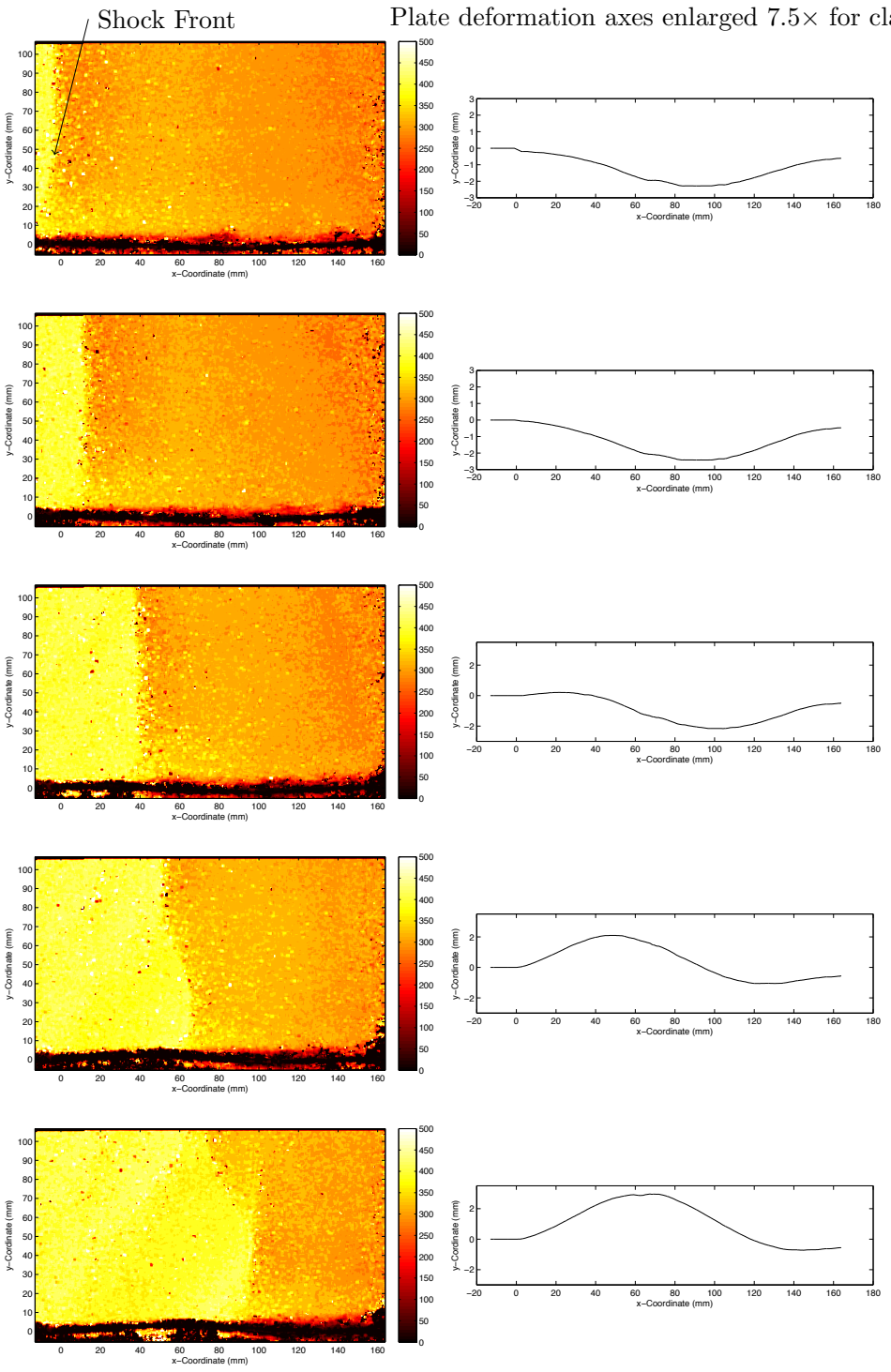


Figure 4.20.: Instantaneous PIV stream wise velocity fields and extracted plate geometries for $l_b = 150\,\text{mm}$ $t = 0.4\,\text{mm}$ plate.

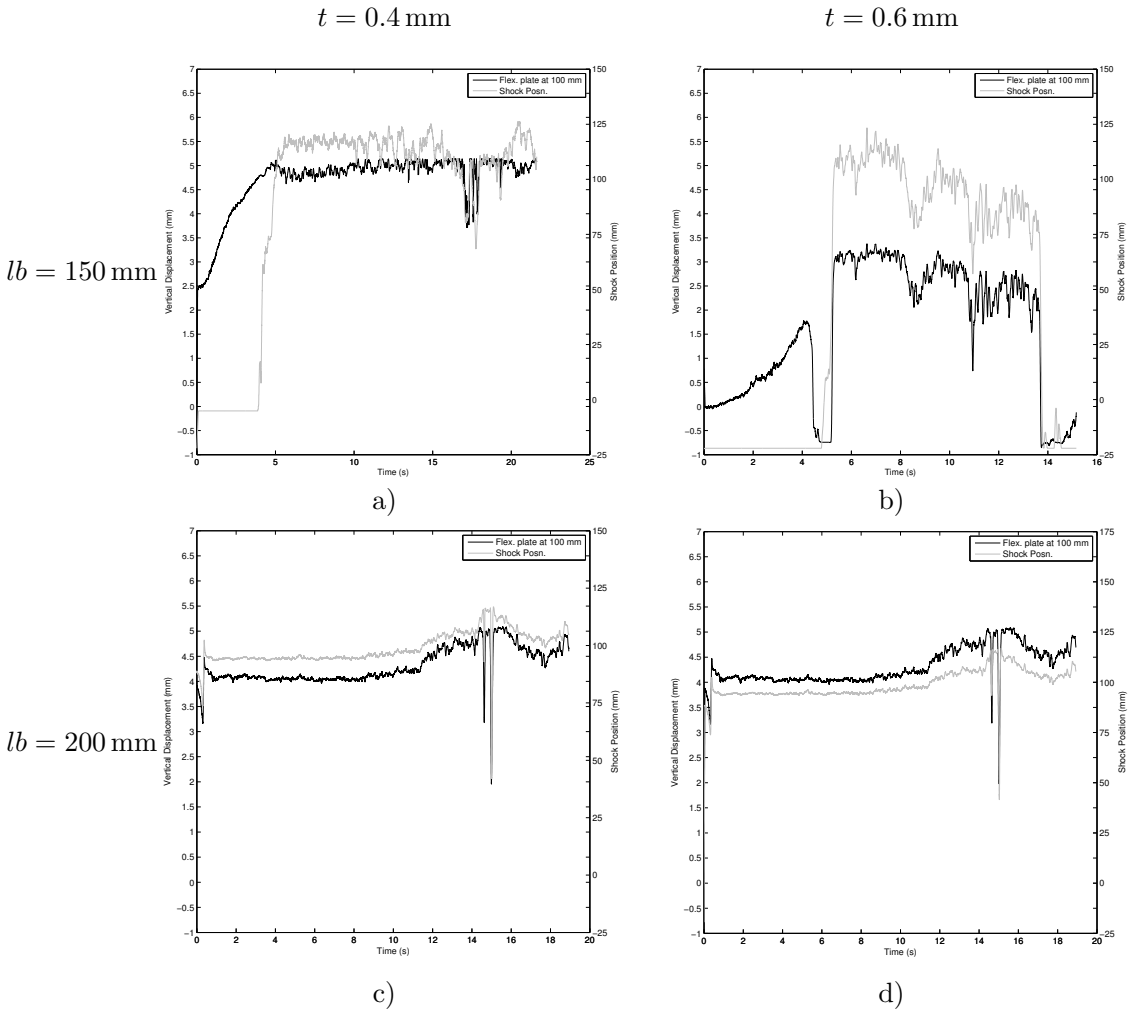


Figure 4.21.: Vertical displacement through time of a single, fixed point on the surface located 100 mm from the beginning of the plate for each test case. a) $l_b = 150\,\mathrm{mm}$ $t = 0.4\,\mathrm{mm}$, b) $l_b = 150\,\mathrm{mm}$ $t = 0.6\,\mathrm{mm}$, c) $l_b = 200\,\mathrm{mm}$ $t = 0.4\,\mathrm{mm}$, d) $l_b = 200\,\mathrm{mm}$ $t = 0.6\,\mathrm{mm}$.

Test case		Avg. Shock position	Avg. Plate Crest Location	Avg. Spacing
l_b	t	($\%l_b$)	($\%l_b$)	($\%l_b$)
150	0.4	0.62	0.364	0.26
150	0.6	0.62	0.43	0.19
200	0.4	0.65	0.55	0.10
200	0.6	0.54	0.45	0.09

Table 4.3.: The streamwise locations of the shock, the plate crest and the distance between the two expressed as a percentage of bump length.

nesses. In particular, the distance between the plate crest and the shock observed to be a function of the main normal shock location and the flexibility of the plate. The stiffest plate $l_b = 150$, $t = 0.6\,\text{mm}$ constrains the movement of the plate crest whereas the more flexible plates $l_b = 200\,\text{mm}$ allow the plate crest to move with the shock. The result is a shorter distance between the crest and the shock. The shock tracking effect is illustrated in figure 4.22 and is beneficial to the shock structure as it minimises the size of any supersonic acceleration that may develop as the flow passes over the crest increasing the strength of the rear shock. The average streamwise distances normalised with l_b are displayed in table 4.3 and show the trend described here. The flexible plates show a smaller distance at $\sim 20\,\text{mm}$ whereas the stiffer plates show nearer 30 mm as the movement is restrained.

The $l_b = 150\,\text{mm}$ $t = 0.6\,\text{mm}$ plate in figure 4.22 shows that throughout the shock loading section of the test case, crest position follows very closely to shock position with a maximum difference of 42.3 mm when the shock was far downstream. The movement remained synchronised throughout the test case however as the mean shock position moves from $\sim 110\,\text{mm}$ between 5.5 s and 8.5 s to $\sim 80\,\text{mm}$ between 11 s and 13.5 s at a distance of 30 mm, the plate crest-shock distance moved 9 mm (29.1 mm to 20.4 mm). The deformations of the plate were being restricted by the boundary conditions which limited the downstream movement of the crest. This was a limit placed upon the plate by the continuity requirements of the material and plate. The peak displacement of the plate is 3.2 mm which remained very steady whilst under shock loading, figure 4.22b.

The movement of the plate crest with respect to shock motion is a unique capability of passive adaptive SCB and stems from the relative stiffness of the plate design which is dictated by the basic characteristics of the plate sizing and material. In terms of shock structure, the ability to have a SCB crest that tracks the motion of the shock provides a platform that has the potential to deal with a variety of different shock

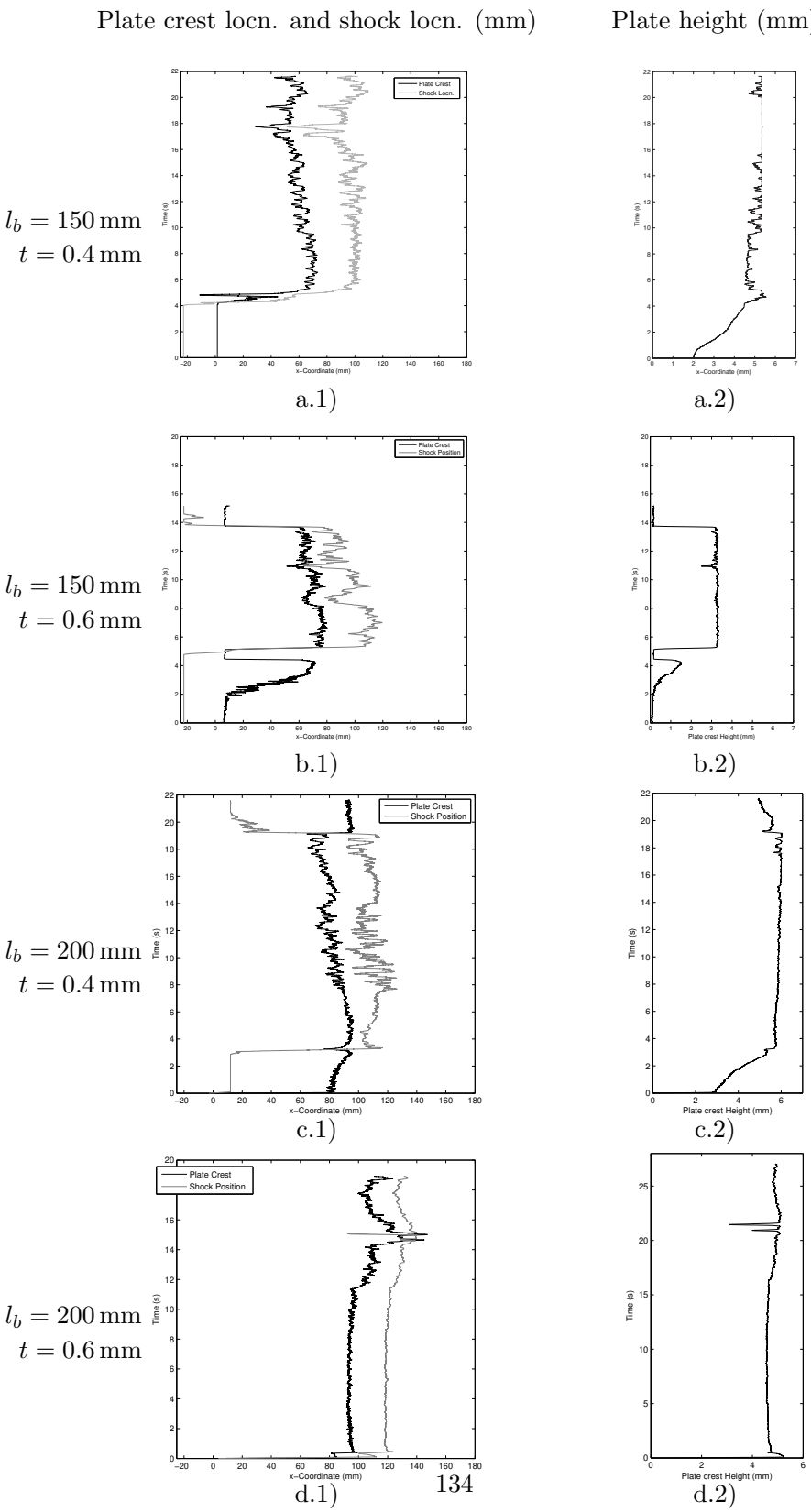


Figure 4.22.: Plate crest tracking through time for the $l_b = 150\,\text{mm}$ t = 0.6 mm flexible plate in a) & b). Graph a) shows the location of the maximum plate displacement with respect to the location of the most rearward shockwave. Graph b) shows magnitude of the displacement due to the aerodynamic loading.

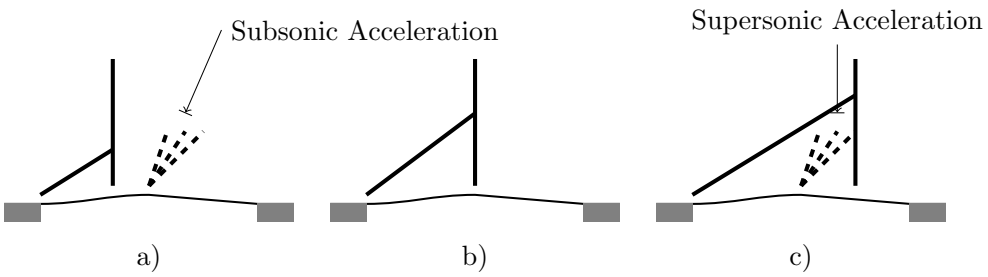


Figure 4.23.: Schematic showing effect of crest position with respect to the rear leg location and subsequent acceleration regions

positions. This characteristic is a major benefit of adaptive SCB. There are however some negative connotations with the ability to track the shock wave with regards to flow quality. Although the region near the crest is capable of minimising the distance over which flow acceleration may occur prior to the rear leg, the possibility of local accelerated flow downstream of the rear leg may increase due to local plate curvature. This effect is illustrated in figure 4.24 and is evident in the more flexible test cases of $l_b = 200\,\text{mm}$ and $t = 0.4\,\text{mm}$ which also exhibited post-shock separation which is indicated by the significant smearing of the shock foot in figure 4.6c.

The unsteady effects of curvature are difficult to quantify precisely due to the time scales involved and the complex interaction in the experimental model. The optical aerodynamic techniques used in this study offer an insight into the coupled FSI, however, the associated time scales are very small and difficult to capture simultaneously with quantitative flow measurements over such a large field of view. In terms of the goals of traditional SCB it is suggested that although SCB are capable of tracking the shockwave (as demonstrated in figure4.22) it may not be beneficial for the shock structure away from the wall around the rear leg. Increased curvature may also exist downstream of the crest resulting in larger deflection angle changes which may have induce separation. Therefore it is recommended that greater control over the surface curvature is required in order to make the best use of adaptive SCB, this could be achieved through the use of actuation.

4.4. Summary of Flexible Plates for Adaptive SCB

The four test cases that have focused upon the plate characteristics have highlighted the key design criteria for passive adaptive SCB. Both the steady and transient ef-

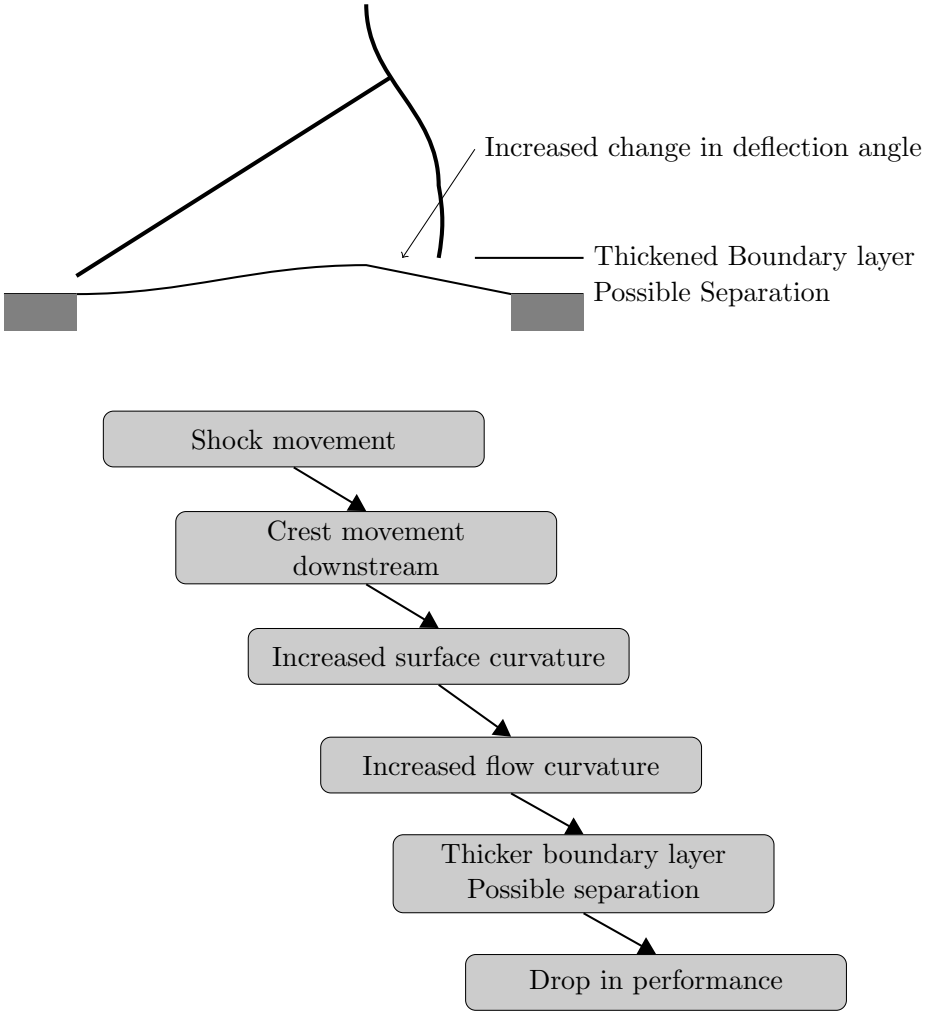


Figure 4.24.: The effects of shock tracking with the crest travelling too far downstream.

fects of the flow on such devices have been evaluated through the use of a quasi-steady aero-structural solver and multiple experimental test cases. The aero-structural solver provides a suitable initial design tool to determine the effects of the influential parameters associated with plate design such as material choice, thickness, length and the width of the plate section and the resultant stiffness/flexibility of the system. Cavity pressure beneath the plate and the subsequent pressure difference is a variable that has been found to heavily influence the performance. This parameter is especially important for a flexible plate based design for adaptive SCB.

The aero-structural solver allowed for variability in the cavity pressure to examine the response and select a suitable cavity pressure for the experimental test cases. Selecting a constant cavity pressure enabled the investigation to focus upon the interaction of the shock as well as avoiding the design of a complex and expensive variable pressure cavity system. The cavity pressure constraint in the experimental test cases matches the average upper surface pressure value as suggested in section 4.1, This is a balance between matching traditional SCB geometries whilst obeying adaptive SCB constraints and not exceeding the yield stresses of the material. This confirms the plate sizing has achieved one of the main goals of adaptive SCB which is to deform in the elastic regime only so the original flat plate can be achieved after shock loading.

The aerodynamic performance of passive adaptive SCB is the biggest hurdle that the devices have to overcome especially when compared to traditional static SCB. The fixed shape of static SCB is optimised and refined to ensure good on-design performance for a given shock loading. The performance can suffer when off-design. Adaptive SCB require an element of flexibility in their design, the shape changes depending upon the loading which is a significant factor in the overall aerodynamic performance. The shock structures in the Schlieren images in figure 4.6 and PIV vector fields in figure 4.12 show the advantages and disadvantages of using a flexible plate for a passive adaptive SCB where the acceleration is minimised through shock tracking but there is significant re-acceleration downstream of the normal shock. This is suggested to be caused by the curvature of the surface, and in combination with the pressure gradient across the shock, caused the flow to separate.

Through the initial sizing process the $l_b = 150\,\text{mm}$, $t = 0.6\,\text{mm}$ plate offered a suitable level of flexibility whilst remaining stiff enough to limit plate deflection. Restraining deformation height also minimised the thickening of the boundary layer which potentially caused separation downstream of the plate crest. This combination of plate length and thickness worked well for the aerodynamic constraints but further control measures to fully constrain the geometry are desirable.

Previous examples in modern SCB studies alter the rear surface of the plate. The designs of Nübler et al. [2012] and Colliss and Babinsky [2012] have examined the rear surface in closer detail and have made significant modifications. One method for implementing into adaptive SCB designs is to introduce fixed boundary conditions that better define the shape of the plate. Such a SCB would benefit from an increased number of constraints to limit deformation and surface curvature which would in turn reduce the resultant flow curvature. The positioning and height of these constraints requires a more rigorous design process. One approach that static SCB have followed is to apply an optimisation procedure to the design problem which would provide the optimal location and displacement of the constraints for maximum performance. This approach is explored in the following chapter.

5. Optimising Designs for Adaptive Shock Control Bumps

The design of both static and adaptive SCB lend themselves well to optimisation procedures. A small number of design parameters are able to influence the overall performance which means that an optimal design can be calculated efficiently. In this chapter the optimisation procedure will be introduced specifically for the case of an adaptive SCB.

The purpose of adaptive SCB is to provide an alternative to 3D SCB as a means to overcome the poor off-design performance of 2D static SCB. The ability to react to the flow above the control region is important to maintain global aerofoil characteristics such as lift and drag coefficients. SCB actuation may also negate any large-scale separation which can typically occur over the crest of an ill-positioned bump. The performance of static SCB with respect to shock position has been documented by Le Balleur et al. [2002] who tested SCB in multiple locations. However the addition of adaptivity brings with it a structural aspect that has not been evaluated in great detail with Lutz et al. [2003], Wadehn et al. [2002] and Rhodes and Santer [2012] being the only studies that have begun to look at this aspect.The goal in this study is to design an optimisation framework that will result in optimal designs for the RAE2822 aerofoil as well as determine best design practices for adaptive SCB.

This chapter will focus upon the main challenges that designing for adaptivity brings over optimising for static SCB and the approach that is required.

5.1. Approach

The aero-structural framework discussed in chapter 3 combines numerical schemes for the aerodynamic and structural aspects of 2D adaptive SCB. The development of flexible plate based designs for adaptive SCB showed that the rear surface may benefit from additional control. The integration of the aero-structural solver in an optimisation procedure is discussed so that a new design approach for adaptive SCB can be outlined. The design moves towards the original concept of Ashill et al. [1992] and is illustrated

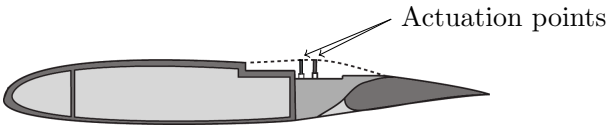


Figure 5.1.: Illustration of expected actuator loading and initial sizings. Adapted from Ashill et al. [1992].

again in figure 5.1. The location and displacement of the actuation points will be subject to an optimisation procedure.

The framework of the optimising process is illustrated in figure 5.2 which shows how the component pieces interact. Each aspect will be discussed in detail in the following sections.

5.1.1. Bump Parameterisation

In order to design an efficient optimisation procedure the problem must first be parameterised. The ideal number of variables is dependent upon the optimisation technique used, however it is generally a balance between number of variables and the required tolerance of the solution. The computation times associated with aerodynamic optimisations multiply with the number of independent design variables. Therefore an efficient choice of design variables is required which are influential enough to affect the flow and sufficiently few in number to ensure reasonable computation times.

The SCB geometries considered in section 2.3.1 included many types of curve. The goal of each is to be able to represent each curve with a minimal number of variables. Referring back to figure 2.12, the loaded beam and wedge geometries would require a minimum of two variables, SCB height and the position along the length. The concave and regular polynomials require a number of coefficients based upon the order of the polynomial. Whilst increasing the number of design variables increases the control over the shape, the complexity of the design also increases.

There are various merits for each curve both aerodynamically and structurally however ultimately, these geometries need to be reproduced in an experimental model to showcase the performance of adaptive SCB. Therefore restrictions such as high stress concentrations, hinges and material constraints need to be considered. Manufacturing the polynomial based solutions would require a large number of constraints that would add to the complexity of the system. A wedge-type geometry would require hinges at the points of inflection and would potentially suffer from a small leakage as the upper

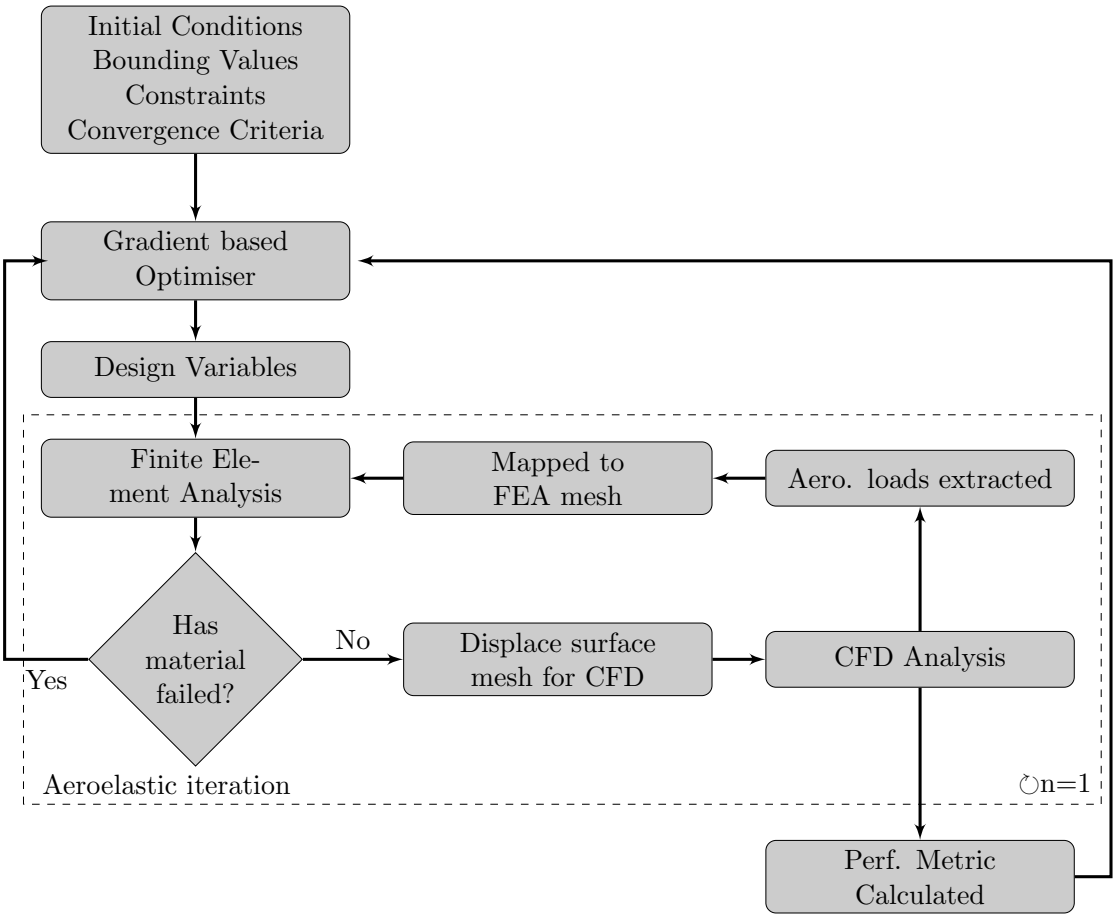


Figure 5.2.: Flow chart for the optimisation process.

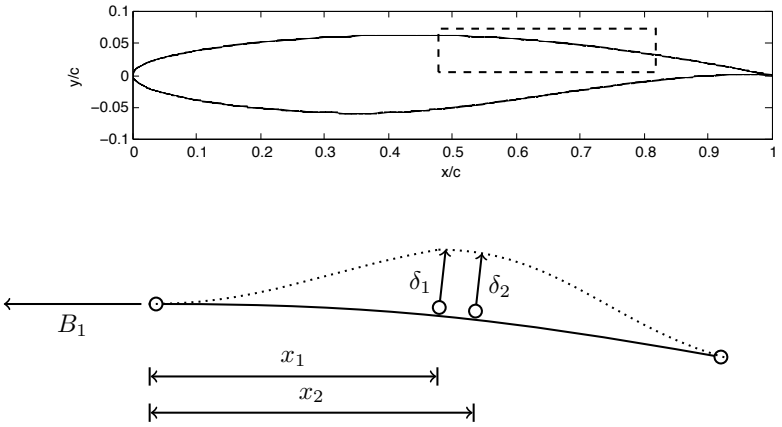


Figure 5.3.: a) The datum RAE2822 aerofoil geometry. b) Design variables for structural morphing to be used during the optimisation procedure.

and lower surfaces could not be sealed effectively.

The loaded beam type geometry offers an attractive solution with a continuous surface with control over the edge constraints to ensure zero displacement and zero slope at each stream wise edge. The beam model can also be deformed by a displacement at a single point which lends itself to an actuation based design. This is a return back to the original concept by Ashill et al. [1992] where each actuator would require two parameters, a deformation height and a location along the SCB of the displacement. Each additional actuator would need a further two parameters to be included in the optimisation. The ideal number of actuators for a 2D SCB was investigated by Rhodes and Santer [2012] who evaluated the ability to replicate the centreline geometry of the *default rounded bump* suggested by Ogawa et al. [2008]. The results showed that two actuation points were enough to provide a suitable representation of the geometry with additional actuators not providing any greater control whilst adding considerable complexity. The geometries of these two SCB are shown alongside each other in figure 2.22.

The design variables illustrated in figure 5.3 were selected for structural and aerodynamic influence and are represented by

$$\Omega = [B_1 \;\; x_1 \;\; \delta_1 \;\; x_2 \;\; \delta_2] \tag{5.1}$$

where B_1 dictates the start of the morphing region which is fixed at 0.2c, x_i provides the chordwise location of the actuation on the pseudo-2D geometry and δ_i denotes the magnitude of the displacement applied.

Bump height and ramp angle have previously been found to be key parameters by Ogawa [2006] and Eastwood and Jarrett [2012] however these work best for wedge type bumps with a constant ramp angle. By using the loaded beam based geometry, the ramp angle continuously changes as seen in figure 4.9. The ramp angle is a function of the actuation height due to the prescribed plate geometry. A second actuation point is included in order to gain greater control over the crest region. Rhodes [2012] produced a similar design which evaluated the deformations subject to actuation without the aerodynamic loading which as seen in the previous chapter is an important factor. The effects of aerodynamic loading require an initial flow solution which is calculated by CFD given the initial the design variables.

Nodes are created at the boundaries B_1 and $B_1 + 0.2c$ and are used to apply the fully-fixed boundary conditions representative of a clamped plate. Allowing the position on the aerofoil to move with respect to the aerofoil enables the best location of the SCB to be found during optimisation. The structure outside these bounding nodes remains unaltered in order to remove any detrimental aerodynamic effects outside the morphing region.

Small out-of-plane displacements of the morphing region $\mathcal{O}(4\,\mathrm{mm})$ are capable of bifurcating the shock as shown by the flexible plate studies. The ability to control the deformation increases the versatility of adaptive SCB. As the flexible passive SCB designs of the previous chapter were entirely deformed by the aerodynamic flow field, the primary purpose of actuation is able to constrain the displacement to limit the effects of the pressure difference. This has the potential to make actuated SCB better over a range of shock positions. The optimisation framework carries out the process outlined in figure 5.2. Each optimiser iteration consists of a series of perturbations to the design variables in equation 5.1. A centred finite-difference scheme is used to perturb the initial conditions and explore the design space systematically in order to build up the sensitivity to each parameter. The optimiser uses the gradient based scheme *fmincon* in the MATLAB optimisation toolbox which calculates an objective function via the performance of each perturbation. Bounding the values of the parameters aids the speed of the optimisation procedure by reducing the size of the design space. The deformed plate geometry is applied to the aerofoil starting at B_1, the range of these values is $0.35c \leq x \leq 0.6c$ which allowed the SCB to be moved completely upstream or downstream of the natural shock position on the clean aerofoil. The range of actuation positions is limited to $0.3l_b \leq x_1, x_2 \leq 0.8l_b$ with $x_1 \leq x_2$, which did limit the number of possible SCB shapes however the wealth of existing optimisation studies for static SCB supported this range [Qin et al., 2008, Yagiz et al., 2012, Lee et al., 2012, Kutzbach et al.,

2004]. Limiting the location of the displacements also takes into account the material constraints by limiting potential SCB geometries with high stress concentrations at the clamped ends. The bump height governed by δ_1 and δ_2 was unbounded to test the optimiser's ability to produce a successful SCB with the addition of an aerodynamic load.

5.1.2. Integration of the Aero-Structural Solver into the Optimisation Process

Aerodynamic Integration

The aerodynamic loading surrounding the adaptive SCB caused a deformation of the plate which in turn affected the pressure distribution around the aerofoil. In controlling the shock through a SCB, the lift distribution will be affected and may be compromised. In a real-world situation this would necessitate a change of angle of attack, altering shock position and potentially SCB effectiveness. It was therefore useful to monitor C_l during optimisation to ensure the required lift distribution and specifically any global loss in lift is negated during shock control. If the value was observed to decrease by more than 1% the design was deemed ineffective and a penalty value was applied to the optimiser. This was added to the constraints of the optimiser and enabled the monitoring of what is effectively a secondary performance measure to strengthen the feasibility of the SCB designs.

The lift coefficient and other aerofoil scale parameters such as drag and L/D have been the performance metric of choice for many studies [Lee et al., 2012, Yagiz et al., 2012, Qin et al., 2008]. However with experimental techniques and computational power increasing there is a significant shift to smaller length scales now that the concept has been proved. The CFD component of the optimisation is capable of providing quantitative information regarding the viscous effects surrounding the SCB which an analytical model would not be able to capture. Boundary layer heights and wall shear stresses have been extracted from the simulation and have aided the evaluation of successful SCB designs on a smaller length scale. Whilst not included in the performance metric these quantities will be used in the post-optimisation analysis to evaluate optimal adaptive SCB geometries further providing the designs passed the structural constraint.

Structural Integration

The structural component is the first aspect of the optimisation process. As the least computationally expensive process within the aero-structural solver, the variables must

first pass the yield stress criteria. In order to ensure that material deformations are elastic and the original retracted geometry can be regained after actuation it is necessary to limit the maximum deformation to a value below the yield stress of the material. This limit will feature as a constraint in the optimisation framework and penalty values will be returned to the optimiser to avoid plastically deformed solutions. To limit the maximum stress present during the deployment, the von Mises equivalent stress is calculated over each element

$$\sigma_{i,eq} = \sqrt{\sigma_{i,1}^2 - \sigma_{i,1}\sigma_{i,2} + \sigma_{i,2}^2} \tag{5.2}$$

where $\sigma_{i,1}$ and $\sigma_{i,2}$ are the principal in-plane stresses for element i. The maximum equivalent stress forms the value to be constrained by the optimisation.

For static SCB, the structural model outlined here would be adequate however due to the flexibility of the system the pressure field imposed on the plate by the fluid had a significant impact on plate deformation. This additional loading needed to be incorporated in to the optimisation process outlined in figure 5.2 which saw the aero-structural solver included into the optimisation procedure. For each perturbation within the optimiser there was an aero-structural iteration which included the initial finite element analysis of the perturbed design variables. If the structural solution had not yielded, a CFD analysis was carried out to provide the aerodynamic pressure field. This was then applied to a second FEA which provides a deformed geometry with actuation and aerodynamic pressures. This geometry was then meshed and the CFD run until convergence. This process represented a single aero-structural iteration and provided the aerodynamic field surrounding an actuated, pressure loaded SCB which was used to calculate the performance metric.

5.1.3. Performance Metric

The performance metric is an important part of the optimisation procedure and selecting a suitable metric determines the effectiveness of the optimisation study. As introduced in the parameterisation section, the design variables needed to be able to significantly influence the solution in order to determine what contributes a good design. The measure of performance is often chosen to be a global aerofoil parameter such as C_l or C_D, however, here it was chosen to be a surface based performance metric to quantify the performance of adaptive SCB with respect to the local pressure distribution.

From the previous research in the field of static SCB outlined in chapter 2, it has al-

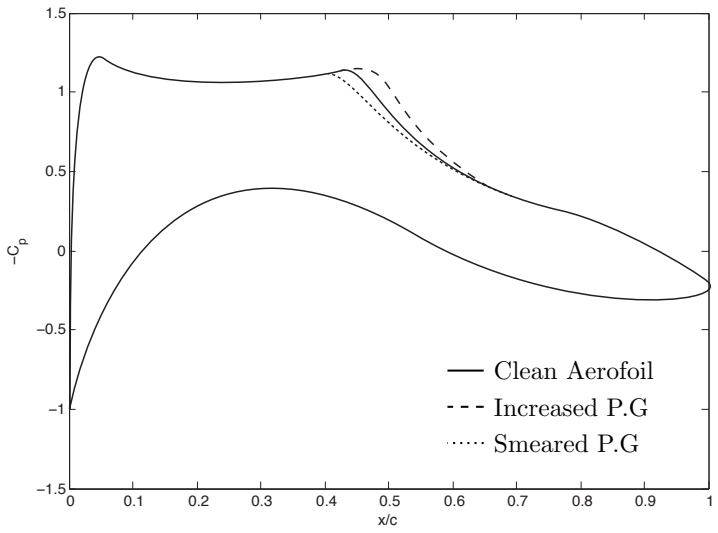


Figure 5.4.: Illustration to highlight the desired pressure smearing alongside the clean aerofoil pressure distribution and an increased pressure gradient.

ready been widely proven that SCB are capable of reducing drag when located beneath a shockwave through optimising for C_l, C_D and L/D. The surface based objective function aims to smear the pressure rise across the shock as much as possible and bridge the gap between optimising for global variables (C_l, C_D and L/D) and small scale experimental studies [Colliss et al., 2014]. The theoretically optimal, smeared C_p distribution over the aerofoil is shown in figure 5.4 with the necessary pressure difference smeared across the control region. Eliminating the shock will remove the negative effects of such a flow feature such as increases in entropy, adverse pressure gradients and sudden boundary layer thickening/separation. By focussing the performance metric in the region of control, the values generated will be much more sensitive to changes in bump geometry rather than a single C_l value which disguises the SCB effect in the pressure distribution over the entire aerofoil.

The optimisation procedure for adaptive SCB can utilise the wealth of research undertaken for static SCB especially for the initial design variable values. The previous research has highlighted the importance of SCB position and SCB height which can be directly influenced through the design variables. It is important to note that whilst the actuation height can be controlled by the optimisation process through δ_1 and δ_2, the aerodynamic loading may actually increase the overall SCB height. The aim of

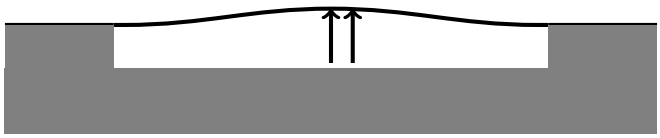


Figure 5.5.: Typical SCB geometry when subject to actuator loading.

this process however is to produce an aero-structurally optimal SCB for a given flight condition. The existing static SCB studies evaluated in Chapter 2 have reduced the size of design space for an effective SCB. The bounds applied to the design variables conform to the following conditions:

$$\begin{aligned} 0.35 &\leq B_1 \leq 0.55 \\ 0 &\leq x_1 \leq 0.99 \\ 0 &\leq \delta_1 \leq 8 \\ 0 &\leq x_2 \leq 0.99 \\ 0 &\leq \delta_2 \leq 8 \\ &\text{With } x_1 < x_2 \end{aligned} \tag{5.3}$$

An aspect specific to actuated SCB is the performance of the plate material under both actuation and aerodynamic forces. The goal of actuated SCB is to be able to deploy and retract upon demand and so the material must not undergo irreversible changes such as plastic deformation. With this in mind, a structural constraint is applied to the optimiser which will heavily penalise any combination of design variable that causes the maximum von Mises Stress to exceed the yield stress as expressed in equation 5.5.

This structural constraint significantly reduces the number of valid shapes that are produced by the optimiser. It effectively limits the actuation heights (δ_1, δ_2) for a given actuator position (x_1, x_2). As such they tend to follow the geometry illustrated in figure 5.5.

The combination of an initial deflection followed by a crest region and a curving rear surface results in broadly similar pressure distributions around the aerofoil. An example of which is illustrated in figure 5.6. One particular feature of the upper surface pressure distribution around the shock region is the presence of inflection points where the gradient changes sign. Physically, these inflection points represent accelerations of the flow which are bad for the overall performance of the aerofoil due to the increased likelihood of secondary shocks.

The inflection points are a direct result of the family of geometries generated by the aero-structural design process which is based upon the geometry of a bending plate.

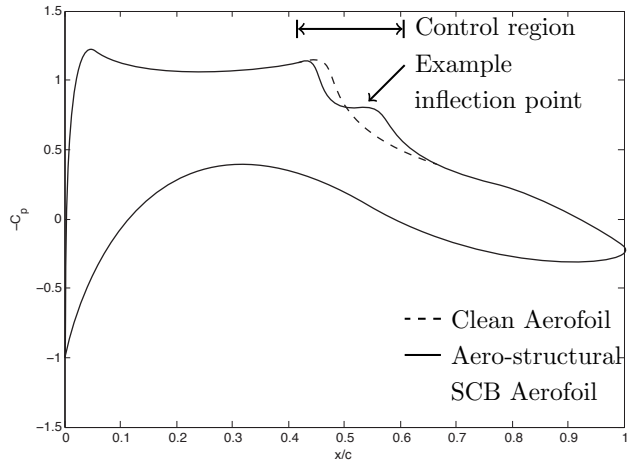


Figure 5.6.: Schematic diagram illustrating a typical pressure coefficient distribution around aerofoil fitted with an actuated SCB.

The presence of such points makes it a suitable attribute to utilise in the objective function.

By applying the design variables to the FE analysis, the structural deformation is computed. The deformed geometry is then applied to the clean aerofoil and the surface remeshed in preparation for the CFD analysis. The resulting pressure field is then applied to the plate and the FE analysis is completed. At this point the stress constraint may or may not be activated. This aero-loaded actuated plate geometry is meshed for CFD and run. The aero-elastically converged solution produces a C_p distribution of which an example has been provided in figure 5.7a which focusses on the shock region. This is the basis for the objective function and performance metric.

The gradient of C_p is then calculated with respect to chordwise distance. It is calculated at the locations above the plate $B_1 \leq x/c \leq (B_1 + l_b)$. The locations where $dC_p/dx = 0$ then form a subset of values which are represented by the circles in figure 5.7b. Combined with the locations at the start and end of the SCB they provide the key locations to optimise and are contained within f below.

$$f = \left[C_p(B_1), \quad C_p\left(x|_{\frac{dC_p}{dx}=0} \right)_i, \quad ..., \quad C_p(B_1 + l_b) \right] \quad \text{for } i = 1...n \tag{5.4}$$

where n is equal to the number of inflection points i.e. where $\frac{dC_p}{dx} = 0$

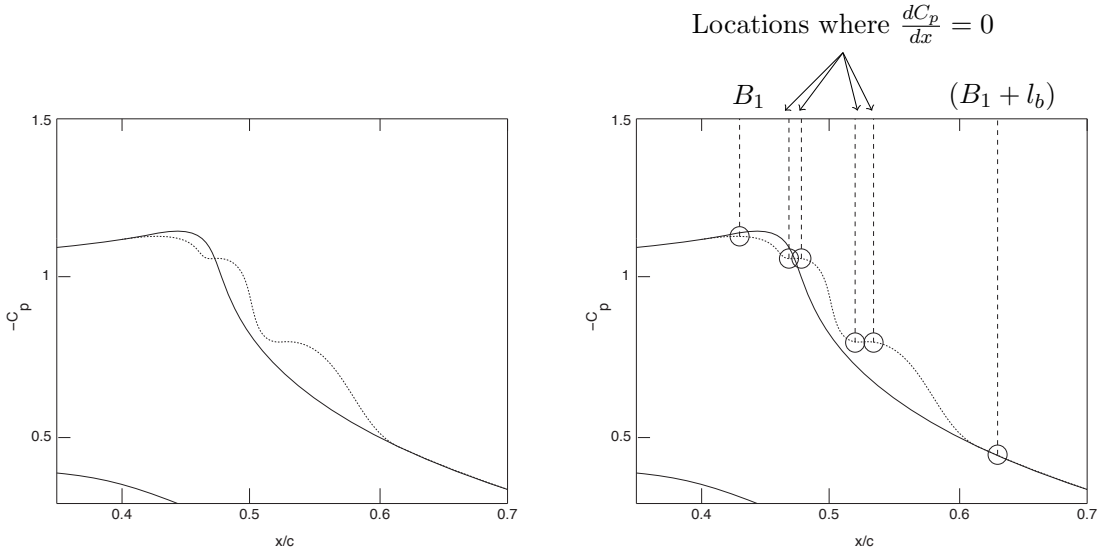


Figure 5.7.: a) An illustration to show a typical C_p distribution over an aerofoil fitted with an aero-structurally designed SCB. b) An annotated version to highlight the the locations that make up f in equation 5.4.

In the unlikely event that there are no locations where $\frac{dC_p}{dx} = 0$, this set contains the C_p values at the start and end of the aero-structurally deformed SCB. The difference between the values in f is used to provide a differential that represents approximate gradients between the inflection points. In order to smear the pressure rise, the largest gradient is targeted and minimised by the optimiser. This produces an objective function of the form:

$$
\begin{aligned}
g &= \max\left(\left|\frac{\Delta f}{\Delta x}\right|\right) \\
\text{s.t.} \quad & \sigma_{max} \leq \sigma_y(1-k) \quad \text{(stress contraint)} \\
\text{s.t.} \quad & 0.99 \leq \frac{C_l}{C_{l,clean}} \leq 1.01 \\
& \text{Optimiser} : \min(g)
\end{aligned}
\tag{5.5}
$$

where the safety factor k is set at 10%, and σ_y is assigned the yield strength of the selected material. C_p is the pressure coefficient. Another constraint is added based upon the change in lift coefficient. It is set to penalise any design that changes the lift coefficient by more than 1%. The goal of the optimiser is to minimise g.
In order to relate the objective function to the clean aerofoil, a performance metric was devised as:

$$M = \left[\left|\frac{\Delta C_p}{\Delta x}\right|_{B_1}^{(B_1+l_b)}\right]_{clean} - \min(g) \tag{5.6}$$

The first term represents an effective pressure gradient of the clean aerofoil between the locations B_1 and $(B_1 + l_b)$.

$$\Delta C_p|_{clean} = \left|\frac{C_p(B_1 + l_b) - C_p(B_1)}{(B_1 + l_b) - B_1}\right|_{clean} \tag{5.7}$$

The value changes depending upon the B_1 value specified in the design parameters of each aero-structural design perturbation. For reference, this is the same term that features in the objective function, g when there are no inflection points in the C_p profile. This means that for the clean aerofoil:

$$\begin{gathered} \frac{\Delta C_p}{\Delta x} = \left|\frac{C_p(B_1+l_b)-C_p(B_1)}{(B_1+l_b)-B_1}\right| \\ g = |\frac{C_p(B_1+l_b)-C_p(B_1)}{(B_1+l_b)-B_1}| \\ \text{and } M = \frac{\Delta C_p}{\Delta x} - g \\ \therefore M = 0 \end{gathered} \tag{5.8}$$

When g is successfully minimised, the performance metric value is highest. This is presented in figure 5.8 and discussed throughout this chapter. Poor placement of a SCB could actually increase the effective pressure differential which could result in negative metric values as seen by iterations 1, 3 and 4 in figure 5.8a. This could have been caused by moving the pressure peak further downstream compared to the clean aerofoil as illustrated in figure 5.4.

The smearing of pressure rise over the SCB reduces the chance of separation due to the reduction in adverse pressure gradient over the upper surface. Upon an aerofoil,

the risk of separation is increased by both the initial curvature and the curvature added by the SCB. This was seen to some extent in Chapter 4 where the flexible plates with higher levels of curvature were susceptible to boundary layer thickening and possible separation. These factors will affect the performance metric which is able to identify poor design choices and produce aero-structurally optimised actuated SCB.

5.2. Results

5.2.1. Optimal Adaptive SCB designs

The aero-structural optimisation procedure took on average eight iterations to produce an optimal design. Optimisation convergence was defined when the changes to the design variables were below 0.001 m which were the manufacturing tolerances on the location of the actuator strips. The design variables explored the design space via the centred finite difference scheme which resulted in 15 initial perturbations to the initial conditions.

Figure 5.8 shows the variation of key parameters throughout the optimisation process from two initial conditions that represent a shorter and taller SCB. For both initial conditions presented, the most influential decision variable was SCB position. This was due to the large pressure gradient across the shock and the sensitivity to surface curvature. It can be seen that in the two initial conditions presented the SCB position converges to 0.43 which positions the shock on the front surface. The optimiser recognises the dominance of SCB location and the evolution of optimal SCB placement can be seen in figure 5.8d. Table 5.1 shows the initial conditions submitted to the optimiser and the subsequent optimal solution.

The performance metric proved to be sensitive to the presence of a SCB which confirmed the choice of this new pressure gradient based performance metric. The optimiser showed that bump position had the greatest effect upon performance primarily due to the change in shock structure around the SCB crest. The performance metric responded to a reduction in actuation height ($\delta_1,\ \delta_2$) but actuation position along the SCB ($x_1,\ x_2$) was not as influential.

The structural constraint set at $\max(\sigma_{vM}) < \sigma_y(1-k)$ is shown to successfully influence the design in figure 5.8e. Once the optimiser iterates and produces a design that exceeds the yield stress, such as iteration 5 of the tall bump initial condition, the design is penalised. The later iterations do not exceed this failure criterion fulfilling the constraints purpose within the optimisation procedure.

	$B_1(\%C)$	$x_1(\%l_b)$	δ_1(mm)	$x_2(\%l_b)$	δ_2(mm)	σ_{max}(MPa)	M
Initial Condition	0.47	0.5	3	0.55	3	308.4	0.57
Optimal Solution	0.43	0.25	1.45	0.5	1.49	170.02	0.5491

Table 5.1.: Optimal SCB decision variables for the initial condition and optimal solution, 2 point actuation.

The effects on the overall lift coefficient are minimal between each iteration, there is a small constant loss compared to the clean aerofoil but as this offset is constant it could be addressed by trimming the aircraft.

Figure 5.9 illustrates the freestream supersonic region and shock location away from the SCB remained stable throughout the iterations with the free stream normal shock at 0.49c with significant changes only occurring within the shock-foot region. Most notable was the shift from the weak shock-boundary layer interaction (SBLI) to a bifurcated shock. This is visible at $\mathrm{x} \sim 0.5\,c$ between the experimental result and the region labelled SCB in figure 5.9.

Comparing the variation of each parameter throughout the iterations shows each parameter has varying influence upon the performance. These iterations also provide a large data source for the off-design flight conditions which is important for the justification of adaptive SCB and is discussed further in section 5.2.2.

In order to design an effective SCB, the ramp section must give a pronounced departure from the existing aerofoil surface. Placing the SCB too far upstream prior to the $y_{u,max}$ location on the aerofoil will continue to accelerate the flow prior the crest and result in a stronger normal shock without any bifurcation. This is similar to the low cavity pressure flexible plate test case in section 4.1. The effect is illustrated in figure 5.10a where the supersonic region can be observed to extend beyond the crest, thus increasing the strength of the shock. Additional viscous losses were also incurred with the stronger shock caused by the thickening of the boundary layer which could lead to separation. Figure 5.10c shows the SCB positioned too far downstream which resulted in significant acceleration of the post-shock flow. The resultant expansion caused large scale curvature of the flow and led to a secondary supersonic region. For an optimal solution, figure 5.10b, a bifurcated shock structure was achieved without any regions of re-acceleration upstream or downstream and was achieved with careful management of the curvature near the shock region.

The curvature of the rear surface of the SCB was determined by the combination of actuation and aerodynamic pressure loading. The FEA results in figure 5.11 show the

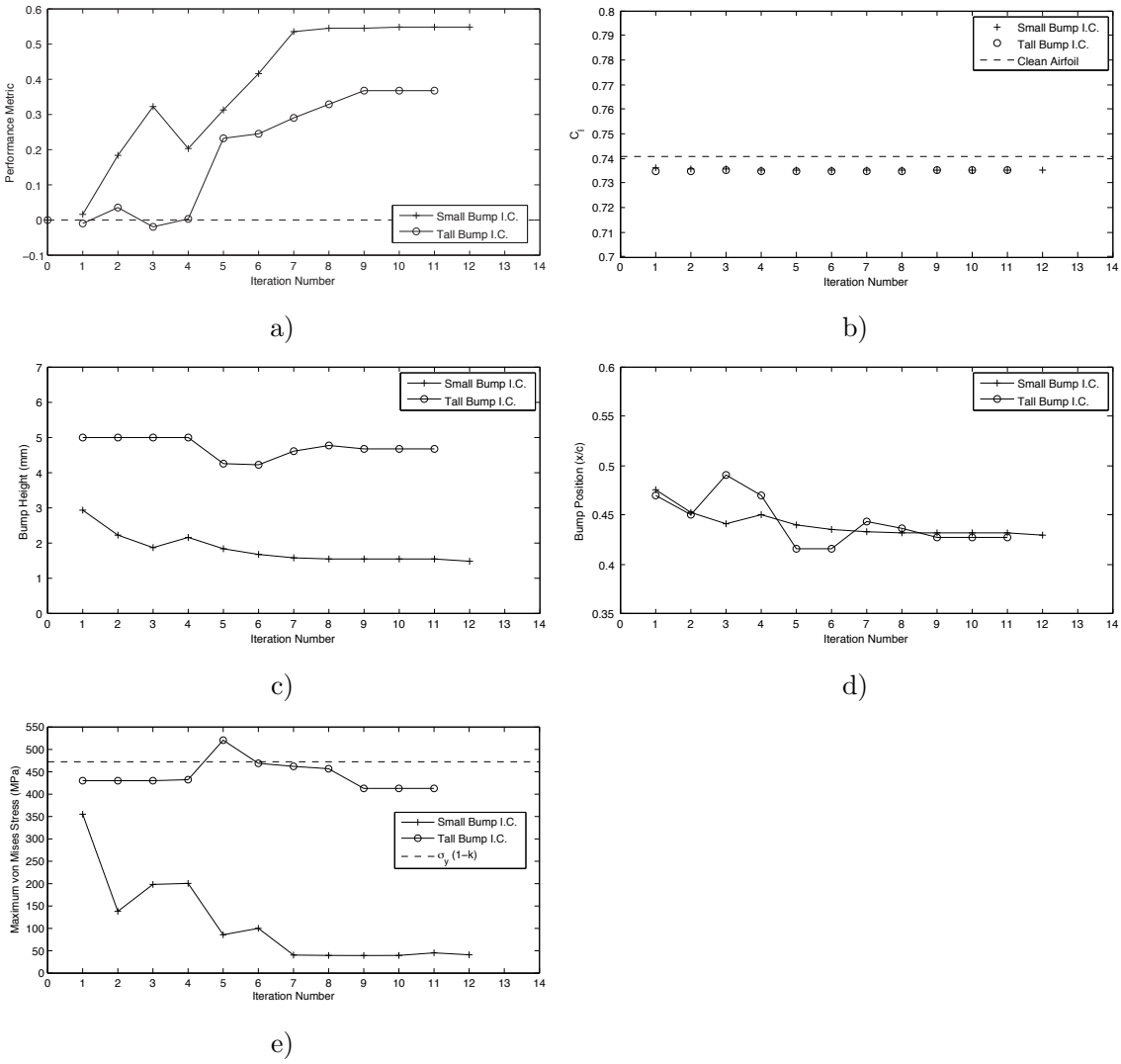
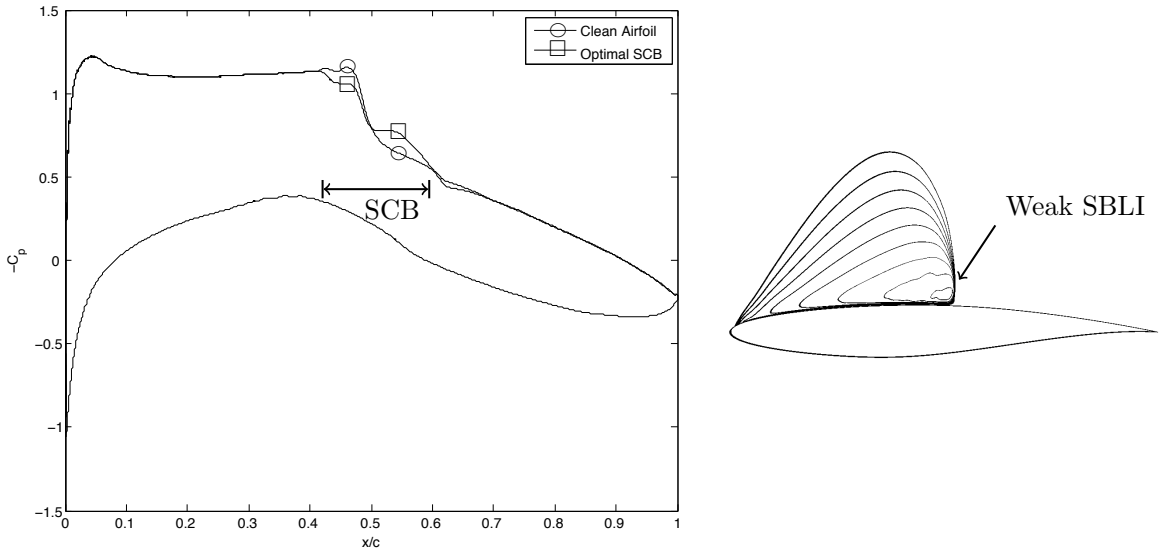


Figure 5.8.: Key performance data through the iterations of the optimisation procedure. a) Performance metric. b) Lift coefficient. c) Bump position. d) Bump height. e) Maximum von Mises Stress within adaptive SCB. Where presented, iteration 0 marks the clean aerofoil.



a) b)

Figure 5.9.: The effect of introducing a SCB. a) Pressure coefficient profiles for the clean aerofoil, $\alpha = 3.19°$, M_∞=0.728, Re $= 6.5 \times 10^6$. b) Mach contours for the clean aerofoil.

geometries and stress distribution surrounding the optimal plate due to the actuation. The addition of the pressure load to the optimal design significantly increases stresses, particularly at the clamped ends. The peak stress was observed at $x = 0.43c$ as a combined result of the pressure and displacement loading. This was where the pressure difference across the plate was at its largest. In combination with the pressure loading the actuation height constrained the deformation of the plate and helped control the curvature.

Figures 5.8a and 5.8c shows that as the optimiser progresses towards an optimal solution, the actuation height decreases slightly. At this aero-structural optimal, the plate exhibits a maximum stress that is well within the yield stress of the material which provides a large safety factor in terms of material failure by plastic deformation. This removes the concern that these plates will fail due to the aerodynamic pressure loading.

The optimal actuation heights represent the target displacement. However SCB performance over a range of bump heights is an important question for adaptive SCB that needs to be answered in order to predict the aerodynamic performance during bump deployment. To investigate this, a parametric study exploring the design space has been carried out and the results are reported in the following section.

5.2.2. Off-Design Performance

During cruise, aircraft are often required to vary speed and altitude. These manoeuvres are likely to change shock location with respect to any SCB installed on a wing [Eastwood and Jarrett, 2012]. Throughout the optimisation process, numerous perturbations were applied to the initial design variables to find an optimal value. These perturbations had positive or negative effects as the optimiser explored the design space. In this section, the off-design performance of a wing with a SCB and how the deployment of a morphing SCB may impact performance is explained.

Non-optimal solutions encountered during the optimisation process provide a wealth of information about off-design performance. Pressure fields from all of the perturbations have been analysed to investigate the effects of a non-optimal design. The most influential variable in overall bump performance is SCB location, in particular the position of the shock relative to the crest of the SCB. This dependency has been identified previously as an important design variable by Qin et al. [2008] and experimentally in the previous flexible plate chapter. The second most effective design variable was the bump height; this dictated the flow quality over the SCB and the overall performance for a given SCB location. This was seen to some extent in the previous on-design section

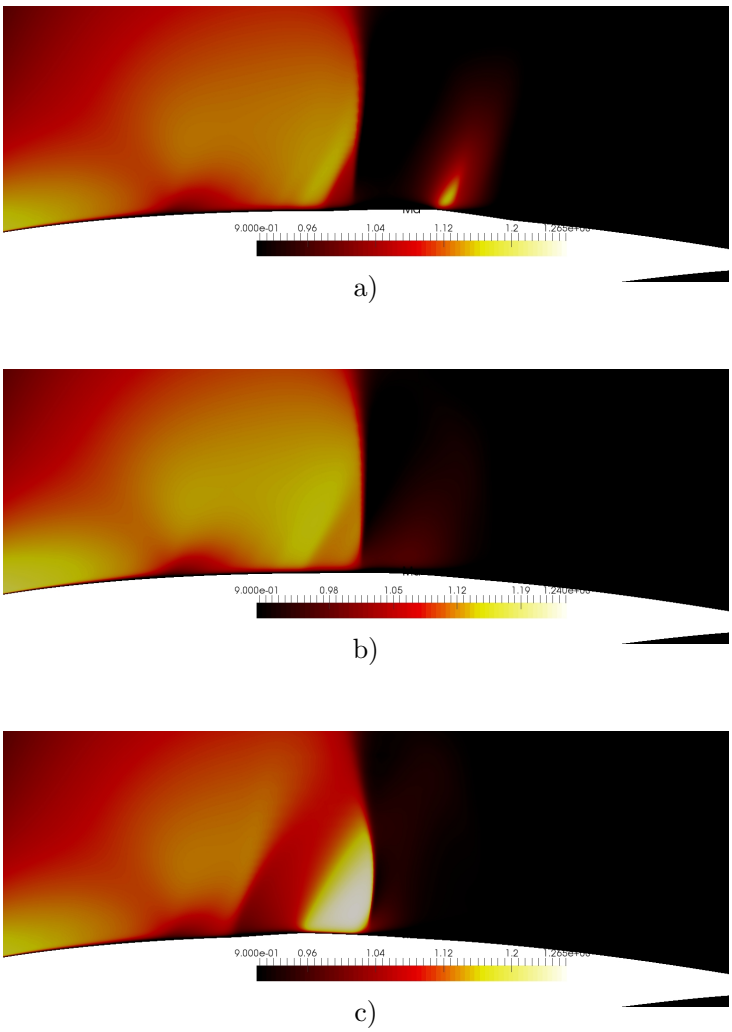


Figure 5.10.: Mach fields showing the effects of SCB position focussing upon the supersonic regions for a) upstream SCB ($B_1 = 0.36$), b) optimal SCB ($B_1 = 0.43$), c) downstream SCB ($B_1 = 0.47$).

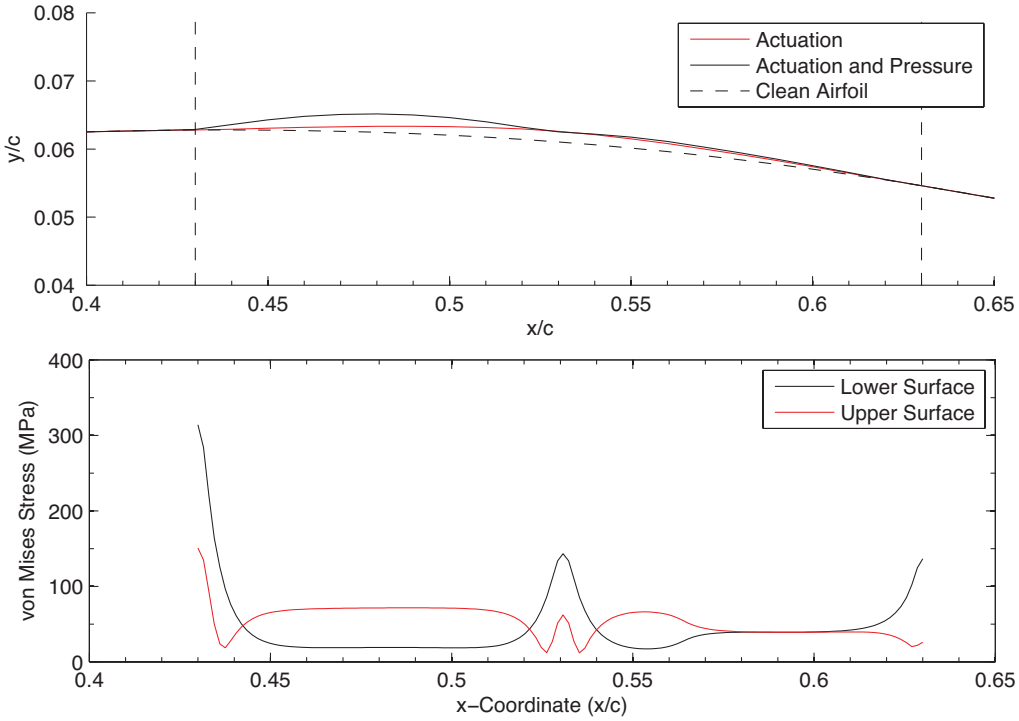


Figure 5.11.: Structural modelling of adaptive SCB. Surface and centreline vertical displacement and centreline von Mises Stress for upper and lower surfaces.

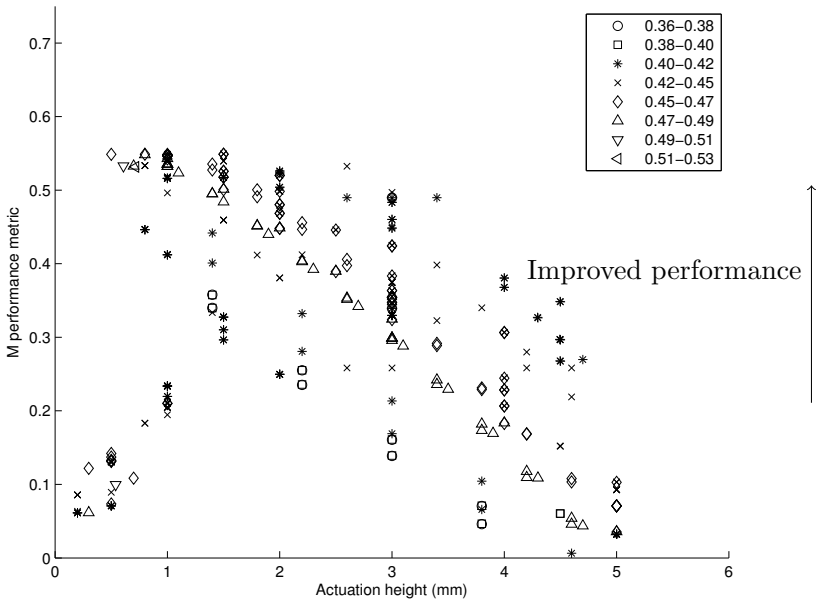


Figure 5.12.: Performance vs. bump height grouped by streamwise positions. The data was extracted from multiple optimisation and parametric runs.

although it was often referred to as the effects of curvature as the two are closely linked.

Grouping the results of both a parametric study and the optimisation perturbations with respect to height and position provided a detailed view of the design space. Figure 5.12 shows how the actuation height of the SCB crest has a significant effect when it comes to maximising performance which is a measure of the SCB ability to bifurcate the shock.

The SCB geometries that form figure 5.12 show the variation in performance with bump height for non-yielding solutions. The limits imposed by the structural constraint were in place during all the perturbations and restricted the overall height and shape of the SCB. For all locations, the presence of a tall bump caused a significant drop in performance. This can be explained by the fact that the undesirable shock structures in figures 5.10a and 5.10c are more often encountered with when taller SCB are tested.

The main trend in figure 5.12 is that taller SCB have worse performance than shorter SCB with the performance metric dropping almost linearly from around 0.55 to 0 as the actuation heights (δ_1, δ_2) are increased. An exception to this trend is observed for small actuation heights (typically $\delta < 1\,\text{mm}$) where performance is poor.

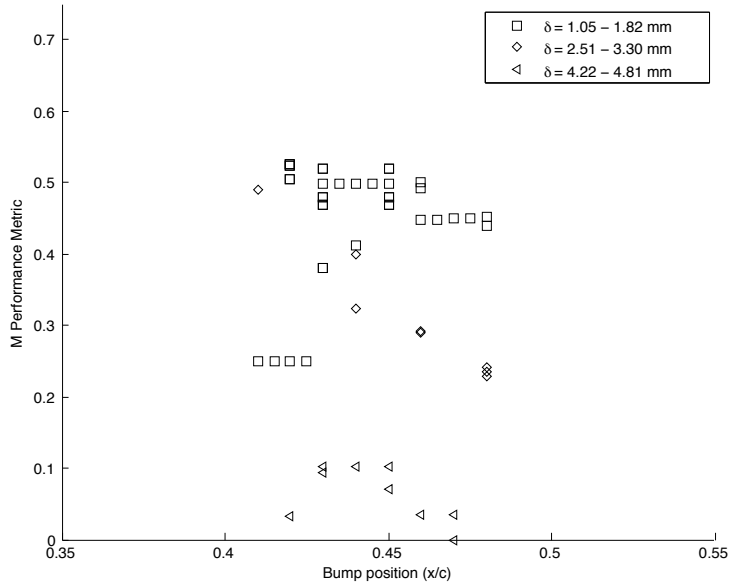


Figure 5.13.: Performance vs. bump position grouped at various heights. Reduced dataset compared to figure 5.12 for clarity

The reason for these two distinct groupings is due to the shock structure. As an actuated SCB is deployed there is some positive effect as the pressure rise is smeared and the pressure gradient is reduced sightly. It is at a displacement of 0.5 mm at which the bifurcated shock structure is first achieved (upper left quadrant, figure 5.12). It is this transition between shock structures that forms the lower bound of beneficial SCB heights. Exploring this lower bound of bump actuation heights is important as the detrimental viscous effects seen with higher bumps are minimised.

The position of this first λ-shock inducing bump ($B_1 = 0.45c$) places the shockwave at $0.4l_b$ which is just on the front surface of the SCB. This placement with respect to the shock was very sympathetic to the flow as there was still a significant stream wise region of curvature after the shock, before the flow was subjected to the large convex curvature around the crest. This minimised the likelihood of curvature-induced separation and reacceleration which was often seen in the flexible plate cases. Whilst this minimised the likelihood of reacceleration, however, it does not make use of the potential that comes with maximising the size of the bifurcation which is directly linked to overall performance [Stanewsky et al., 2002].

By identifying the groups of bump position in figure 5.12 it can be seen that there are

some better performing locations. The common trait is that the best performing designs place the crest immediately downstream of the shockwave. The effects of separation are discussed further in the following section but these optimal designs balance the ability to initiate an efficient bifurcated shock and manage the surface curvature in the shock vicinity.

Figure 5.13 shows the performance variation with bump start position. Alternate height ranges were selected to show banding between SCB heights. The performance jump identified in figure 5.12 between a normal and bifurcated shock structure can be seen for the smallest actuation heights, $1.05 < \delta < 1.82$ mm where the metric rises from ~ 0.25 to 0.55. A subsequent slight drop in performance can be seen as the position of the SCB progresses downstream from 0.43. Slightly taller SCB $2.51 < \delta < 3.30$ mm show how relatively good performance can be achieved when the SCB is optimally positioned $B_1 = 0.43c$. But as the SCB is positioned too far downstream the performance drops off much quicker than the smaller SCB. This goes some way to highlight the wider performance envelope of smaller pressure loaded SCB which are more effective for a wider range of shock positions.

The sensitivity of the flow to the shock position/crest location ratio previously documented by Qin et al. [2008] is supported here. The shock position on the clean aerofoil was calculated to be at 0.495c. With crests found near $0.5\,l_b$ the best performing bumps were within the range $0.43 \leq B_1 \leq 0.45c$. This placed the SCB crest location between $0.51 \leq x_1 \leq 0.575c$ and put the rear shock leg on the front face of the SCB. This was the traditional position governed by the overall pressure field with subsonic flow down the rear face of the SCB. The structural constraint seemed to have little effect on the optimal position between the rear leg and the SCB crest.

The position of the crest with respect to the start of the bump, x_1, x_2, had little effect on the performance metric with no correlation found in the range of values permitted. The range covered by the optimisation was $0.3 \leq x_1, x_2 \leq 0.7c$ which was primarily restricted by the structural constraint as positions outside of this range significantly increased the maximum stress levels at the clamped edges and were penalised.

With the optimiser suggesting smaller bump heights are capable of superior on-design and off-design performance, the stresses within the system are reduced which will prolong the life of the system with respect to fatigue loading. Repeatable deployment is one of the keys to the use of adaptive SCB and this optimisation study has highlighted that optimised actuated SCB can remain within the elastic regime.

From figure 5.12 and 5.13, the best performing actuation heights are within the range $0.8 \leq \delta_1 \leq 1.7$ mm and the addition of a structural constraint to the optimisation has

not limited the bump heights nor their ability smear the pressure rise. Figure 5.14 shows the effect of varying SCB height and how the pressure distribution changes. Figure 5.15 shows the Mach contour plots of the same SCB heights. These pressure coefficient profiles represent bumps at the optimal position, $B_1 = 0.43c$ whilst increasing the SCB crest height. This was done to represent a SCB during deployment with the actuation height increasing beyond the optimal value. The aerofoils with larger actuation displacements exhibit large low pressure regions between $0.52 \leq x \leq 0.63c$ which included regions of separated flow as indicated by the wall shear stress in figure 5.16. This was because the plate curvature around the crest region was too great for the flow to remain attached.

As the actuation height increased, the maximum ramp angle of the front surface of the SCB increased, together with the strength of the oblique shock and resulting pressure gradient. This can be seen by the increasingly sharp rise in C_p observed at the very upstream extent of the control region, $0.41 < x < 0.43c$. The greater initial oblique shock strength reduced the Mach number present over the front surface of the SCB and reduced the strength of the rear leg as illustrated by the smaller rise in C_p around $0.47 < x < 0.50c$. This minimised the chance of post-shock separation due to the adverse pressure gradient which is monitored by the wall shear stress. But means the Mach number downstream of the rear leg is very close to 1 and so reacceleration is more likely.

Figure 5.16 shows how the stream wise wall shear stress varies along an optimally positioned SCB over a range of heights. For solutions shorter than the optimal solution, the flow remained attached over the SCB. For taller SCB ($\delta > 1.75\,\text{mm}$) a separation bubble appeared around the crest indicated by $\tau_w < 0$. Despite the flow reattaching the presence of a separation bubble was not ideal for maintaining boundary layer health This also confirmed the position-height relationship as an important characteristic for the pressure gradient, the shock structure and the viscous contribution to the overall aerofoil performance.

Global Aerodynamic Performance

The aero-structurally optimised SCB do not cause flow to separate over the crest. This shows the effectiveness of the pressure gradient based performance metric. In contrast to other optimisation studies [Lee et al., 2011a,b, Yagiz et al., 2012, Qin et al., 2008] the performance metric is designed to include an element of flow quality in the control region at the highest optimiser level. The global variables such as $C_l, L/D$ are included

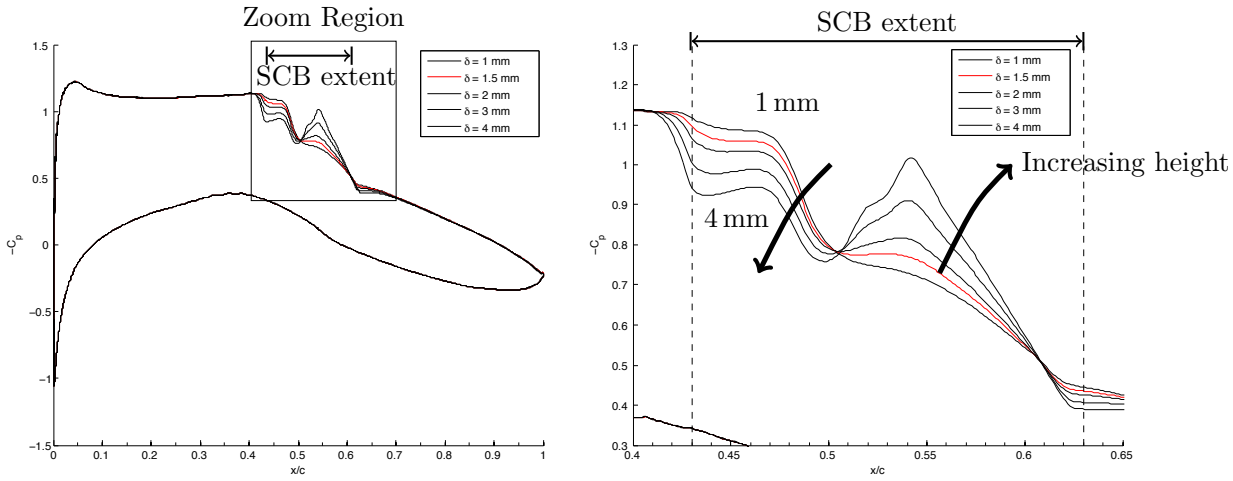


Figure 5.14.: Pressure coefficient profiles for optimally positioned SCB with varying bump heights with a fixed location of $X_1 = 0.43c$

for monitoring purposes but because static SCB are a proven concept there is little worth focussing upon the lift coefficient to assess the SCB performance. Figure 5.17 shows the L/D values for an optimally positioned SCB for the range of heights also shown in figures 5.14 and 5.16.

Figure 5.17 shows that the maximum change in L/D was quite small with $\Delta L/D < 0.6\%$ with respect to the clean aerofoil. By analysing the pressure profiles from figure 5.14 and the resultant lift-drag components the source of the L/D was found to be a slight decrease in C_l as actuation height increased. The addition of an aero-structurally optimised SCB does not appear to affect the global aerofoil performance characteristics but managed the shock region very well. This paves the way for the use of much stronger shock waves to maximise the region of low pressure on the upper surface.

5.3. Summary of Optimal Adaptive SCB Design

The aero-structural optimisation procedure has resulted in a new family of SCB geometries that are capable of bifurcating the shockwave and reducing the stream wise pressure gradient. This was the target for adaptive SCB with the design evolving from a purely flexible plate to include small actuators to control the displacement. The added control not only constrains the displacement at the actuation locations but also the curvature which was seen to have a large effect when left un-constrained as in the previous chapter.

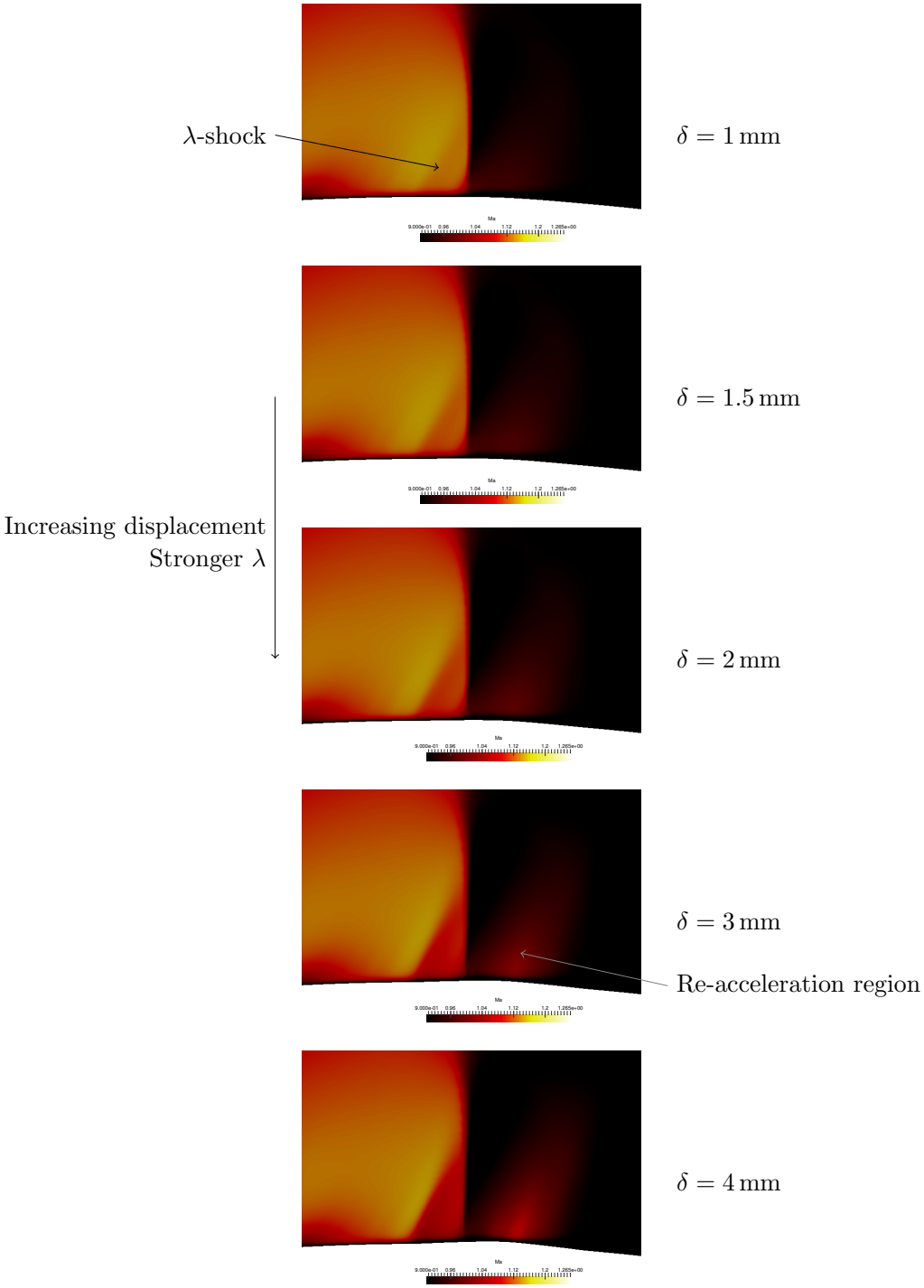


Figure 5.15.: Mach values plots for increasing actuator displacement. $\delta = 1,\ 1.5,\ 2,\ 3,\ 4\,\text{mm}$. at bump location $X_1 = 0.43c$.

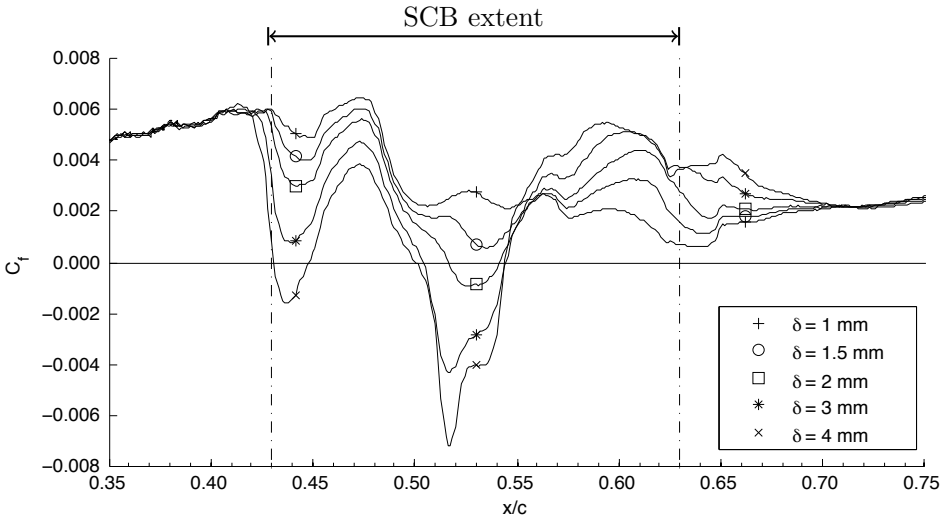


Figure 5.16.: Wall shear stress coefficient for varying bump height in the optimal location $X_1 = 0.43c$.

The optimiser has successfully incorporated the combined actuator and aerodynamic pressure loading and improved the precision and quality of the aerodynamics in aerostructural studies in terms of the resolvable length scales. The small scales were possible due to the quality of the mesh used in the CFD with $y^+ < 5$. Figure 5.15 shows the increase in the size of the low pressure re-acceleration region as the actuation height and therefore curvature increases above the optimal value.

An estimation of the shock structure during deployment was made from the quasi-steady assumption where the shock structure is purely a function of the plate geometry at that time. The effects of deployment were presented in figure 5.14 and 5.15 which showed large pressure gradients downstream of the shock if the actuation became too large $\delta > 3\,\text{mm}$. In combination with the actuator load, these may cause the flow to separate however the resolution of the solution allows for wall shear stress to be calculated reliably which is usually a good indicator of separation. The ability to identify these elements of small scale features was included in the performance metric: strong adverse pressure gradients followed by reacceleration regions are typical of SCB that trigger separated flow. The pressure gradient based performance metric aimed to bring the issue of flow quality to the highest level within the optimiser rather than merely a post-optimisation processing technique.

The optimal solution provides attached flow over the surface of the SCB which aims to maximise total pressure recovery. This was aided by the use of two actuation points

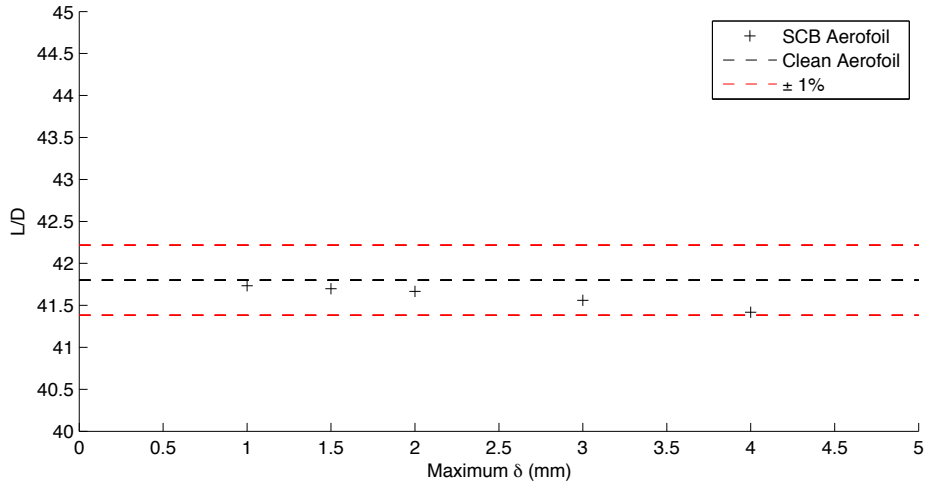


Figure 5.17.: L/D variation for increasing bump height. Clean aerofoil L/D ratio included for comparison.

which gave greater control over the surface curvature around the crest region and consequently the flow curvature than was possible with just a flexible plate.

The next challenge is to incorporate these optimal SCB in to an experimental test rig to compare against the unconstrained flexible plates to further validate the design introduced in this section. In particular the transient response of the actuated SCB during deployment is to be considered.

6. Actuated Adaptive SCB

The research presented in this study has seen the design approach evolve from a passive flexible plate to a stiffer, tightly constrained optimised design featuring multiple actuators. In this chapter, the optimised SCB geometry will be tested amongst actuated designs in a blowdown supersonic wind tunnel facility in order to assess performance. The main goal of actuated adaptive SCB is to bifurcate the shock wave as stated in chapter 4. This will be evaluated in this chapter by analysing the shock structures present. Through a similar approach to that adopted for the flexible plates in chapter 4, the aerodynamic and structural response will be discussed individually before detailing the fluid-structural interaction.

6.1. Optimal SCB Test

The optimal SCB design from chapter 5 was selected for the experimental model. The values were

The manufacture of the adaptive SCB test cases began with an identical process to that of the flexible plates. The test plates are designed to share common features and are produced on the same machine fixture. The addition of the spanwise actuation required additional components to enable the linear actuators to apply a uniform displacement across the width of the plate via spanwise strips of 5 mm key-stock which was wide enough to ensure a suitable thickness for the attachment of the actuators whilst remaining narrow enough to represent a line load across the span at a single stream wise location.

Figure 6.1 shows the plate geometries witnessed in the experimental model for actuation with and without aerodynamic loading. The geometry from the optimiser is also included and matches very well with respect to the plate geometry in the experi-

	$B_1(\%C)$	$x_1(\%l_b)$	δ_1(mm)	$x_2(\%l_b)$	δ_2(mm)
Optimal Solution	0.43	0.25	1.45	0.5	1.49

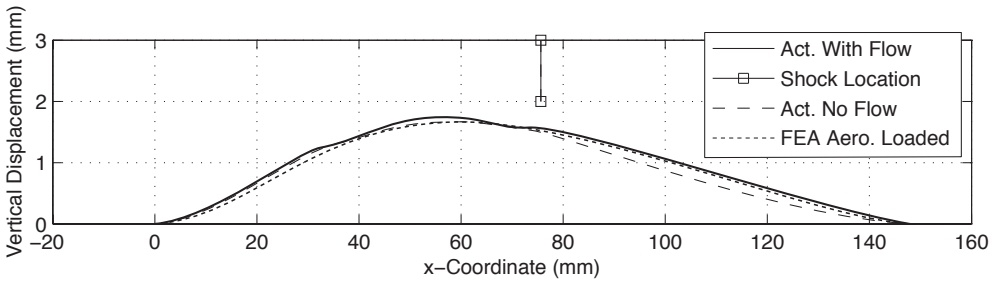


Figure 6.1.: A comparison between the predicted and experimental optimal SCB geometries with and without aerodynamic loading. $l_b = 150\,\text{mm}$ $t = 0.6\,\text{mm}$, $\delta_1 = 1.42\,\text{mm}$ at $0.25l_b$ ($x = 37.5\,\text{mm}$), $\delta_2 = 1.49\,\text{mm}$ at $0.5l_b$, ($x = 75\,\text{mm}$)

ment. There are small differences around the actuation locations at 37.5 mm and 75 mm which were due to the length-wise distance the actuator load was applied. In the physical model the strips measured 5 mm whereas it was possible in the FEA model to reduce them down to a single element in the mesh approximation with size $\mathcal{O}(1\,\text{mm})$.

These flat spots are present throughout the Schlieren image capture and are the result of interpolating across the thickness of the actuator supports. The model is installed in the working section to evaluate the transient performance of the optimal SCB to supplement the quasi-steady aero-structural optimisation. During the tunnel run, the optimal SCB is subject to a naturally oscillating shock within the working section of the blowdown wind tunnel. As with the flexible plate test cases in chapter 4, a constant total pressure ratio is maintained across the working section which aims to place a normal shock centrally on the SCB with some degree of inherent natural unsteadiness.

Figure 6.3 shows the vertical displacement of the plate and the shock position throughout the run. Figure 6.2c shows the variation of plate crest height. It can be identified using both figures 6.2 and 6.3 that immediately prior to the shock entering the frame at $t = 6\,\text{s}$, the most flexible region of the plate at 112.5 mm rises to a height of 1 mm.

As the shock passes on to the optimal SCB, the cavity pressure drops and the pressure differential across the plate drops causing a temporary reduction in the plate crest height. This is visible between 6 s and 7 s in figure 6.2. Either side of this loading there is also a reasonably large crest height at 5 s and between 7.2 s and 9.5 s. These deformations are due to the pressure differential across the plate as the tunnel was started. Once the tunnel was fully started ($t \geq 10\text{s}$), the flexible plate the actuators restrain the plate and the maximum plate displacement was limited to 1 mm until actuator deployment at $t \approx 16\,\text{s}$.

The actuation was applied for 5 seconds which is indicated in figures 6.2 and 6.3. The actuation is clearly defined between 16.1 s and 21.1 s. However it can be observed that the deployment time (0.3 s) is significantly shorter than the retraction time (1.0 s). This is likely because of the lower pressure on the upper surface of the plate aiding deployment and the actuators having to overcome this force during retraction.

Actuation of the SCB significantly changes the surface displacement beneath the shock, despite small actuation displacements. The evolution of the shock structure during actuator deployment is displayed in figure 6.4 and it can be seen that prior to deployment the shock structure is straight with only slight smearing at the wall courtesy of the boundary layer, figure 6.4.2. Figure 6.4.3 shows a Schlieren image when the shock is over the most flexible region of the optimal SCB. The shock structure is still a classical normal shock perpendicular to the wall however close to the wall, there is a slight build up of pressure waves that suggest additional curvature courtesy of a deformed surface. It should also be noted that in this region, there is also the reflection of an un-cancelled Mach wave from the nozzle that affects the local density gradient which the Schlieren technique is capturing but this is not thought to be important.

Figure 6.4.4 shows the shock structure during deployment. A bifurcation can be identified however the strength of the front leg is quite weak and the pressure waves only begin to coalesce some height above the surface. Figure 6.4.5 shows a more defined front leg that indicates a higher density gradient closer to the surface. The final image figure 6.4.6 shows the optimal SCB returned to the original flat plate geometry once the shock had retreated and tunnel was shut down.

The location of the shock throughout the run is presented alongside the location of the plate crest in figure 6.5a. Figure 6.5b shows the plate crest height throughout time and between the two graphs the transient FSI can be identified.

The deformation due to subsonic loading is present when $t < 6\,\mathrm{s}$ in the most flexible region of the SCB downstream of the actuation points. Between $6\,\mathrm{s} < t < 15\,\mathrm{s}$ the plate is retracted and the shock is very unsteady over the flat surface. This was not observed in the purely flexible plates of chapter 4 as there were no displacement constraints to maintain a flat surface. The previous lack of displacement constraint allowed for an element of separation however it also promoted higher levels of curvature over the rear surface. In contrast, the addition of actuators allows for control of the curvature upon deployment which delayed the likelihood of post-shock separation on the rear surface due to the levels of surface curvature. The effect of this control is exhibited in figure 6.4.4 in the rear leg of the bifurcated shock which remains relatively normal to the surface.

Figure 6.6 shows a comparison to a much larger actuation displacement $\delta_1 = 2\,\mathrm{mm}$,

$\delta_2 = 3\,\text{mm}$ in figure 6.6b the curvature around the crest of the plate is much lower in the optimal case the result is increased flow-field curvature. The comparison is indicated by the curvature of the rear leg in figure 6.4.4 and 6.6.4b.

The benefits of reduced curvature around the crest are that the boundary layer does not have to overcome significant changes in surface curvature and hence is more likely to remain attached. The Schlieren method does provide an insight into boundary layer heights however the density gradient variations across the boundary layer are very faint even with a horizontal knife-edge and edges of the boundary layers appear to be in very similar locations between the optimal and over-deployed cases in figures 6.4 and 6.6 respectively. The over-deployed SCB extends beyond the optimal value with $l_b = 150\,\text{mm}$ $t = 0.6\,\text{mm}$, $\delta_1 = 2\,\text{mm}$, $\delta_2 = 3\,\text{mm}$.

Figure 6.4 illustrates that during actuation, the shock remains in a comparatively steady location at a distance of 80 mm from the front of the SCB. It remains at this location throughout actuation. The deployment of the SCB caused the shock to move to this position. Prior to deployment $6\,\text{s} < t < 15\,\text{s}$, the normal shock was seen to oscillate over the front surface of the plate with amplitudes $\approx 15\,\text{mm}$. The surface deformation steadies the normal shock and fixes the location of the front leg. downstream of the plate crest compared to the flat plate with an average separation of 20.6 mm. This is in comparison to a 30 mm spacing for the equivalent $l_b = 150\,\text{mm}$ $t = 0.6\,\text{mm}$ flexible plate SCB (table 4.3) which was the stiffest passive flexible plate tested. The other, more flexible plates kept a distance of approximately 20 mm between the crest and the shock as they were significantly more flexible. With the optimal SCB, the plate system is made significantly stiffer by the addition of actuation. The surface curvature is the other effective change which has been minimised over the rear surface allowing the shock to sit closer to the crest. This minimises the any reacceleration upstream of the rear-shock leg avoiding an increase in shock strength.

The advantage of an optimally designed actuated SCB is the ability to deploy the SCB in an unsteady flow field and benefit from bifurcating the shock and minimising the negative effects associated with surface deformations such as re-acceleration regions and curved shock structures. The effects of SCB deployment beyond this optimal value are analysed in the following section with comparisons to the equivalent flexible plate test case.

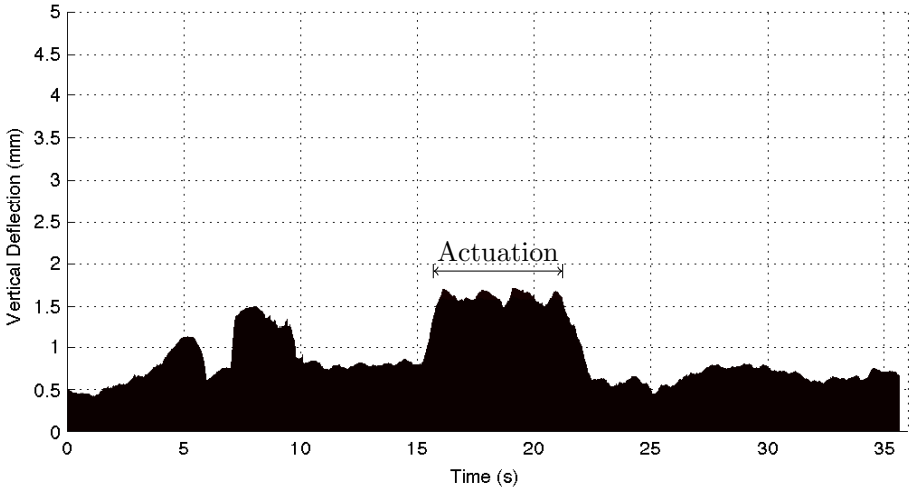


Figure 6.2.: Plate crest height through time. Optimal plate $l_b = 150\,\text{mm}$ $t = 0.6\,\text{mm}$, $\delta_1 = 1.42\,\text{mm}$ at $0.25l_b$, $\delta_2 = 1.49\,\text{mm}$ at $0.5l_b$.

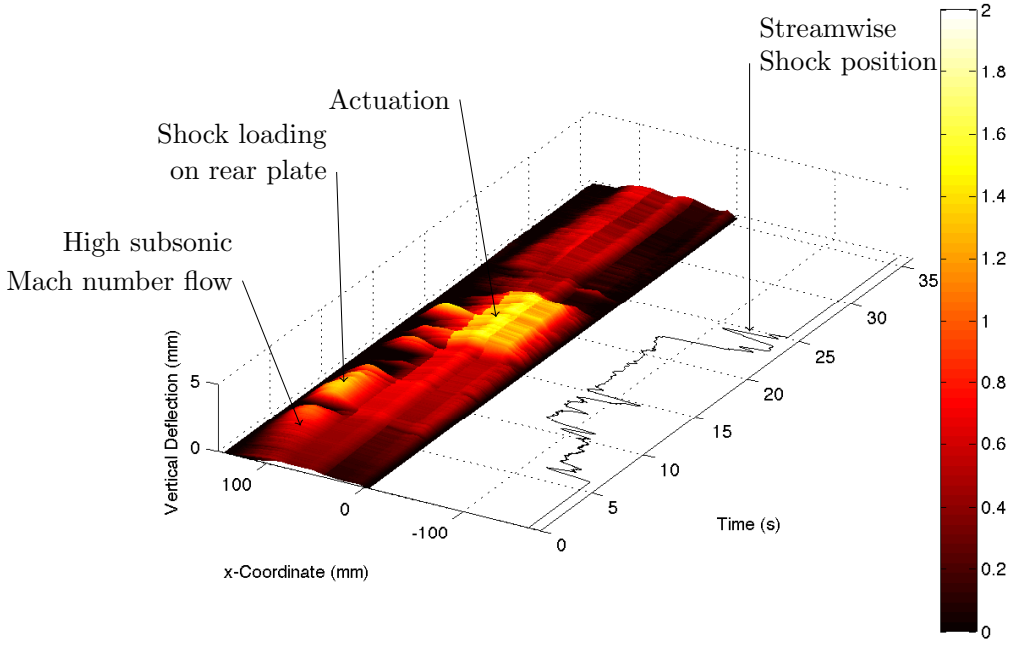


Figure 6.3.: Plate displacement through time for the $l_b = 150\,\text{mm}$ $t = 0.6\,\text{mm}$, $\delta_1 = 1.42\,\text{mm}$ at $0.25l_b$, $\delta_2 = 1.49\,\text{mm}$ at $0.5l_b$ actuated plate. Shock position moved upstream by 180 mm for presentation.



1) No aerodynamic loading

2) Retracted SCB

3) Retracted SCB

4) Deployed SCB

5) Deployed SCB

6) Shock Retreat

Figure 6.4.: Test case breakdown for optimal test cases. $l_b = 150\,\text{mm}$ $t = 0.6\,\text{mm}$ $\delta_1 = 1.42\,\text{mm}$, $\delta_2 = 1.49\,\text{mm}$ actuated plate.

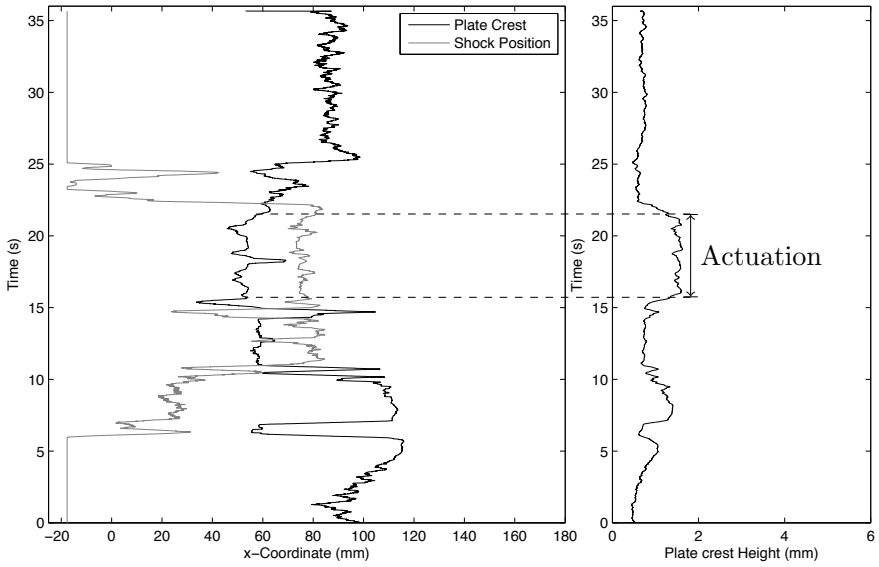


Figure 6.5.: Plate crest tracking through time for the $l_b = 150\,\text{mm}$ $t = 0.6\,\text{mm}$ optimal plate. a) Shows the location of the maximum plate displacement with respect to the location of the most rearward shock. b) Shows the magnitude of the displacement of the plate crest.

6.2. Experimental Response of an Actuated SCB

The general response of each actuated SCB test case can be broken down into three stages which are:

1. Subsonic flow over an un-deployed adaptive SCB
2. Supersonic flow over an un-deployed adaptive SCB
3. Supersonic flow over a deployed adaptive SCB

The first is encountered during start-up with the flow above the plate remaining subsonic. The second is where there is transonic flow over the plate and the actuators remain un-deployed. The third is where the flow is transonic and the actuators are deployed. These three distinct loading cases result in significantly different aerodynamic flow fields and plate geometries. The following sections will compare the effect of actuation and aerodynamic loading upon the aerodynamic and plate response between the optimal, over-deployed and flexible SCB.

6.2.1. Aerodynamic Response

Figure 6.6 shows the shock structure during test cases for the $l_b = 150\,\text{mm}$, $t = 0.6\,\text{mm}$ flexible and actuated plates. In figure 6.6a the plate geometry was a function of the pressure loading surrounding the shock and the pressure difference across the plate. The stiffness of the system could only be varied by the pressure difference across the plate which is directly affected by the cavity pressure. The only other parameters affecting the stiffness of the system were plate length and thickness which were fixed.

In figure 6.6b, the shock structure is shown as it passes over the over-deployed actuated plate. The shock structure throughout the run is presented with a clear difference between retracted and deployed states. The normal shock structure seen in figure 6.6b.2. and 6.6b.3. is very similar to the rigid wall Schlieren image in figure 3.20, chapter 3. There is some curvature close to the wall in figure 6.6b.2 where the location of the normal shock is above the most flexible region of the plate after the downstream actuation point which occurs for optimal and over-deployed SCB.

In the first stage of aerodynamic loading, with the flow remaining subsonic over the plate, there is little detail regarding the aerodynamics that can be directly obtained with Schlieren imaging due to the small variations in density gradient. This segment of the run is more relevant to the plate dynamics which are discussed in section 6.2.2.

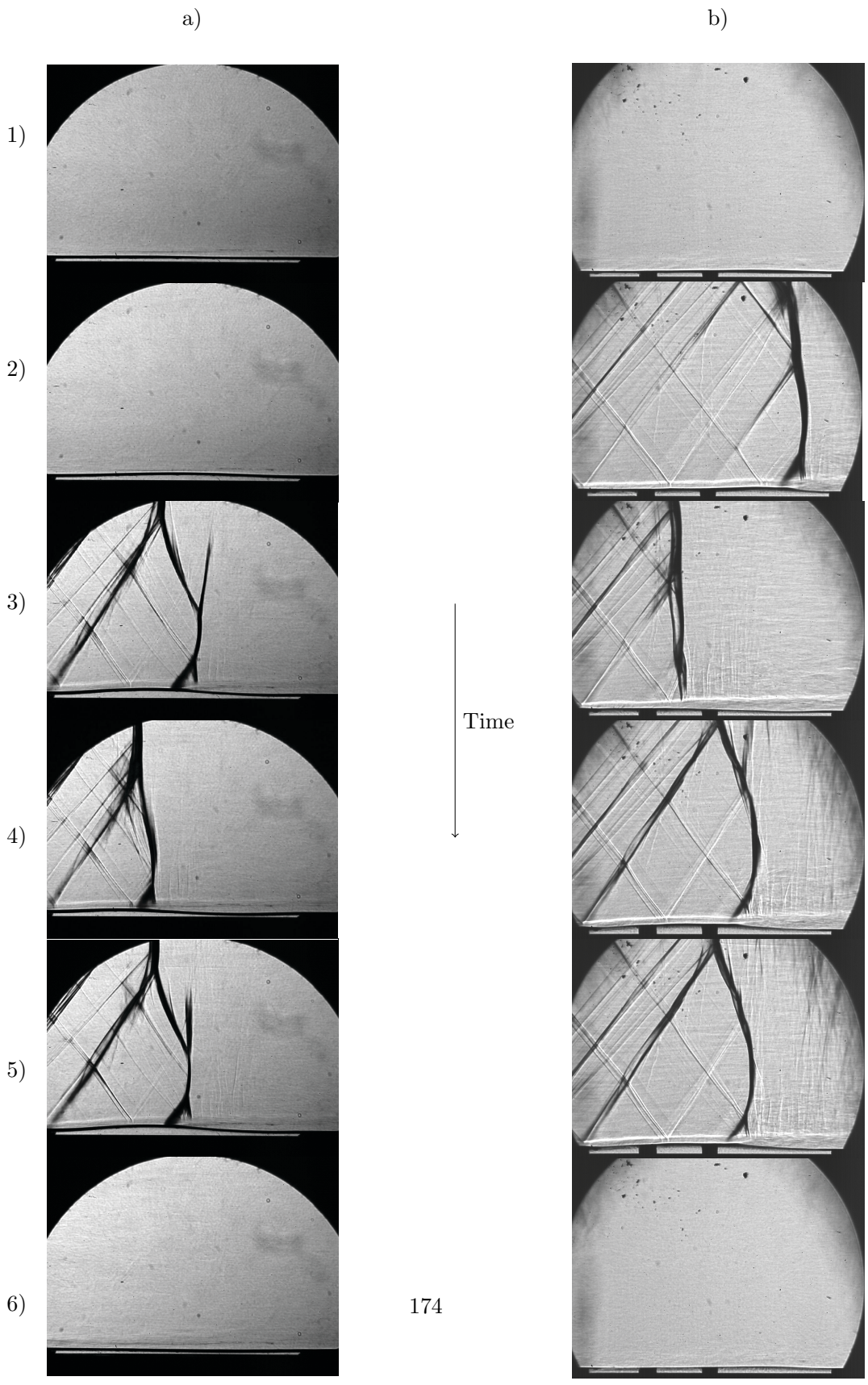


Figure 6.6.: Test case breakdown for both flexible and actuated test cases for the times presented in figure 6.22. Left hand side panel shows 6 images throughout $l_b = 150\,\text{mm}$ t $= 0.6\,\text{mm}$ flexible plate. Right hand side panel shows 6 images throughout $l_b = 150\,\text{mm}$ t $= 0.6\,\text{mm}$ $\delta_1 = 2\,\text{mm}$, $\delta_2 = 3\,\text{mm}$ actuated plate.

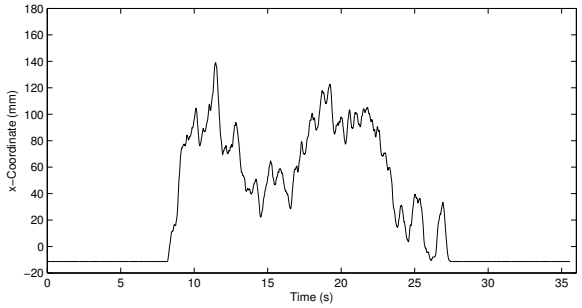


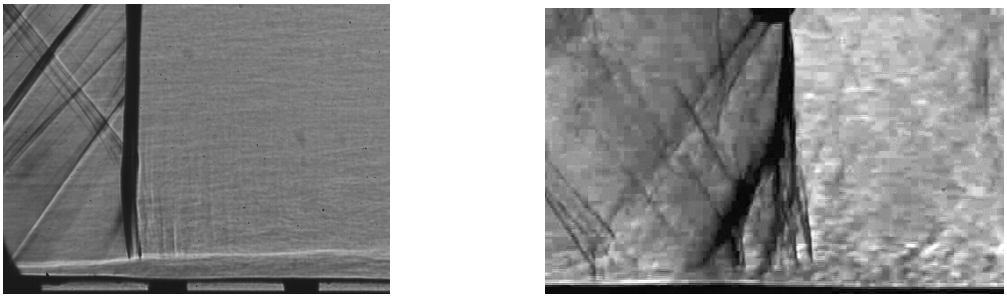
Figure 6.7.: Shock location during the over-deployed actuated SCB $l_b = 150\,\text{mm}$ $t = 0.6\,\text{mm}$ $\delta_1 = 2\,\text{mm}$, $\delta_2 = 3\,\text{mm}$.

The structure of the shock in the second stage is similar to a normal shock wave in a constant cross-section working section with rigid walls, with the comparison made in figure 6.8. In this single instantaneous Schlieren image the shock wave is located at a position of $0.2l_b$ with a clearly defined shock front. Figure 6.8 shows that both shocks are vertical with comparable smearing near the wall indicated by the pressure waves immediately upstream of the normal shock.

In both the actuated SCB and deployed cases, figures 6.9a and 6.9b, a thickening of the boundary layer can be identified across the shock and the heights are of a similar magnitude suggesting the un-deployed SCB has a similar effect upon the boundary layer as a Mach 1.4 normal shock on a flat rigid wall.

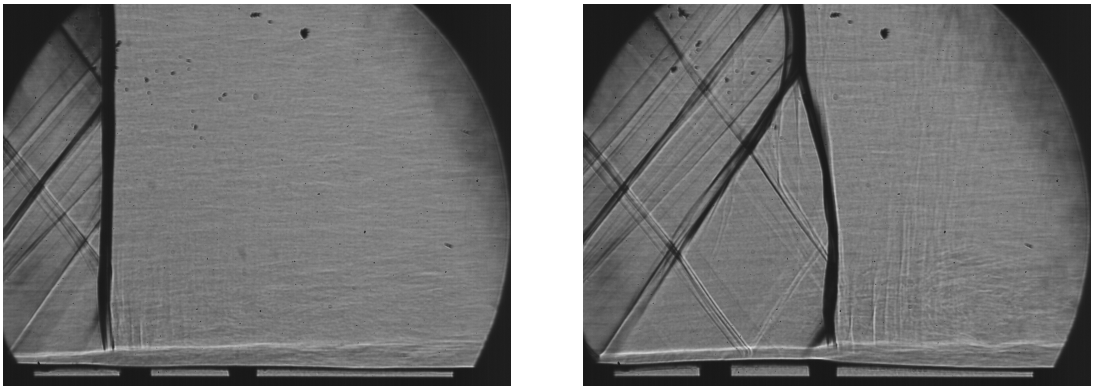
As introduced in the previous section, the position of the shock over the un-deployed adaptive SCB was similar to the rigid wall setup. Dynamically the behaviour is comparable with shock location varying $\pm 50\,\text{mm}$. The importance of this is that when the SCB is un-deployed, there is little effect upon the flow structure. This is a very promising characteristic for adaptive SCB and a strong case for their integration upon aircraft wings where it is desirable that their effect when un-deployed is negligible. One of the primary goals of SCB is to be able to deploy and trigger the bifurcation of the shock whilst remaining discrete at all other times.

Figure 6.10 shows snapshots during actuation the shock changes from a vertical, normal shock to the λ-structure. The bifurcation occurs as soon as the bump height passes beyond 1 mm in good agreement with the trend observed in figure 5.12. The significance of this value is that it is still able to provide a λ-shock but also minimises plate deformation which is beneficial for prolonging the life of the adaptive SCB as the stresses within the material are lower.



a) b)

Figure 6.8.: Shock structure in the working section. a) Normal shock, retracted actuated SCB, $l_b = 150\,\text{mm}$, $t = 0.6\,\text{mm}$. b) Rigid wall normal shock. The two Schlieren images in figure 6.8 were obtained at different frame rates, exposure times and knife-edges so these comparisons can only be inferred.



a) b)

Figure 6.9.: Shock structure over adaptive SCB $l_b = 150\,\text{mm}$, $t = 0.6\,\text{mm}$. a) Normal shock (un-deployed SCB) b) Bifurcated shock (deployed plate) $\delta_1 = 2\,\text{mm}$, $\delta_2 = 3\,\text{mm}$.

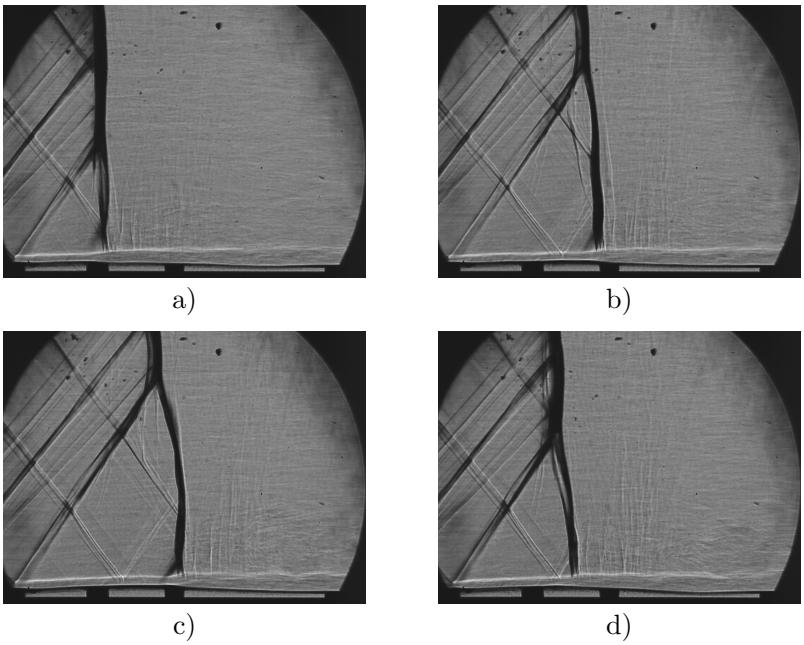


Figure 6.10.: Shock structure over a deployed adaptive SCB at various times during the example test case. a) Immediately prior to the actuation signal at 9.75 seconds b) Immediately after the actuation signal at 9.90 seconds c) During established bifurcation at 11.5 seconds. d) After the retract signal was sent to the actuators at 13 seconds.

The shock structures for the second and third stages are shown in figure 6.9 with the actuators retracted in figure 6.9a and deployed in figure 6.9b. Figure 6.9b represents the average shock structure in this stage with a well defined bifurcation. The successful bifurcation of the shock is a testament to the success of the initial plate sizing in chapter 3 and the optimisation studies of chapter 5. From an aerodynamic viewpoint, the most influential characteristic is the actuation height and the resultant surface deflection. Figures 6.6, images b.3 and b.4 show the bifurcation of the shock with the traditional oblique shock forming from the start of the actuated SCB. Here the front leg is slightly more defined than in the optimal case (figure 6.4) because the overall displacement is higher and therefore the effective ramp angle is greater. The height of the first actuator determines the angle at which the flow close to the wall has to deviate. This causes the formation of pressure waves which coalesce into an oblique shock to form the front leg of the bifurcated shock. The difference between the optimal SCB with $\delta_1 = 1.42\,\text{mm}$ and the over-deployed case at $\delta_1 = 2\,\text{mm}$ can be seen in the 'thickness' of the front leg in the Schlieren images in figures 6.4, image 4 and 6.6, images b.4. The second actuation point continues to deflect the flow away from the wall up until the crest. Figures 6.11, images d,e,f show that the pressure waves appear to coalesce 50 mm from the surface.

As discussed in chapter 5, the rear section of the SCB is extremely influential in the overall shock structure and the efficiency of the device. Chapter 4 showed how the surface curvature has a direct link to flow curvature and subsequent shock loading. The curvature surrounding the plate crest region is controlled by this second actuation point and it can be seen in figure 6.9b that the addition of these actuator displacements eliminates the re-acceleration downstream of the plate crest. The removal of the re-acceleration region is apparent throughout the entire 3 seconds of actuation for the over-deployed case when compared to the equivalent fully flexible case in chapter 4.

The addition of the actuators increased the stiffness of the actuated SCB for both deployment heights tested. The actuators restrained the deformation of the plate during pressure loading. Comparing the actuated SCB to the $l_b = 150\,\text{mm}$, $t = 0.6\,\text{mm}$ flexible plate test case in chapter 4, the large vertical deformations observed in the flexible plate test were limited throughout the run to small deformations of the flexible regions while in the retracted state. The inclusion of actuation not only provides a steady-state displacement but also changes the response of the plate as the shorter sections between constraints do not deform to the same extent as the unconstrained flexible plates because of the additional actuator constraints. The deformation of the plate during stages 1, 2 and 3 is important for the eventual integration of adaptive SCB in on and off-design conditions and is discussed in the next section.

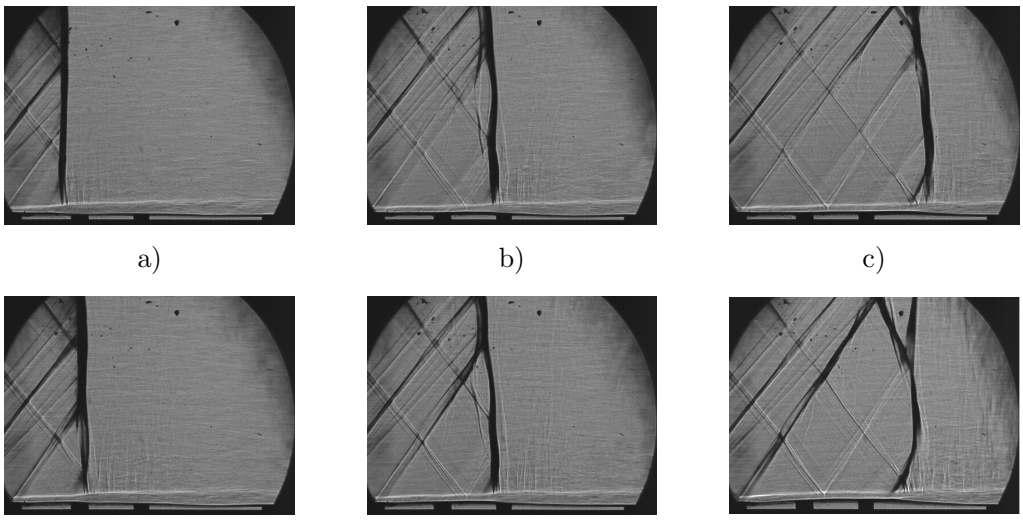


Figure 6.11.: Effect of shock position on shock structure over actuated plate $l_b = 150\,\text{mm}$, $t = 0.6\,\text{mm}$. a) Retracted $x_{shock} \sim 0.2l_b$. b) Retracted $x_{shock} \sim 0.5l_b$. c) Retracted $x_{shock} \sim 0.75l_b$. d) Deployed $x_{shock} \sim 0.2l_b$. e) Deployed $x_{shock} \sim 0.5l_b$. f) Deployed $x_{shock} \sim 0.65l_b$.

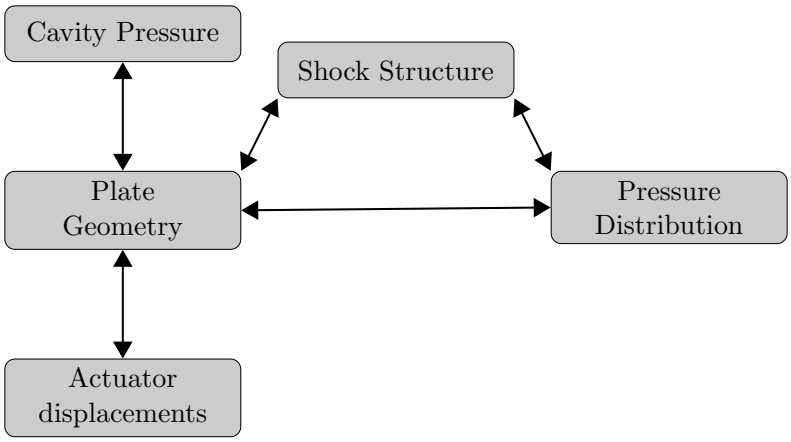


Figure 6.12.: The interdependencies of shock structure, pressure gradient and plate geometry with the addition of actuation constraints.

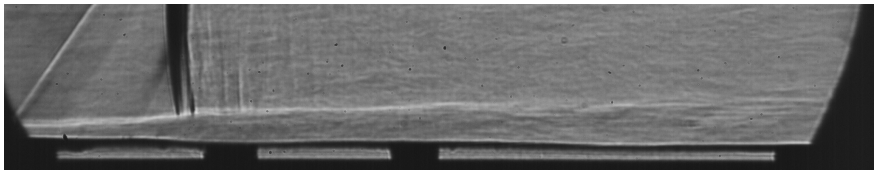


Figure 6.13.: Un-deployed Actuated SCB under the harsh shock loading environment.

6.2.2. Plate Response

The plate response during each loading stage has been introduced through the aerodynamic effects. The focus in this section is the plate deformation and the large scale, steady features that occur. During stage 1, subsonic loading, the decreasing pressure in the flow field and subsequent cavity pressure combined to create a pressure difference across the plate. This pressure difference affected each section of the actuated plate differently with the general behaviour illustrated in figure 6.12 which extended the interdependencies surrounding shock interaction to include actuation.

The dynamic loading upon the actuated SCB introduces sudden changes to the pressure field above the plate. In addition to bifurcating the shock the actuated SCB must remain within the structural limits of the material in order to achieve its goal of flat plate to flat plate having undergone deployment. Maintaining an elastic deformation has been a recurring theme during the design process and was an influential design variable in the initial sizing studies. The effect of each of the loading stages upon the plate geometry will be analysed here.

The interaction between the flow and the plate begins during the tunnel start-up where high subsonic Mach numbers are present over the actuated SCB. This is an effect witnessed in the early panel flutter studies by Dowell [1972] and is experienced here in the most flexible portion of the plate, $x > 0.5l_b$.

The un-deployed SCB in figure 6.13 shows a flat un-deployed SCB under shock loading. Downstream of the second actuation point, the flexibility of the system begins to have an effect on the longest section of plate which can be seen by the variation in figure 6.14. Through the same mechanism as the flexible plate cases, the distance between geometric constraints provided a level of flexibility that allowed a slight negative deformation under the subsonic aerodynamic loading. Such oscillations between positive and negative displacements were also observed by Dowell [1966].

The pressure driven flow reduced the cavity pressure which is thought to be the cause of the depression of the most flexible downstream section of the plate immediately prior

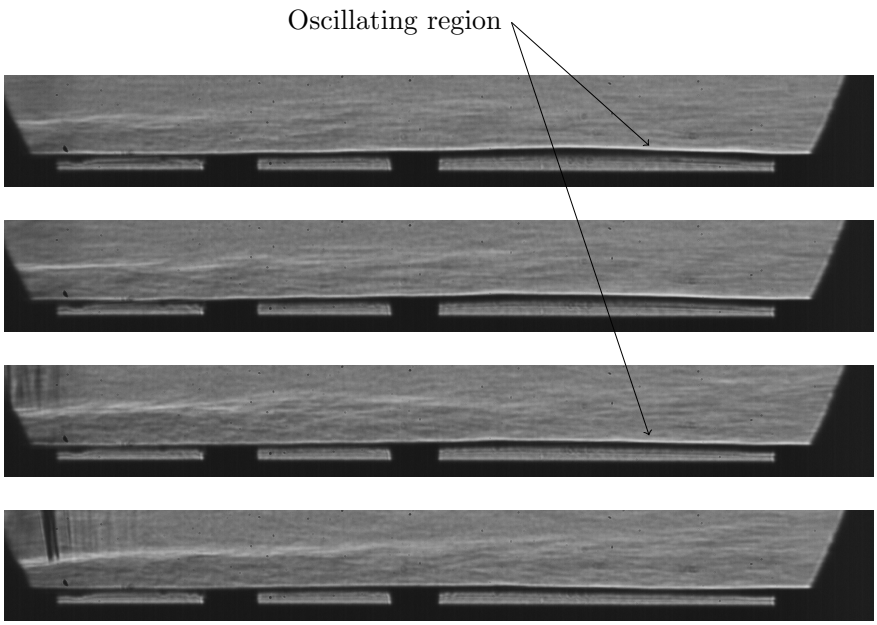


Figure 6.14.: High subsonic Mach number loading $M_2 \approx 0.74$

to shock loading, $4.2 < t < 5.2\,\mathrm{s}$ up to the point where the shock passes over the second actuator at $t = 10\,\mathrm{s}$ in figure 6.22.

During the second loading stage the plate is subject to the stream wise pressure gradient that occurs across a Mach 1.4 normal shock as well as the existing pressure differential across the plate. In the un-deployed state with the shock loading in figure 6.9a, the low pressure supersonic region on the front surface of the plate is thought to be drawing air from within the cavity. This is because in the experimental model there are small gaps between the edges of the plate and the side walls of the wind tunnel. This imperfect seal allows for air to travel between the upper and lower surfaces of the plate which may introduces another pressure driven flow around the plate. With the shock at $0.2l_b$, the front of the upper surface is subject to low pressure supersonic flow and the rear $0.8l_b$ is subject to higher pressure subsonic flow.

Upon actuation, the actuators deploy to the pre-set heights, $\delta_1 = 2\,\mathrm{mm}$ and $\delta_2 = 3\,\mathrm{mm}$. The multiple effects of stage 3 loading are harder to distinguish as there are many factors contributing to the plate deformations.

Being able to control the maximum displacement of the plate was an important feature of adaptive SCB, particularly when the shock is in a non-optimal location. Building upon the work of the passive flexible plates in chapter 4, where the plate crest followed

the motion of the shock, the actuation aimed to control the position of the crest. The shortfalls with this mechanism in flexible plates were the levels of curvature of the plate and the resultant shock structure. The geometries formed by the aerodynamic loading resulted in large levels of curvature immediately downstream of the crest which cause undesirable accelerations of the flow.

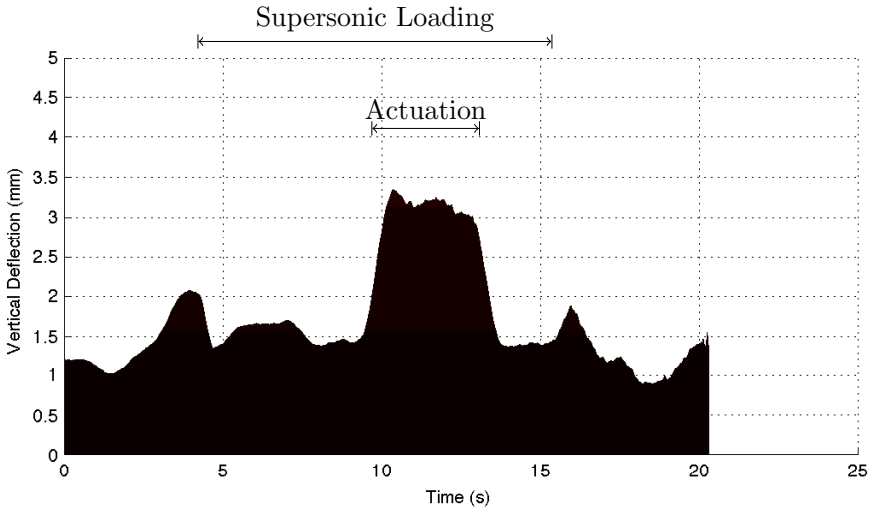
The deployment of the actuated SCB without aerodynamic loading was recorded using the same Schlieren technique as the wind-on test cases. Figure 6.16 shows the deployment of the plate for 3 s with no aerodynamic loading and the maximum vertical displacement of the wind-off test case with the desired 3 mm achieved with a deployment time of 0.3 s and a retraction of 0.35 s which can be seen in figure 6.15.

The effect of the aerodynamic flow field upon the actuators was an increase in deployment and retraction time. In the wind-off cases the deployment time is 0.3 s which is very similar to the time taken for deployment under aerodynamic loading.

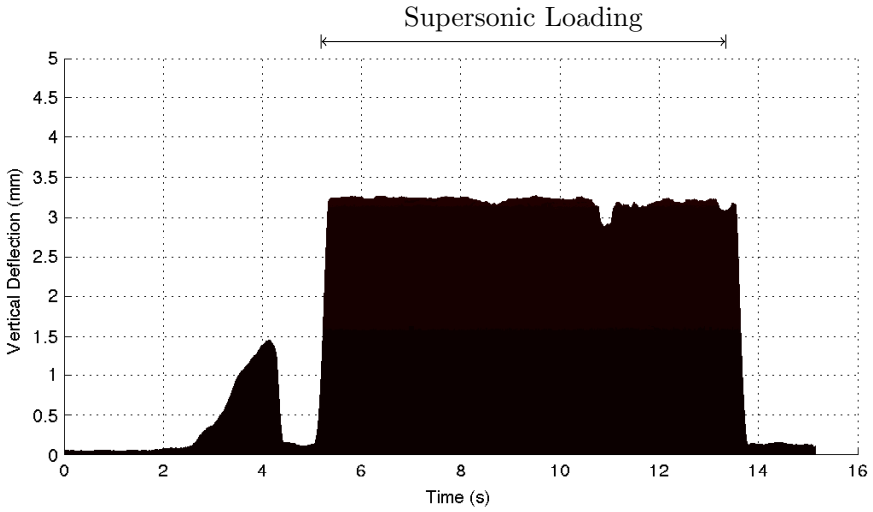
The technique of extracting the plate geometry from the Schlieren imaging did result in some variations due to the algorithm used. A few of these discrepancies can be seen in the region between $2.7 < t < 5.7$s of figure 6.16 where apparent variations of around 0.1 mm of plate deformation can be observed. This could be due to some instantaneous variations in the light source or particles moving through the collimated light causing the algorithm to mis-calculate. However these values are very small and only affect a few images in each capture so a filtering algorithm to identify these and replace them with a central average was used.

Figure 6.17 shows the average plate geometries during SCB deployment with and without aerodynamic loading. The geometries produced are very similar over the front surface of the SCB with the actuators restraining the movement due to the aerodynamic loading. The regions where the actuators are present around 37.5 mm ($0.25l_b$) and 75 mm ($0.5l_b$) are calculated via interpolating the deformations immediately downstream and upstream of the actuators. This explains the slight flat spot at 37.5 mm, the effect of the actuation at 75 mm is disguised somewhat by the local curvature of the plate. Where the two geometries differ is downstream of the second actuation point. The difference over the rear surface does not exceed 1 mm however it does suggest that the pressure difference across the rear surface of the SCB is caused by a difference in aerodynamic loads on the over-depoloyed SCB. This is the same effect seen in the optimal SCB in figure 6.1.

The variation between the flow and no-flow geometries observed in figure 6.16 also highlights the stiffness of the various sections. Between the start of the plate and the first actuator and the first and second actuation points, the geometries differ very little



a)



b)

Figure 6.15.: Plate crest height variation over time. a) Actuated plate $l_b = 150\,\text{mm}$ $t = 0.6\,\text{mm}$, $\delta_1 = 2\,\text{mm}$ at $0.25l_b$, $\delta_2 = 3\,\text{mm}$ at $0.5l_b$. b) Flexible plate $l_b = 150\,\text{mm}$ t $= 0.6\,\text{mm}$.

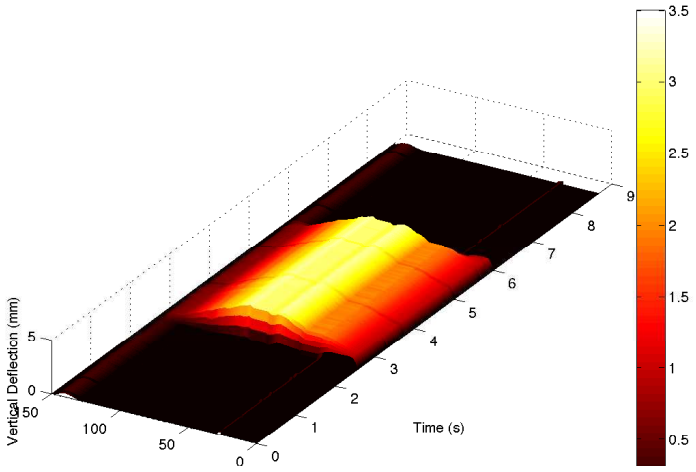


Figure 6.16.: Plate crest height for Actuated plate $l_b = 150\,\text{mm}$, $t = 0.6\,\text{mm}$, $\delta_1 = 2\,\text{mm}$ at $0.25l_b$, $\delta_2 = 3\,\text{mm}$ at $0.5l_b$ with no aerodynamic flow field.

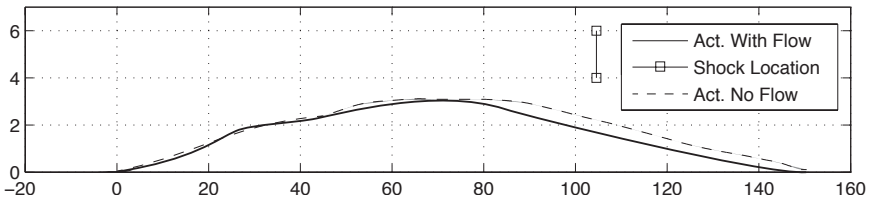


Figure 6.17.: A comparison between the actuated SCB geometries with no aerodynamic loading and with shock loading.

owing to the stiffness of these sections by virtue of the closely positioned constraints. The section of the plate between the second actuator and the end of the plate is approximately twice the length and as such is sensitive to the surrounding pressure differences. The increased distance between the constraints reduces the stiffness and for a given pressure difference, the longer section will naturally deform more. These differences separate the aerodynamic loading and the actuator loading and further highlight the importance of the cavity pressure and surrounding pressure differences in the adaptive SCB design process. The surrounding pressure field and the cavity pressure directly effect the levels of curvature in the actuated SCB which were managed to a greater extent than the flexible plate test cases. The following section will investigate the plate curvature for the aerodynamically loaded actuated SCB and highlight the benefits of the addition of actuation to the plate curvature and resultant flow curvature from a FSI approach.

6.2.3. Fluid-Structure Interaction

Building upon the flexible plate studies of chapter 4 it is proposed that the curvature of the plate is an important SCB design characteristic with respect to the quality of the bifurcation. The traditional SCB parameters such as length, bump height and position all still contribute to the overall performance but for adaptive SCB based upon a flexible skin section, the curvature around the crest region is critical in producing the desired bifurcation. This is most noticeable when the flexible plate test cases are compared with the optimal and actuated SCB in figure 6.18.

The instantaneous relationship between the plate and the flow curvature is crucial in ensuring the aerodynamic performance of adaptive SCB is comparable to the existing static SCB. One of the shortfalls of the purely flexible plate design was the common

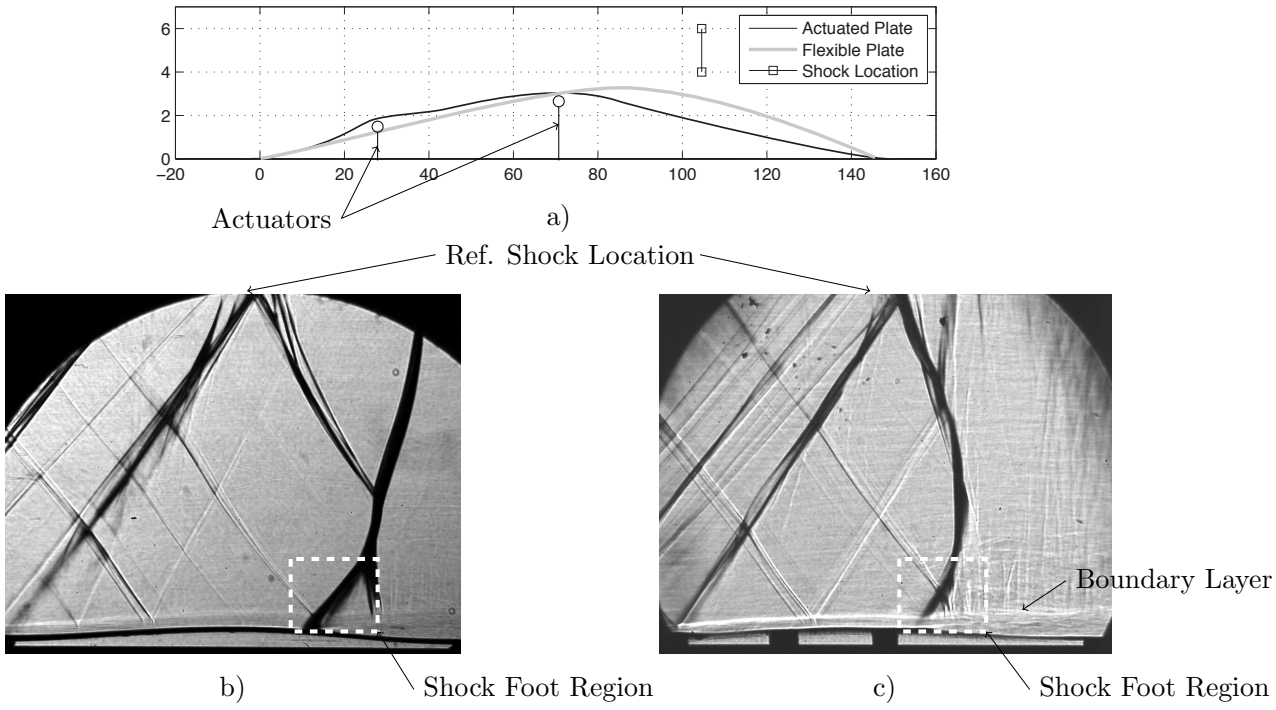


Figure 6.18.: Comparison between flexible and actuated plate geometries with a constant rear leg shock position. a) Extracted plate geometries. b) Flexible plate shock structure. c) Over-deployed actuated plate shock structure.

reacceleration of the flow immediately downstream of the rear leg. The combination of near sonic flow conditions and substantial plate curvature meant that a secondary shockwave occurred which introduces further total pressure losses.

The geometry downstream of the crest has been the subject of investigation by Colliss and Babinsky [2012] and Nübler et al. [2012] who elongated the rear surface of the SCB to exert some control over the downstream boundary layer which was susceptible to separation behind the crest. This was as a result of the adverse pressure gradient and surface curvature combining to detrimental effect. The solid nature of the rear slope of this SCB means that the curvature is set by the physical model and does not vary with respect to the flow field ensuring optimal bifurcation for the flow conditions. With adaptive SCB, the flow field does affect the curvature of the surface and so extra constraints were required to maintain suitable levels of curvature and the successful bifurcation. An important dynamic in the FSI is the movement of the plate crest with respect to the shockwave. Figure 6.19 shows the stream wise location of the plate and the shock for the $l_b = 150\,\text{mm}$, $t = 0.6\,\text{mm}$ flexible plate case from chapter 4. The initial subsonic rise of the plate can be seen as the accelerating flow increases the pressure difference across the plate, this drops prior to shock loading which lasts until tunnel shutdown. There was always some distance between the crest of the plate and the shockwave however it never exceeded 30 mm during shock loading suggesting the structure was limiting the constraint. The distance is at its largest when the shock was at its most downstream location which means a larger area of the plate is subject to the low pressure supersonic flow. The continued movement downstream of the plate crest is limited by the stiffness of the plate. The increased stiffness of the actuated SCB alters the FSI between the plate and the shock and is particularly noticeable in figure 6.22c. Between the initial shock entrance and the actuation, the plate crest tracks the shock position with large downstream excursions in shock position resulting in large movements of the plate crest location. This is apparent at $t \approx 6\text{s}$ with a shock position $x_{shock} = 130\,\text{mm}$ and a movement of the plate crest to 125 mm with a height of 1.9 mm. This is a large deformation considering the actuators remain retracted however this is because the shock is over the most flexible region of the plate between the second actuation point and the end of the plate.

Figure 6.18 shows that when the actuated SCB is deployed, the fixed deflection and location of the actuators fixes the crest location to a region just upstream of the second actuation location. There are some variations in the plate crest location during actuation. These are, however, comparatively small at 0.2 mm and are due to the small variations and optical distortion in the Schlieren technique. The addition of the geomet-

ric constraints inhibits the crest to track the shock wave but may also provide a stable shock location on the rear surface which is supported by the steadied location during actuation in figure 6.5. The benefit of being able to track the shock was to minimise the distance of the re-acceleration region between the plate crest and the rear leg is limited which avoids the strengthening of the rear leg. The movement of the crest too far downstream increased the levels of surface curvature around the crest to such an extent that the flow was reaccelerated. In contrast to the actuated plate, the amount of curvature seen for the downstream shock position with the flexible plate SCB were high enough to re-accelerate the post-crest flow and cause a secondary shock structure as seen in figure 6.18.

The maximum curvature relative to the horizontal experienced by the over-deployed actuated SCB was 2.5^o which was restricted by the displacement of the actuators. The optimal SCB generated a peak surface deflection of 2.0^o. The Schlieren images in figures 6.4 and 6.6 suggest that this was sufficient to trigger the oblique shock but low enough to eliminate re-acceleration downstream of the shock.

Figure 6.18 compares the instantaneous plate geometry for both the flexible, optimal and over-deployed actuated plates with the same shock location. These geometries are significantly different, especially over the aft half of the plate and suggest that the geometry and the resulting curvature have a key part to play in the formation of the shock structure. The front legs generated by the plate displacement of flexible and over-deployed plates are of a similar angle $\sim 56^\circ$ away from the wall however the rear leg structures are very different. One potential cause for this is the location of the plate crest. Without constraints, the crest of the flexible plate is allowed to sit much further back than the actuated crest which allows the supersonic flow between the two legs to accelerate for much longer. As the flow accelerates around this increased curvature, the entire flow field in this region turns and the expansion waves generated interact with the main rear leg which caused the curvature in the rear leg below the triple point figure 6.6.

By limiting the displacement of the plate and the subsequent streamwise position of the crest, the levels of curvature that the flow field is subjected to were reduced and it is thought that this is why a favourable shock structure is developed in the optimal and over-deployed SCB. The optimal actuator displacement values reduce the curvature of the rear leg to a level that was almost perpendicular to the plate observed in figure 6.4.

In figure 6.18, a secondary bifurcation was formed at the rear leg that is reminiscent of the strong shock structure observed for $M > 1.5$ shockwaves on rigid walls [Seddon, 1967]. This suggests that the additional surface curvature has separated the boundary

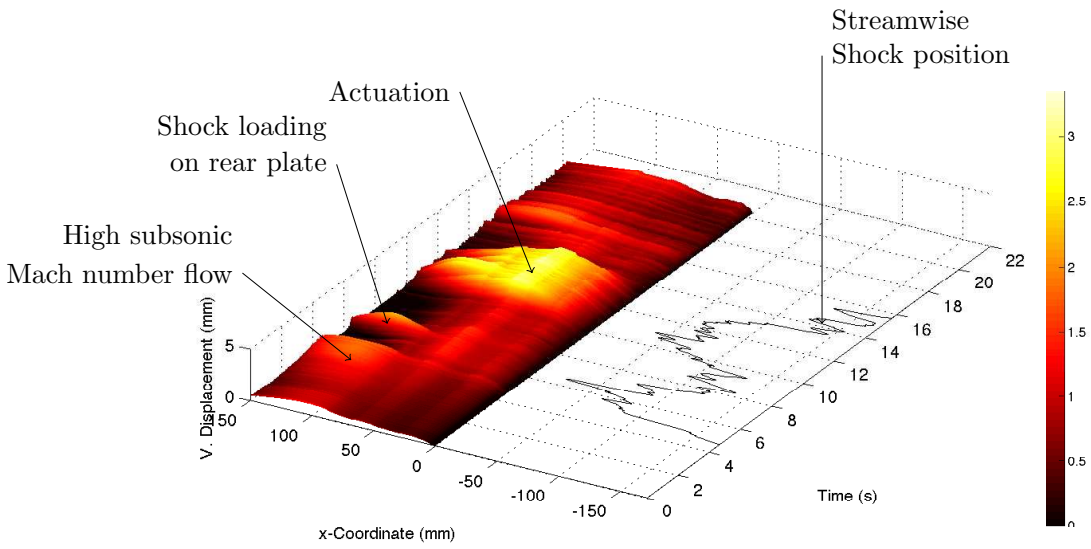


Figure 6.19.: Plate displacement through time for the $l_b = 150\,\text{mm}$ $t = 0.6\,\text{mm}$, $\delta_1 = 2\,\text{mm}$ at $0.25l_b$, $\delta_2 = 3\,\text{mm}$ at $0.5l_b$ actuated plate

layer.

Further experimental techniques could be applied to this actuated plate in order to determine the level of boundary layer thickening and separation in greater detail however due to the large field of view and long recording times experiment, PIV was not suitable with recording times of a few seconds and LDA would not have provided information about the plate displacement and the flow structure simultaneously. The shock structures collected from Schlieren imaging show great potential having successfully bifurcated the shock which is a key performance characteristic of SCB. This single bifurcated shock structure shows potential for the use of actuated plates as a viable design platform for adaptive SCB.

6.2.4. Dynamic Plate Response

The dynamic plate response of the deployed SCB was still caused by the dynamic shock loading even with these regions of increased stiffness. Figure 6.21 shows the vertical displacement of a point on the plate surface that is tracked during the aerodynamic loading. The tracked point is at $0.66\,l_b$ placing it in the downstream flexible region of the plate. For the actuated plate in figures 6.21a and 6.21b, typical oscillations during high

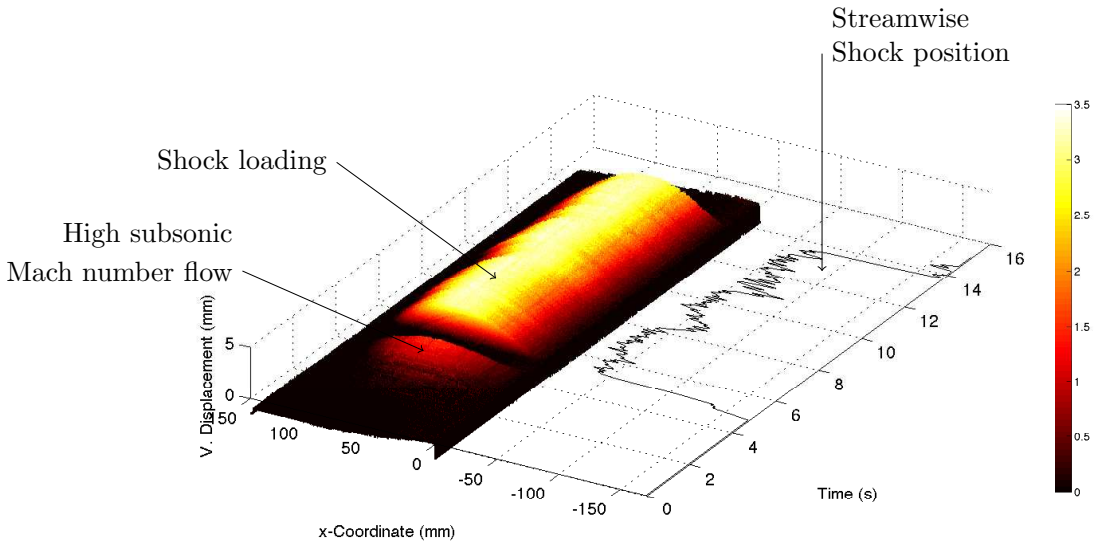


Figure 6.20.: Plate displacement through time for the $l_b = 150\,\text{mm}$ t $= 0.6\,\text{mm}$ Flexible plate

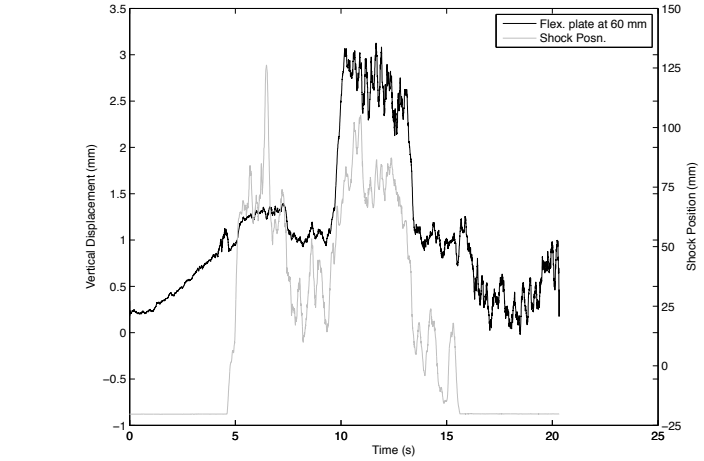
subsonic loading $0 < t < 4.5$s were very small, $\mathcal{O}(< 0.1\,\text{mm})$. During shock loading the oscillations in vertical displacement were very sensitive to shock location with vertical displacements of the tracking point varying from $\sim$0.3 mm for $\sim$ 25 mm shock movement to $\sim$ 1.4 mm increase in vertical displacement for a large shock movement of $\sim$ 70 mm around t = 6.2s in figure 6.21b.

These oscillations and deformations were driven by the shock system and the flexibility of the plate in similar mechanisms to the purely flexible plates in chapter 4. Despite increases in stiffness due to the actuation constraints across the span of the plate, the level of flexibility required to deform enough to trigger the bifurcation still made the plate susceptible to the dynamic shock loading.

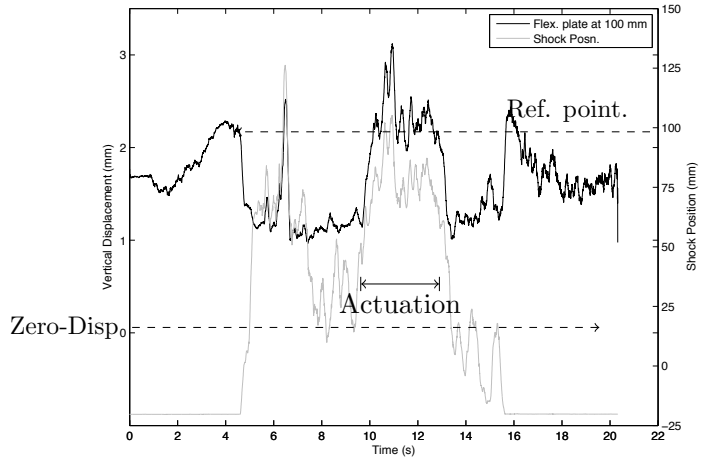
The increased stiffness that allows for the successful bifurcation also has an effect upon the unsteady response of the plate. Figure 6.21a and 6.21b showcase the plate and shock movement at positions equivalent to 60 mm ($0.4l_b$) and 100 mm ($0.66l_b$). The main difference between the selected locations is the distance from a constraint. The 60 mm and 100 mm positions are both $\sim 0.15l_b$ from the nearest constraint however the 100 mm position is located in the downstream flexible region of the SCB. In terms of plate deflection the upstream location of 60 mm is in a much stiffer part of the actuated SCB. This can be seen in figure 6.21a at $t \approx 6.5$s where there is a large downstream excursion of the shock. The 100 mm location responds to the change in pressure load by rising up to 2.5 mm for a very short period of time in figure 6.21b. In comparison, the 60 mm location in figure 6.21a does not rise and the deformation remains near the same magnitude as before and after the shock excursion. The geometry of the plate as it responds to the rear leg shock movement is visualised in figure 6.19.

The response of the two locations in figure 6.22b,c immediately after shock loading, $t > 15.5$s, shows the effects of a sudden change in the pressure loading. The removal of the shock and the pressure loading sees the stiff region around the 60 mm location begin to return towards the subsonic loading case with displacements around 1 mm albeit with a much greater unsteadiness when compared to the tunnel start-up $0 < t < 4.2$s. The response of the more flexible region recorded at 100 mm sees a large increase in the surface deformation despite the low pressure supersonic region disappearing upstream. After this sudden rise, the retracted SCB responds to the decelerating subsonic flow in a way similar to the start-up albeit reversed. The oscillations as a result of the removal of the shock loading are subtle but can also be viewed in figure 6.19 with the banding of colours towards the end of the test case.

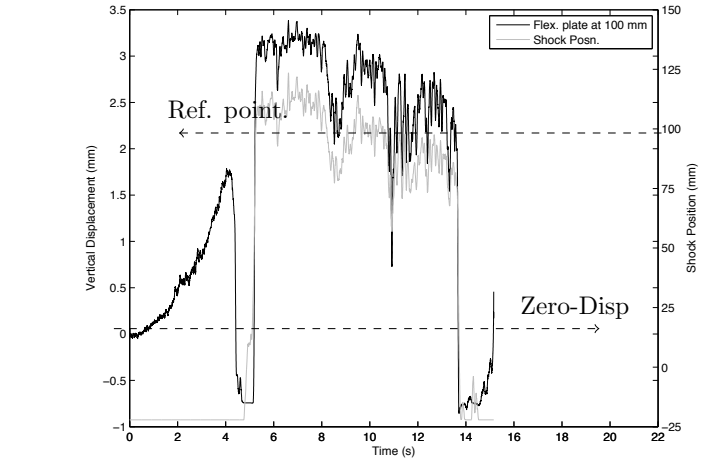
At the end of the wind tunnel test, the geometry returns to the flat plate. Although a seemingly small aspect, the actuated SCB design has proved to be capable of not only



a)



b)



c)

Figure 6.21.: Transient plate displacement at multiple locations throughout time. Shock location is also included for reference. a) Actuated Plate, plate displacement at 60 mm streamwise location. b) Actuated Plate, plate displacement at 100 mm streamwise location. c) Flexible Plate, plate displacement at 100 mm.

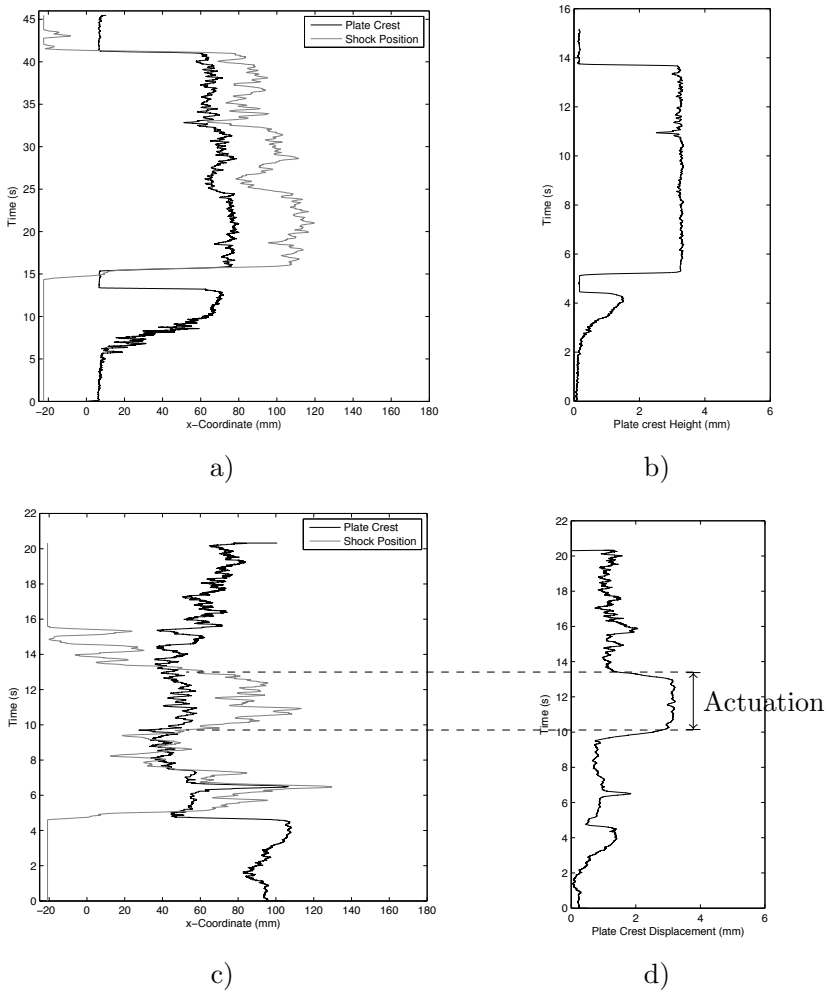


Figure 6.22.: Plate crest tracking through time for the $l_b = 150\,\text{mm}$ t $= 0.6\,\text{mm}$ flexible plate in a) & b) and the $l_b = 150\,\text{mm}$ t $= 0.6\,\text{mm}$ actuated plate in c) & d). Graphs a) & c) show the location of the maximum plate displacement with respect to the location of the most rearward shockwave. Graphs b) & d) show magnitude of the displacement due to the aerodynamic loading.

withstanding the shock loading but also capable of deploying and retracting therefore meeting the goals of adaptive SCB set out in chapter 2.

6.3. Summary of Actuated Adaptive SCB

The ability of adaptive SCB to deploy and retract as shown here is proof of concept for this flexible plate and actuator based design. The results in the preceding sections demonstrate that actuated SCB can not only bifurcate a shock in the same way as a traditional static SCB but the design can also withstand the aerodynamic loading which is a challenge specific to actuated SCB. The aerodynamic loading affects the steady plate geometry and flow features as well as the shorter time scale unsteadiness.

The FSI between the flexible actuated plate and the aerodynamic flowfield is primarily affected by the pressure gradients across the upper surface and the pressure difference across the plate. The analysis of instantaneous Schlieren images of the optimised and over-deployed SCB in figures 6.4 and 6.6 show a normal shock when the actuators remain un-deployed. Upon actuation, the normal shock structure is successfully bifurcated with no reacceleration over the rear surface as seen in the flexible plates. This confirms that actuated SCB exert an element of control over the geometry of the plate that facilitates the desired shock structure to be achieved. However it is the height of the actuation that determines the level of curvature of the plate and ultimately the curvature of the important rear shock leg.

The instantaneous Schlieren images presented in figure 6.6 and the plate displacement-shock position relationship in figure 6.19 show the effectiveness of actuated SCB in exerting a degree of control over an unsteady flow field. Traditional static SCB are often experimentally tested with shock holding plates [Ogawa et al., 2008, Colliss and Babinsky, 2012] which severely restrict the motion of the shock to evaluate on-design conditions. Stabilising the shock to maintain an approximately constant position means that off-design conditions have to be tested via the physical movement of the shock holding plate. Often this requires a new experimental setup and cannot be altered mid-test. In the current study the natural unsteadiness of the wind tunnel was utilised as a source of large scale oscillations which are more representative of the shock oscillations on transonic wings subject to atmospheric unsteadiness.

Using this approach, this actuated SCB showed some potential performance benefit under the unsteady aerodynamic loading. In the retracted state the normal shock structure was maintained throughout with only some slight curvature when the position was above the rear surface of the SCB. During actuation the main normal shock above

the triple point was free to move which dictated the location of the rear leg of the shock. In the instances where the main shock was upstream of the deployed SCB, the normal shock structure is apparent as if no control device were there and the small actuation heights of the optimal SCB did not cause local supersonic regions. This result further supports the use of adaptive SCB as a beneficial device with the ability to perform in unsteady flows which are a natural feature of the transonic environment.

The secondary achievements that can be extracted from these results relate to the direction of research that should be taken from this investigation. The addition of actuation allows for the control of not only the height of the SCB but also the local curvature of the plate. This supports the work carried out by Colliss and Babinsky [2012] and Nübler et al. [2012] who extended the rear surface which reduced the surface curvature and the likelihood of re-acceleration or separated flow on the downstream rear surface.

The surface curvature of actuated SCB is controlled locally by the actuation points. The span wise actuation strips contributed greatly to the requirement of a 2D deformation and the results confirmed the effectiveness of 2D SCB at bifurcating the shock wave.

The actuated plate design also revealed the effects of stiffness upon the plate dynamics. The regions upstream of the second actuation points were much stiffer due to the shorter distances between constraints. The benefits of this are that these regions do not deform when subject to aerodynamic loading whether in a retracted or deployed state. The flexible region downstream of the second actuator does affect the shock structure when the main normal shock is directly above. However, the effect is limited to some slight curvature near the wall.

The comparison between the fully-passive flexible plate based design and the actively controlled actuated SCB shows the potential of the adaptive SCB particularly over the important rear surface of the SCB. The ability to bifurcate the shock wave and to complete the task in the unsteady transonic environment shows that the initial plate sizings and the inclusion of panel flutter studies were a suitable addition to the adaptive SCB design process alongside the aero-structural optimisation procedure.

7. Conclusions

Throughout this work it has been the goal to showcase the potential of an adaptive SCB. The preceding chapters have introduced the transonic and supersonic flow regimes and highlighted potential applications that could benefit from an element of flow control. Existing flow control devices were evaluated with the positive and negative affects recorded. Static SCB have shown promise for being able to manage the flow in the shock region however they were susceptible to changes in the shock strength or location. An approach to improve upon this off-design performance was to make the SCB adaptive so they could to respond to the flow. The conclusions of this study are summarised here in four sections followed by a fifth section containing recommendations for future work.

7.1. Adaptive SCB Design

In order to produce a device that met the design requirements, the initial concept had to be scrutinised to evaluate the fundamental nature of the problem. The initial concept proposed by Ashill et al. [1992] formed the starting point and the interaction between a flexible plate and the transonic flow field became apparent. This required the development of a number of methods:

- A 2D Aero-structural solver was developed in order to evaluate the effects of the aerodynamic flow field upon a flexible plate. The following outcomes were realised:
  - A RANS based CFD solver [OpenFOAM, 2017] and a FE structural solver [ABAQUS, 2007] were successfully coped. This allowed for the prediction of the FSI effects surrounding the plate. A design based upon the original concept was shown to be able to perform and successfully bifurcate the shock whilst meeting the structural constraints.
  - The structural constraint was monitored throughout the aero-structural iterations and the stresses within the plate did not exceed the structural constraint and remained within the elastic regime.

  - The aero-structural solver provided a base to study the effects of numerous plate dimensions and material choices for adaptive SCB. Previous static SCB provided the benchmarks in terms of overall SCB height and length.
  - Zero slope at the plate ends and a geometrically smooth transition on to the SCB was achieved by the boundary conditions constraining the movement of the plate were selected as built-in constraints.

- A converging-diverging Mach 1.4 nozzle was developed and installed into the supersonic wind tunnel. This provided a flow field representative of the transonic environment similar to that experienced on the upper surface of transonic aircraft wings. Experiments using this facility yielded the following results:
  - High-frequency Schlieren Imaging was used in order to capture the FSI present under aerodynamic loading. Significant outputs from this were:
    * A simultaneous data source containing information on the shock structure and location and the deformation of the plate.
    * Allowed for long time-scale recordings that were able to capture the interaction between the shock and the plate from low subsonic flow speeds, to shock loading and then back to subsonic velocities during tunnel shutdown.
  - PIV was used to quantify the effect of adaptive SCB upon the flow field. These measurements showed:
    * Validation of successful application of PIV to study flexible surfaces in transonic flows.
    * Numerical insight into the flow velocities and deflections caused by adaptive SCB.
    * Accurate determination of plate centreline deformation under aerodynamic loading from laser shed reflections.
    * Simultaneous quantitative FSI measurements.

7.2. Flexible Plates for Adaptive SCB

The development of a purely passive device capable of utilising the pressure differences surrounding the Mach 1.4 shockwave was a new direction for SCB design. The 2D aero-structural solver enabled the quick testing of plate parameters such as length, width

and thickness as well as material constraints and boundary conditions. The result of this was a new family of SCB geometries that solely relied upon the flexibility of the plate and the interaction with the aerodynamic loading. The main outcomes of this study are as follows:

- Four test cases were designed with influences from existing static SCB designs as well as cues from studies investigating panel flutter. The cases provided a range of plate stiffnesses which were evaluated using numerical and experimental methods.
  - Numerically, a 2D aero-structural solver showed that the initial concept provided a suitable base from which to evaluate the effect of plate stiffness. The following conclusions were drawn from these numerical studies:
    - The cavity pressure was found to be a very influential parameter in the overall geometry of the plate under shock loading. High values of cavity pressures produced surface geometries more akin to traditional static SCB and also induced high levels of stress within the material. The yield stress of the material set a limit on the maximum deformation possible to remain within the elastic regime and return to a flat plate when the aerodynamic loading was removed.
    - An optimal cavity pressure was found to approximately equal the average pressure on the upper surface of the plate. This was implemented in the experimental model too.
    - Destructive panel flutter was not predicted by the aero-structural solver with only small oscillations of the order of the plate thickness. This was also observed in the experiments.
  - Experimentally, transonic wind tunnel tests revealed that each of the passive adaptive SCB minimised the distance between the plate crest and the shockwave. The flexibility of the plates allowed for the crest to track the shock downstream. The downside to this was that as the crest moved further downstream, the surface curvature increased significantly and often resulted in a stronger shock which was more likely to trigger separation or a secondary shockwave developed downstream.
- The passive adaptive SCB based upon the flexible plate design successfully bifurcated the shock through the introduction of a front shock leg induced by the concave curvature of the upstream section of the plate.

- It was also observed that more flexible plates tested produced surfaces with higher curvatures. This had a direct impact upon the shock structure resulting in curved rear shock legs beneath the triple point.

- The most promising test case was $l_b = 150\,\text{mm}$, $t = 0.6\,\text{mm}$ which was the stiffest plate tested. It was flexible enough to allow for a response to the aerodynamic loading yet stiff enough to limit the displacement of the plate. Most importantly the surface curvature mitigated undesirable effects such as downstream separation or strong reacceleration of the flow which might lead to a secondary shockwave.
  - Increasing the plate stiffness restrained the plate and minimised surface displacement. This limited the levels of boundary layer thickening downstream of the shockwave.
  - Plate stiffness also affects the surface curvature which determines the flow curvature. The high stiffness of this test case was observed to have a positive influence on the flow field well above the plate. Namely to maintain these favourable bifurcated shocks.
  - The length of the flexible plate was an influential parameter when it came to increasing stiffness. The shorter and thicker the plate the lower the maximum surface deflection angle over the front and rear surfaces. The long, thin plate, $l_b = 200\,\text{mm}$ $t = 0.4\,\text{mm}$ had a maximum surface deflection angle of 5.6° whereas the $l_b = 150\,\text{mm}$ $t = 0.6\,\text{mm}$ was 2.7°. The cases with a higher deflection angle also exhibited reacceleration downstream of the crest.

7.3. Optimising Designs for Adaptive Shock Control Bumps

The evolution of adaptive SCB design towards a passive approach showed that in order to maximise the potential of such a device, control may be beneficial. The addition of control required careful design and an optimisation process was developed to determine the ideal location and height of actuation to maximise performance.

- The gradient based optimiser *fmincon* in the MATLAB optimisation toolbox utilised in conjunction with the 2D aero-structural solver in order to determine a design that met both aerodynamic and structural requirements. The following observations were made:

  - The surface based performance metric was a new approach and enabled local flow features that arose due to the addition of SCB to feature in the top level of the optimiser.
  - The performance metric aimed to quantify and assess the smearing of the shock and the optimised result is capable of smearing the pressure rise associated with the shock. This reduces the adverse pressure gradient to a manageable level which reduces the likelihood of shock-induced separation and post-shock separation. This means that stronger shockwaves could be controlled which has applications to Natural-laminar-flow wings which typically feature stronger shockwaves.
  - C_l and C_d values were observed during the optimisation and were found to not change significantly between the iterations with the maximum change in L/D was 0.01.
  - The combination of a 2D RANS solver and the structured mesh of 300k cells were selected as a compromise between solution accuracy and overall optimisation time.
  - The yield stress formed part of the structural constraint to limit the SCB design to elastic deformation. In one instance, the optimiser produced a design that violated the constraint and a penalty value was applied to the performance metric. The following iterations did not breach the constraint which shows the structural constraint influencing the optimisation process.
  - An optimal solution was found that successfully bifurcated the shock with minimal surface deflection with $B_1 = 0.43\,c$, $x_1 = 0.25\,l_b$, $\delta_1 = 1.45\,\text{mm}$ $x_2 = 0.5\,l_b$, $\delta_2 = 1.49\,\text{mm}$. This resulted in a maximum von Mises Stress of 170 MPa which is well within the yield stress of Al-7075-T6 at 525 MPa.
  - An optimal solution with two control points allowed for greater control over the rear surface when compared to the purely flexible plates of Chapter 4.

- The main driving force behind adaptive SCB is the ability to deploy and retract so that in scenarios when a SCB would not be beneficial, the original aerofoil surface could return. The off-design performance section identified the response due to a SCB that was ill-positioned or of a non-optimal height which may arise if there is a sudden change in the flow field such as during aircraft manoeuvre.
  - It was found that short SCB $< 1\,\text{mm}$ were capable of bifurcating the shock over a broad range of locations between $0.41\,c < B_1 < 0.48\,\text{c}$ where B_1 repre-

sents the start of the plate. This range of optimal performance suggests that small SCB heights can successfully bifurcate the shock over a wide range of shock positions. This is beneficial in the event of a significant shock movement, when the SCB actuation time is too slow to respond to the change in aerodynamic flow field.

- The minimum displacement heights that could still achieve the bifurcation of the shockwave were identified with a displacement of 0.5 mm with the starting location of 0.45c. Similar performance is achieved up to a displacement of 2 mm but this is dependent upon location.
- The effects of over-deployment were studied by enforcing actuation heights of up to 4.5 mm with significant reacceleration regions observed downstream of the crest in a similar fashion to the flexible plate test cases. Post-crest separation was also observed for adaptive SCB with an actuation height above 2 mm. This stems from the contribution of excessive surface curvature and adverse pressure gradient.
- A plot of performance metric against actuation height was produced that neatly captures the above trends in Chapter 5.

7.4. Actuated Adaptive SCB

- An actuated adaptive SCB has been optimally designed and tested in a transonic wind tunnel. The device has been observed to successfully bifurcate a Mach 1.4 shockwave upon demand with the shock structure changed from a typical normal shock to a well defined λ- shock. The experimental rig, that is capable of being actuated in a transonic wind tunnel, is a significant step in the design of adaptive SCB.
  - During shock loading with a retracted SCB, the surface remained flat for a large range of shock positions thus avoiding the large deformations that occurred with the purely flexible plates. It was in instances where the shock was directly situated on the most flexible rear surface of the actuated SCB which saw some slight curvature in the shock near the wall. Observed flow features are summarised below:
    * The normal shock structure was maintained above the undeployed SCB.
    * The enforced 2D deformation across the span at the two streamwise

locations constrained the plate to the desired displacements in excellent agreement with predictions of the aero-structural solver.

* Linear actuators provided smooth deployment and retraction and were able to perform as required under the significant aerodynamic loading.

– The optimal actuated SCB performed well and fulfilled the goal of bifurcating the shock even in an unsteady flow field which is representative of the dynamic environment of transonic wings and supersonic intakes where these may eventually be fitted.

* The optimal geometry was successfully deployed during many experimental test cases.
* The surface deflection fixes the front leg of the bifurcation which dictates the strength of the rear leg.
* The actuated adaptive SCB allows the rear leg of the shock to move in response to unsteady variations in flow conditions whilst maintaining the bifurcation upstream.
* This has a positive effect in reducing the amplitude of unsteady shock oscillations and the SCB forms an inherently stabilising surface.

7.5. Recommendations for Further Work

These two paths cover both the fundamental mechanics behind the FSI and the development of adaptive SCB. Each direction will benefit in the renewed focus upon FSI's in recent times with numerical and experimental techniques now capable of obtaining information at time scales small enough to produce unsteady data. It is hoped that the concepts discussed in this thesis will help develop the understanding of FSI's involving shockwaves and flexible plates in the fundamental sense and with an application to flow control.

This combined aero-structural approach for designing adaptive SCB has highlighted the complex FSI that occurs between flexible panels and shockwaves. It has brought together the existing research on static SCB and taken inspiration from panel flutter studies. In terms of recommendations for further work there are two channels. The first is to investigate the FSI surrounding shockwaves and plates. The second area is on a more applied level with the development and integration of adaptive SCB in mind.

7.5.1. FSI surrounding plates and shocks

- Experimentally vary cavity pressure to investigate plate dynamics to further understanding of this fundamental FSI.
- To produce a plate displacement field using DIC (Digital Image Correlation) and synchronise with PIV for quantitative analysis of the FSI.
- Investigate the frequencies present in the flow and plate for different shock loading scenarios. It could also be beneficial to investigate non-shock loading cases involving subsonic and supersonic flow over the top of the plate to apply modern numerical and experimental techniques to the early panel flutter studies.

7.5.2. Application of Adaptive SCB

- Perform tests on actuated SCB at different Mach numbers between 1.2 and 1.5 to explore the importance of shock strength and widen the applicability of this research to a range of applications including NLF wings and intakes.
- To develop the aero-structural solver to accommodate three dimensional fluid and structural solvers in a strongly coupled manner to pass surface information between iterations to improve the accuracy and representation of this FSI.
- To use a Pitot rake to quantify the effects of the bifurcation through the monitoring of total pressure recovery downstream. This would allow comparisons with other studies involveing static SCB.
- The development of a hinge mechanism would overcome some of the issues that were encountered with high levels of curvature and the effectiveness of the spanwise loading strips. Allowing freedom to rotate with the plate surface would enable the use of the linear actuators over a much wider range of plate stiffnesses.
- An element of closed-loop active control for adaptive SCB could be designed in order to further broaden the performance envelope.
  - A breathing cavity could be used with upstream and downstream bleeding to vary the pressure within. The variation in cavity pressure could be used to affect the surface deflection as well as the dynamics of the system depending upon the flow above the SCB.

– To explore optimal actuation heights with respect to incoming Mach number to enable optimal bump deployment across a wide range of operating conditions.

Bibliography

ABAQUS. Dassault Systèmes, Providence, RI, USA, 2007.

R. J. Adrian and J. Westerweel. *Particle Image Velocimetry*. Cambridge University Press, 2011.

AGARD-AR-138. Experimental Data Base for Computer Program Assessment. Technical report, NATO Advisory Group for Aerospace Research and Development.

P.J. Ashill, J.L. Fulker, and K.C. Hackett. Research at DERA on sub boundary layer vortex generators (SBVGs). In *AIAA Paper 2001-0887*, 2001.

P.R. Ashill, J. L. Fulker, and A. Shires. A Novel Technique for Controllling Shock Strength of Laminar-Flow Aerofoil Sections. In *First European Forum on Laminar Flow Technology*, pages 175–183, 1992.

H Babinsky and J.K. Harvey. *Shock Wave-Boundary-layer Interactions*. Cambridge University Press, 2011.

R. W. Barnell and M.Y. Hussaini. *Natural Laminar Flow and Laminar Flow Control*. Springer-Verlag, 1992.

T. Bein, H Hanselka, and E Breitbach. An adaptive spoiler to control the transonic shock. *Smart Materials and Structures*, 9(2):141–148, April 2000.

J. Birkemeyer, H. Rosemann, and E. Stanewsky. Shock control on a swept wing. *Aerospace Science and Technology*, 4(3):147–156, April 2000.

G. Bisignani. Vision 2050. *International Air Transport Association*, (Montreal - Geneva), 2010.

P. J. K. Bruce. *Transonic Shock / Boundary Layer Interactions Subject to Downstream Pressure Perturbations*. PhD thesis, Magdalene College, University of Cambridge, 2008.

Bibliography

P. J. K. Bruce and H Babinsky. An experimental study into the flow physics of three-dimensional shock control bumps. *Journal of Aircraft*, 49(5):1222–1233, 2012.

P. J. K. Bruce and S. P. Colliss. Review of research into shock control bumps. *Shock Waves*, October 2014.

R. Bur, B. Benay, B. Corbel, and M. Délery, J. Study of Control Devices Applied to a Transonic Shock Wave/Boundary Layer Interaction. In *Drag Reduction by Shock and Boundary Layer Control: Results of the Project EUROSHOCK II*, chapter 11, pages 133–152. Springer, 2002.

P. Busquin, P. Argüelles, M. Bischoff, B.A.C. Droste, R. H. Evans, W. Kröll, J.L. Lagardère, A. Lina, J. Lumsden, D. Ranque, S. Rasmussen, P. Reutlinger, R. Robins, H. Terho, and A. Wittlöw. European aeronautics: a vision for 2020 a synopsis. *Air & Space Europe*, 3(3-4):16–18, 2001.

L.M. Campo, D. B. Helmer, and J.K. Eaton. Validation Experiment for Shock Boundary Layer Interactions : Sensitivity to Upstream Geometric Perturbations. In *53rd AIAA/ASME/ASCE/AHS/ASC Structures, Structural Dynamics and Materials Conference 20th AI 23 - 26 April 2012, Honolulu, Hawaii AIAA 2012-1440*, number April, pages 1–18, 2012.

S P Colliss and H Babinsky. An experimental investigation of t hree-dimensional shock control bumps applied to transonic airfoils. In *50th AIAA Aerospace Sciences Meeting including the New Horizons Forum and Aerospace Exposition 09 - 12 January 2012, Nashville, Tennessee*, number January, pages 1–15, 2012.

S P Colliss, H Babinsky, K. Nübler, and T. Lutz. Vortical structures on three-dimensional shock control bumps. In *51st AIAA Aerospace Sciences Meeting including the New Horizons Forum and Aerospace Exposition*, number January, pages 1–15, Grapevine (Dallas/Ft. Worth Region), Texas, 2013. AIAA.

S. P. Colliss, H. Babinsky, K. Nübler, and T. Lutz. Joint Experimental and Numerical Approach to Three-Dimensional Shock Control Bump Research. *AIAA Journal*, 52 (2):436–446, February 2014.

P.H. Cook, M.A. McDonald, and M.C.P. Firmin. Aerofoil RAE 2822 - Pressure Distributions, and Boundary Layer and Wake Measurements. *Experimental Data Base for Computer Program Assessment, AGARD Report AR 138.*, 1979.

Bibliography

J. C. Crown and W. H. Heybey. Supersonic Nozzle Design. Technical Report 2, U.S. Naval Ordnance Laboratory, 1950.

G. Dargel and P. Thiede. Assessment of Shock and Boundary Layer Control Concepts for Hybrid Laminar Flow Wing Design. In *Drag Reduction by Shock and Boundary Layer Control: Results of the Project EUROSHOCK II*, chapter 21, pages 383–414. Springer, 2002.

Jean M Delery. Shock wave/Turbulent Boundary Layer Interaction and It's Control. *Progress in Aerospace Sciences*, 22:209–280, 1985.

G. Dietz. Passive Shock Control Concept for Drag Reduction in Transonic Flow. *Journal of Aircraft*, 42(3):794–799, May 2005.

E. Dowell. Nonlinear oscillations of a fluttering plate. *3rd and 4th Aerospace Sciences Meeting*, 4(7), January 1966.

E. H. Dowell. Panel Flutter: A Review of the Aeroelastic Stability of Plates and Shells. *AIAA Journal*, 8(3):385–399, 1970.

E. H. Dowell. Panel Flutter - NASA SP-8004. Technical Report June, 1972.

E. H. Dowell and H. M. Voss. the Effect of a Cavity on Panel Vibration. *AIAA Journal*, 1(2):476–477, 1963.

J.P. Dussauge and S. Piponniau. Shock/boundary-layer interactions: Possible sources of unsteadiness. *Journal of Fluids and Structures*, 24(8):1166–1175, November 2008.

J.P. Eastwood and J. P. Jarrett. Toward Designing with Three-Dimensional Bumps for Lift/Drag Improvement and Buffet Alleviation. *AIAA Journal*, 50(12):2882–2898, December 2012.

R. E. Gordnier and R. Fithen. Coupling of a nonlinear finite element structural method with a Navier Stokes solver. *Computers & Structures*, 81(2):75–89, February 2003.

A. Hartmann, M. Klaas, and W. Schröder. Time-resolved stereo PIV measurements of shockboundary layer interaction on a supercritical airfoil. *Experiments in Fluids*, 52 (3):591–604, March 2011.

B. König, M. Patzold, T. Lutz, E. Kramer, H. Rosemann, K. Richter, and H. Uhlemann. Numerical and Experimental Validation of Three-Dimensional Shock Control Bumps. *Journal of Aircraft*, 46(2):675–682, March 2009.

Bibliography

A. Kurganov and E. Tadmor. New high-resolution central schemes for nonlinear conservation laws and convection-diffusion equations. *Journal of Computational Physics*, 160(1):241–282, 2000.

M. Kutzbach, T. Lutz, and S. Wagner. Investigations on Shock Control Bumps for Infinite Swept Wings. In *2nd AIAA Flow Control Conference, June 27-July 1, 2004, Portland, OR*, pages 1–10, 2004.

J. C. Le Balleur, P. Girodroux-Lavigne, and H. Gassot. Prediction of Transonic Airfoil/Wing Flow and Buffet with Control Using a Time-accurate Viscous-Invscid Interaction Approach. In *Drag Reduction by Shock and Boundary Layer Control: Results of the Project EUROSHOCK II*, pages p285–313. Springer, 2002.

D. S. Lee, L. F. Gonzalez, J. Periaux, and G. Bugeda. Double-shock control bump design optimization using hybridized evolutionary algorithms. *Proceedings of the Institution of Mechanical Engineers, Part G: Journal of Aerospace Engineering*, 225(10):1175–1192, July 2011a.

D. S. Lee, J. Periaux, E. Onate, L. F. Gonzalez, and N. Qin. Active Transonic Aerofoil Design Optimization Using Robust Multiobjective Evolutionary Algorithms. *Journal of Aircraft*, 48(3):1084–1094, May 2011b.

D.S. Lee, G. Bugeda, J. Periaux, and E. Onate. Robust active shock control bump design optimisation using hybrid parallel MOGA. *Computers & Fluids*, March 2012.

J. C. Lin. *Review of research on low-profile vortex generators to control boundary layer separation*, volume 38. 2002.

X. Liu and L. C. Squire. An investigation of shock/boundary-layer interactions on curved surfaces at transonic speeds. *Journal of Fluid Mechanics*, 187:467, April 1988.

T. Lutz, A. Sommerer, and S. Wagner. Parallel Numerical Optimisation of Adaptive Transonic Airfoils. In *IUTAM Symposium - Transonicum IV*, pages 265–270. Kluwer Academic Publishers, 2003.

B. Massey and J. Ward-Smith. *Mechanics of Fluids*. CRC Press, eighth edition, 2006.

H. Maxwell and J. L. Jacocks. Non-Dimensional Calculation of Turbulent Boundary Layer Development in Two-Dimensional Nozzles of Supersonic Wind Tunnels. Technical Report January, 1962.

Bibliography

A. McCabe. Design of a Supersonic Nozzle. *London: Her Majesty's Stationary Office*, 1967.

D. C. McCormick. Shock/boundary-layer interaction control with vortex generators and passive cavity. *AIAA Journal*, 31(1):91–96, January 1993.

C. Mei, K. Abdel-Motagaly, and R. Chen. Review of non-linear panel flutter at supersonic and hypersonic speeds.pdf. *Applied Mechanics Reviews*, 52(10):321–332, 1999.

E. Millholen II, W. and R. Owens, L. On the Application of Contour Bumps for Transonic Drag Reduction (Invited). *AIAA Journal*, 0462:1–19, 2005.

NASA. http://www.grc.nasa.gov.WWW/wind/valid/raetaf/raetaf.html, 2017. Last accessed 12th February 2017.

K. Nübler, T. Lutz, Ewald Krämer, S P Colliss, and H. Babinsky. Shock Control Bump Robustness Enhancement. In *50th AIAA Aerospace Sciences Meeting including the New Horizons Forum and Aerospace Exposition*, number January, Nashville, Tennessee, 2012.

H. Ogawa. *Experimental and Analytical Investigation of Transonic Shock-wave / Boundary-layer Interaction Control with Three-dimensional Bumps.* PhD thesis, Clare Hall College, Cambridge University, 2006.

H. Ogawa, H. Babinsky, M. Patzold, and T. Lutz. Shock-Wave/Boundary-Layer Interaction Control Using Three-Dimensional Bumps for Transonic Wings. *AIAA Journal*, 46(6):1442–1452, June 2008.

OpenFOAM. www.openfoam.org, 2017. Last Accessed 12th February 2017.

M. Pätzold. Numerical Optimization of Finite Shock Control Bumps. In *44th Aerospace Sciences Meeting and Exhibit*, pages 1–13, Reno, Nevada, 2006.

S. Piponniau, J. P. Dussauge, J. F. Debiève, and P. Dupont. A simple model for low-frequency unsteadiness in shock-induced separation. *Journal of Fluid Mechanics*, 629: 87, June 2009.

N Qin, W S Wong, and A Le Moigne. Three-dimensional contour bumps for transonic wing drag reduction. *Proceedings of the Institution of Mechanical Engineers, Part G: Journal of Aerospace Engineering*, 222(5):619–629, August 2008. ISSN 0954-4100.

Bibliography

M. Raffel, C. E. Willert, S. Wereley, and J. Kompenhans. *Particle Image Velocimetry: A Practical Guide*. Springer, 2007.

O Rhodes. *Optimal Design of Morphing Structures*. Phd thesis, Imperial College London, 2012.

O Rhodes and M Santer. Aeroelastic Optimization of a Morphing 2D Shock Control Bump. In *53rd AIAA/ASME/ASCE/AHS/ASC Structures, Structural Dynamics and Materials Conference 20th AI 23 - 26 April 2012, Honolulu, Hawaii AIAA 2012-1440*, pages 1–17, 2012.

W. Roberson, R. Root, and D. Adams. Fuel Conservation Strategies: Cruis Flight. *Boeing: Aero Quarterly QTR_04 — 07*, pages 22–27, 2007.

H. Rosemann and J. Birkemeyer. Experimental Investigation of the Transonic Airfoils ADIF and DA LVA-1A and the ADI Sheared Wing wih and without Control. In *Drag Reduction by Shock and Boundary Layer Control: Results of the Project EUROSHOCK II*, chapter 20, pages 359–382. Springer, 2002.

H Rosemann, J Birkemeyer, and A Knauer. Shock Control by Adaptive Elements for Transportation Aircraft Wings. In *RTO AVT Symposium on Active Control Technology for Enhanced Performance Operational Capabilities of Military Aircraft, Land Vehicles and Sea Vehicles, Braunschweig, Germany, 8-11 May 2000*, pages 8–11, 2000.

F. Sartor, G. Losfeld, and R. Bur. PIV study on a shock-induced separation in a transonic flow. *Experiments in Fluids*, 53(3):815–827, June 2012.

G.B. Schubauer and W.G. Spangenberg. Forced mixing in boundary layers. *Journal of Fluid Mechanics*, 8(1):pp. 10–32, 1960.

J. Seddon. The Flow Produced by Interaction of a Turbulent Boundary Layer with a Normal Shock Wave of Strength Sufficient to Cause Separation . Technical report, Guggenheim Aeronautical Laboratory, California Institute of Technology, Pasadena, California, 1967.

G. S. Settles. *Schlieren and Shadowgraph Techniques*. Springer, 2001.

A.H. Shapiro. *The Dynamics and Thermodynamics of Compressible Fluid Flow, Volume 1*. Ronald Press, 1953.

Bibliography

A. Sommerer, Th. Lutz, and S. Wagner. Numerical Optimization of Adaptive Transonic Airfoils with Variable Camber. In *Proceedings 22nd ICAS Congress, Harrogate, UK*, 2000a.

A. Sommerer, Lutz. Th., and S. Wagner. Design of Adaptive transonic Airfoils by Means of Numerical Optimization. In *Proceedings ECCOMAS 2000: European Congress on Computational Methods in Applied Sciences and Engineering*, page 379, 2000b.

P.R. Spalart and S.R. Allmaras. A One-Equation Turbulence Model for Aerodynamic Flows. In *30th Aerospace Sciences Meeting and Exhibit*, volume 0439, Reno, Nevada, 1992.

E. Stanewsky. Aerodynamic benefits of adaptive wing technology. *Aerospace Science and Technology*, 4(7):439–452, October 2000.

E. Stanewsky, J Délery, J. L. Fulker, and W. Geissler. *Euroshock - Drag Reduction by Passive Shock Control: Results of the project EUROSHOCK*. Friedrich Vieweg & Sohn Verlagsgesellschaft mbH, 1997.

E. Stanewsky, J Délery, J. L. Fulker, and P. de Matteis. *Drag Reduciton by Shock and Boundary Layer Control: Results of the Project EUROSHOCK II*. Springer, 2002.

J. Threadgill and P. Bruce. Shock Wave Boundary Layer Interaction Unsteadiness: The Effects of Configuration and Strength. In *54th AIAA Aerospace Sciences Meeting*, San Diego, California, USA, 2016.

James a. S. Threadgill and Paul J. K. Bruce. Unsteadiness in Shock Wave Boundary Layer Interactions across Multiple Interaction Configurations. *53rd AIAA Aerospace Sciences Meeting*, (January):1–17, 2015. doi: 10.2514/6.2015-1977.

Yun Tian, PeiQing Liu, and PeiHua Feng. Shock control bump parametric research on supercritical airfoil. *Science China Technological Sciences*, 54(11):2935–2944, September 2011.

M. Tucker. Approximate turbulent boundary layer development in plane compressible flow along thermally insulated surfaces with application to supersonic tunnel contour correction, 1950.

J. J. Vallee. Application of Shock and Boundary Layer Control to a Business-jet Aircraft. In *Drag Reduction by Shock and Boundary Layer Control: Results of the Project EUROSHOCK II*, pages 433–449. Springer, 2002.

Bibliography

B. Van Leer. Towards the Ultimate Conservative Difference Scheme, V. A Second Order Sequel to Godunov's Method. *Journal of Computational Physics*, 32(1):101–136, 1979.

V. V. Vedeneev, S. V. Guvernyuk, A. F. Zubkov, and M. E. Kolotnikov. Experimental observation of single mode panel flutter in supersonic gas flow. *Journal of Fluids and Structures*, 26(5):764–779, 2010.

Miguel Visbal. Viscous and inviscid interactions of an oblique shock with a flexible panel. *Journal of Fluids and Structures*, (1975), 2014.

M.R. Visbal. On the interaction of an oblique shock with a flexible panel. *Journal of Fluids and Structures*, 30:219–225, April 2012.

W. Wadehn, A. Sommerer, Th. Lutz, D. Fokin, G. Pritschow, and S.Wagner. Structural Concepts and Aerodynamic Design of Shock Control Bumps. In *ICAS 2002 Congress*, 2002.

Jerry Westerweel, Gerrit E. Elsinga, and Ronald J. Adrian. Particle Image Velocimetry for Complex and Turbulent Flows. *Annual Review of Fluid Mechanics*, 45(1):409–436, 2013.

W.S. Wong, N. Qin, N. Sellars, H. Holden, and H. Babinsky. A combined experimental and numerical study of flow structures over three-dimensional shock control bumps. *Aerospace Science and Technology*, 12(6):436–447, September 2008. ISSN 12709638.

Bedri Yagiz, Osama Kandil, and Y. Volkan Pehlivanoglu. Drag minimization using active and passive flow control techniques. *Aerospace Science and Technology*, 17(1): 21–31, March 2012.

A. Appendix: Design and Manufacture of Wind Tunnel

The framework for a supersonic wind tunnel has been tested at Mach 2 and the wall pressure measurements confirm a Mach 2.02 flow in the working section. The examples of shock control in chapter 2 are primarily aimed towards normal shocks which are only really feasible below Mach 1.5 due to the large total pressure losses above this level. Therefore in order to simulate the shock strength upon a NLF aerofoil a Mach 1.4 nozzle was proposed in order to achieve a similar shock strength to that on the upper surface of the wing. This will allow for the testing of SCBs on both a macro (bump geometries) and micro (flow structure) scale.

The current facility consists of four 12 m^3 high-pressure tanks storing dried air at 2.7MPa. The temperature of which is atmospheric and within the range 290< T_{atm} <300K with a unit Reynolds number of approximately 2.2×10^7 /m. The upstream pressure is managed via a PID control system in LabView that is able to maintain the steady stagnation pressure level to within ± 0.01 bar.

A.1. Converging-Diverging Nozzle

The principles behind a converging-diverging nozzle were developed by de Laval in 1888 in which subsonic flow is accelerated to sonic conditions by the means of a favourable pressure gradient and a converging cross-section. When M = 1 the cross-sectional area needs to increase in order to continue accelerating the flow, this is shown in equation A.1 and is the only way to achieve supersonic velocities.

$$(\mathrm{M}^2 - 1)\frac{\mathrm{dV}}{\mathrm{V}} = \frac{\mathrm{dA}}{\mathrm{A}} \tag{A.1}$$

The design of such nozzles that produce a high quality flow field is very difficult and the iterative design process begins with the breakdown of the nozzle into three key areas: subsonic compression, throat and supersonic expansion regions.

Supersonic Expansion

The diverging region of the nozzle is a critical part of the nozzle as the accuracy of this section determines the quality of the flow in the tunnel working section. Many investigative articles [Shapiro, 1953, Maxwell and Jacocks, 1962, McCabe, 1967] along with review type articles, [Crown and Heybey, 1950] have tried to analyse the methods available for designing supersonic nozzles from a physical perspective rather than a mathematical point of view.

The method of characteristics featured in nearly all of the solutions evaluated, Busemann's, Puckett's and also Foelsch's methods, (reviewed by Crown and Heybey), all begin with an initial inflection that results in Prandtl-Meyer expansion waves emanating from the corner. The inviscid analytical solution can handle this however in practise a discrete turning angle is not ideal for the boundary layer and will be discussed further in §A.1.1. After the initial expansion the methods differ but that of Puckett and Foelsch began to quantify this to be half of the maximum turning angle for a given Mach number. This then set the angles of the expansion waves and hence the downstream concave section could be calculated to cancel these waves. Visualisations of these calculations are presented in figure A.1. The accuracy of the recreated area ratio is to within 0.01% of the Mach 1.4 isentropic value.

The element of viscosity complicates the procedure as not only does it effect the wall-reflection angle of the Mach waves, varying density gradients, but also the affective area ratio along the length of the nozzle. The most common method to overcome this was to introduce a boundary layer thickness correction which opens up the rearward section to allow for boundary layer growth. The method apparent in the present Mach 1.4 nozzle was developed by Tucker [1950] and has been successfully implemented in the existing Mach 2 nozzle.

A.1.1. Throat Region

The structure of the throat section relies heavily upon the turning properties of transonic Mach numbers and the corresponding gradients. Two-dimensional CFD results suggested that by using the existing setup as depicted in figure A.2 that the sonic line would be extremely curved; to the extent where the pressure waves emanating from the initial expansion were affected and as such were not cancelled by the wall further downstream. This feature is discussed in §A.1.2. The result of this would have been a working section with many undesirable pressure waves.

The initial expansion region has so far been approximated as a sudden $\nu/2$ change

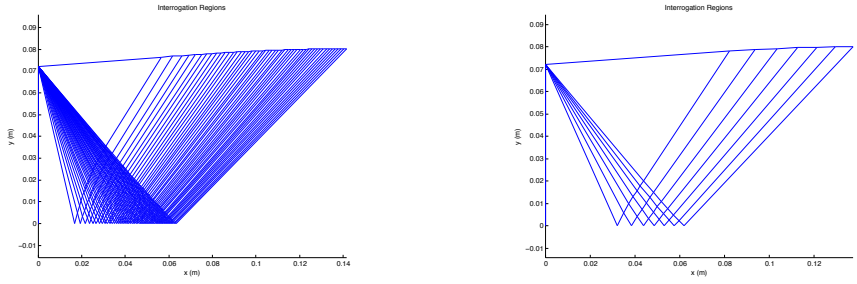


Figure A.1.: Method of characteristics generated nozzle. a) Large number of Mach waves. b) Low number of Mach waves

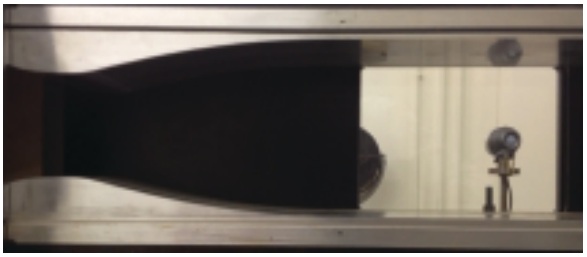


Figure A.2.: Mach 2 wind tunnel

but in practise a smoother round would preserve the health of the boundary layer sensitive transonic region. By applying a round that ensured a smooth transition between the subsonic and supersonic regions, the radius of curvature was determined by complementing the subsonic section and incorporating a $^{\Delta\nu}/_{l} = 1$ mm/° change up to $\nu/2$ where it met the diverging section from §A.1.

A.1.2. Subsonic Contraction

Due to the favourable pressure gradient present at this stage the subsonic compression is often designed by creating a smooth curve from the upstream sections to the throat. In the existing Mach 2 nozzle this was achieved by using a hyperbolic function shown in equation A.2, this was used for the section immediately upstream of the throat and inverted for initial compression.

$$y^2 = 1 + \frac{x^2}{2R} \tag{A.2}$$

The existing compression stage to the throat was split between a polymer resin and a machined aluminium block. The ramp angle of the resin section, (66°), was too great for the near-sonic conditions present so close to the Mach 1.4 throat despite the favourable pressure gradient present. As such geometries with reduced gradients had to be tested in order to accelerate the flow towards the throat without separation occurring during initial expansion and also to minimise the curvature of the sonic line.

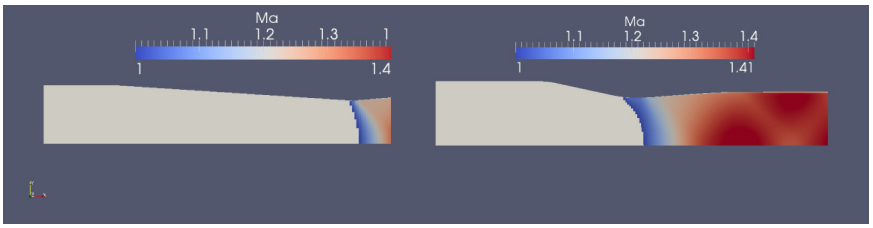


Figure A.3.: a) Controlled contraction gradient (-0.4) geometry. b)Controlled contraction gradient (-1.2) geometry.

It was found that by controlling the gradient of the geometry produced by the hyperbolic curve, the turning angle of the flow could be restrained to such a point that the detrimental separation after the initial expansion was negated. By limiting the maximum gradient the length of the subsonic compression stage became much longer and requires further modification to the upstream section of the tunnel. Other negative effects that could arise due to this increase in length are increases in boundary layer height, however due to the significant favourable pressure gradient over this region the subsonic portion has little effect, [McCabe, 1967]. Despite the expense and complexity the benefits of a straighter sonic line and clean expansion are feasible.

The success of this nozzle will be revealed upon installation within the supersonic wind tunnel and analysed with the Schlieren imaging system. Most of the pressure waves that emanate from the initial expansion are expected to be cancelled out prior to the working section. The boundary layer height is expected to be $\backsim \mathcal{O}(5\text{ mm})$.

B. Appendix: PIV Calculations

Magnification Factor

$$M_0 = \frac{\text{Sensor size}}{\text{Field of View}} = \frac{25.6\,\text{mm}}{165\,\text{mm}} = 0.155 \tag{B.1}$$

f = 105 mm, z_0 = XX

$$\frac{1}{f} = \frac{1}{z_0} + \frac{1}{Z_0} \tag{B.2}$$

Particle image diameter

$$d_\tau = \sqrt{{M_0}^2 {d_p}^2 + d_{diff}^2} \tag{B.3}$$

The particle image diameter is an influential variable in the quality of the PIV study. Raffel et al. [2007] conducted a Monte-Carlo optimisation study on the effect of particle image size upon the RMS-uncertainty of the results. The results showed that for single exposure double frame imaging the optimal values of particle image size varied between $2 < d_\tau < 2.5$ for window sizes of 16, 32 and 64 pixels whereas for a double exposure single frame the optimal values were much closer together with a value of $d_\tau \sim 1.6$pixels. By aiming to achieve similar values, the uncertainty in the particle image diameter in order to avoid peak locking. This is caused by errors in the sub-pixel approximation methods which skew the correlation algorithms which are attempting to find the precise location of the peak intensity.

Diffracted limited minimum image diameter

$$d_{diff} = 2.44(1 + M_0)\lambda f^{\#} d_{diff} = \quad 8.11\,\mu\text{m} \tag{B.4}$$

$f^{\#}$ is the ratio of the focal length to aperture. With a fixed focal length lens the ratio directly affects the size of the aperture and hence the amount of light that enters the lens. Whilst a low $f^{\#}$ allows for more light to pass through the aperture the optical quality is reduced. This is due to the smaller f-numbers having a significant effect upon the depth of thickness, equation/refe:Depth which becomes problematic when attempting to track

small seed particles. Typically $f^{\#} > 5.6$ provide a suitable level of light intensity for a depth of field that is manageable in transonic flows Raffel et al. [2007].

The diffraction limited imaging diameter is an artefact of observing light on a plane from a distance. The reader is again referred to Raffel et al. [2007] in particular chapter 2.6 which provides a very good description of the physics behind the limit. The value d_{diff} represented the smallest particle image that can be obtained for a given experimental setup. This lower bound dictates the field of view than can be obtained for a given lens/sensor arrangement.

Particle image diameter - pixel pitch ratio Raffel et al. [2007]

$$\frac{d_\tau}{d_r} \approx 2 - 4 \tag{B.5}$$

This factor is based upon RMS error values with the requirement that the particle image diameter covers between two and four pixels. This is in order to provide the correlation algorithms with a large enough region of intensity to calculate the displacement. With a sensor size of 25.6 mm and a resolution of 2560 pixels, the pixel pitch is 10 μm, this is equivalent to 86.96μm in the image plane.

Out-of-plane Motion

$$|\Delta z| < \frac{1}{4}\Delta Z_0 \tag{B.6}$$

In order to preserve the quality of the results the out-of-plane movement is ideally minimised, of course there are three-dimensional flows where this is unavoidable but the premise is that any given particle should not disappear between the two frames. This can be estimated from a basic understanding of the flow as $|\Delta z| = u_z \Delta t$ however this can be difficult to predict. In such cases it is common to trial reduce Δt to reduce the overall movement of the particles or to increase the thickness of the laser sheet ΔZ_0.

In-plane Motion

$$|\Delta X| < \frac{1}{4}D_I \tag{B.7}$$

$$\text{where} \quad D_I = \text{window size} \times d_r$$

Through a similar method to the initial estimation of the out-of-plane velocity, an initial in-plane velocity can be used to aid the optical setup of the experiment. From a wealth of previous experiments a rule-of-thumb method to ensure suitable velocity measurements is to allow the particles to move a quarter of the interrogation window

each δt. This effectively controls the sizing of the experiment in terms of camera position, lens focal length and ultimately the field of view and the length scales that will be possible to resolve from the results. A typical starting point is to assume a standard interrogation window of 32×32 pixels. Calculating the physical size of one pixel at $10\,\mu$m and $M_0 = 0.115$ a distance can be found.

The velocity of the fluid can be approximated by assuming isentropic flow relations between the settling chamber and the working section providing there are no discontinuities in the form of shock waves. With the total temperature of the fluid being at atmospheric conditions $T_0 \approx 300\,k$ and the flow being accelerated to Mach 1.4, the static temperature is calculated to be $T \approx 215\,K$ using the following relationship:

$$\frac{T_0}{T} = 1 - \frac{(\gamma - 1)}{2} M^2 \tag{B.8}$$

$$\begin{aligned} dt =& \frac{1}{4} . \frac{D_I}{M_0 \times U_{approx}} \\ dt =& \frac{1}{4} . \frac{32 \times 10 \times 10^{-6}}{0.115 \times 411.48} \\ dt =& 1.69\,\mu\text{s} \end{aligned} \tag{B.9}$$

Where U_{approx} is calculated as follows:

$$\begin{aligned} U_{approx} =& M\sqrt{\gamma RT} \\ U_{approx} =& 1.4\sqrt{1.4 \times 287 \times 215} \\ U_{approx} =& 411.48\,\text{m/s} \end{aligned} \tag{B.10}$$

Spatial gradient limitation

$$M_0 |\Delta u| \Delta t < d_\tau \tag{B.11}$$

The variation of the local displacement should not exceed the particle image diameter. This parameter aims is often used after the image collection during PIV processing in order to determine sutiable values for the magnification factor and Δt.

Depth of field

$$\begin{aligned} \delta_z \cong& 4 \left(1 + \frac{1}{0}\right)^2 f^{\#2} \lambda \\ \delta_z =& 6.27\,\text{mm} \end{aligned} \tag{B.12}$$

As the all of the particles lying within the $\pm(\delta_z/2)$ of the plane produces images that are captured on the CCD. This leads to the requirement of:

$$\delta_z \cong 4\left(1+\frac{1}{0}\right)^2 f^{\#2}\lambda \geq \Delta Z_0 \tag{B.13}$$

M_0	FOV	$f^{\#}$	λ	d_{diff}	d_τ	δ_z	dt
0.155	$165 \times 110\,\mathrm{mm}^2$	5.6	532 nm	8.11μm	8.12μm	6.27 mm	1.69μs

Table B.1.: Key PIV experiment setup parameters.